THE UNIVERSITY *of* EDINBURGH

Towards Implanted Biosensors: Methods for Miniaturising and Protecting Peptide-Based Electrochemical Sensors

Ahmet Uçar

Thesis submitted for the degree of Doctor of Philosophy

The University of Edinburgh

2020

Ah, kimselerin vakti yok
Durup ince şeyleri anlamaya

Kalın fırçalarını kullanarak geçiyorlar
Evler çocuklar mezarlar çizerek dünyaya

======

Oh, no one's got the time
to stop'n think about fine things

With broad brush-strokes they move along
Sketching homes kids graves onto the world

Gülten Akın
(Translated by Saliha Paker and Mel Kenne)

Lay Summary

A drug or treatment which perfectly cures our neighbour is not necessarily as effective for us. This is because each person is a combination of their genetic inheritance, lifestyle, microbiome, the presence or impact of other conditions and environmental influence. Personalised therapy could potentially offer the most efficient treatment option for each individual patient and can help to enhance the treatment efficacy for major diseases. To achieve this, clinical and diagnostic data need to be taken from specified locations in the body, to provide significant and specific information about the disease and the patient. For cancer, one important location is the microenvironment of a tumour, which includes many types of biochemical systems: proteins, enzymes and cells, some of which are found in varying amounts and with established roles as cancer signallers and thus can be used to classify patients. Specifically, an enzyme family, the proteolytic enzymes (called proteases), are linked to all steps of cancer development, spread and even suppression. Therefore, selective and sensitive detection of proteases inside tumours would enable increased understanding of each individual cancer case and inform corresponding treatment development such as radiotherapy.

It is not however so simple to place a sensing device into the body and take continuous and long term measurements. First of all, the sensor should be tiny enough to avoid any damage to the body (implant site) or itself during surgical implantation and over the course of measurements. Secondly, it should be biocompatible and it is thus less affected by biofouling, which is the passivation of the active sensing area by fibrous capsules and proteins due to the immune response against foreign substances. For a biocompatible device or material, this immune response can be minimised and tolerated for short durations, i.e. to allow the required analyses to be completed.

Accordingly, this research has investigated key developments to enable this approach; the effects of miniaturisation and of protection of a specific peptide-based electrochemical biosensor which has been developed for protease detection. Results have revealed for the first time that this sensing system is able to be miniaturised either using commercial microelectrodes or on in-house developed microelectrode and nanoelectrode arrays. Also, anti-biofouling properties were seen to be improved by incorporating a pH-triggered dissolving polymeric coating which also offered controllable delayed activation. This work, in summary, has contributed to the development of this peptide-based electrochemical biosensor system and enhanced its potential for application as an implanted biosensor.

Abstract

There is real interest in developing selective and sensitive tools to detect protease activity; these play pivotal roles in cancer progression with changes in their amounts and types linked to several pathological processes such as tumour formation, evolution and even suppression. Peptide-based electrochemical assays have been shown to offer several potential advantages over other tools and techniques for development into sensing systems. However, their implantation and use *in vivo* is complex as they face serious limitations when considering two vital requirements for implantation: sensor miniaturisation for ready implantation and localised measurement and controlled anti-biofouling protection. This study presents the investigation and analysis of these miniaturisation- and protection-related issues and the development of solutions as key steps towards the localised *in vivo* application and measurements.

The first part of the presented work focuses on the potential for assay miniaturisation. This used commercial platinum microelectrodes which were modified with self-assembled monolayer (SAM)-based protease sensing probes. Building on previous macroelectrode studies, which have explored and optimised the use of different SAM structures, redox labelling, anchor type and various spacers of different lengths, further optimisation was carried out with the aim of developing and defining an optimum microelectrode protocol. Comparison of the quantitative analytical performance of macro- and microelectrode systems established the feasibility of developing miniaturised platforms for efficient and clinically-relevant protease detection. Interestingly, significant differences were observed such as an enhanced reproducibility and decreased cleavage rate for the microelectrodes, which were thought to be indicative of variation in the SAM probe film structure on these electrode surfaces caused by differences in film deposition kinetics. This decreased cleavage (response) rate was mitigated by measurement at normal body temperature which was shown to increase kinetics and suggested the possibility of more rapid in vivo sensing.

These miniaturisation findings on commercial microelectrodes were translated to in-house microelectrodes fabricated as platinum thin film-on-silicon chips. Initial results showed reduced SAM probe stability. As the use of stronger SAM probe anchoring (through tripod-anchored probes) did not solve this problem, the underlying reason was attributed to structural differences between the surfaces of commercial and in-house electrodes, resulting in enhanced Pt detachment in the latter. Increasing metal film thickness and post-fabrication annealing did

not completely overcome this problem, and the remaining decrease in stability was attributed to increased Pt surface roughness and destabilisation through successive electrochemical oxidation and reduction during acidic cleaning. An alternative electrochemical reductive cleaning method was thus developed and tested on enhanced electrode sensing systems; arrays of microelectrodes (MEA) and microcavity nanoband edge electrodes (MNEE) were fabricated, cleaned using this reductive method, characterised using typical redox couples and then tested for protease sensing. Gratifyingly, these systems were found to be sufficiently reproducible and stable for sensing. Although functionalised MNEEs achieved significantly higher current densities, there was no great enhancement of response rate from decreasing electrode size from micro to nano, consistent with the fact that diffusional transport is not the rate determining step in this cleavage reaction. Given the variability of probe film deposition characteristics and the resulting cleavage rates, the applicability of potential-controlled SAM probe deposition for controlling probe film formation was investigated as a proof-of-concept study.

The second part of this work concentrated on the development of a sensor protection and activation strategy against biofouling. A pH-triggered dissolvable polymeric coating was drop-cast onto clean and probe-modified electrodes and then characterised in terms of the delayed activation time, enhancement in anti-biofouling properties and retention of sensing characteristics. These results demonstrated that reproducible delayed sensor activation was achieved and controlled by optimising parameters such as coating thickness, homogeneity and density through the coating method and temperature. Comparative evaluation of polymer-coated and uncoated probe-modified electrodes in a biologically relevant medium also revealed significant improvement in their anti-biofouling characteristics.

Acknowledgements

PhD is already a tough journey by its nature. It would not have been thus possible to complete without support from the names mentioned below.

First of all, I'd like to express my sincere gratitude to my supervisors, Prof. Alan F. Murray and Prof. Andrew R. Mount for all their guidance, analytical perspectives and time which they have provided to me throughout this study. Also, Prof. Mark Bradley was always there and open for any scientific discussion whenever I have asked for help.

I'd like to thank the Republic of Turkey, Ministry of National Education for providing me financial support under the YLSY doctoral scholarship programme. Royal Society of Chemistry should be also acknowledged for enabling me to attend conferences through granted funding.

Colleagues mean a lot for scientific research. Therefore, I want to thank Dr. Eva Gonzalez-Fernandez for all aspects of electrochemistry knowledge that she shared with me, Dr. Matteo Staderini for chemical synthesis, Dr. Andrew Piper, Dr. Ewen O. Blair and Dr. Ilka Schmueser for electrode fabrication. Also, thanks to the IMPACT team (Andreas, Anthony, Cami, Dan, Jamie, Jon, Stewart) as well as the present and former members of the Mount Research Group (Damion, Dimitrios, Fiona, Hannah, Ian, Justin, Nigel, Simon and Ugne).

Friends are the ones keeping a person sane in this craziness. All of our discussions while drinking coffee or playing a game or a sightseeing has been lots of fun; Anil, Kerem, Muhammed and Tezcan. Members of Senturk family have been always helpful and caring; Melike, Sinan and my new pal Atlas. It has been also great to have many other lovely friends in Edinburgh including Bibo, Bozkan, Ceren, Ekrem, Esra, Gokcen, Hakan, Hasan, Meric, Merve, Oguzhan, Tulin and Zeynep. Although my former colleagues, Merve and Pinar, and all-time pals Erkan, Goksel, Ismail, Ozan and Mustafa are kilometres away now, I know only a phone call or a message will be enough for them to be stand by me.

Family is the core of the life. Hence, I am pleased to become more resembled to you while time flies, Birgul and Suleyman.

Dedicated to the memory of my grandparents.

Contents

Chapter 1

==========

Introduction

1.1 Motivation

All humans are different. Each person is specified by a combination of genetic inheritance, lifestyle and environment. It is also the main reason why people exhibit dissimilar health conditions during their life such as having particular diseases, different responses to the same therapy and varying recovery rates. Personalised therapy (also called as personalised medicine) aims to deliver the optimum and the most efficient treatment to each patient, identified by extensive analysis of clinical and diagnostic data sets in combination with genomic information [1]. Although it is only a few decades old, it has been already established that personalised therapy improves the chances of a cure in major diseases such as cancer, where early diagnosis and informed treatment have the most significant effect on survival [2]. A personalised therapy plan for preventing, monitoring and treating cancer usually consists of

(i) estimating the potential of developing cancer
(ii) finding the most appropriate techniques/strategies to minimise additional risks
(iii) comparative analysis of the group of people showing similar monitoring/screening to select the most effective treatment with the lowest side effects
(iv) determination of recurrence possibilities to inform longer term monitoring [3].

However, the rapidly changing and heterogeneous nature of the cancerous tumour microenvironment is a challenge for the determination of an optimal therapy procedure. This characteristic feature of tumours requires monitoring their real time status in terms of localised and transitory changes in such factors as hypoxia, pH and key biomarkers which are expected to show whether and how tumours will respond/have responded to courses of radiotherapy and/or chemotherapy [4]. In the light of the knowledge that proteolytic enzymes, also called proteases, are one of the key biomarkers found in tumour microenvironment and are related to all stages of cancer formation and progression [5], development of selective and sensitive detection tools are needed to investigate and understand protease activities and how these relate to cancer progression and diagnosis.

The latest developments in protease assays, employing peptide-based electrochemical biosensors prepared using self-assembled monolayers (SAMs) on electrode surfaces, have attracted widespread attention [6]. Despite peptide-based electrochemical protease assays have been shown to offer sensitive and rapid responses, it was emphasised that there is still an unmet

need of the biosensor development for disease-related proteases, in addition to commonly used models, and the characterisation of their feasibility/performance as well as corresponding interference-related challenges in a complex biological environment [6]. Previous background works showed the sensitive detection of trypsin in a buffer including some protein-based and ionic interferents [7], and the activity of polymorphonuclear neutrophil directly from blood samples [8]. This demonstrates their great potential in personalising the therapy by undertaking a pivotal role in unravelling the complicated protease-tumour connections. This study thus concentrates on the production of useful miniaturisation and protection strategies to enhance the development of peptide-based electrochemical biosensor systems further, bring them closer to implantation and *in vivo* biosensing. Beyond this, it is believed that the validity and relevance of this study's findings with prospective electrochemical biosensor research contribute significantly to the knowledge in the area.

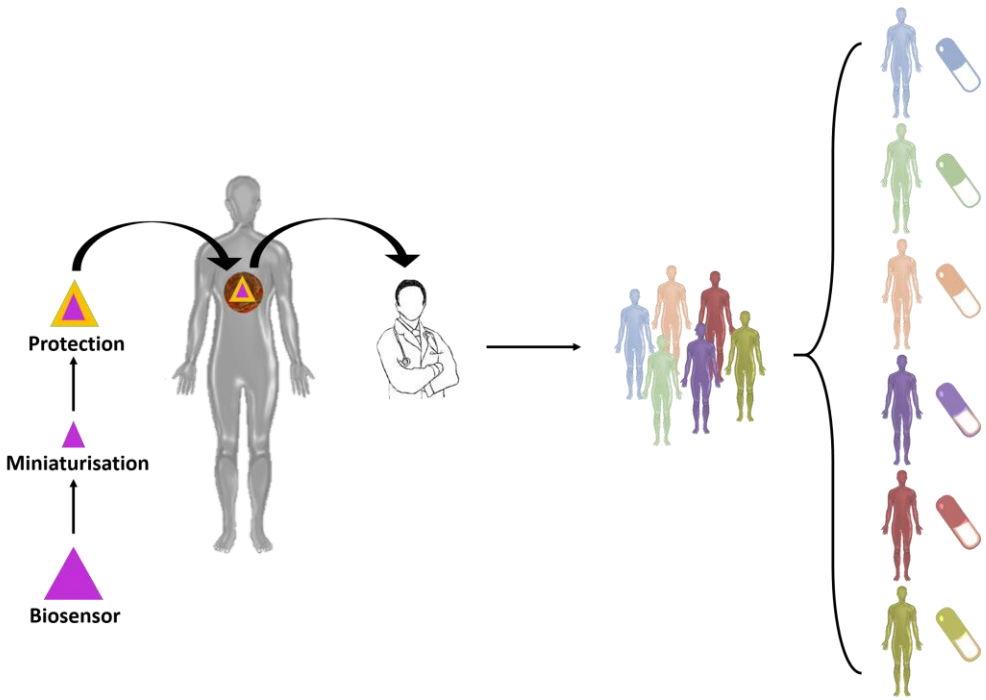

Figure 1-1: Schematic illustration of using implantable biosensors for personalised therapy. Implantable biosensing devices enhanced with effective miniaturisation and protection strategies can enable *in vivo* measurements, deliver these valuable clinical and diagnostic data to the clinicians and the most efficient treatment can then be applied to each specified patient.

1.2 Problem Statement

Developing an electrochemical peptide-based protease sensor system which can be implanted into a solid tumour and successfully measures time-dependent changes in protease quantity and activity would promote the personalisation of cancer therapy markedly. However, two main concerns for an implantable sensor project need to be addressed:

Miniaturisation

An implantable biosensor should be as small as possible. This is vital in order to ease the pain of the implantation process, to minimise the possibility of damage to the targeted tissue or sensor platform, to enable local measurement and to reduce the extent of local wound healing/foreign body response [9]. Production of electrodes in smaller dimensions (scaling-down) is a requirement for the miniaturisation of an electrochemical biosensor and it is also very effective for the sensor performance [10]. Luckily, state of the art microfabrication techniques enable and extend the use of micro- and nanoelectrodes in medical applications. In addition, more numbers of electrodes with smaller dimensions can be patterned (in arrays) onto a defined substrate area compared to larger electrodes, which will eventually contribute to the multiplexed measurement opportunities (of control samples and other target analytes). However, it should be noted that arrays have bigger footprints and their use might result in increases in the biosensor dimensions. Therefore, the electrode design needs to be optimised carefully, considering all these possible impacts. The kinetics, for example, is another variable which might be seriously affected due to the changes in mass transport when chemical recognition (sensing) elements are immobilised on smaller electrode surfaces. It is also worth noting that there are not enough settled models of the formation and re-organisation of SAM-based recognition probes, although SAMs have been studied for a long time and pretty much explored [11]. This might lead to more questions to appear, especially when the recognition elements are immobilised onto a minimised electrode region via self-assembly. Furthermore, electrode/substrate material used for the fabrication/miniaturisation of biosensors is vital and it should be cost-efficient, sensitive, biocompatible and ease of use (and access) [12]. Although gold (Au) is known as the most common substrate for SAMs of thiols, platinum (Pt) is preferred for long-term implant applications lately due to less corrosion observed compared to Au [13]. This requires comparative analysis of Au and Pt electrodes to understand which provides more feasibility for SAM-based recognition elements.

Biocompatibility

The second major concern for an implantable biosensor is foreign body response (FBR) which may arise in a combination of short term (non-specific protein adsorption, acute inflammation) and long term effects (biofouling). Although these have been found to influence any implanted material (more or less depending on a biocompatibility characteristics), even short term effects will be most likely deteriorating for an (electro)chemical biosensor. Because even if a number of electrochemical biosensor systems does not consist of an open and active recognition layer directly interacting with environment (but mostly they do), fibrous encapsulation as a long term effect of FBR, will be fatal for the detection inhibiting their access to targeted analytes. Accordingly, a sensor system employing redox tag-labelled SAM-functionalised peptides immobilised onto an electrode surface as the recognition element will specifically need a strategy which can maintain *in vivo* sensing, whilst being less/no affected by biofouling.

1.3 Objectives

This PhD study has targeted to address the problems stated in the previous section by;

- Developing a peptide-based electrochemical biosensor for detection of trypsin using conventional bulk platinum microelectrodes and investigating the effects of electrode miniaturisation on sensor performance in comparison to the gold and platinum macroelectrode-based sensing platform

- Translating the optimised sensor to in-house fabricated thin film platinum micro- and nanoelectrode architectures on silicon chips

- Evaluating the impact of potential-assisted SAM probe deposition method in terms of preparation time and sensor performance

- Analysing the feasibility of pH-responsive dissolvable polymeric coatings for delayed activation and biofouling protection of electrochemical protease and pH biosensors

Accordingly, this study aims to explore the feasibility of an optimised and miniaturised electrochemical protease biosensor which is protected and then activated by a pH-dissolvable polymeric coating.

1.4 Thesis Outline

This thesis consists of eight chapters in total focusing on background and theory, experimental methods for preparation and analysis, optimisation, characterisation and derived conclusions with some suggestions of future work.

Chapter 2 presents background information on cancer, the significance of the tumour microenvironment for cancer monitoring and the employment of biosensors for this purpose. Also, this is a literature review of the challenges and limitations of *in vivo* biosensing and a number of biosensor protection technologies. The theoretical perspective is also given of electrodes, electrochemical techniques and enzyme kinetics.

Chapter 3 describes the several experimental methods and procedures used for the synthesis of sensing probe molecules, electrode fabrication, biosensor preparation and electrochemical characterisation.

Chapter 4 firstly introduces the principle for peptide-based electrochemical protease detection, summarising background information on optimisation and characterisation of the proposed system developed using conventional gold macroelectrodes. New experimental findings obtained using conventional platinum macro- and microelectrodes are then presented to unveil the differences in sensor performances between platinum macro- and microelectrode-based systems, for the first time. They are investigated in terms of the variations in the probe conformation on electrode surface, kinetics and thermodynamics of enzyme-substrate cleavage and the effects of non-specific binding.

Chapter 5 analyses the similarities and dissimilarities in biosensor performance while the protease sensing system is further miniaturised by translating from using conventional microelectrodes to employing novel platforms: in-house fabricated platinum thin film single microelectrodes, microelectrode arrays (MEA) and microcavity nanoband edge electrode arrays (MNEE). The efficiencies of some proposed solutions to an experienced stability problem of sensing probe molecules on thin film electrode surfaces are also examined.

Chapter 6 investigates the feasibility of a proof of concept work where self-assembled monolayer based sensing probe molecules are immobilised onto electrode surfaces in minutes by a potential-assisted technique, in comparison to the overnight incubation which is a common procedure performed without any external interference.

Chapter 7 explores the applicability of commercial pH-responsive transient polymeric coatings to the protease and pH biosensor platforms for delayed activation and protection against biofouling. The optimisation and performance of these coatings are investigated using bare and probe-functionalised electrodes.

Chapter 8 gathers the findings and contributions of this work and suggests development work which might improve this biosensor platform further and lead to a fully implantable device.

Chapter 2

Background and Theory

2.1 Cancer and Tumour Microenvironment

Cancer can be simply defined as uncontrolled growth and reproduction of abnormal cells in the body. It is one of the major diseases today, as this growth can spread and be fatal when it is not effectively treated. World Cancer Report 2014 which was prepared by the International Agency for Research on Cancer (IARC) designated it as a leading cause of deaths worldwide, and estimated an increase in the number of annual diagnosed cancer cases from 14 million to 22 million within the next two decades [14]. It is also predicted that more than half of the people born in the United Kingdom after 1960 will be diagnosed with cancer at some point during their lifetimes [15]. According to the recent report of American Cancer Society, more than 1.7 million diagnosed new cancer cases and 0.6 million deaths caused from the cancer-related reasons are expected to occur in 2019 in the United States [16]. Figure 2-1 presents the list of these estimated numbers of new diagnosed cases and deaths classified according to a specific cancer type. This shows that prostate, lung & bronchus and colon & rectum cancers are the three leading types of new estimated cases for men, with prostate cancer being replaced by breast cancer in women.

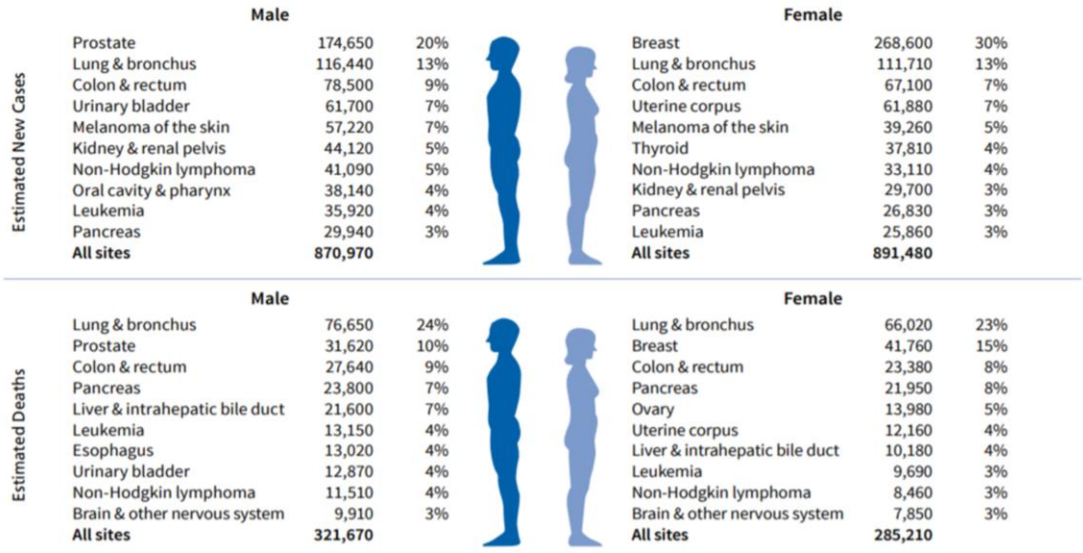

Figure 2-1: Estimates of new cancer cases and deaths expected to occur in the United States in 2019 [16].

The features which lead to cancer formation can be environmental and/or inherited. Despite these huge estimated new case numbers and fatality rates, nearly half of the diagnosed cases are thought to be avoidable and/or preventable as it is now known that the main reasons are a

combination of smoking, obesity, physical inactivity, too much consumption of alcohol and unprotected exposure to sunlight UV as well as some viruses and bacteria [16]. This is also confirmed by the decreasing rates of new cases and deaths associated with lung, bladder and larynx cancers consistent with reduced tobacco use, while the rates are increasing for other types such as uterus, postmenopausal breast, and colorectal cancers which are related to excess weight and physical inactivity in recent decades [17].

Notwithstanding this, it is unlikely that action to address such issues will be completely effective to prevent all cancers. Hanahan and Weinberg have suggested six different capabilities which tumours acquire during cancer development and it is thought that these capabilities most likely exist in all types of human tumours [18]. These include self-sufficiency in growth signals, insensitivity to growth-inhibitory signals, evasion of apoptosis, limitless replicative potential, sustained angiogenesis and tissue invasion and metastasis [18]. *Self-sufficiency in growth signal* can be described as the independency of growth signals produced by tumours themselves, instead of being depended on the signal generation stimulations applied for healthy tissue. In addition to the generation of their own growth signals, they need to avoid growth-inhibitory signals in order to maintain proliferation. *Apoptosis* is a controlled cell death mechanism, which normally takes place to avoid an uncontrolled growth in cell populations and to secure sustainability. This is resisted by tumours e.g. by having a phenotype of unlimited replicative potential which can make tumour cells immortal. This resistance can be also contributed by *angiogenesis* (the formation of new blood vessels) which results in the supply of vital oxygen and nutrients to maintain cell growth, *tissue invasion* (direct tumour extension into neighbouring tissues) and *metastasis* (the spread of tumour cells to distant sites of the body through the lymphatic and/or circulatory system). After a decade, a follow-up study added two more significant further attributes to this list, the reprogramming of energy (glucose) metabolism and evading immune destruction [19]. The analysis of these capabilities reveals the complexity and significance of the tumour microenvironment. As defined by angiogenesis, blood vessels of tumours develop to supply oxygen and nutrition from normal neighbouring cells. However, tumour cells proliferate faster than normal cells in the body and this still causes the consumption of this supply after some time and in some areas. This eventually results in *hypoxic* (oxygen-deficient) regions within the tumour microenvironment and these regions have been shown to be radiotherapy- and chemotherapy-resistant [20]. The correlation between this lower oxygenation level and reduced prognosis associated with the condition of tumour after radiotherapy, surgery, chemotherapy or radiosensitizer processes was studied for patients diagnosed with head and neck cancer [21], [22]. In addition to hypoxia, lower extracellular pH and glucose levels in tumours can also offer further local

variations compared to normal tissue [23], [24]. The complexity of tumour microenvironments is not only promoted by these differences, but there are also many cell types, which are effective in the processes related to cancer progression, such as cancer cells and cancer stem cells, neutrophils, mast cells, endothelial cells, pericytes, fibroblasts, platelets, macrophages and lymphocytes (Figure 2-2) [25], [26]. All these cell types found in the tumour microenvironment have specific links to many different states of the cancer formation and progression. For example, cancer and cancer stems cells have oncogenic mutations to initiate tumour formation, neutrophils have been found to be increased in colon, gastric and lung cancer as well as being shown to increase metastasis in animal models, endothelial and mast cells correlate with poor prognosis, pericytes are vital for sustainability of blood vessels, fibroblasts are tumour promoters in later stages, platelets are excessively observed in malignant tumours and lymphocytes (T, B and NK cells) have varying effects for the immune system – cancer relationship [26].

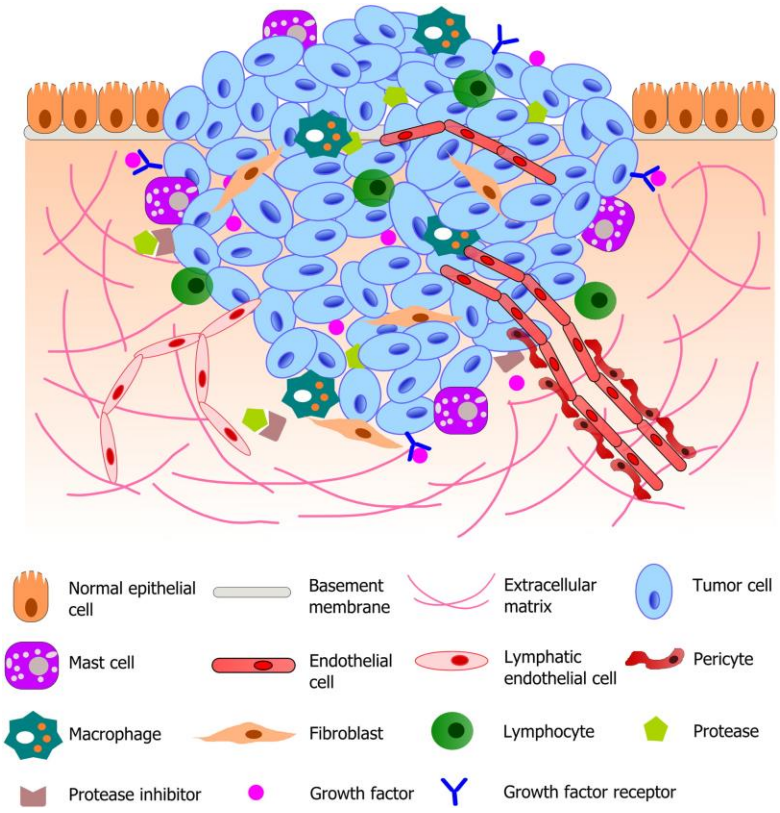

Figure 2-2: Schematic illustration of the complex tumour microenvironment [25].

This tumour microenvironment, as illustrated in Figure 2-2, also includes proteolytic enzymes (proteases) which catalyse proteolysis, defined as the cleavage of proteins into smaller peptide chains or amino acids. They are grouped into five different main classes: serine, cysteine,

aspartic, threonine and metalloproteinases. As they play significant roles in the activity and interactions of proteins, they are vital elements in many physiological and pathophysiological conditions such as DNA replication/transcription, cell proliferation/differentiation, angiogenesis, ovulation, fertilization, wound repair, haemostasis, blood coagulation, inflammation, autophagy, necrosis, apoptosis and many others [27]. Correspondingly, they are also associated with cancer with essential influences in all tumour progression steps, tumour formation, growth, metastasis and invasion [28]. The most significant members of the protease family which have direct links to cancer have been identified as [28];

- Caspases, as they are closely related to apoptotic cell death [29]
- Cathepsins, due to their links to prognosis, malignancy and metastatic potential [30]–[32]
- Matrix metalloproteinases (MMPs), being responsible for peritumour tissue degradation and metastasis formation [33]
- Urokinase-type plasminogen activator (uPA), associated with frequent and earlier metastatic interactions, especially in prostate cancer [34], [35].

Furthermore, other proteases, not only the ones detailed above, might have important links to cancer, such as trypsin, which is a serine type digestive enzyme, found to be involved in colorectal carcinogenesis, promoting proliferation, invasion, metastasis and thus leading to poor prognosis and shorter disease-free survival [36].

Figure 2-3 shows some examples of individual proteases which have interactions with different cell types found in tumour environment. On the other hand, recent studies revealed that more than 30 proteases which belong to three different main groups have also tumour-suppressive effects, including induction of apoptosis (by caspase 3, 5, 6, 7, 8, 10), activation of *autophagy* (the controlled mechanism for the removal of useless or dysfunctional components in a cell) (by autophagin 3), angiogenesis inhibition (by MMP19, gelatinase B, ADAMTS, a disintegrin and metalloproteinase with thrombospondin motifs, 1, 8, 9, 15, 18) and inhibition of proliferation (by cathepsin L, ras-converting enzyme 1) [37].

Therefore, considering its unstable and variable characteristics compared to normal tissue, the tumour microenvironment (and the above detailed proteases) can be introduced as key players in developing personalised treatment of cancer patients [38], [39].

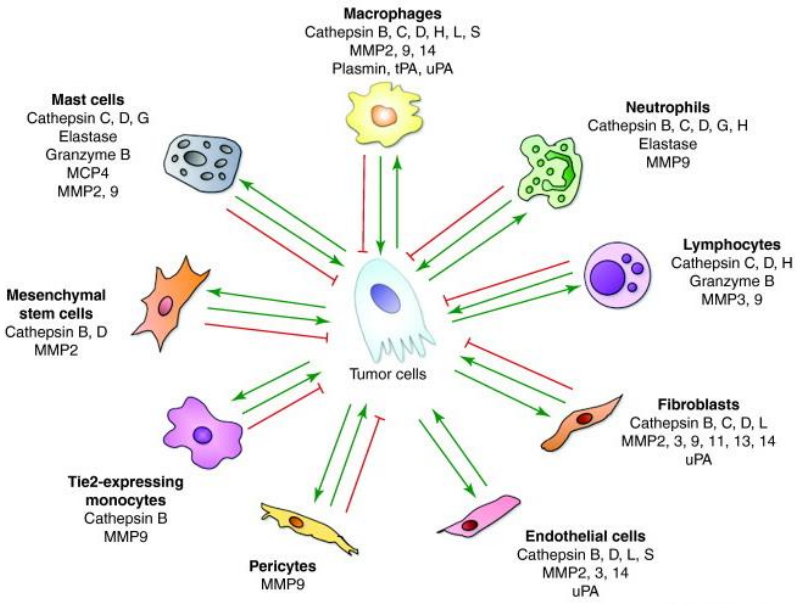

Figure 2-3: Major cell types and contributing proteases found in the tumour microenvironment [28].

2.2 Biosensors

A chemical sensor can be described as a self-contained device which enables real-time analysis of a test sample and provides information (a signal) in terms of the amount (concentration) of a targeted chemical substance (termed as the analyte) in the sample [40]. As depicted in Figure 2.4, a chemical sensor consists of two main elements; (1) a recognition element which interacts with the analyte and this interaction results in a change in physical and/or chemical properties depending on the concentration of the analyte and this change is translated by (2) a transduction element that converts the resulted change to another detectible/measurable quantity (the signal).

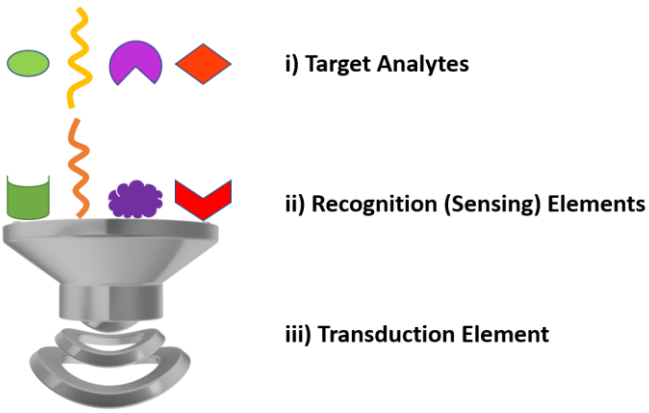

Figure 2-4: Schematic illustration of a chemical sensor, an assembled device consisting of two main components, a recognition and a transduction element in order to interact with a target analyte.

When the recognition system of the sensing device is based on a biochemical or biological analyte, the term biosensor is often used instead of the term chemical sensor and the recognition element is a biorecognition element (or bioreceptor) [40]. The range of applications for biosensors is extremely broad [41] and it can include disease diagnosis and monitoring [42], environmental monitoring [43], drug discovery [44], food quality [45] and toxicology analysis [46]. The most appropriate recognition and transduction methods can be determined from the many possibilities and then optimised for the desired application. Biological systems such as enzymes, peptides, cells, aptamers and DNAs have been used as biorecognition elements in many studies. This builds on natural selection which results in specific and sensitive biorecognition elements for a biological analyte. The biorecognition and selectivity can be based on a combination of different types of chemical/biochemical interactions including affinity interactions, nucleic acid hybridisations, substrate-enzyme catalysis reactions or gas and vapor sorption [40]. In order to ease the detection of biological analytes, biosensors often employs labels (e.g. enzymes, fluorescent dyes, isotopes, nanoparticles, redox probes) which can be defined as molecules attached to the analytes (molecules of interest) to detect their activity or presence [47]. However, labels might change intrinsic physical properties of the analytes and they might have some important drawbacks such as increased material costs, complex sensor designs and possibility of decreasing affinity between the biorecognition element and the analyte [48]. In order to avoid these possible effects, label-free biosensing was developed and it has become a trending approach which enabled the detection of the analytes based on their physical properties (size, weight, impedance, charge, refractive index etc.), without a need of any particular label [48].

Similar to recognition methods, various transduction techniques are available depending on a type of biorecognition element utilised. Most common types of transduction are based on thermal changes, mechanical effects (mass-based changes), electrical (resistive and capacitive) changes, electrochemical and optical methods [40]. In the biosensors where thermal changes are being used as transduction method, the enthalpy of reaction, often as a result of enzyme-activated catalytic reactions, gives rise to the change in temperature which is converted to a resulting signal [40]. These calorimetric assays can be used for sensing the heat produced due to the interaction of bacteria or pesticides with particular enzymes. They are really good assays but only when ΔT is significantly large, for example in the case of a change in chemical bonds such as bond-breaking or bond-formation. Also, it is hard to measure ΔT, especially *in vivo* due to difficult measurement technologies. These assays are also not very target-specific as differences in heat could be resulted from any non-specific interaction.

In other cases, the interaction with an analyte might be designed to lead to a change in electrical properties of recognition elements, such as resistance [49] or capacitance [50] which can be obtained as output signal. Although the choice depends on some variables (i.e. analyte type, analyte concentration, measurement environment), majority of biosensors employs mass-based, optical and electrochemical transduction methods, as illustrated in Figure 2-5.

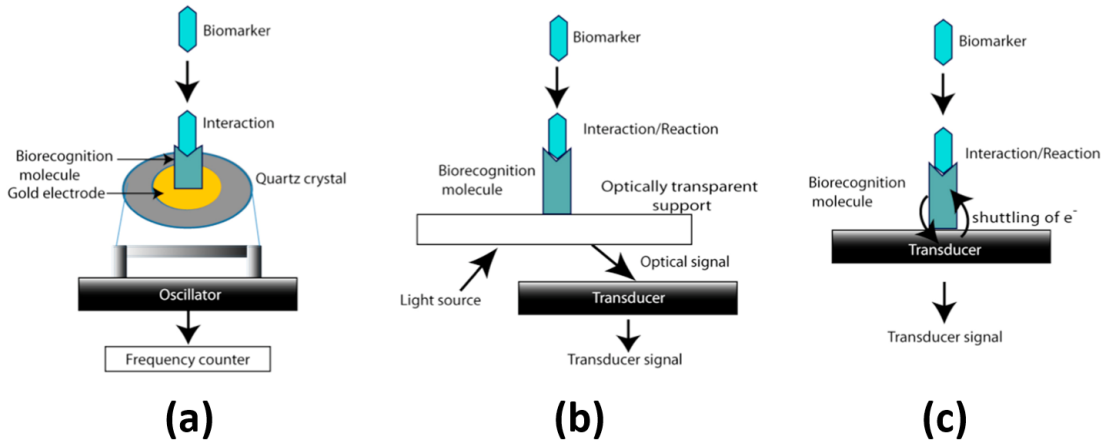

Figure 2-5: Schematic representation of a) mass-based, b) optical and c) electrochemical transduction systems in biosensors. Adapted from [58].

In the biosensors using a mass-based transduction method, there is a piezoelectric quartz crystal as a transducer (Figure 2-5a). This quartz crystal oscillates at a (resonance) specific frequency under an applied AC voltage. However, when the target analyte interacts/binds to the immobilised receptor, the quartz crystal gains mass and its resonant oscillation frequency decreases. Owing to a piezoelectric characteristic, this change in the frequency is converted to a voltage value and measured by a wave sensor. As being a more sophisticated form of these, surface acoustic wave (SAW) sensors [51] are produced by microfabrication and they offer stability, rapid responses and most significantly very high sensitivities of around ~10^{-15} g, to detect even single molecules. This enables the detection of very small analytes such as viruses, bacteria, nucleic acids and hormones [52]. In addition to all these traditional recognition and transduction techniques, the advancements in nanotechnology in the recent years paved the way for the development of nanobiosensors, where nanomaterials such as quantum dots, carbon nanotubes, graphene etc. are used as labels, carriers or signal amplifiers [53], [54]. They are also integrated to paper-based diagnostics providing cheaper, easier, more rapid and sensitive measurement possibilities [55].

Optical transduction (Figure 2-5b), on the other hand, benefits from the emergent interactions (dispersion, reflection, absorption, scattering, transmission, fluorescence, luminescence, surface plasmon resonance) occurring between light and matter [56]. Developments in the optical biosensor area also improved significantly by the application range of label-free detection methods, where the analyte and recognition element can directly interact without any requirement for immobilisation of another sensitive probe attached with a signal generating label [57]. In this way, these biosensors are able to detect and/or monitor a high number of samples in real time. However, they require a detector (spectrophotometer) to convert and measure the resulting signals and this usually causes their miniaturisation to be more challenging than other types of biosensors. This limits their resolution/sensitivity and applicability for *in vivo* measurements [42].

Electrodes are used as transducers in electrochemical transduction and they are responsible for converting and reporting the interaction between analyte and recognition element as a change in different electrochemical outputs such as current, potential, conductance or impedance [58]. Electrochemical biosensors (Figure 2-5c) are widely used in biosensing for many years and offer vital advantages including enhanced sensitivities and low detection limits as well as the capability of electrodes to be readily modified with varying biorecognition moieties [59]. Thanks to these virtues, for example, electrochemical-based glucose sensors have been successfully commercialised and considerably used now by many diabetes patients to self-monitor their glucose levels in blood with rapid response times without the need for going to a hospital to take a blood test [41], [60]. This has been a significant achievement in terms of the historical perspective of biosensing, because glucose sensors dominate the biosensor market with an approximately 70% share (of $31.5 billion, the market value estimated to be reached by 2024), also considering the increase in the rates of diagnosis with diabetes (having a prevalence of 8.5%, among the adult population, in 2014, while it was estimated as 4.7% in 1980), as well as the requirement for diabetics to keep their blood sugar levels under observation at specific intervals [41], [61], [62]. Moreover, there is a growing interest in the electrochemical detection of the blood concentration of lactate, leading to the development of commercial lactate monitoring devices for clinical and sports medicine purposes, because the level of this fermentation product was found to be increasing after intensive exercises and it has been also linked to ischemia, trauma and haemorrhage as a relation to oxygen depletion [59], [63]. In addition, there are many other electrochemical-based biosensor applications which have been commercialised by different companies located all over the world and being used for clinical, food & environmental analysis and biowarfare identification purposes [64].

Although the above-given progress and achievements of biosensors, there are, of course, some requirements as well, which should be fulfilled in route to commercialisation. These can be summarised as followed [65];

- Doing a market analysis for a biosensor which to be developed for detection of a particular target analyte
- Investigation of contribution to existing knowledge and determination of know-how points to be (or already) obtained for recently developed biosensor technology
- Characterisation and assessment of the biosensor performance while in use and following the storage time (of minimum 6 months after which a biosensor should be still responsive)
- Making stability/durability, cost and ease of production analyses for each component found in the biosensing device
- Specification of hazards and ethical concerns which might be arisen due to the use of the produced biosensor.

2.2.1 Biosensors for the Detection of Cancer Biomarkers and Proteases

In many cancer cases, tumour growth proceeds rapidly and/or the metastasis occurs into other parts in the body until the patient is diagnosed and assigned to the most appropriate treatment programme. This situation leads to an inoperable tumour placement in tissue or incurable (even with an intense radio- or chemotherapy) cancer development in vital organs such as the brain, lung, pancreas etc. Moreover, the conventional methods used for cancer diagnosis including biopsies as well as ultrasound and magnetic resonance imaging focus on the phenotypic properties of tumours, and they are thus thought not to be efficient enough to provide its detection at an early stage [58]. Furthermore, when it is considered that a particular type of cancer consists of very complex disorders with various genetic or epigenetic-induced reasons, instead of being a simple disease, one can understand that there is an urgent need for the development of alternative detection technologies based on individual patient circumstances [66]. Concisely, cancer therapy can be personalised depending on the condition of cancer, the habits of the patient and the responses during treatment.

The detection and monitoring of biomarkers, which can be described as molecules (proteins, hormones, enzymes, nucleic acids) that undergo significant changes in amount, can be used as the basis of these advancements. They are classified into three subgroups, (i) diagnostic

biomarkers which are related to the detection of the disease, (ii) prognostic biomarkers which are related to the possibilities of the recurrence and (iii) predictive biomarkers which are related to the responses of the cancer against the treatment [58]. In recent years, much effort has been spent on the investigation and identification of cancer-specific biomarkers and Table-1 lists below some examples, which are typically detected in body fluids (blood, saliva, urine, cerebrospinal and amniotic fluid) and tumour tissue/cell, and found to be activated in a particular cancer type [67].

Table 2-1: Common biomarkers used for cancer detection and monitoring [67].

Cancer Type	Biomarkers
Breast	miR-155, miR-261, CA15-3, EGFR, VEGF165, BRCA 1, ErbB2, HER2, Mucin-1
Prostate	miR-103a, miR-106a, miR-107, PSA, Pro2PSA, GSTP1, p63, PCA3
Liver	miR-100-5p, mir-122, α-Fetoprotein, HCCR-1
Lung	miR-106a-5p, miR-10b-5p, miR-141-3p, KRAS, ALK, CEA
Melanoma	mir-221 , ERK, EGFR, HER3, NCOA3
Gastric	miR-29c, miR-148a, CA19-9, CEA
Brain	miR-10b, MGMT, COX-2, p14arf
Ovarian	miR-92, miR-93, miR-126, CA 125, HE4, Mesothelin
Bladder	miR-126, miR-141-3p, NMP22, FDP, IL-8, hOGG1, COX-2, BTA

Abbreviations: CA: Carbohydrate antigen; **EGFR:** Epidermal growth factor receptor; **VEGF165:** Vascular endothelial growth factor-165; **BRCA 1:** Breast cancer susceptibility gene 1; **ErbB2:** Erb-b2 receptor tyrosine kinase 2; **HER:** Human epidermal growth factor receptor; **PSA:** Prostate specific antigen; **GSTP1:** Glutathione S-transferees P1; **PCA3:** Prostate cancer gene 3; **HCCR-1:** Human cervical cancer oncoprotein-1; **KRAS:** Kirsten rat sarcoma viral oncogene homolog; **ALK:** Anaplastic lymphoma kinase, **CEA:** Carcinoembryonic antigen **ERK:** Extracellular signal-regulated kinase; **HER3:** Human epidermal growth factor receptor 3; **NCOA3:** Nuclear receptor coactivator 3; **MGMT:** Methylguanine methyl transferase; **COX-2:** Cyclooxegenase-2; **HE4:** Human epididymis protein 4; **NMP22:** Nuclear matrix protein 22; **FDP:** Fibrin degradation products; **IL-8:** Interleukin 8, **hOGG1:** Human 8-oxoguanine DNA N-glycosylase 1; **BTA:** Bladder tumor-associated antigen.

These given biomarkers can be used for various clinical applications as they are related to different phases of the cancer progression. For example, carbohydrate antigen 125 (cancer antigen 125) is used for monitoring therapy and detecting the recurrence of ovarian cancer, human epidermal growth factor receptor 2 (HER2) helps to choose a suitable therapy for breast cancer, α-Fetoprotein is used for diagnosis and staging in liver cancer cases and prostate-specific antigen (PSA) is utilised for cancer discrimination and screening [68]. Although each marker should be expected to correspond to a distinct change in terms of tumour formation or progression, detection of multiple biomarkers at the same time is required in some cases for specific cancer diagnosis. For example, PSA levels also increase in men with benign prostate disease if a prostatectomy operation is not performed and only doing a PSA-monitoring might thus be misleading for prostate cancer diagnosis [69]. This lower cancer specificity of some biomarkers requires multiple biomarker detection and analysis by utilising integrated multiplexed measurement options.

The literature includes a considerable number of works where many biomarker types have been shown to be detected using different approaches. For example, multi-walled carbon

nanotubes (CNT) were fabricated and used in an immunosensor developed on screen printed carbon electrode array and achieved the detection of prostate cancer-related PSA (with a limit of detection, LoD: 5 pg/mL) and bladder cancer-related IL-8 (LoD: 8 pg/mL) in this way [70].

Another immunosensor approach was used by Zhao *et al.* for the detection of liver cancer-related α-fetoprotein with a LoD of 0.07 pg/mL. This was based on the conjugation of capture antibody attached chitosan-modified screen printed electrodes and signal antibody-labelled single wall carbon nano horn structures with in-situ grown nanogold, which is exposed to oxidation at +1.3 V for 30s, followed by a cathodic differential pulse voltammetry (DPV) scan in 0.1 M HCl [71]. Furthermore, immunosensor-based detection of α-fetoprotein is also available using mass-based techniques. This was shown by a sensor system based on hybrid nanomaterial (gold nanoparticles and nano hydroxyapatite) coated piezoelectric crystals which were labelled with anti-α-fetoprotein antibodies [72]. In a similar system, ferritin which is a significant prognostic marker for malignant lymphoma, cervical and breast cancer, was captured by anti-ferritin antibodies that were immobilised onto quartz crystal microbalance (QCM) [73].

In another study, electrochemical hybridisation-based genosensor was developed by firstly modifying gold electrodes with peptide nucleic acid (PNA) as a SAM layer and then accumulating with indigo carmine, which showed a decrease in its DPV current upon hybridisation with the target DNA (15-mer sequence unique to p53 tumour suppressor gene), giving a LoD of 4.31 pM within a linear range of 0.01 – 10 nM [74].

Carcinoembryonic antigen (CEA), an important biomarker of lung, breast, gastrointestinal and ovarian cancer was detected using optical techniques such as fluorescence resonance energy transfer (FRET) which based on the fluorescence quenching ability of palladium nanoparticles towards upconverting nanoparticles [75], and chemiluminescence (CL) assays which based on the signal amplifier gold nanoparticles [76] or immunomagnetic beads formed by superparamagnetic iron oxide nanoparticles [77]. The lowest LoD estimated among these CL assays was 0.8 pg/mL obtained by FRET method.

Human epididymis protein 4 (HE4) was detected by Yuan *et al.* in blood samples from patients with ovarian cancer, with a LoD of 4 pM [78]. The sensor system was based on localised surface plasmon resonance (LSPR) technique where silver nanoparticles were used as a nanochip substrate for capture antibody.

A significant breast cancer biomarker, carbohydrate antigen 15-3 was shown to be detectable label-free [79]. This was achieved developing an electrochemical immunosensor based on the incorporation of N-doped graphene sheets which significantly enhanced the electron transfer and gave a LoD: 0.012 U/mL.

The capture and detection of miRNA let-7b was achieved from human breast, cervical and lung adenocarcinoma cell lines with a 0.3 fM LoD, where the sensing platform was based on Fe_3O_4@Ag magnetic nanoparticles and surface-enhanced Raman scattering (SERS) technique [80].

In a different work reported by Gruhl and Länge, SAW-based biosensor enabled the detection of the breast cancer markers HER-2 and a tissue inhibitor of metalloproteinases (TIMP-1) with LoDs of 2 ng/mL and 10 ng/mL, respectively [81]. Besides, it was shown that two different methods can be integrated to make a biosensor platform more sensitive against target analytes, and advantages of both can be benefitted in this way. In a very recent work by Wang *et al.*, acoustics and microfluidics were combined to create an acoustofluidic biosensor and utilised to provide size-based isolation of salivary exosomes, which thought to be improving diagnosis and prognostic screening of human papillomavirus (HPV)-associated mouth and throat (oropharyngeal) cancer [82].

In addition to the serious functions of these given biomarkers, the significance and individual distinctness of protease activity in almost all stages of cancer has been previously detailed. Consequently, they also should be considered as vital biomarkers which need to be detected and monitored in order to help determination of the most convenient, efficient and personalised treatment. Typically, they are known to be responsible for protein regulation in the body, hydrolysing peptides by cleaving them between two amino acids and breaking down into two shorter peptide chains. As depicted in Figure 2-6, a protease can cleave a peptide chain at a specific hydrolytic site, which to be recognised by the protease. For example, when amino acid AA-4 corresponds to a positively-charged lysine or arginine in this case, it is enough for trypsin to cleave the peptide, whereas the sequence typically should be LVPRGS (See Glossary for amino acid abbreviations) for thrombin [6]. There are also examples in literature using different peptide sequences for the detection of other proteases such as MMP-9 (peptide: GPLGMWSRC) [83], cathepsin B (peptide: LRFG) [84] and caspase-3 (peptide: DGADAGGC) [85]. Therefore, the composition of a comprehensive databank of peptide sequences is really important in terms of achieving the perfect selectivity (where signal change

is obtained against only target, not for any other non-specific substances), because a considerable part of protease sensing research employs peptides as recognition elements.

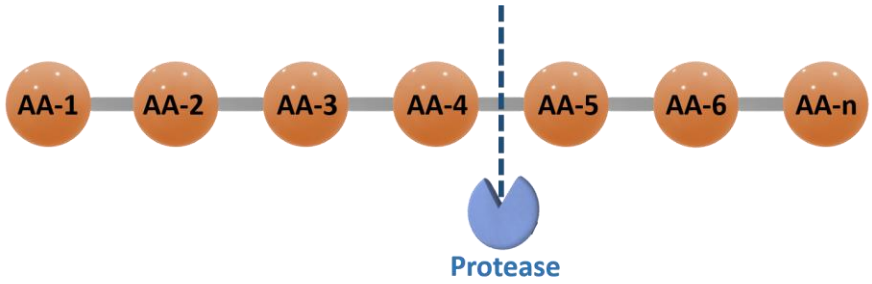

Figure 2-6: Schematic representation of a peptide chain cleaved by a substrate-specific protease at a particular hydrolytic site. Adapted from [6].

Protease biosensors can be classified as affinity and activity assays. In affinity-based protease sensing, their detection and quantification are practiced with respect to their binding to a substrate, instead of their activities; whereas in activity assays, their catalytic functions are targeted because a cleavage is measured [6]. This eventually provides more analytical, sensitive and disease-related information [6]. Several techniques were previously benefitted to develop protease assays and they can be briefly exemplified including the detection of HIV-1 by FRET [86], thrombin by bioluminescence resonance energy transfer (BRET) [87], MMPs by nanoparticle-integrated colorimetric assay [88] and magnetic nanoparticles [89], caspase-3 by SPR [90] and trypsin by fluorescence [91], SERS [92], enzyme-linked [93] and liquid crystal-based assays [94].

Despite all these accomplishments where different approaches have been employed, it is worth noting that established biomarker detection methods have drawbacks e.g. enzyme-linked immunosorbent assay (ELISA) or polymerase chain reaction (PCR) have slow response times, expensive material costs and inability of continuous real time monitoring [58]. In addition, the inability of optical techniques for multiplexed measurements and incompatibility of mass-based techniques for miniaturisation are serious limitations for *in vivo* biosensing. This drives a growing interest in developing electrochemical-based new generation sensing platforms to achieve individual specific biomarker detection. Specifically, electrochemical peptide-based protease assays are thus of greater significance in this respect, offering an huge promise for monitoring/screening the real-time status of a tumour and personalising cancer treatment, if they can be developed on microdevices and placed into a solid tumour [95]. This would be an inevitable challenge -if not impossible- for majority of the aforesaid techniques. The detailed

discussion (with some critical background) of electrochemical peptide-based protease sensors can be found in Section 4.1.

In addition to all these, an EPSRC-funded research project, Implantable Microsystems for Personalised Anti-Cancer Therapy (IMPACT) [4], [95] has aimed to develop new strategies to personalised cancer treatment using fabricated, miniaturised and implanted smart sensor chips. This is expected to allow chemo- and/or radiotherapy to be more sensitively targeted against cancer cells, by measuring time-dependent status of an individual tumour.

2.2.2 Miniaturisation

Miniaturisation is one of the emerging trends in analytical sciences in recent years, since scaling down the systems/materials reduces preparation times, production costs, sample volumes, human-induced errors, amounts of chemical waste significantly as well as enhanced device performance and eases implantation [96]. Miniaturisation is far more than simple downscaling. It allows greater portability, ease of operation and analysis.

The origin of miniaturisation of analytical devices and their components actually was in the fabrication of miniature gas chromatographic analysers, micropumps and microvalves in the 1980s, and has now evolved to micro- (μm) and nanoscale (nm) devices [97]. The development of *micro total analysis systems* (μTAS), so-called "lab-on-a-chip technologies" has also promoted the interest in miniaturisation with the aim of integrating all steps such as sample preparation (even including chemical synthesis), analyte separation and detection together on a microchip [96], [98]. Also, there has been always a great interest in miniaturising biosensors. Analytical sensing devices applicable to biosensing were first manufactured on the macroscale nearly seven decades ago (Clark's oxygen sensor [99]), whereas today's biosensor elements proceed into the fabrication in nanoscales [100], consisting of materials like nanowires, nanoparticles, carbon nanotubes, nanorods and graphene. The main reason of this is to increase sensing capabilities and enable *in vivo* measurements. In addition, the successful integration of biology and electronics fields (leading to the field of bioelectronics) combining biological substances and silicon chips was an important milestone in biosensor miniaturisation [101].

These are mostly attributed to the development of microtechnology and advanced fabrication techniques starting from 80's which then facilitated micro and nano patterning technologies for recognition components, microfluidic biosensors (lab-on-a-chip) and

microelectromechanical system (MEMS)-based biosensors. All of these are widely benefitted in biomedical and many other applications [102].

Miniaturised systems propose significant advantages such as [102];

- decreasing the need for expensive materials thus lowering the production costs
- the ability to manipulate measurement environment
- multiplexed detection
- integration of separate elements
- they are less affected by non-uniform sample distributions.

Although miniaturised biosensors typically exhibits above-mentioned advantages, decreasing sensor dimensions is a potential of new drawbacks in some cases which might include increased response times, reduced sensitivity, loss of linearity and drifts. These would be a noteworthy limitation particularly for dynamic environments. Therefore, a miniaturised device should be either optimised and/or re-designed according to the consideration of application-specific balance between these variables. It is also possible to utilise other strategies based on fluid flow, thermal gradient, electric field, internal motors to minimise the response times [103]. Further information can be found in Section 5.1.

2.3 The Development of Implantable Devices and Biofouling

2.3.1 The Significance of Implantable Technologies

The advancements achieved in the area of biosensing so far paved the way for diagnosis and monitoring of several diseases. However, the majority are based on lab bench analysis of the samples taken from patients using methods (e.g. bloodletting, needle biopsy, colonoscopy) which might be uncomfortable and even destructive or harmful sometimes e.g. by promoting infection or affecting disease rate. These circumstances can cause patients to feel more reluctant to engage with examination and therapy. More importantly, bench-based analysis is not able to give rapid and continuous information that can be vital for diagnosis and treatment of rapidly changing diseases such as cancer. However, this challenge raised for bioanalytical devices/biosensors could be dealt if they can be converted into implantable devices which can be placed into the body to monitor the real-time events through *in vivo* measurements. Critical changes related to the disease can then be way to an electronic receiver outside which will be

interpreted by clinicians afterwards. Of course, implant technology can be used also to inform drug delivery devices, in addition to bioanalytical platforms. This methodology is thought to become central in enabling the personalised therapy in coming years [104].

The development of devices for continuous glucose monitoring can be considered as the first achievement of implantable biosensing. As clinic-based measurement techniques using extracted blood samples from diabetic patients have been time consuming and stressful, huge glucose sensor market progressed fast, leading to production of firstly the devices designed for home use by patients themselves on extracted blood samples [105] and more recently implantable versions, which can offer long term measurements for up to 180 days [106]. Another type of implantable biosensor, an intravascular blood gas sensor, was also developed by Paratrend (Diametrics Medical Inc.) combining electrochemical and fibre optic-based techniques for the detection of pH, P_{CO2} and P_{O2} [107]. Another study focused on the detection of glucose, lactate and pyruvate found in brain, where an enzyme-based biosensor was developed and implanted to the medial prefrontal cortex of anaesthetised rats, because that the levels of these substances have been thought being related to changes in brain energy metabolism and thus corresponding neurological disorders [21], [108]. The sensor was found to be sensitive to basal levels of all three substances and some externally-induced (glucose and insulin administration) changes. Moreover, using a miniaturised Clark-type electrochemical oxygen sensor, real-time oxygen tension was measured in an anesthetized rat intestine, during ischaemia and hypoxia conditions [109]. Furthermore, a silicon-based bioresorbable sensor was fabricated by Rogers and his colleagues, combining the materials which are already known to be resorbable due to hydrolysis and/or metabolic action, then implanted to rat models to demonstrate its applicability for monitoring pressure and temperature [110]. Additionally, this work showed the platform can be integrated with a data-communication system and can also be modified to detect fluid flow, motion and pH changes. As a first attempt to use an implantable biosensor for a cancer case, an implantable device with a semi-permeable membrane was fabricated and included with nanoparticles of magnetic relaxation switches [111]. Although this MRI-assisted device was performed for only short term applications such as *in vivo* determination of soluble cancer biomarkers, it is thought that it can be possible to adapt it to sense chemotherapy drugs/biomarkers and metabolites as well. Of course, implantable technologies are not only limited to biosensors, but also offer opportunities for drug delivery applications. For example, fabrication of microelectromechanical systems (MEMS)-based silicon chips have been suggested for this purpose, to include a set of reservoirs which can be filled with a particular drug and then the chip can be implanted to a target location of the body. The idea has been based on the external stimulus-induced

activation and opening of a thin layer material (seal) which protects the reservoir until the time of planned delivery. This method was first suggested by Robert Langer and colleagues in 1999 [112], and then adapted and used in different works including magnetically controlled docetaxel delivery for the treatment of diabetic retinopathy disease [113], batteryless insulin pump [114], human parathyroid hormone fragment delivery for osteoporosis treatment as first-in-human testing [115] and many others [116]. In addition to MEMS-based devices, drugs can be loaded into various polymers and hydrogels which do release the loaded drugs when they are exposed to external stimuli like temperature, magnetic field or pH following the implantation [117]. Despite the performances not yet tested *in vivo*, there are also other interesting examples in literature, where a smart design has been fabricated to improve the operability of the device to perform as a biosensor and a drug delivery system in combination. In the first one, pH sensitive hydrogel, poly(HEMA-co-DMAEMA), which was loaded with glucose oxidase, catalase and insulin, was diffused by glucose when exposed to body fluid and swollen by gluconic acid which is an enzymatic conversion product of glucose, leading to the release of insulin, where the amount and rate of the release based on glucose concentration [118]. The later one used polypyrrole–gold bilayer as an electroactuated flapping seal for a drug loaded well [119]. In this work, the biosensing was achieved by polymerised hydrogel glucose biosensor which was immobilised on the backside of a gold cap.

It should be emphasised that most of the proposed materials and devices in this area might have been stated as ready to implantation, but not actually subjected to human clinical trials yet. Because, the approval of a device developed for a medical purpose takes considerable time as it requires to be found as successful in all stages of bench analysis and animal trials. As a significant criterion, they should be characterised and confirmed in terms of the sensor performance, durability, robustness and passiveness against host immune responses to be induced in the case of an implantation.

2.3.2 Host Immune Responses and Biofouling

All materials/devices enhance host immune responses when implanted, as a result of the self-protection mechanism of the body [120]. This interaction occurring between the material and tissue is one of the major problems challenging implantable biosensor and drug delivery platforms, and thus is a serious limitation for an efficient and long-term utilisation. Biofouling can be described as non-specific cell and/or protein adsorption and causes most of the implanted devices to lose their functionality by surrounding their active sensing area and in

long-term provoking a tissue reaction, called as foreign body response (FBR) [21]. Therefore, it can be seen as the most destructive stage of the host immune responses. Because material-tissue interaction-induced adverse effects might be bidirectional, the possibility arises of local tissue damage formation in addition to local disruption in the device. All implantable elements should therefore be characterised in terms of their biocompatibility prior to any clinical testing [121]. Likewise, if a device is to be clinically approved following these characterisations, it should be fabricated at the beginning according to the regulations of an established organisation such as International Organisation for Standardisation (ISO), which published the relevant standards document ISO 10993: Biological Evaluation of Medical Devices [21], [122]. This emphasises, at this juncture, the significance of understanding the stages of the inflammation in order to be able to evaluate biocompatibility and ensure biocompatible device production.

As illustrated in Figure 2-7, the main stages of inflammation [21] exhibited by the host against an implanted device can be mainly classified to

- tissue injury
- blood-material interactions
- provisional matrix formation
- acute and chronic inflammation
- granulation tissue formation
- fibrosis/fibrous encapsulation.

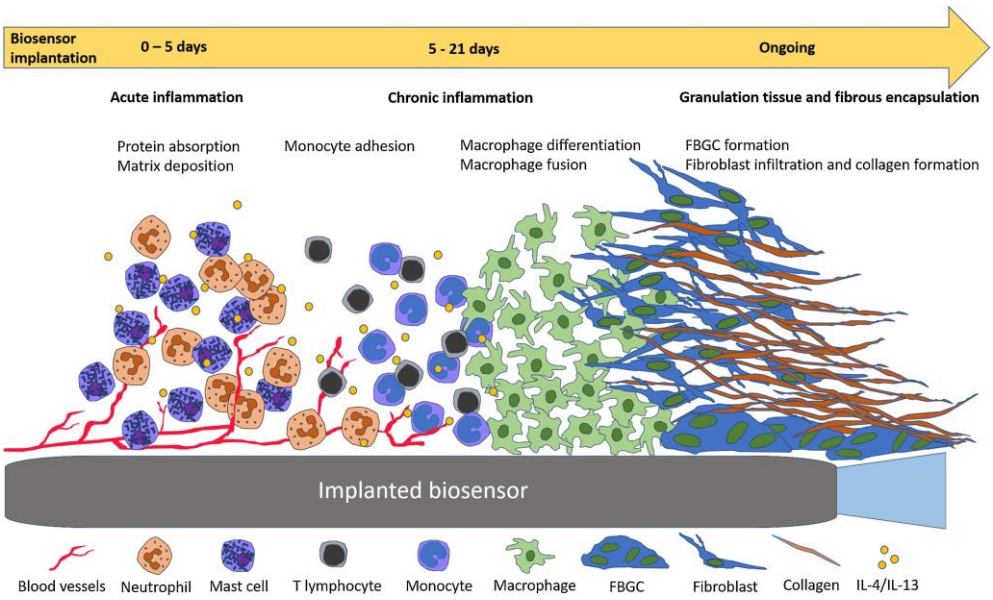

Figure 2-7: Schematic diagram of the inflammation stages caused by an implanted device/material [21].

Blood-material interactions and provisional matrix formation are first and early (within minutes to a few hours) inflammatory responses activated due to an injury to vascularised tissue and usually include protein absorption, thrombosis and blood clot formation [123]. The provisional matrix might include and release fibrin, platelets, inflammatory and endothelial cells to help to healing of the injured tissue. This early response is followed by sequential acute and chronic inflammation. Acute inflammation also continues for a short duration (minutes to a few days, usually less than a week) similar to blood-material interactions. Neutrophils consisting of polymorphonuclear leukocytes and PMNs are transferred from blood vessels into the implanted area and nearby tissue, where the localisation of leukocytes leads to the release of proteolytic enzymes (proteases) and they all together try to phagocytose the foreign materials [124]. In addition to neutrophils, mast cells, interleukin-4 and interleukin-13 proteins have also significant roles in the determination and governance of the host response [124]. Chronic inflammation, taking place following the acute inflammation, proceeds for a significantly longer period (weeks to years) and it is characterised by the presence of macrophages, monocytes and lymphocytes, where toxicity or infection are also commonly seen problems [123]. Foreign-body reaction can be considered as a succeeding phase after the chronic phase and is characterised by the formation of foreign body giant cells (FBGC) and also the presence of degradative enzymes and inflammatory mediators [21]. Furthermore, the size and geometry might be also effective in the biocompatibility characteristics of implanted materials and devices. Veiseh *et al.* placed various materials (plastics, metal, ceramic and hydrogel-based) in different dimensions into rodent and non-human primate animal models to check any correlation between the material size/shape and biocompatibility [125]. They observed that all materials which are spherical and of 1.5 mm, or in greater dimensions, resulted in more biocompatibility compared to smaller dimensions and other geometries. It was also stated that this correlation was independent of surface area and it was valid for all tested material types. On the other side, Bhushan and his colleagues have been recently inspired from mosquitoes and fabricated a microneedle of significantly reduced dimensions and a different shape than commercially available options, in order to ease the drug delivery and blood drawing [126]. These microneedles were designed to include two small needles, one of which releases a numbing agent when inserted, whereas the other one (which was suggested to be more flexible and able to vibrate) draws the blood or releases the drug. Although the later work has not been tested *in vivo* for biocompatibility yet, both together demonstrate the importance and extent of the miniaturisation as well as the design of implanted material and devices.

Although it is possible to control the FBR in some cases by alterations in the surface properties of an implanted material if it is biocompatible, it is very difficult to completely avoid from the fibrosis/fibrous encapsulation which initiated by macrophages. This capsule simply surrounds the implant and isolates it from the relationship with the tissue environment, being a serious hindrance against the functionality of a biosensor [127].

It is also worth noting that these inflammation stages have been characterised mostly in normal tissues so far, not in a tumour tissue, except only a few works. The first one is an early study of Mahoney and Leighton, where only minimal extent of FBR was observed against a cotton thread implanted into rodent tumours, in comparison to the one placed into normal tissue [128]. Other one is a more recent work by Gray *et al.* where a tumour xenograft model was developed and used to investigate the performances of six different materials (silicon dioxide, silicon nitride, Parylene-C, Nafion, biocompatible epoxy resin and platinum, all of which are planned to be included in tumour pH and O_2 sensors of the same project) in terms of FBR activation in a solid tumour [109], [129]. The study concluded that no biofouling and variations were observed in other events including tumour necrosis, proliferation, apoptosis, immune cell infiltration or collagen deposition.

2.3.3 Different Approaches to Enhance and Protect Implantable Materials and Devices against Host Responses

The advancements in bioelectronics and the increasing number of implantable sensor/material-based applications day by day necessitate the development of different strategies for their protection against biofouling as well as smart activation within the body. Figure 2-8 shows some of these strategies that referred to different techniques such as surface functionalisation, microfabrication, polymer chemistry and biosynthesis. Each of these examples will be briefly summarised below as a reference to a reader regarding which methods have been practicable and compatible with a particular biosensor or drug delivery application.

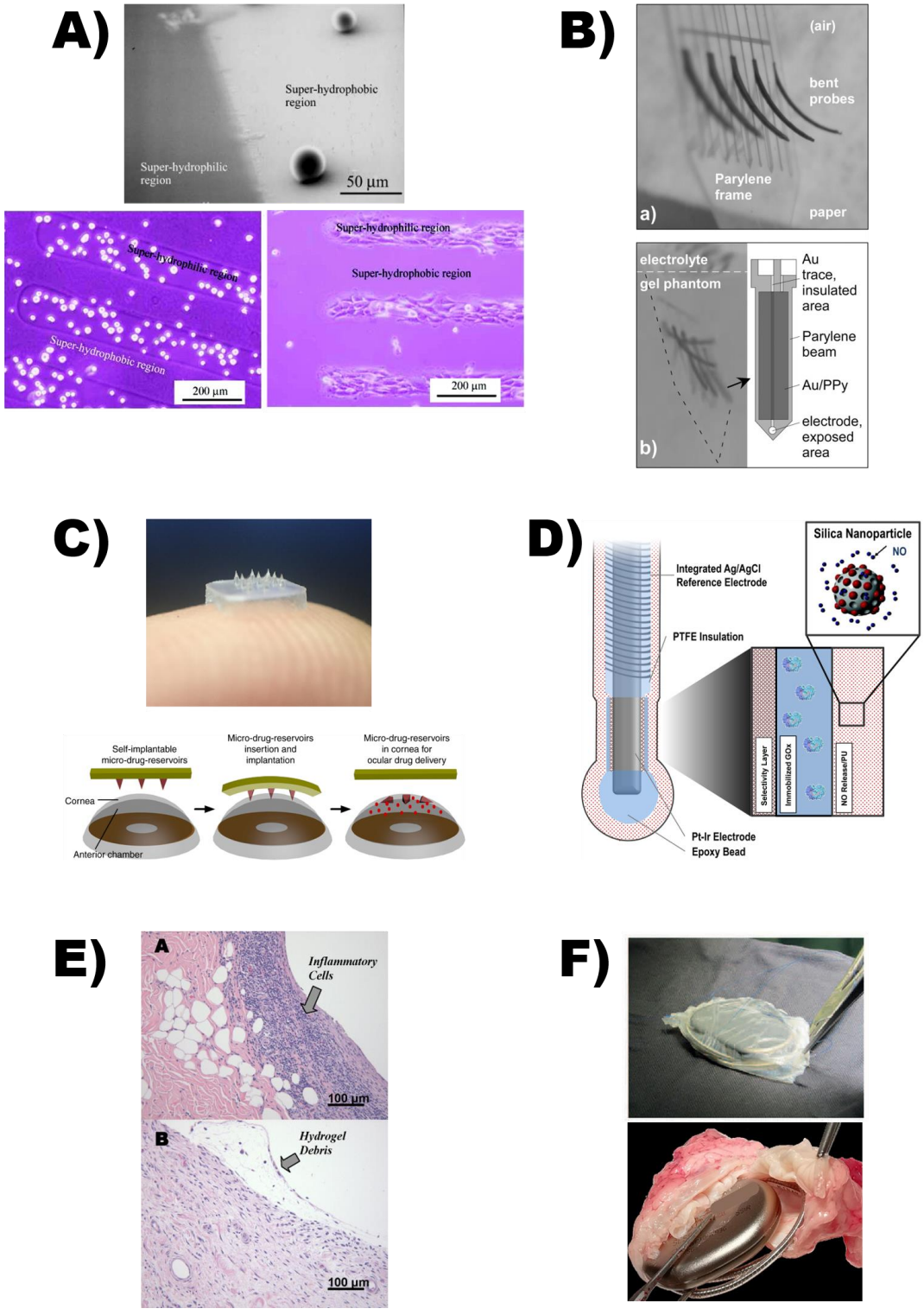

Figure 2-8: Various biofouling protection techniques for implantable devices based on A) surface modification [130], B) conjugated polymer actuation [131], C) microneedle reservoirs [132], D) NO-releasing coatings [134], E) biocompatible hydrogel coating [136] and F) biosynthesised membrane [137].

In the first work, micropatterned superhydrophilic and superhydrophobic surfaces were created by plasma vapor deposition of *n*-octadecyltrimethoxysilane self-assembled monolayer and vacuum ultraviolet (VUV) irradiation onto Si wafers, before they were used as substrates for mouse 3T3 fibroblast cells or protein adsorption using 10% fetal bovine serum in phosphate-buffered saline, PBS (Figure 2-8A) [130]. It was found that the superhydrophilic areas of micropatterned surfaces were more favorable for attachment of the cells after the evaluation of cultured cells for both 1 h and 24 h. Although the proliferation of cells adhered on the superhydrophilic areas occurred immediately, constant contact was observed to be necessary for proliferation for the cells on the superhydrophobic regions. For protein adsorption, a similar preference was observed where the extent of proteins on flat hydrophilic surfaces found to be higher than flat hydrophobic surfaces.

Another study showed the potential of a polymer, polypyrrole (PPy) doped with dodecylbenzenesulfonate (DBS) to work as a smart actuator in implantable neural interface devices (Figure 2-8B) [131]. For this purpose, the microfabricated bilayer design was electrochemically cycled at 22 ^{o}C or 37 ^{o}C, in aqueous NaDBS or artificial cerebrospinal fluid; where it was found that the performance of deflection (bending) was similar in both environments, although the increase in the temperature consumed 70% more charge, effecting the bending amount negligible. These polymer actuators can be used as caps to protect electrodes or drug-loaded cavities during implantation and partly inflammation, and they can be activated on-demand.

As depicted in Figure 2-8C, a flexible eye patch which can host drug-loaded micro reservoirs was fabricated as a self-implantable device which is activated upon the gentle thumb pressing on the ocular surface in order to release the load either with biphasic kinetics or sequentially for different drugs [132]. It was shown that the sustained release can be controlled and prolonged up to two weeks using different matrices to load the drug molecules.

Another type of biofouling protection can be performed using nitric oxide-releasing elements, as it is known for a while as a successful inhibitor of platelet and bacterial adhesion [133]. Soto *et al.* showed that NO-releasing silica nanoparticles can be included into polyurethane coatings and integrated with the needle-type glucose biosensor which was then implanted into a swine model and evaluated for 10 days (Figure 2-8D) [134]. It was emphasised that NO release improved the analytical performance of the *in vivo* glucose sensor and it was thought that coating are capable of releasing even higher NO extent for longer durations up to several weeks which would be very significant for long term glucose screening in diabetic patients.

Biocompatible hydrogels are also drawing attention in recent times, as they could possess a significant potential as a component of implantable biosensor and/or a drug delivery matrix [135]. Yu and his colleagues developed a novel hydrogel which based on a copolymer of hydroxyethyl methacrylate and 2,3-dihydroxypropyl methacrylate, where its porosity and mechanical properties were then optimised with the addition of N-vinyl-2-pyrrolidinone [136]. Eight sensors consisting of platinum / glucose oxidase / epoxy-polyurethane / N-vinyl-2-pyrrolidinone hydrogel were implanted in rats subcutaneously and evaluated for 4 weeks. It was observed that all sensors remained functionable until 21 days, while only 3 of them survived at the end of 4 weeks period when also biological evaluation was carried out and it was showed that the thicknesses of the fibrous capsules encapsulating the hydrogel-coated sensors were less than the ones without the hydrogel (Figure 2-8E).

In a very recent work by Robotti et al., the performance of microengineered non-resorbable biosynthesized cellulose membranes (micropatterned with designed geometries) was evaluated in terms of anti-fibrotic protection of a pacemaker which was implanted into a chronic minipig animal model [137]. Biological assessments were done after 3 and 12 month-periods following the implantation. It was reported as a conclusion that the biosynthesised cellulose membranes reduced the average thickness of the fibrotic tissue by 66%, in comparison to the control pacemakers which were not wrapped with a membrane (Figure 2-F). This might offer a potential for easier cardiac surgery conditions and less risky circumstances for patients.

Despite the detailed achievements of the summarised examples which can offer good opportunities for drug delivery or label-free biosensing, most of the electrochemical biosensor platforms typically require labels (redox tags etc.) as their sensing (recognition) elements which either need to be in a direct contact with the target analyte or integrated with a membrane layer. In both cases, non-specific binding of proteins and cells, or biofouling will be induced and affect the sensor performance when they are implanted into any location of the body. This therefore presents a highly challenging problem with respect to implantation and biocompatibility of probe-based electrochemical biosensors. Luckily, many biocompatible materials based on polymers, hydrogels, SAMs and peptides are available to produce anti-fouling interfaces [138]. However, their feasibility and compatibility is not fully explored when in combined/integrated with SAM-based electrochemical systems. This underlies the significance of their potential and thus research interest in order to develop SAM-based electrochemical platforms with enhanced biocompatibility.

2.4 Self-Assembled Monolayers

Self-assembled monolayers (SAMs) are formed by the spontaneous formation of molecules as a monolayer on a substrate surface by adsorption. Following successful initial adsorption, they usually reorganise to form ordered monolayer structures. Because of their significant potential as a cheap, simple and well-controlled surface coating method, their fundamentals have been widely studied and they have been employed in plenty of applications. Although a monolayer film was first observed by Langmuir in 1917 where he observed the formation of one-molecule-thick amphiphile film, the SAM concept was initially suggested by Zisman and his colleagues in 1946 where they studied the spontaneous formation of alkylamine monolayers on a platinum substrate [139]–[141]. SAMs can be considered as enhancement of Langmuir-Blodgett films where a monolayer or multilayers of molecules can be transferred from a liquid/gas interface onto a solid substrate [142], because SAMs offer ease of fabrication owing to their self-organisation characteristics.

There is usually a stronger interaction in SAMs between head groups and substrate atoms (Figure 2-9). Particular groups (tails) within SAM molecules can be also functionalised on-demand depending on an application. Since the time when first suggested, SAMs with different head groups and their interactions between varying substrates were reported in a number of studies including thiols on metals (gold, silver, copper, palladium, platinum and mercury) [143], silanes on silicon or glass [144], [145] and acids on metal oxides [146].

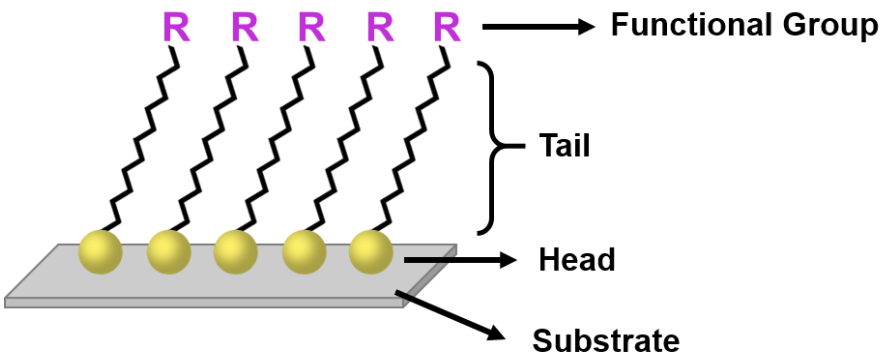

Figure 2-9: Schematic illustration of a typical self-assembled monolayer (SAM).

SAM formation (growth) is produced by two main processes [147]:

(i) the solution-phase transport of molecules to solid-liquid interface and their adsorption
(ii) self-organisation on the surface.

Both of these processes are based on both thermodynamics and kinetics, resulting in the growth that is determined or controlled by changes in variables such as temperature, concentration, surface structure and interactions. For example, the adsorption rate of SAMs can be diffusion-controlled, adsorption-controlled or both in a mixed regime [147]. Figure 2-10 established SAM formation mechanisms which correspond to two hypothetical isothermal paths observed at T_1 (a temperature below the triple point, T_{triple} which can be defined as the temperature value at which the solid, liquid and vapor phases of SAMs coexist in equilibrium) and T_2 (a temperature above T_{triple}) in the quasi-equilibrium phase diagram which was produced based on the experimental evidences [147].

Instead of a continuous path, a common SAM formation is thought to follow the phases included in the diagram:

(i) low density 2-D vapor phase where SAM molecules are randomly dispersed on the surface
(ii) intermediate 2-D liquid phase where some of SAMs are not conformationally well-ordered
(iii) high density 2-D solid phase where close packed and well-ordered molecules are present.

At lower temperature case, T_1, SAM molecules are firstly adsorbed and create a dilute vapor phase. Afterwards, a solid-vapor mixed state appears at a low surface concentration where the nucleation and growth of solid phase islands are observed and isolated vapour phase molecules surround them. Then, they together further propagate and spread to create an ordered monolayer on the surface. It is slightly different and more complicated at higher temperature, T_2. At a certain surface concentration, an intermediate low density phase appears, where molecules then nucleate and grow. However, as also illustrated in the same figure, this phase might be a disordered 2-D liquid phase or an ordered 2-D solid-like but lower density phase where lying molecules can be observed.

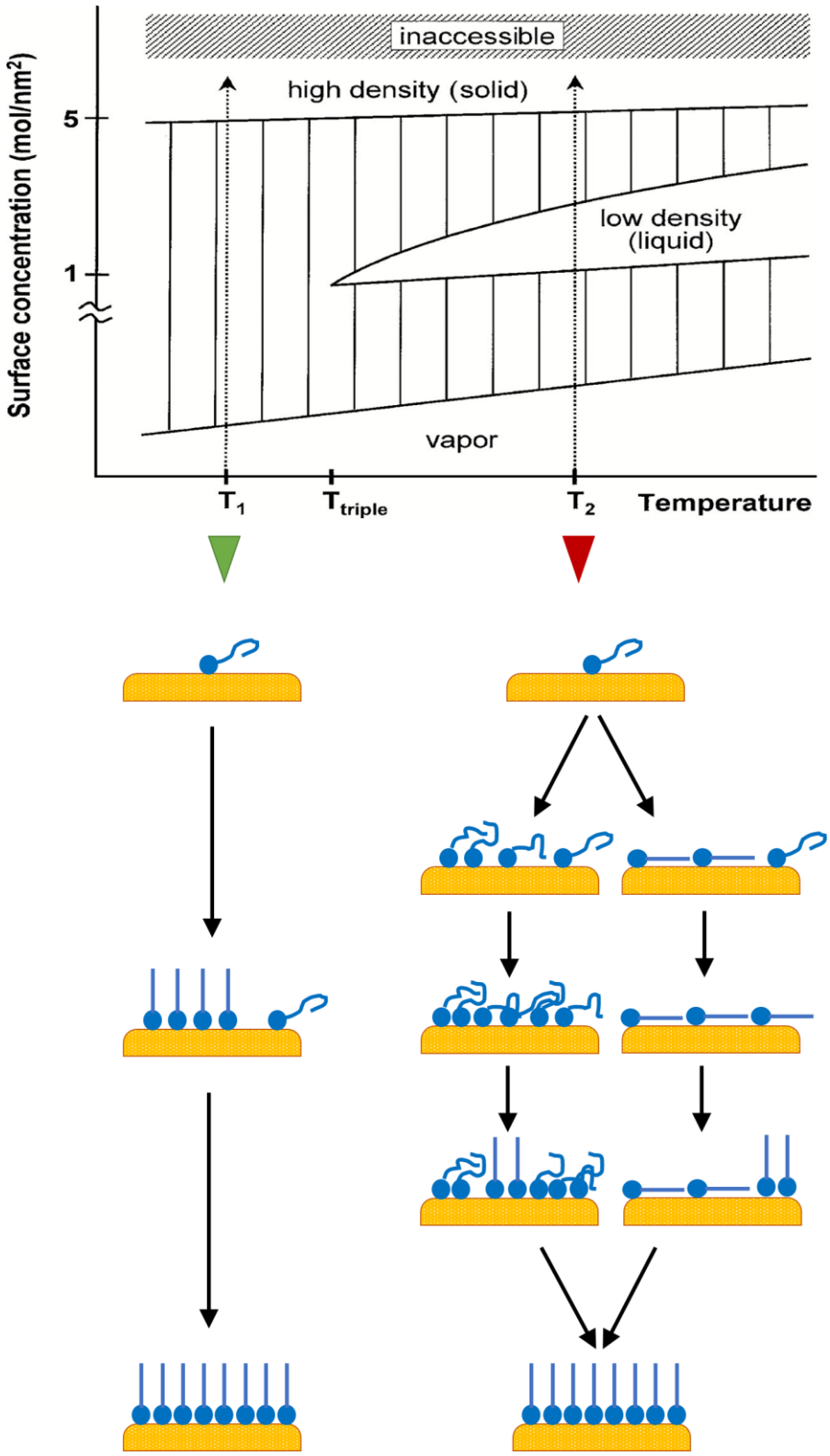

Figure 2-10: Schematic illustration of the differences in growth of a generic SAM system with respect to two hypothetical isothermal paths (at a temperature T_1 or T_2) indicated in the quasi-equilibrium phase diagram. Adapted from [147].

In both conditions, ongoing adsorption creates a conversion from the low density phase to the high density phase where solid phase islands again surrounded by liquid or vapour phase molecules, which eventually grow and cover the substrate surface in an ordered orientation. However, it has been noted that this summary is the simplest form of the SAM formation mechanisms and more complex dynamics are very likely to be seen especially at non-equilibrium conditions [147]. Although the given isothermal paths in Figure 2-10 are hypothetical, it was previously shown by experimental studies that there are distinct growth mechanisms taking place at varying temperatures. For instance, Carraro *et al*. showed that island growth was seen at temperatures below 16 °C, homogeneous growth dominated at temperatures above 40 °C and a mixed regime was observed at intermediate temperatures during the self-assembly of octadecyltrichlorosilane-based monolayers on silicon oxide surfaces [148]. In another work, Messerschmidt and Schwartz presented that the monolayer growth mechanism of octadecylphosphonic acid on sapphire surfaces was also dependent on the temperature [149]. In this work, the nucleation of close-packed and vertical islands and 2-D vapor-solid phase transition was observed at lower temperatures (2 °C), while a continuous 2-D liquid-solid phase transition was seen instead at higher temperatures (22 °C). There was again a mixed regime at an intermediate temperature (15 °C) where both formation mechanisms were seen to be dominating simultaneously at different locations of the surface. It is also known that the SAM growth process may be affected by a number of other variables. For example, Bain et al. observed that the formation of alkyl thiols including longer chain tails (with a number greater than 8) on gold substrates was more controlled compared to SAM molecules with shorter chains [150]. Furthermore, it was found that there was an inverse proportion between the resulting film quality and the solubility of thiol in the solvent used [151]. The presence of SAM defects (pinholes) on surfaces is another common issue related to a complex mechanisms and the lack of a controlled deposition technique [152]. Although the kinetics (rate) of SAM surface coverage was found to be affected from several variables including the nature and concentration of the SAM molecule, solvent type, chain length and adsorption energies [147], the fastest step was attributed to initial chemisorption (typically occurs in seconds/minutes), which was followed by a little slower (3-4 times) chain straightening step, and its re-organisation which takes place 35-70 times slower [153].

In order to precisely understand the characteristics of SAM layers and investigate the presence of any defects, different analytical techniques can be utilised including a) electrochemical methods, b) mass-based techniques, c) optical spectroscopy, d) contact angle measurements, e) scanning probe microscopy and f) surface-sensitive electron spectroscopy (Figure 2-11) [141]. Electrochemical methods such as cyclic voltammetry (CV) and electrochemical

impedance spectroscopy (EIS) have been used to provide significant information related to SAM layer thickness, film quality and possible defects [154]. Mass-based (piezoelectric) techniques such as quartz crystal microbalance (QCM) or surface acoustic wave (SAW) equipments have been utilised to monitor the relative changes in mass on a substrate, which occur due to the SAM adsorption or the selective binding of analytes to already immobilised receptor SAMs, thus the quantity of adsorbate molecules and the corresponding kinetics have been analysed [155]. Optical spectroscopy have been employed to explore a variety of SAM properties such as identification of the functional parts by IR spectroscopy [156], surface monolayer coverage by UV-vis [157] and fluorescence spectroscopy [158] as well as SAM layer thickness by ellipsometry [159] and SPR [160]. In order to understand the wettability characteristics of SAM-adsorbed surfaces, contact angle measurements can be carried out as a simple method. In this way, composition and structure of the adsorbed layers have been initially and easily assessed prior to the utilisation of any complex technique [161]. Furthermore, surface wettability (hydrophilic/hydrophobic) is really a determinant variable in terms of the biocompatibility of materials, thus the wettability characterisation for SAMs has been stated as being fundamental [162]. Of course, the structure of the substrate to be covered by SAM molecules should be also considered as another parameter in addition to the SAM chemistry, because both are known to be important in determining the wettability. Another useful method which gives insight related to SAM orientation, packing and surface potential is scanning probe microscopy, which includes atomic force microscopy (AFM) [163], kelvin probe force microscopy (KPFM) [164], scanning tunnelling microscopy (STM) [165] and scanning electrochemical microscopy (SECM) [166]. Although they are grouped under the same category, each has fundamental differences in terms of the types and functions of the scanning probes [167]. Surface-sensitive electron spectroscopy techniques (e.g. X-ray photoelectron spectroscopy, XPS or Auger electron spectroscopy, AES) have been also used to make an elemental analysis, providing deeper chemical information about the adsorbates [168]. Because of that controlled and reproducible SAM formation is not typically simple due to occurring in multiple stages, it might be required to have comprehensive characterisation that can only be achieved by combining some or all of these analytical techniques, instead of utilising a single one.

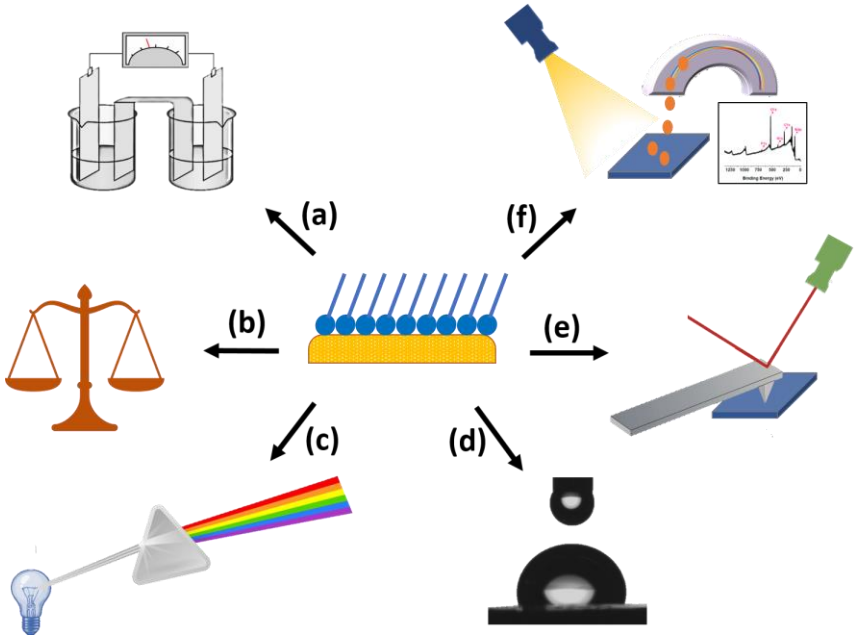

Figure 2-11: Common analytical techniques used for SAM characterisation can be given as a) electrochemical methods, b) mass-based techniques, c) optical spectroscopy, d) contact angle measurements, e) scanning probe microscopy and f) electron spectroscopy.

SAMs have been employed in a variety of applications including wettability alterations, pH and ion sensing, biocompatible functionalisation, lubricant and corrosion-protective coatings as well as biosensing. For example, Wang *et al.* achieved superhydrophobic (with a contact angle of ~153º) and superhydrophilic (with a contact angle of 0º) surfaces by adsorption of *n*-octanoic acid and *n*-propanoic acid, respectively, onto initially-modified (by electrochemical deposition to result in micro- and nano hierarchical structures) copper films by immersing in ethanolic solutions for 12 h [169]. This alteration was attributed to the chain length of acids, where short chain ones were found to be disordered and methyl groups were exposed, whereas longer chain acids were more well-packed and ordered which enhanced the proportion of hydrophobic methyl groups [169]. This structural distinction between shorter and longer chains was also consistent with the previously mentioned observation of Bain *et al.* regarding alkyl thiols on gold [150]. They have been also used for pH sensing e.g. Hickman *et al.* deposited ferrocenyl thiol (ferrocene as pH-insensitive reference) and quinone thiol (quinone as pH-sensitive indicator) onto gold microelectrodes and measured the voltammetric changes between the oxidation and reduction peaks of quinone to detect pHs between 1 and 11 [170]. In addition to pH sensing and wettability alterations, there are examples where SAM molecules were employed to control and design cell (or protein)-surface interactions. For example, Chang *et al.* showed that the ratios of two SAMs with functional groups -NH_2 and -COOH (becoming

NH_3^+ and COO^- based on pH) on substrate surfaces can be accordingly changed to modify the surface charge density which lead to the alterations in the cell adhesion [171]. The increase in the surface potential was found to promote the adhesion density of laminin-dominant epithelial cells without any significant change in their morphologies which were attributed to the stronger adsorption of positively charged laminin. Contrastingly, morphology changes were observed in fibroblasts with greater adhesion to NH_3^+, attributed to the presence of negatively charged fibronectin which exhibited stronger interaction to the positively charged surfaces. Other work by Widge *et al.* showed that combined SAM systems containing mixtures of thiolated poly(alkylthiophene) and alkanethiols functionalised with a neural cell adhesion molecule (binding antibody, NCAM), improved the biocompatibility of neural electrodes (with ongoing neurite outgrowth up to 7 days) [172]. Coatings of self-assembled monolayers have not only been applied to enhance the biocompatibility of biomaterials, but also for tribological purposes such as creating more lubricious [173] and corrosion-resistant materials [174]. In addition to these useful applications, they are commonly employed as recognition moieties to build biosensing platforms, owing to these advantages: (i) easy, stable and well-ordered formation, (ii) a cellular compatible structure for biomolecule adhesion, (iii) easy modification of the head and functional group depending on the application, (iv) minimised amount required for surface coverage, (v) practical shelf life (stability/durability) and (vi) applicability of varying techniques for their detailed characterisation [175]. Although there are some accompanying limitations; (i) high sensitivity of immobilised biological substances towards changes in external variables (pH, temperature, ionic conductivity) and corresponding fluctuations in their activity, (ii) lack of chemical inertness, (iii) instability against thermal and electric field changes, (iv) contamination and impurity problems which might hinder the sensing [175], biological recognition and host-guest interactions by SAMs have been successfully investigated using the techniques given in Figure 2-11 and utilised for the detection of DNA, antibody-antigen interactions, enzymes, vitamins and many others so far, as previously reviewed in detail [141].

Of the various approaches to SAM design, redox-active SAM molecules which are immobilised onto electrode surfaces have drawn significant recent attention. As shown in Figure 2-12, these consist of a mixed monolayer; a redox centre, a bridge and a diluent [176]. They can be easily prepared and then the electron transfer which occurs between redox centre and underlying substrate (electrode) is monitored by various electrochemical techniques, some of which have been detailed in Section 2.6. The role of the flexible or conjugated bridge is to enable electron transfer, by connecting the electrode surface and the redox moiety, while the

diluent molecules are used to create an enough space between two individual SAMs in order to ease the electron transfer for flexible, bending bridges, to increase accessibility of analytes and to hinder any possible interaction between analogous redox centres [176]. The structure of the bridge element is especially significant for redox-active SAMs in terms of electron transfer kinetics and binding of the target analyte and this is why it is generally selected based on a specific application. The literature includes studies on alkane bridges, functional groups, conjugated bridges and peptide bridges [176]. It should be also noted here that redox-labelled peptide-based SAM molecules distinctly vary from others, offering densely packed stable surface films and further recognisability e.g. to enzymes, in addition to their investigations which made quite understandable the relationship between the electron transfer mechanisms and peptide/SAM surface conformation [177].

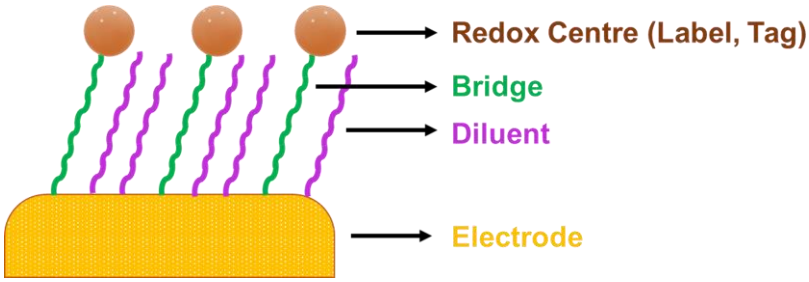

Figure 2-12: The structure of redox-active SAM molecules. Adapted from [176].

2.5 Electrochemistry

2.5.1 Reduction-Oxidation (Redox) Reactions

Electrochemistry is the study of interrelationship between electrical changes (current and voltage) and chemical reactions. For example, an induced change in the potential might be seen as a result of a chemical reaction, or an applied potential can lead to a difference in the mechanism of a chemical reaction. Electrochemical reduction-oxidation reaction, where the transfer of electron(s) between chemical species creates an oxidised and corresponding reduced form, is one of the main types of chemical reactions studied under the title of electrochemistry. The following reaction (Figure 2-13) where $2e^-$ and nH^+ is transferred between leuco-methylene blue (LMB, reduced form) and methylene blue (MB, oxidised form) is a common redox system used throughout this work. Of course, it should be noted that the number (n) of H^+ transferred depends on the pH and pKa of MB and LMB.

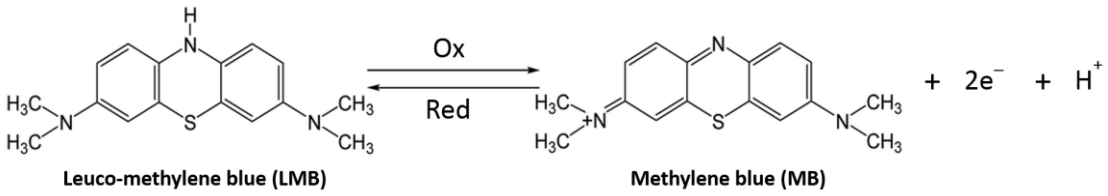

Figure 2-13: Typical reduction-oxidation reaction between leuco-methylene blue (LMB) and methylene blue (MB).

The redox reactions generally occur at the interface of a bulk solution and a metal electrode surface. In this case, the leuco-methylene blue (reduced form of methylene blue) which is in a close proximity or bound to the electrode surface is oxidised reversibly when a specific potential, $E > E'$ is applied and converted to methylene blue. This results in the transfer of two electrons into the electrode surface and the formation of a current which is then measured by an electrochemical technique in the external circuit. Conversely, when $E < E'$, MB turns to LMB and $2e^-$ per MB are donated from the electrode.

The relationship between the electrode potential and the concentration of reacting chemical species in an electrochemically reversible electron transfer can be defined by the Nernst equation below [178];

$$E = E' + \frac{RT}{nF}\ln\left(\frac{C_{ox}}{C_{red}}\right) \tag{2.1}$$

where E is the applied potential, E' is the formal potential (the potential when $C_{ox} = C_{red}$) of the reaction, n is the number of electrons transferred per mole of reagent/product, R is the universal gas constant, T is the temperature in Kelvin, F is the Faraday constant and C_{ox} and C_{red} are the concentrations of oxidised and reduced forms of the chemical species. At the electrode surface, E' is replaced by the standard electrode potential E^{θ}, when C_{ox} and C_{red} are replaced by the activities a_{ox} and a_{red}, instead of the concentrations. Activity can be defined as a measure of the effective concentration of substances in non-ideal (real) solutions and thus can be affected from some variables such as solution composition, pressure and temperature. Activity and concentration can be converted into each other using the relation, $a = \gamma \cdot C$ where γ is the activity coefficient.

In non-equilibrium conditions, however, the Nernst equation would not able to define the relationships between the electrode potential and other variables. Because the electrode potential will be different from the equilibrium potential, when there is a current passing through the electrochemical cell. In this case, Butler-Volmer equation (equation 2.2) [179] can define the current density at the electrode in terms of the overpotential ($\eta = E^* - E$) which is the difference between the electrode potential (E) at equilibrium and the electrode potential (E^*) when there is an external current passing through the cell;

$$j = j_0 \{ e^{(1-\alpha)\eta F/RT} - e^{-\alpha\eta F/RT} \} \quad (2.2)$$

where j is the current density, j_0 is the exchange-current density (equal opposite current density at equilibrium), α is the transfer coefficient, η is the overpotential, F is the Faraday constant, R is the universal gas constant and T is the temperature.

2.5.2 Three-Electrode Cell

In order to measure the changes in these electrical parameters during the redox reaction, a standard three-electrode cell was used in this work (Figure 2-14). This setup consists of working, counter and reference electrodes. The working electrode (WE) is the main location where the redox reaction takes place. The reference electrode (RE), having a fixed potential, holds/controls the potential at the working electrode in defined values, by applying a potential difference between them. In this way, the controlled potential of the working electrode by the reference electrode can lead the chemical reaction occurring and its rate can be measured from the current passing between the working electrode and the counter (auxiliary) electrode (CE) which completes the electrical circuit and provides the required current for the working electrode. They are usually used in larger dimensions compared to the size of working electrode to avoid any limitation in its current. Macro-, micro- and nanoelectrodes were used as the working electrodes, silver/silver chloride (Ag| AgCl| KCl (3 M)) as the reference electrode and in-house built platinum-coated silicon dioxide chip as the counter electrode in this work.

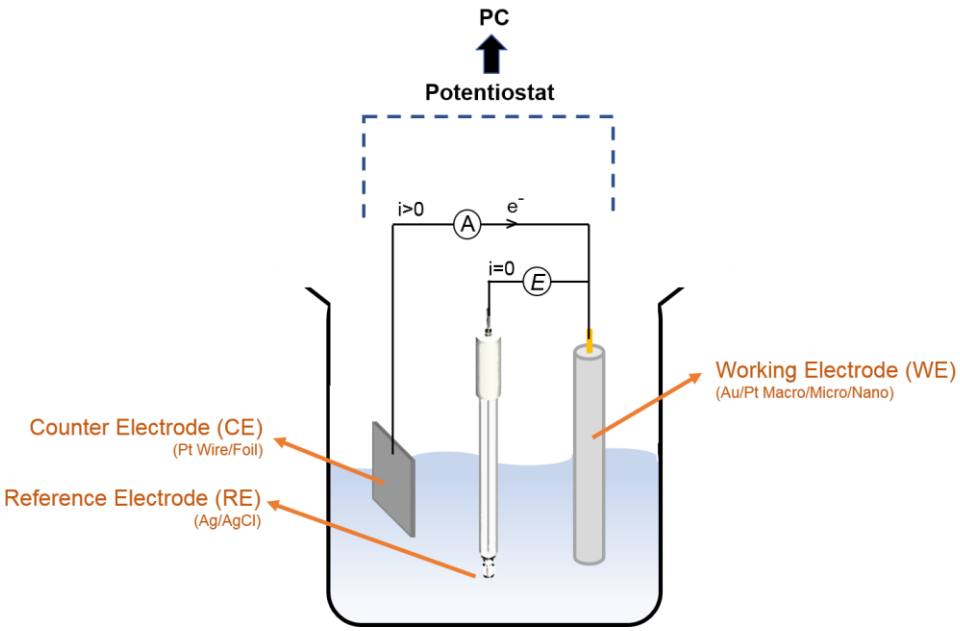

Figure 2-14: Schematic of the three-electrode measurement system.

2.5.3 Characteristics of Macro-, Micro- and Nanoelectrodes

Size (or dimensions) is highly significant and effective parameter determining electrode response. Specifically, microelectrodes and nanoelectrodes (typically between 1 nm and sub-micron) exhibit several differences over macroelectrodes which are larger than 100 µm and usually on the millimetre scale or above. These include lower currents, lower capacitances, higher signal-to-noise ratios, reduced footprint and enhanced mass transport. Although they present lower currents compared to macroelectrodes, they have higher current densities and signal to noise ratio, because current density is defined as the current passing per a unit area, which is proportional to the square of the electrode radius, r^2 for a disc-shaped electrode, whereas the current is proportional to the radius of the disc, r [180]. Therefore, it is established that current densities increase in order from macroelectrodes to microelectrodes to nanoelectrodes.

The rate of an electrochemical reaction can be affected by two factors; rate of electron transfer and mass transport. Mass transport is the movement of chemical species, which are able to undergo redox reactions, from the bulk solution to the electrode surface. There are three modes of mass transport, which are diffusion, migration and convection [178]. Diffusion occurs during a chemical reaction due to a concentration gradient which forms between reduced and oxidised species at the solution-electrode interface. If the reduction takes place at the electrode

surface, for example, the concentration of oxidised species will be less at the electrode than in bulk solution, which results in the movement of oxidised species in the bulk solution towards electrode, whereas reduced species move to the bulk solution. Migration is the motion of charged species based on electrostatic forces often induced by potential gradient. Convection is the transport mode based on mechanical forces such as stirring and vibration. Although natural convection always exists and influences current densities of the electrodes, this effect is minimised for microelectrodes and nanoelectrodes where diffusion is significantly higher which makes natural convection comparatively negligible [181], [182].

A diffusion field (layer) develops when reactant species are depleted at the electrode surface and this field provides more substances to be moved towards the electrode to contribute to continuity of reaction (Figure 2-15). The thickness of the diffusion field formed on a macroelectrode is larger than electrode and this promotes linear (planar) diffusion [182]. On an electrode with smaller dimensions, e.g. microelectrodes or nanoelectrodes, the thickness of diffusion field is similar to electrode and this results in hemispherical (radial) diffusion to dominate [182].

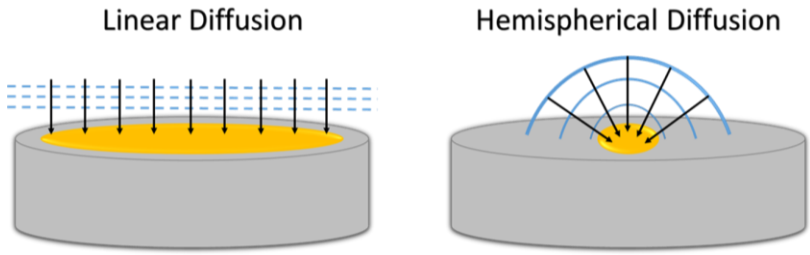

Figure 2-15: Diffusion field (layer) profiles at the interface of the electrode-bulk solution. This results in species to move towards the electrode surface. It can occur either as linear (planar) diffusion which is commonly valid for macroelectrodes or hemispherical (radial) diffusion which dominates when electrode size is reduced.

It is established that hemispherical diffusion is much more efficient than linear diffusion and thus leads to several advantages for microelectrodes and nanoelectrodes over macroelectrodes such as steady state currents which are independent of time, reduced convection, higher current densities and lower noise-related issues [183], [184]. Especially for sizes reduced to the nanoscale, reduced *iR* drop also adds to these advantages. This can be defined as the potential difference between the extent applied by the potentiostat and the actual potential at the working electrode, induced by the electrolyte resistivity [185]. Reduced *iR* drops can thus open additional possibilities for measurement in more resistive environments [185].

Because microelectrodes and nanoelectrodes present lower amplitudes of currents due to their reduced electrode area, they are often fabricated in arrays in order to maximise the measured signal [186]. It should be noted that hemispherical diffusion and its advantages can be still secured for electrode arrays as well as enabling currents of similar amplitudes to macroelectrodes as long as the electrodes act independently [154], [187]. To achieve this, the interelectrode spacing should be optimised to avoid any overlap/interaction between the diffusion fields. If neighbouring electrodes are located too close in a proximity, the overlapping of diffusion fields can cause hemispherical diffusion to become linear, leading to the macroelectrode behaviour which would not be desired for many applications where miniaturised electrodes are employed (Figure 2-16). Optimal spacing depends on the timescale of an experiment [188] (See Section 5.3).

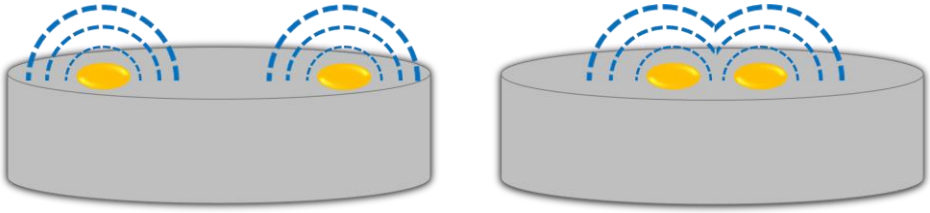

Figure 2-16: Diffusion fields might overlap at the surfaces of electrode arrays due to smaller interelectrode spacings.

2.6 Electrochemical Techniques

There are many electrochemical techniques which can be used for the analysis of electrochemical reactions. The three types of electroanalytical methods [189] are (i) *conductimetric (impedimetric)* where the response is analysed with respect to the conductance of the solution, (ii) *potentiometric* where the potential difference between two electrodes (working and reference) is measured when a current is applied, and (iii) *amperometric (voltammetric)* where the current is measured at a fixed applied potential between working and reference electrodes. The most appropriate technique should be chosen carefully because each technique offers advantages for particular purposes and range of applications [189]. Based on our need which requires the sensitivity due to monolayer detection, the amperometric techniques including cyclic voltammetry, square wave voltammetry and chronoamperometry were used in this work. In the following sections, the principles of these techniques and the resulting response and its analysis are outlined.

2.6.1 Cyclic Voltammetry (CV)

Cyclic voltammetry (CV) is the most commonly employed technique in electroanalysis because it can provide both qualitative and quantitative information about redox reactions, electron transfer kinetics and adsorption processes [184]. In this technique, the potential applied at the working electrode is swept linearly from a starting potential, E_1 to a final potential, E_2 and then back again at a constant sweep (scan) rate, *v*. This gives a triangular potential waveform. The currents obtained as a result of these applied potentials are measured by the potentiostat and a current vs potential plot is generated, which is called a cyclic voltammogram. A particular range of potentials applied to the working electrode is always chosen in order to promote the redox reactions of the electroactive species under electrochemical investigation [182]. A typical cyclic voltammogram and a triangular potential waveform is shown in Figure 2-17. The arrows in the figure show the potential sweep direction. According to this, when a higher potential is linearly swept at the working electrode from E_1 to E_2, a neutral chemical species M is oxidised and becomes M^+, which is then reduced and turns back to initial form when the potential is swept backwards. The slope of the applied potential waveform can give the scan rate in voltage (measured against a reference electrode) per second.

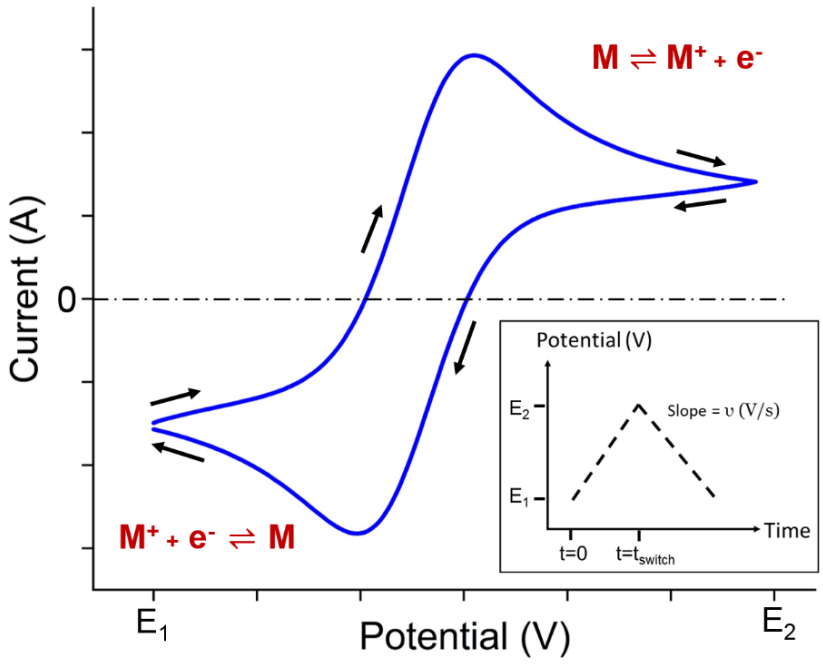

Figure 2-17: Triangular potential waveform applied to the working electrode and a resulting typical cyclic voltammogram for the reversible redox reaction of $M^+ + e^- \rightleftharpoons M$ in a solution containing both M and M^+. Adapted from [184].

For a fully reversible system, the peak current is defined by the Randles-Sevcik equation [184],

$$i_p = 0.4463nFAC\sqrt{\frac{nF\nu D}{RT}} \quad (2.3)$$

where n is the number of electrons, A is the electrode area in cm^2, C is the bulk concentration in mol/cm^3, D is the diffusion coefficient in cm^2/s, v is the potential scan rate in V/s, T is the temperature in Kelvin, F is the Faraday constant in C/mol and R is the universal gas constant in J/mol·K. This establishes that the peak current is directly proportional to the bulk concentration and electrode area at fixed scan rate, and it increases with the square root of the scan rate. This dependence on the scan rate is actually indicative of a mass transport-controlled reaction when linear diffusion e.g. to a macroelectrode is occurring [184]. An increase in the scan rates results in less time for diffusion and a corresponding decrease in the diffusion layer thickness at the electrode, leading to higher currents [190]. However, this equation, and the linear relationship between i_p and $v^{1/2}$ is only valid for freely diffusing redox species in bulk solution. If the redox species were adsorbed onto the electrode surface and rapid (electrochemically reversible) electron transfer occurs, the rapid reaction of this fixed amount of species results in the peak current becoming directly proportional to the scan rate, instead of its square root (See equation 4.5).

As well as the peak current, the position of these peaks in the voltammogram is also characteristic of the processes occurring at the working electrode. It has been established for an electrochemically reversible reaction that the difference between the anodic ($E_{p,a}$) and cathodic ($E_{p,c}$) peak potentials (called the peak separation, ΔE_p) is $59/n$ mV at 298 K [190]. For such a reversible (Nernstian) response, this can then be used to determine the number of transferred electrons. It should be emphasised that electrochemical and chemical reversibility are not the same. While chemical reversibility refers to the stability of the analyte against chemical side reactions when carrying out multiple oxidation and reduction cycles, electrochemical reversibility describes rapid electron transfer kinetics between the electrode and electroactive species. In the case of electrochemical reversibility, electron transfer is often easy due to a low transition state barrier compared to the thermal energy and Nernstian equilibrium and a balance between appreciable reduction/oxidation rates is observed. If a reaction is electrochemically irreversible, electron transfer becomes slower and more difficult due to a high transition state barrier; net oxidation or reduction reactions thus require much larger changes in reduction/oxidation overpotentials (potentials to be made much more

negative/positive of the formal potential) for a reaction to occur, leading to a wider peak separation and domination of either oxidation of reduction.

Cyclic voltammetry has been employed for the characterisation of macroelectrodes and microelectrodes for many years, and their characteristic responses are well-established. Although they typically result in peak currents for macroelectrodes due to linear diffusion, a sigmoidal shape for micro- and nanoband edge electrodes is observed due to hemispherical diffusion (Figure 2-18) [191]. Unlike macroelectrodes, these microelectrodes and nanoelectrodes show diffusion-controlled, steady-state mass transport behaviour indicative of these diffusion limited currents being stable and independent of time. Therefore, macroelectrode currents are expected to change with varying scan rates, unless scan rates are so high that the diffusion layer thickness is much smaller than the electrode dimension and hemispherical diffusion has not been established, whereas scan rate should not affect the currents registered for such micro- or nanoelectrodes [183], [185], [192]. However, even in this case, the diffusion layer thickness still grows with time, and if micro- or nanoelectrodes are fabricated in arrays instead of individual electrodes and they are located sufficiently close as explained in Section 2.5.3, at slow scan rates neighbouring diffusion fields may overlap and this may eventually lead to linear diffusion again occurring, and the reestablishment of peak currents in voltammograms.

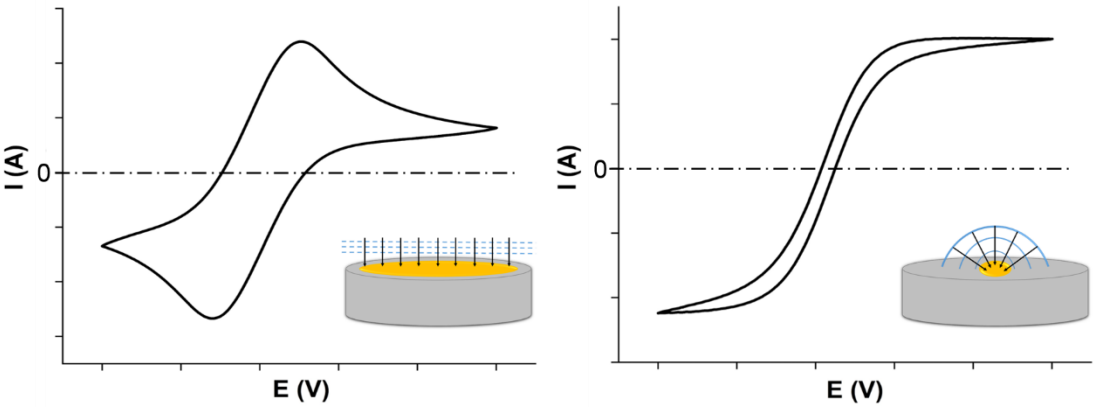

Figure 2-18: Characteristic CV responses of macro- and microelectrodes as a result of linear or hemispherical diffusion.

The equations for the diffusion limited current, i_L, registered at large overpotentials when the current has become independent of potential, for different types of electrodes previously reported [182], [192] are found below:

Single microdisc: $i_L = 4nFDCr$ (2.4)

Single hemispherical microelectrode: $i_L = 2\pi nFDCr$ (2.5)

Microelectrode (disc) array (with no overlap): $i_L = 4nNFDCr$ (2.6)

Nanoband edge electrode (disc) array (with no overlap): $i_L = 0.956nNFDCr$ (2.7)

Nanoband edge electrode (square) array (with no overlap): $i_L = 0.956nNFDCL$ (2.8)

where *n* is the number of electrons, *N* is the number of electrodes in the array, *F* is the Faraday constant, *D* is the diffusion coefficient (cm^2/s), *C* is the bulk concentration (mol/cm^3) of the redox species in the solution, *L* is the edge length (cm) and *r* is the radius (cm) of an individual electrode in the array.

2.6.2 Square Wave Voltammetry (SWV)

Square wave voltammetry (SWV) is a type of linear sweep method related to CV, which combines a superimposed square wave potential waveform on the staircase potential applied to a working electrode, when using a PC-controlled potentiostat [189] (Figure 2-19). In this way, the current at the working electrode is measured while the potential of the working electrode (with respect to the potential of reference electrode) is linearly swept in time. The square wave is typically characterised by a pulse height (square wave amplitude, ΔE_p), the staircase height (ΔE_s), the pulse time (width of the pulse, t_p) and the period of cycle (t_s) [184]. The square wave frequency, f is related to the pulse time, $f = 1/2t_p$. Typically, the staircase height is small compared to the pulse height, as shown below.

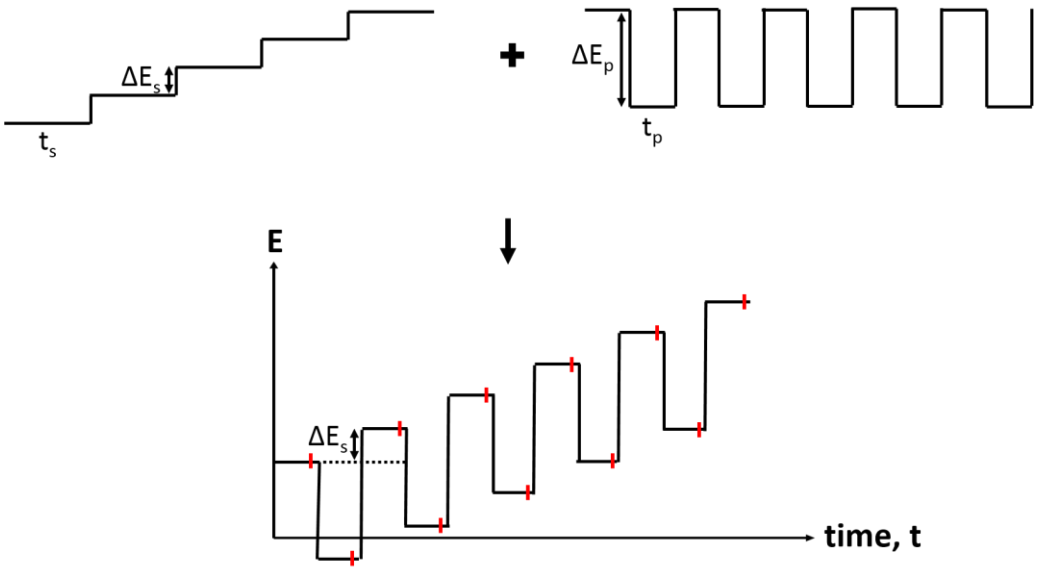

Figure 2-19: Schematic waveform for SWV technique which consists a staircase potential (with a staircase height of ΔEs and a cycle period of t_s) and a superimposed square wave (with an amplitude of ΔE_p and a pulse width of t_p). Red lines show the time points for the collection of the currents which take place two times per each scan at the end of the forward and backward potential pulses. Adapted from [184].

As also illustrated in the figure with red lines, the current is collected at two times, typically at the end of the forward and backward potential pulses. This current sampling technique minimises the effect of non-Faradaic capacitive (charging e.g. double-layer) current on the final signal. When the sum of the forward and backward current for each square wave is calculated and plotted against the potential applied, any peaks in the resulting curve correspond to redox reactions, and the peak height and area can give information about the concentration of reactant and products. The relationship between the magnitude of the peak and the concentrations is given by a modification of Cottrell equation [191] (See Section 2.6.3);

$$i_p = \frac{n\,F\,A\,C\sqrt{D}}{\sqrt{\pi t_p}}\,\Delta\Psi_p \qquad (2.9)$$

where i_p is the SWV peak current, n is the number of electrons, F is Faraday constant, A is the electrode area in cm^2, C is the concentration in mol/cm^3, D is the diffusion coefficient in cm^2/s, t_p is the width of the potential pulse and $\Delta\Psi_p$ is a dimensionless parameter fixing the SWV peak height, relative to the limiting response in normal pulse voltammetry. It was previously suggested that $\Delta\Psi_p$ can be only estimated by mathematical modelling and simulations, and it is independent of the frequency and concentration for a reversible electrochemical reaction [193]. This means that i_p is proportional to the concentration. Also, a linear relationship

between i_p and the square-root of the frequency is a criterion of a reversible electrochemical reaction of a dissolved redox couple [193].

Because square wave voltammetry technique offers many advantages such as reduced analysis duration, short potential pulses and higher detection limits (higher sensitivity), this is one of mostly used techniques in electroanalysis and therefore can be found available in most of the conventional potentiostats [184].

2.6.3 Chronoamperometry (CA)

Chronoamperometry (CA) is the measurement of the changes in the current of an electrode over time while the potential at the electrode is jumped from a rest potential to a fixed reaction potential. It can be also called potential step voltammetry. The starting potential value is typically the point where species are electrochemically inactive [182], whereas the second applied potential corresponds to a value which promotes the species to undergo redox reactions typically under mass transport-limited control. The relationship between the current and time is described by the Cottrell equation [178] for the linear diffusion on an electrode and mass transport controlled reaction of the oxidation of e.g. M to M^+;

$$|i| = \frac{n\,F\,A\,(C_\infty - C_0)\sqrt{D}}{\sqrt{\pi t}} \tag{2.10}$$

where i is the current, n is the number of electrons, F is Faraday constant, A is the electrode area in cm^2, C_∞ is the bulk solution concentration of the M in mol/cm^3, C_0 is the concentration of M at the electrode surface in mol/cm^3, D is the diffusion coefficient in cm^2/s and t is the time in s. According to this relationship, |i| gets closer to zero with time because of the progressive depletion of M at the electrode surface. This oxidation of M to M^+ also results in a drop (or even disappearing) in a large peak typically found in the current-time plot, due to the high concentration gradient of M at the electrode surface. Chronoamperometry has been used in this study to apply varying oxidative and reductive potentials at the electrode surface in order to test whether the potential-assistance makes any difference in the deposition rate of SAM-functionalised probe molecules.

2.7 Enzyme Kinetics

Enzymes are biocatalytic substances most of which are proteins but there are some which are nucleic acid-based. They have an active site where the substrate specific catalytic activity occurs; typically through binding followed by reaction. Experimental evidence shows that the specific binding between the substrate and enzyme can be explained by either one of two model approaches [194]:

(i) a "lock-and-key" model where the three-dimensional structure, conformation and multiple interactions (bonding) between the substrate and enzyme compounds are totally complementary

(ii) an "induced fit" model where active site needs some major conformational rearrangements induced by the substrate for successful binding.

The substantial binding energy can be provided by the combination of a variety of bonds such as hydrogen bonding, van der Waals (vdW) bonding or electrostatic (ionic) bonding. The types of the binding interaction may vary across different types of enzymes (nucleases, kinases, proteases, isomerases, polymerases) or even within the same enzyme family. Although each enzyme has a specific substrate preference, enzymes may be grouped according to similarities in their structures and catalysis mechanisms. For example, a protease group called serine proteases have commonly three amino acids (serine, histidine and aspartate) which are responsible for hydrolysing the peptide bond in the substrate [195]. There exists a pocket at the active site of the serine proteases, where the substrate specificity is driven by the chemical nature of this pocket [195]. This is because an amino acid next to the cleavage site in the substrate inserts into this pocket during catalysis and interacts there with a specific amino acid of the protease [195]. Figure 2-20 shows an example of this, where the pocket at the active site of trypsin contains aspartate, a negatively charged amino acid, which can build an ionic interaction with positively charged arginine or lysine moieties found in the specific substrates [195].

Correspondingly it is possible to summarise that the specificity of enzyme-substrate binding might be various for different enzyme families and groups, and they can be altered by the conformation of substrate compounds as well as the contributions of the molecules at the enzyme active site. Still, the features of enzyme structures have been well-defined by long standing research efforts and fortunately increased the understanding of the basis for catalysis mechanisms.

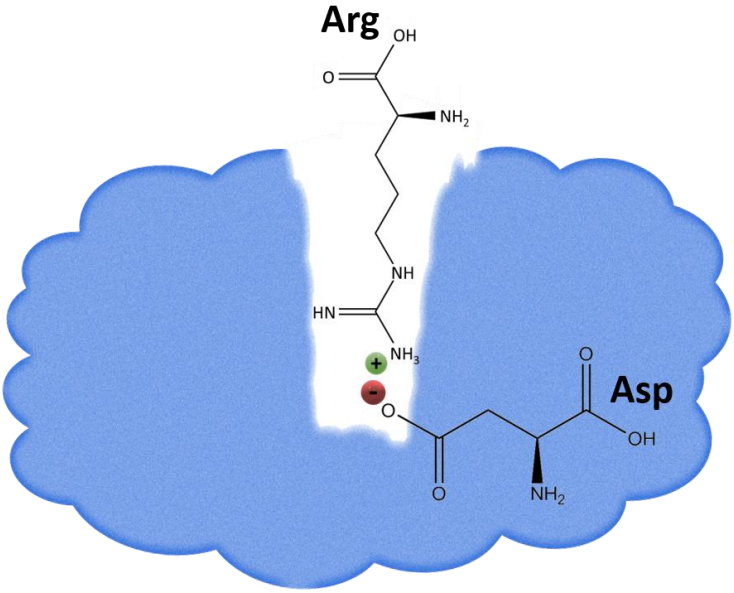

Figure 2-20: Schematic illustration of trypsin binding to the substrate via ionic interaction. Adapted from [195].

The Michaelis-Menten mechanism proposes two steps for the kinetics of reactions catalysed by enzymes. In the first step, an enzyme-substrate complex is formed, followed by either the formation of products in the second step or the release of the unaltered substrate [179]. This can be also expressed using the rate constants,

$$E + S \underset{k_{-1}}{\overset{k_1}{\rightleftarrows}} ES \xrightarrow{k_{cat}} P + E \tag{2.11}$$

The mechanism suggests three fundamental features for the enzyme-catalysed reactions [179]:

(i) Initial rate of product formation is proportional to the total amount of enzyme concentration, $[E]_0$ for a given initial concentration of substrate, $[S]_0$.

(ii) The rate of product formation is proportional to $[S]_0$ if $[S]_0$ is in low concentrations for a given $[E]_0$.

(iii) For a given amount of $[E]_0$ and a high concentration of $[S]_0$, the formation rate of product [P] is independent of $[S]_0$ amount. In this case, it reaches the maximum rate (velocity) value, υ_{max}.

According to these, the product formation rate can be stated as,

$$\upsilon = k_{cat}\,[ES] \tag{2.12}$$

where k_{cat}, also called turnover number, is the rate constant which equals the number of substrate molecules reacting to form product per enzyme molecule in a second and [ES] is the concentration of the enzyme–substrate complex. When the system is in steady-state conditions, there will be no change in [ES] which means [179],

$$d[ES]/dt = 0 = k_1\,[E][S] - k_{-1}\,[ES] - k_{cat}\,[ES] \tag{2.13}$$

$$[ES] = (k_1 / (k_{-1} + k_{cat}))\,[E][S] \tag{2.14}$$

And this then turns to the Michaelis-Menten equation, when an enzyme-substrate interaction specific Michaelis constant, K_M is defined as $((k_{-1} + k_{cat}) / k_1)$,

$$\upsilon = \frac{k_{cat}[E]_0}{1 + \frac{K_M}{[S]_0}} \tag{2.15}$$

When $K_M >> [S]_0$, the rate will be proportional to proportional to $[S]_0$ and the equation will change to $\upsilon = (k_{cat} / K_M)\,[S]_0\,[E]_0$.

However, when $[S]_0 >> K_M$, it will be independent of $[S]_0$ and reach the maximum velocity, $\upsilon = V_{max} = k_{cat}\,[E]_0$, as this can also be seen in the Figure 2-21 below.

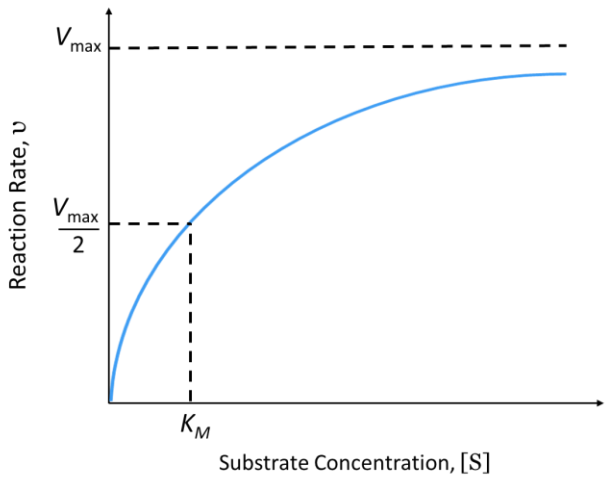

Figure 2-21: Relationship between the reaction rate and substrate concentration for an enzyme-catalysed reaction.

Chapter 3

Experimental Methods & Materials

3.1 Materials and Reagents

Trypsin (MW 23.4 kDa), bovine serum albumin (BSA) (MW 66.5 kDa), calcium chloride, casein (MW 24 kDa), dopamine hydrochloride, ethanol, isopropyl alcohol, sodium dodecyl sulfate (SDS), trypsin inhibitor (Glycine wax, soybean), 6-mercaptohexanol (MCH), 2,2′-(ethylenedioxy)diethanethiol (DT) and 10x phosphate-buffered saline (PBS) were purchased from Sigma Aldrich (UK) and used as received without any further purification. Amino acids were purchased from GL Biochem Ltd. (Shanghai). Eudragit® L 100-55, L 100 and S 100 polymeric powders were supplied by Evonik Nutrition & Care GmbH. All reagents were of analytical grade. Protease-free deionised water (Millipore Milli Q, 18.5 MΩ-cm) was used for the preparation of all solutions.

3.2 Synthetic Methods

The chemical probes used throughout this work were synthesised by Dr. Matteo Staderini and/or Dr. Nicolaos Avlonitis. Further details of the experimental protocols for the synthesis of the redox-labelled peptides (both substrate and control probes) with mono or tri-branched (tripod) anchor can be found elsewhere [7], [196], [197]. The following summary focuses on the description of the general procedures and the main synthetic steps.

N-(carboxypropyl)methylene blue **(4)** was synthesised (Figure 3-1) using the previously described procedure [7], [198]. *N*-Methyl-*N*-(carboxypropyl)aniline **(2)** was prepared starting from commercially available materials. *N*-methyl aniline (1 equiv.) and ethyl-4-bromobutyrate (1.1 equiv.) were dissolved in acetonitrile. To this solution 2,6-lutidine (1.15 equiv.) was added and refluxed overnight. *N*-Methyl-*N*-(carboxypropyl)aniline **(2)** (1 equiv.) was obtained following base mediated hydrolysis of **(1)**. 2-Amino-5-(dimethylamino)phenylthiosulfonic acid **(3)** was prepared in-house by using Wagner`s protocol [199] and then **(2)** and **(3)** (both 1 equiv.) were mixed and dissolved in a mixture of methanol/water (2.5/1 v/v) and heated to below reflux (60 °C). To this reaction mixture silver carbonate (50% w/w) was added in portions and refluxed for 2 hours. After 2 hours, the reaction mixture was cooled to room temperature, filtered and concentrated under reduced pressure. The product, *N*-(carboxypropyl)methylene blue **(4)** was isolated by dry column chromatography, eluting with a gradient of chloroform/methanol/acetic acid.

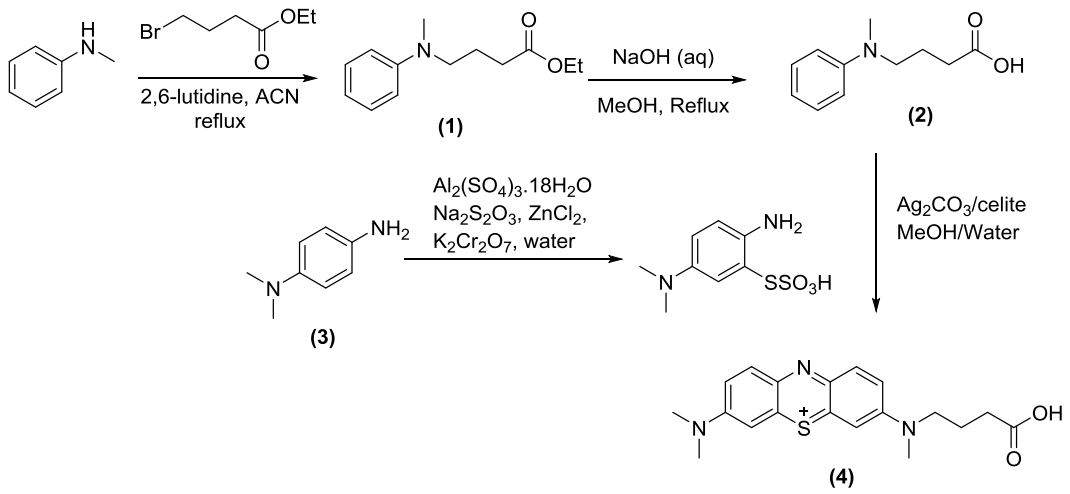

Figure 3-1: Synthesis of *N*-(carboxypropyl)methylene blue [7].

After synthesis of carboxylic acid derivative of the methylene blue, redox-labelled peptides **(5)** (Figure 3-2) were synthesised via Fmoc solid-phase peptide synthesis (SPPS) chemistry. Aminomethyl polystyrene resin was first functionalized with 4-[(2,4-dimethoxyphenyl)-(Fmoc-amino)methyl]phenoxyacetic acid linker (Fmoc-Rink-amide linker). The resin was swollen in dichloromethane (DCM) and the Fmoc group deprotected using piperidine (20% in DMF (N,N-dimethylformamide)) to obtain the free amine for the coupling of each amino acid, PEG or alkyl spacer. The carboxylic acid group on the amino acids/spacer/redox agent (including Fmoc-PEG(2-12)-OH, Fmoc-8-Aoc-OH, Fmoc-Phe-OH, Fmoc-D-Phe-OH, Fmoc-Arg(Pbf)-OH, Fmoc-D-Arg(Pbf)-OH, Fmoc-Cys(Trt)-OH or N-(carboxypropyl)methylene blue) were activated using *N*,*N*,*N*′,*N*′-tetramethyl-O-(1*H*-benzotriazol-1-yl)uronium hexafluorophosphate (HBTU) with N,N-Diisopropylethylamine (DIPEA) in DMF. To achieve activation, the reaction mixture was stirred for 2 min and then transferred into a SPPS cartridge and the reaction shaken for 3 hours. The mixture was washed three times in succession with DMF, DCM and methanol. The Kaiser test [200] was performed to check completeness of coupling at each step. Afterwards, to enable cleavage from the resin, the TFA-based cleavage cocktail (TFA/EDT/water/TIS 94/2.5/2.5/1 v/v) was added to the pre-swollen resin and stirred for 3 hours at room temperature. After three hours, the reaction mixture was filtered, and the resin was washed again with the cleavage cocktail to ensure the collection of all the peptide. The filtrate was added into cold diethyl ether and the solid was collected by centrifugation (x3). The resulting solid was dissolved in water/acetonitrile mixture (1/1 v/v) and purified by semi-preparative reverse-phase high-performance liquid chromatography (RP-HPLC) system (Agilent 1100 equipped with a Zorbax Eclipse XDB-C18 reverse-phase column).

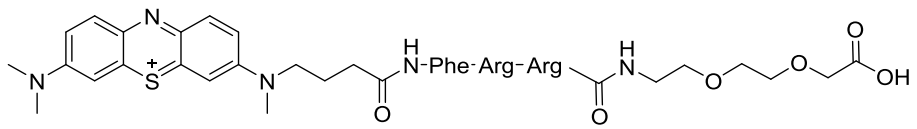

(5)

Figure 3-2: Chemical structure of the synthesised redox-labelled peptide probe (MB-Phe-Arg-Arg-PEG-2-COOH) [197].

As shown in Figure 3-3 and 3-4, mono- and tripod-anchor were synthesised by the multistep reactions previously described [7], [197]. Both probes (mono or tripod-anchored) were synthesized using N-(3-Dimethylaminopropyl)-N′-ethylcarbodiimide hydrochloride (EDC.HCl) and hydroxybenzotriazole (HOBt) chemistry. To a solution of compound **(5)** in DMF, EDC.HCl (3 equiv.) and HOBt (3 equiv.) were added and the reaction mixture was stirred for 2 hours to ensure complete activation. To this solution, the mono- or tripod-anchor was added and stirred for 24 hours at room temperature. The solvent was evaporated under reduced pressure and all protecting groups were hydrolysed with the addition of the TFA-based cleavage cocktail. The mixture was stirred for 30 min and the progress of deprotection was monitored by analytical HPLC (Agilent 1100 equipped with a Phenomenex Kinetex® 5 µm XB-C18 100 Å LC column). After complete conversion, the solvent was evaporated *in vacuo* and the reaction was purified by semi-preparative RP–HPLC. #

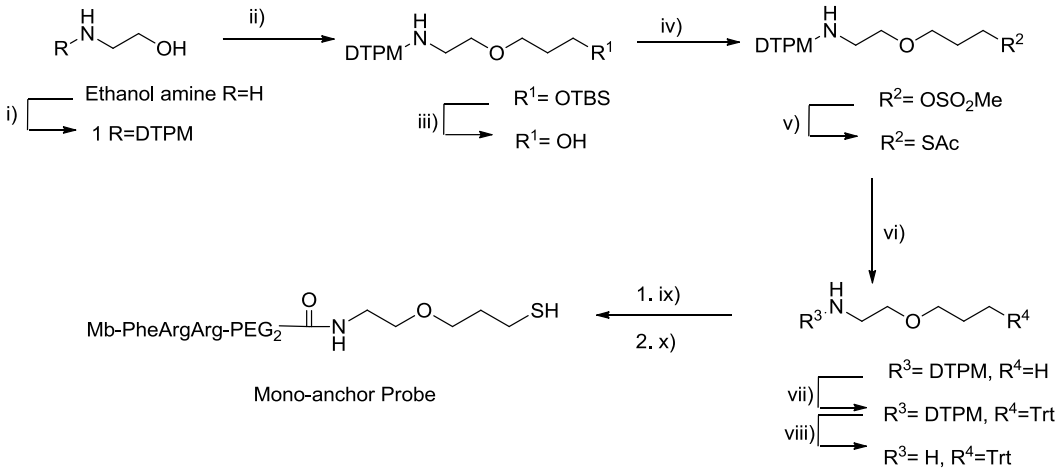

Figure 3-3: Synthesis of mono-anchored redox-labelled peptide probe. Reaction conditions: i) DTPM-NMe_2, MeOH, overnight; ii) (3- Bromopropoxy)-tert-butyldimethylsilane, NaH, DMF, 24 h; iii) TBAF, THF, overnight; iv) $MeSO_2Cl$, Et_3N, DCM, 3 h; v) KSAc, anhydrous THF, overnight; vi) HCl/MeOH (1/4), 3 h, reflux; vii) triphenyl methanol, TFA, overnight; viii) hydrazine monohydrate, anhydrous THF, 1 h; ix) redox-labelled peptide product (MB-Phe-Arg-Arg-PEG-2-COOH, Figure 3-2), HOBt, EDC, DMF, 24 h; x) TFA/EDT/water/TIS, 30 min [197].

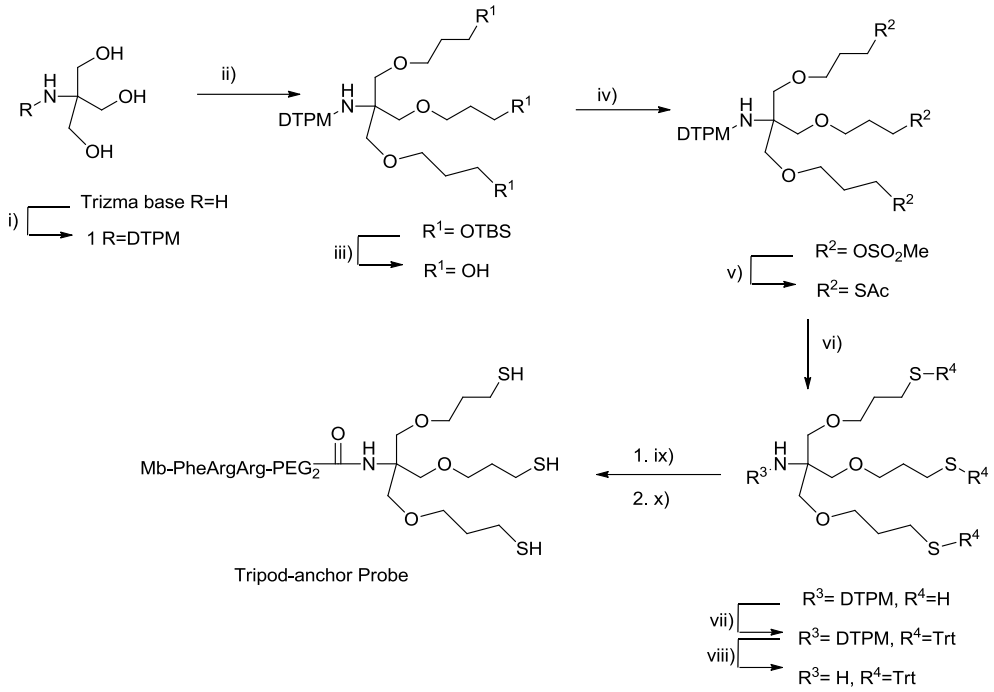

Figure 3-4: Synthesis of tripod-anchored redox-labelled peptide probe. Reaction conditions: i) DTPM-NMe_2 1, MeOH, overnight; ii) (3-bromopropoxy)-tert-butyldimethylsilane, NaH, DMF, 24 h; iii) TBAF, THF, overnight; iv) $MeSO_2Cl$, Et_3N, DCM, 3 h; v) KSAc, anhydrous THF, overnight; vi) HCl/MeOH (1/4), 5 h, reflux; vii) triphenylmethyl chloride, DCM, 3 h; viii) hydrazine monohydrate, 1 h; ix) redox-labelled peptide product (MB-Phe-Arg-Arg-PEG-2, Figure 3-2), HOBt, EDC, DMF, 24 h; x) TFA/EDT/water/TIS (94/2.5/2.5/1), 30 min [197].

3.3 Electrodes

The working electrodes used throughout this work were either commercial (conventional) or non-commercial (in-house fabricated). Commercial electrodes consisted of macro (2 mm-diameter) and micro (25 µm-diameter) gold and platinum disc electrodes (Figure 3.5) purchased from IJ Cambria, UK. All experiments in Chapter 4 and part of the work in Chapter 5 were performed using these electrodes. In addition, for the characterisation of potential-controlled deposited SAM probes in Chapter 6 and polymeric coatings in Chapter 7, commercially available (Metrohm Dropsens, UK, Figure 3.6) screen-printed electrodes (SPEs) were used: gold 4 mm-diameter (DRP-C220BT). Non-commercial electrodes used in this work were fabricated in-house (as thin Pt layer electrodes on Si substrates) at the Scottish Microelectronics Centre (SMC) by Dr. Ewen Blair, Dr. Jamie Marland, Dr. Ilka Schmueser and/or Dr. Andrew Piper, and used to perform experiments, mainly for Chapter 5. The fabrication details for single microelectrodes as well as micro- and nanoelectrode arrays are given below.

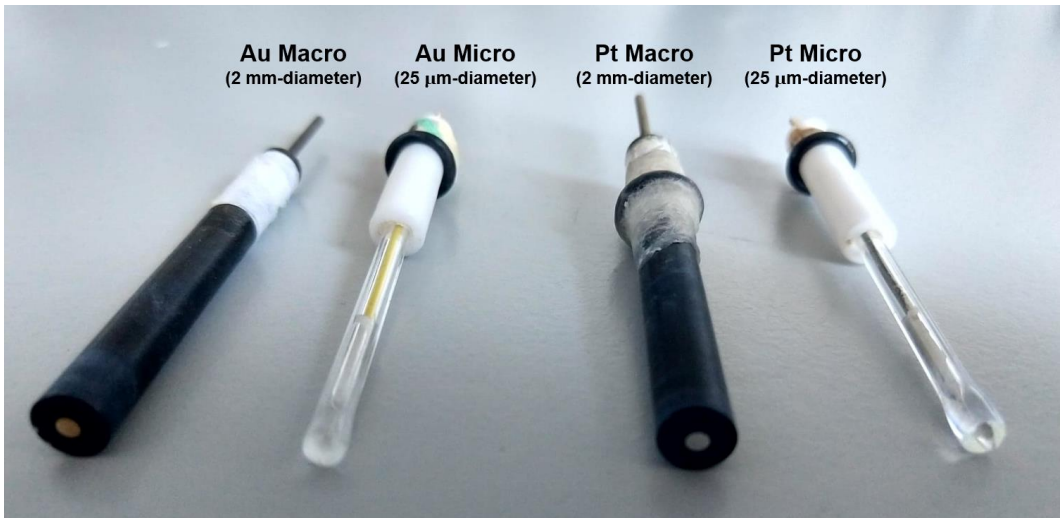

Figure 3-5: A photograph of the bulk gold and platinum macro- and micro disc electrodes.

Figure 3-6: A photograph of Dropsens screen-printed gold electrode of 4 mm-diameter.

3.3.1 Fabrication

Standard photolithography, deposition and etching techniques [182], [183], [185], [201] were used for the in-house fabrication of single microelectrodes, microelectrode arrays (MEA) and microcavity nanoband edge electrode arrays (MNEE) in this work. Figure 3-7 illustrates the schematic process flow of the photolithography, deposition and etching steps. Firstly, positive photoresist layer is coated on a material to be patterned and exposed to UV light through a photomask, leading to a patterning of exposed and unexposed photoresist areas as well as the development and thus removal of the exposed photoresist from the substrate. Then residual pattern of the photoresist is used as a protecting layer in the selective etch of the underlying material and the patterned material is left when it is removed.

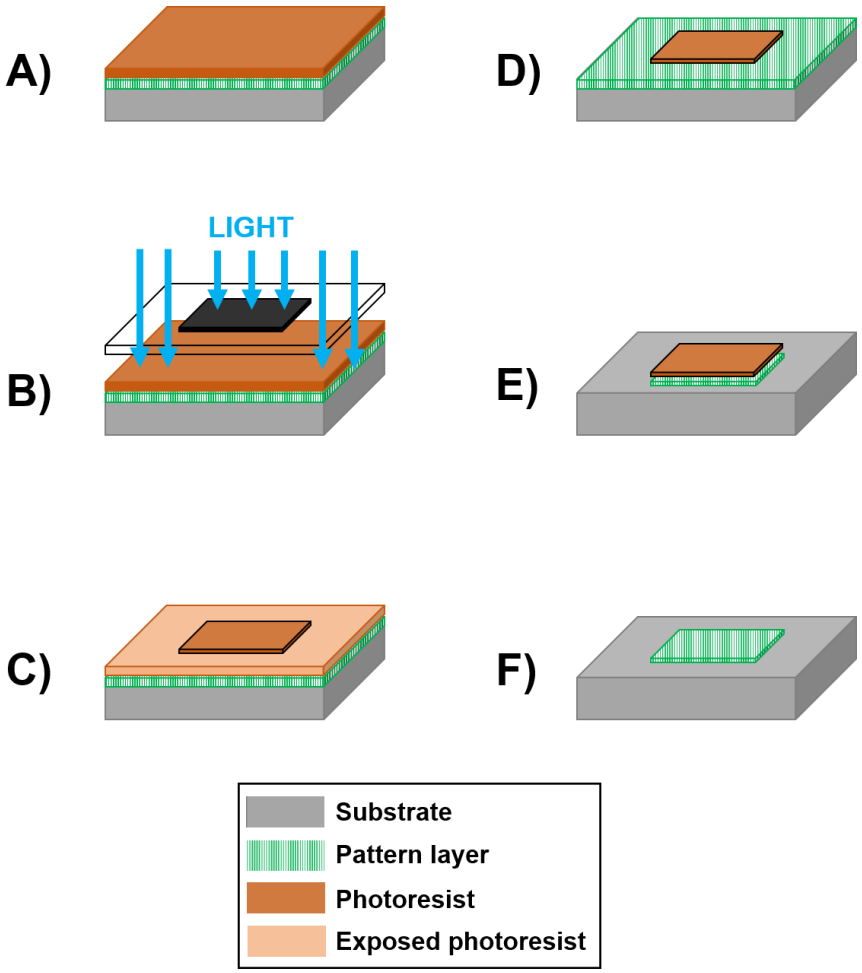

Figure 3-7: The photolithography and etching process. A) Positive photoresist layer is coated on a material to be patterned and B) exposed to UV light through a photomask, leading to C) a patterning of exposed and unexposed photoresist areas and D) the development and thus removal of the exposed photoresist from the substrate. E) Residual pattern of photoresist is used as a protecting layer in the selective etch of the underlying material and then F) removed, leaving the patterned material.

Using this process flow, architectures of the fabricated single microelectrodes and arrays were designed to consist of a patterned platinum electrode layer which was deposited onto a thermally-oxidised silicon dioxide insulation and a Ti adhesion layers and a top silicon nitride insulation layer patterned to define the sizes of the electrode regions and the contact openings (Figure 3-8). As shown, the last etching step (F-2) of both $Si_{3.1}N_{3.9}$ and Ti/Pt metal layers, instead of $Si_{3.1}N_{3.9}$ only, makes the only difference between MEA and MNEE devices, leaving a Pt nanoband at the edges of the defined area of the microcavity.

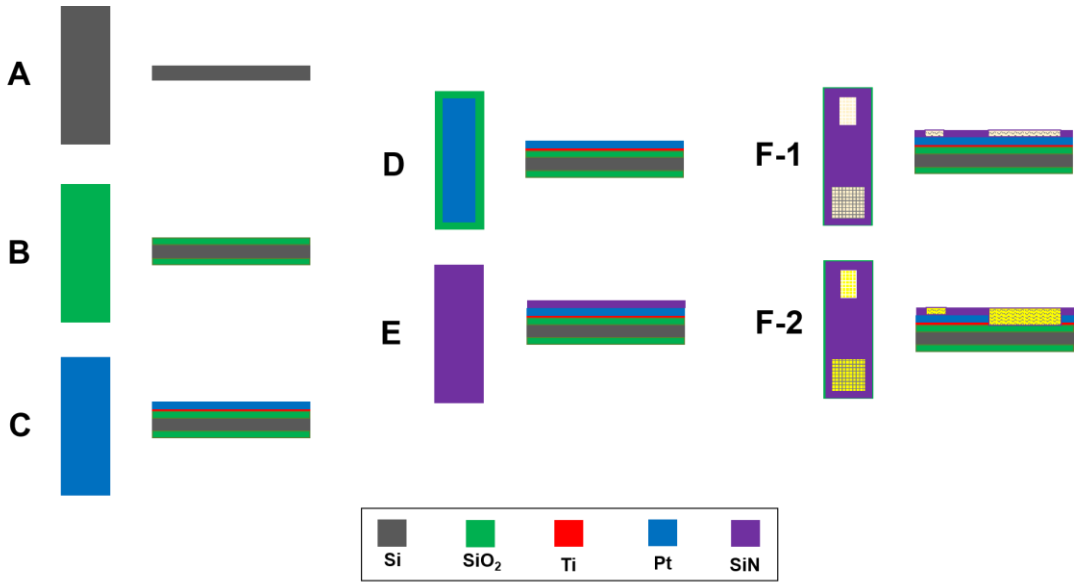

Figure 3-8: Top view and cross-sectional schematic diagrams (not to scale) of the fabrication steps involved in the development of single microelectrodes, microelectrode arrays (MEA) and microcavity nanoband edge electrode arrays (MNEE). A silicon wafer (A) was insulated with an oxide layer by thermal oxidation (B) and a platinum layer was deposited on a titanium adhesion layer (C). The metal film was patterned to avoid the possible exposure of metal around the perimeter of the final diced chip (D). This was followed by the deposition of low-pressure chemical vapour deposited (LPCVD) silicon-rich silicon nitride as the top insulator (E). Then the electrodes and contact pads were formed by etching holes into the top insulator. This resulted in the single microelectrode or MEA (depending on the mask layout and patterning) via only etching the $Si_{3.1}N_{3.9}$ layer (F-1) or the MNEE via etching of both $Si_{3.1}N_{3.9}$ and Ti/Pt metal layers (F-2). The colour code of materials is given below. Adapted from [185] [201].

3.3.2 Single Microelectrodes

The importance of using miniaturised electrodes of controlled dimensions to determine fundamental and reproducible sensor response and their advantages over commercial bulk electrodes are extensively discussed in Section 2.5.3. A set of such microelectrodes was therefore fabricated in-house and used to characterise SAM-functionalised peptide-based biosensor performance for this work. They used the same architectures as the previously designed, produced and well-characterised microelectrodes, for different applications within the group [182], [183], [202].

There were two different electrode designs used to fabricate the single microelectrodes involved in this work; thin track (TT) and superthin track (STT) devices. Figure 3-9 shows both devices with optical microscope images of the electrode and contact track areas as well as the photolithography mask layouts used for their fabrication. Although they have identical system dimensions (35 mm x 3.75 mm x 0.55 mm), contact pad areas (3 mm x 5.8 mm of that

exposed 2.8 mm x 5.6 mm), electrode shapes and dimensional ranges, their contact track areas differs from each other which results in a varying area of the top insulator. The reason the contact track width was reduced from TT to STT devices was to reduce the area in which a failure of the top insulator might occur (critical area reduction). This failure point, such as a hole or crack, can expose the contact track metal which would lead to the electrode area increasing when dipped into the solution for aqueous measurements. This increase in the electrode area results that the microelectrode does not have a well-defined area anymore, which lead to a failed device. The critical area reduction also results in different resistances between the electrodes and the contact pads, which is observed to be higher for the superthin track electrodes than thin track electrodes.

The detailed fabrication run sheet for the development of single microelectrodes (including layer thicknesses) can be found in Appendix-1. For both device designs fabricated and tested, 4-inch <100> n-type Si wafers were used to fabricate 40 individual devices including disc-shaped electrodes, with five different diameters respectively: 10, 20, 30, 50, and 100 µm. The reason for using only disc-shaped ones (instead of squares or any other) as in-house built electrodes was to make an equitable performance comparison between these in-house fabricated electrodes and the commercial bulk disc electrode results which are analysed in Chapter-4.

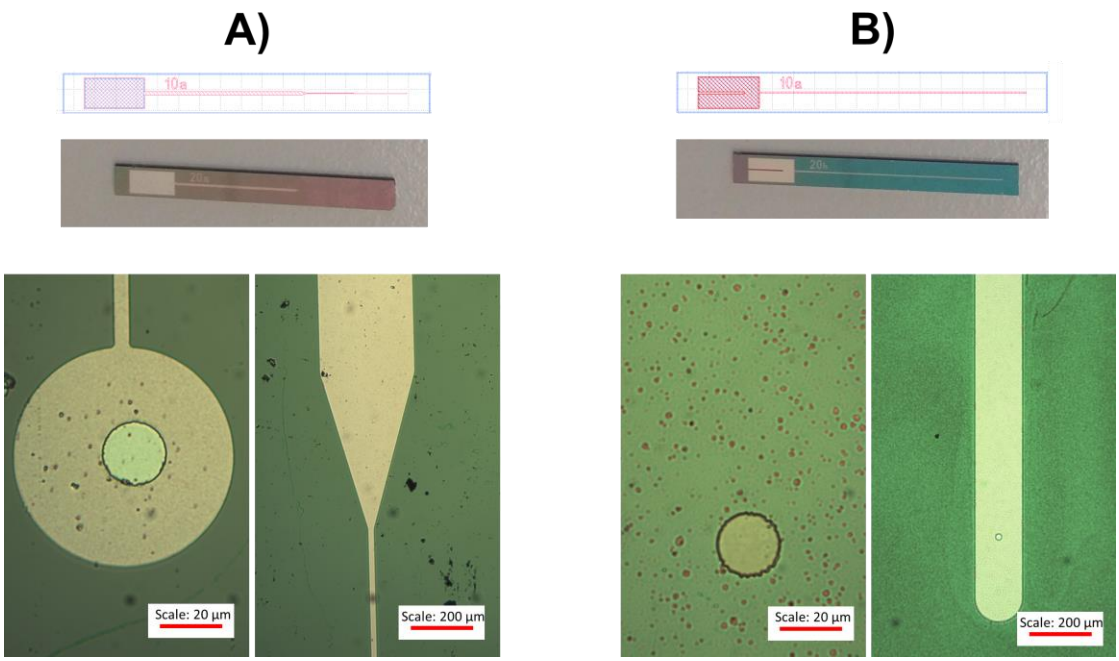

Figure 3-9: Top: mask designs used for photolithography process and photographs of in-house fabricated single disc microelectrodes with 20 µm-diameter; A) superthin track and B) thin track devices. Lower: optical microscopy images of the electrodes and contact tracks.

3.3.3 Microelectrode (MEA) and Nanoelectrode (MNEE) Arrays

In addition to the single microelectrodes, microelectrode arrays (MEA) and microcavity nanoband edge electrode arrays (MNEE) were also fabricated and tested in terms of biosensing performance as substrates for SAM-based probes. Again, standard photolithography, deposition and etching techniques were used to obtain reproducible and well-defined MEA and MNEE devices [185], [201]. This time, a variety of different electrode structures was fabricated on each wafer, including arrays of disc-shaped microcavities with a diameter of 10, 20, 30 µm and separated by 1D, 2D, 3D and 4D, where D is equal to the diameter distance of each microcavity. It means that, a MEA described 20µm-4D for example, consists of an array of disc microelectrodes with a diameter of 20µm, each separated by 80 µm distance from its neighbour electrode. The electrodes in an array are located in the square alignment. The area of the occupying array on a device was 5 × 5 mm^2. Figure 3-10 shows a photograph of a MEA 20µm-4D device, with optical microscopy images of that and a MNEE 10µm-2D. As it can be clearly seen, the colour difference of the electrodes (light grey for Pt in MEA, dark grey for SiO_2 in MNEE) in these images indicates the successful etching of the metal layer and the formation of the nanoband in the MNEE devices [203]. Again, a detailed fabrication run sheet for the development of the MEAs and MNEEs (including layer thicknesses and the number of electrodes included per array) can be found in Appendix-2.

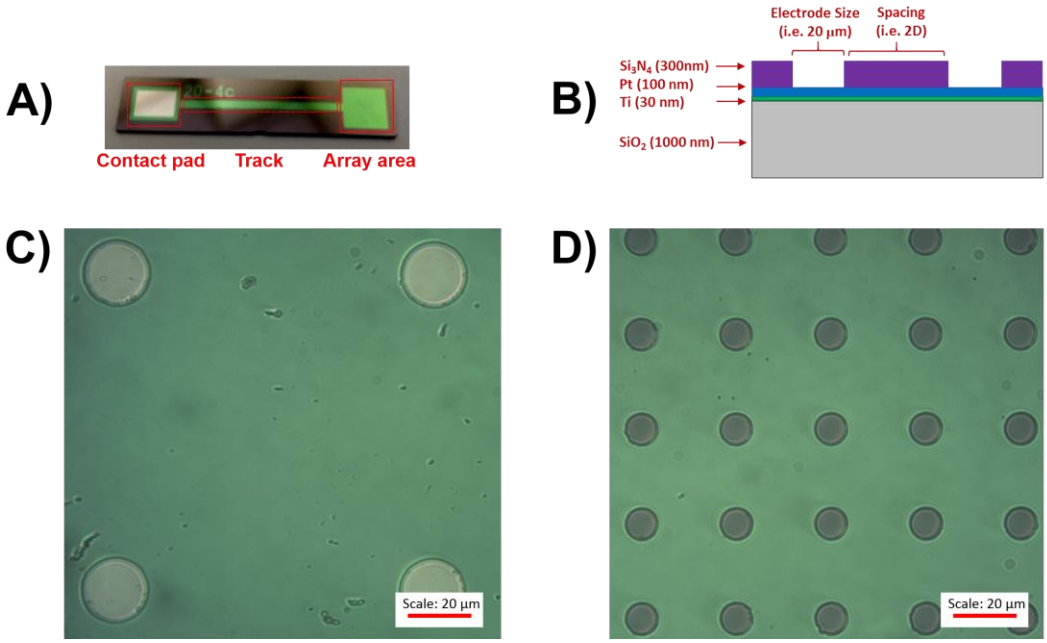

Figure 3-10: A) A photograph of a microelectrode array (MEA 20µm-4D) and B) cross-sectional schematic diagram (not to scale) for a MEA 20µm-2D device with constituent material layer thicknesses. Optical microscope images of C) a microelectrode array (MEA 20µm-4D) and D) a microcavity nanoband edge electrode array (MNEE 10µm-2D) are also given.

3.4 Sensor Preparation and Characterisation

3.4.1 Electrode Cleaning

In order to obtain reliable and reproducible responses from the SAM-functionalised probes which were immobilised onto the electrodes, surfaces should be both clean and similar in terms of roughness before immobilisation of the probe molecules. Therefore, optimised protocols were developed by many experimented observations through this work. As a result of this, one can summarise that optimised protocols used for cleaning of electrodes depend on the material (platinum or gold) and type (commercial bulk or in-house built thin metal film on silicon chip or screen-printed ink). The cleaning of commercial macro and micro gold and platinum bulk disc electrodes (Figure 3-5) consists of three steps. Firstly, gold electrodes were immersed in a piranha solution (prepared as 3:1 v/v mixture of sulfuric acid, H_2SO_4 (95%) and hydrogen peroxide, H_2O_2 (30%), CAUTION! piranha solution is strongly oxidising and should be handled with care!) and platinum electrodes were dipped into concentrated H_2SO_4 (95%) for 10 min to remove organic residue from their surface. Then, they were successively polished to a progressively finer surface finish using a polishing cloth and a sequence of aqueous slurries containing first 1 μm, then 0.3 μm and finally 0.05 μm alumina particles (Buehler, Germany). This step was applied to achieve consistent surface roughness/smoothness in each experiment. Finally, each electrode was subjected to an electrochemical cleaning step by carrying out CVs, performing a number of cycles of *E* (between 0 and +1.6 V for gold, between -0.35 and +1.6 V for platinum) vs Ag| AgCl| KCl (3 M) in 0.1 M H_2SO_4 at a potential scan rate of 100 $mV \cdot s^{-1}$ until having reproducible and similar CVs to the characteristic voltammograms reported [201], [204], [205]. Some examples of characteristic CVs for cleaned gold and platinum macro- and microelectrodes are given in Figure 3-11. As seen in both Au macroelectrode and microelectrode cleaning CVs, a single Au oxide reduction peak (which seems sharper for microelectrode) can be observed at 0.8 V. Additionally, multiple oxidation peaks overlapped between 1.0 – 1.5 V are characteristic marks for a clean gold surface. For both Pt macro- and microelectrodes, there is a similar peak around 1.5 V which shows oxygen evolution. For Pt macroelectrode, the peak which is observed around 0.3 V signifies the Pt oxide reduction, whereas a sigmoidal response can be seen instead for Pt microelectrode, which presents the O_2 reduction. Usually, a couple of peaks are also seen between -0.35 – 0 V, which presents hydrogen evolution, adsorption and desorption. However, the current ranges used for the plots are not narrow enough to exhibit all of these characteristic features.

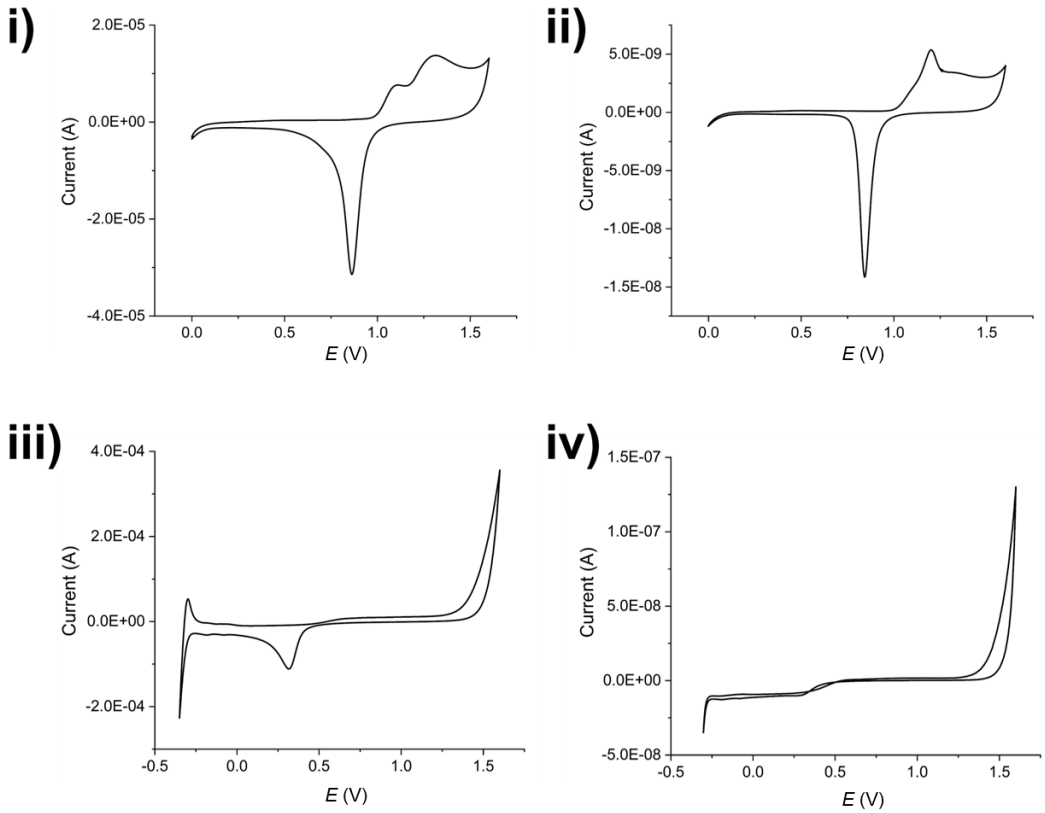

Figure 3-11: CVs of commercial i) Au macroelectrode (2 mm-diameter), ii) Au microelectrode (25 µm-diameter), iii) Pt macroelectrode (2 mm-diameter) and iv) Pt microelectrode (25 µm-diameter) recorded in 0.1 M H_2SO_4 (between 0 and +1.6 V for Au, between -0.35 and +1.6 V for Pt) at a scan rate of 100 $mV.s^{-1}$ vs Ag| AgCl| KCl (3 M) reference electrode.

On the contrary to bulk electrodes, only electrochemical cleaning was applied to other electrode types (in-house fabricated single microelectrodes, MEAs, MNEEs and commercially available SPEs), because concentrated acid cleaning or alumina polishing step would be extremely harsh and damaging condition. Their characteristic cleaning CVs and the development of an alternative electrochemical (reductive) cleaning technique are discussed in Chapter 5.

3.4.2 Sensing Layer Preparation

3.4.2.1 Probe Immobilisation by Incubation (without any applied potential)

Extending the established macroelectrode protocol [7], the respective probe layer was formed as a mixed monolayer SAM (redox-tagged peptide, DT and MCH) on a freshly cleaned electrode surface. Two different methods were followed for this purpose; dip coating for commercial bulk electrodes and drop-casting for in-house built electrodes and SPEs. For dip coating, the electrodes were immersed overnight at 4 °C in a 40 μM solution of the redox-tagged peptide (either substrate: containing cleavable L-amino acids or a control: containing uncleavable D-amino acids) and freshly prepared DT (600 μM for macroelectrodes, 150 μM for microelectrodes) in ethanol. After washing with ethanol, the resulting SAM-modified electrode was immersed in 1 mM MCH in ethanol (for 1 h for macroelectrodes and 10 min for microelectrodes). It should be noted that these differences in the optimised SAM deposition protocol are consistent with the expected enhancement in sensitivity and mass transport kinetics of reactions at microelectrodes. Finally, washing was carried out, firstly in ethanol and then in 1x PBS. For other type of electrodes, probe molecules were drop-cast on electrode surfaces. To do this, 10 μL of probe solution (with or without DT depending on a purpose) in 1x PBS was pipetted and then slowly released onto the flat electrode surfaces as uniformly as possible. 1x PBS was used as solvent for this type of electrodes, instead of ethanol, to avoid evaporation before adsorption of SAM-modified molecules. The rest of the steps were followed as detailed above, keeping all the concentrations and durations identical. The modified electrodes were stored in 1x PBS at 4 °C until use.

3.4.2.2 Potential-Controlled Probe Immobilisation

In addition to the probe immobilisation which was processed by incubation without any applied potential, SAM-based probes were also immobilised by an electrochemical potential-controlled technique. To achieve this, freshly cleaned and characterised electrodes were immersed in 1x PBS solutions containing SAM-based probes, followed by the immediate initiation of the previously programmed NOVA software protocol. The protocol was based on the application of the desired potentials for specific time periods by chronoamperometry (CA) and then monitoring the surface SAM coverage by rapid CV scans and SWV measurements. The solution was changed from PBS to ferri/ferro cyanide (FFC) between CA and CV steps for SAM integrity tests as there was a need for external redox agent to monitor the coverage through the redox reaction.

3.4.3 Electrochemical Measurements

All electrochemical measurements were carried out using a conventional three-electrode electrochemical cell (Figure 2-14) which was driven by a computer-controlled AutoLab PGstat-30 Potentiostat running the GPES 4.9/NOVA 1.11/NOVA 2.1 software (Metrohm Autolab B.V., The Netherlands). An in-house built platinum-coated silicon dioxide chip was used as an auxiliary electrode. Previously described electrodes were used as working electrodes depending on the specific type of experiments which are detailed in the following chapters. All the working electrode potentials, *E*, were applied with respect to and are reported relative to a Ag| AgCl| KCl (3 M) reference electrode (Bioanalytical Systems, Inc., USA). The same reference electrode was used and abbreviated as Ag/AgCl for the rest of the work. A Lauda Eco Silver thermostatic bath (VWR International Ltd, UK) with an external pumping system and a water-jacketed glass cell (Figure 3-12) was used to control the temperature of all the experiments conducted at 25 °C or 37 °C. Origin 2018, MATLAB R2015a and/or MS Office Excel 2016 software was used for the analysis of the data. A code (See Appendix-3) was created in MATLAB for peak height calculations and enabled faster analysis of the time-consuming overnight experiment data.

Figure 3-12: Photographs of the water-jacketed glass cell integrated with three-electrode system inside the Faraday cage and the thermostatic bath (Lauda Eco Silver) used for temperature-controlled experiments.

The SAM-modified working electrodes from Section 3.4.2 were immersed in buffer solutions (usually prepared with 1x PBS, as it has an optimum pH, 7.4 for biological activity) and subjected to electrochemical measurements using square wave voltammetry (SWV, applying *E* at a frequency of 60 Hz, with an amplitude of 25 mV and a step potential of 5 mV) until a stable background signal was obtained. After addition of the target enzyme (trypsin), or the proteins (BSA, casein, FBS) for characterisation of non-specific binding/biofouling, the SWV signal was continuously monitored with time. Following the established analysis method for gold macroelectrodes[7], [196], the resulting signal is expressed as the relative change in the SWV peak current with respect to the initial peak current (henceforth called the % signal change).

3.5 Preparation and Characterisation of Polymeric Coatings

In order to prepare sensors as the substrates for polymer coatings which were tested in terms of delayed response (activity) and anti-biofouling characteristics, previously detailed protocols (Section 3.4.2.1) were followed. Gold SPE working electrode surfaces (unmodified or probe-modified) were coated with the pH responsive polymers Eudragit® S100. To achieve this, polymeric powder was first dissolved in isopropanol at one of three different concentrations (8, 16 or 32% (w/v)). 10 µL of this solution was then drop-cast on a modified or an unmodified (bare) electrode surface, either as a single layer or consecutive layers of 10 µL (1-layer, 2-layers or 3-layers). After drop-casting, the solvent isopropanol was left to evaporate at room temperature. Polymer-coated electrodes were then allowed to dry and stabilise for an additional couple of hours before use. Figure 3-13 illustrates all steps which were involved in the preparation of the polymer-coated electrodes for anti-biofouling and delayed activity assessments. They were then incubated in solution of 1x PBS (characterisation-optimisation) or 5 mM FFC (for unmodified electrodes as an external redox agent is required to monitor bare electrodes) or DMEM-FBS mixture (biofouling characterisation) of which the fixed pH value was measured using Fisherbrand Hydrus 400 pH meter (Thermo Fisher Scientific, UK), and then electrodes were subjected to electrochemical characterisations with time using CV and SWV measurements to monitor the dissolution of the coated polymer layers. For both CV and SWV measurements performed, methylene blue potential window (-0.05 to -0.4 V vs Ag/AgCl) was selected for probe-modified electrodes and the FFC potential window (0 to 0.5 V vs Ag/AgCl) was selected for unmodified electrodes, as expected. In all experiments, the redox signal (peak current height at a fixed redox potential (*E*) of either methylene blue or

FFC) was monitored until it reached the maximum value and did not change any further with time, which corresponded to the complete dissolution of the polymer coating. The resulting signal was expressed as 100% (because the initial redox signal was zero for all cases, proving barrier polymer layer integrity) and the relative change (% signal change) in the redox signal was evaluated with respect to this value and plotted versus time.

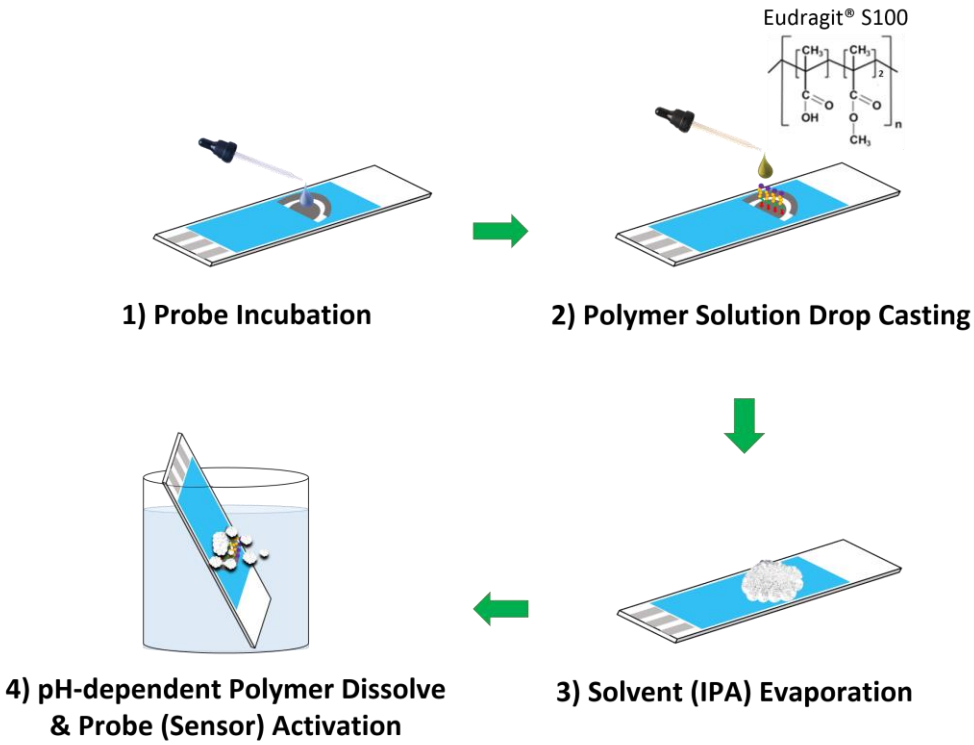

Figure 3-13: Representation of the modification and activation of a probe-modified screen-printed electrode surface with a pH responsive, transient polymeric coating of Eudragit® S 100.

Chapter 4

==========

Protease Sensing using Microelectrodes : Comparison to Macroelectrodes

4.1 Introduction

Proteases (also called as peptidases) are enzymes that catalyse the hydrolysis of amide bonds in a peptide chain, thus breaking the peptides into smaller chains or single amino acids. Their dysregulation is widely recognised as playing a significant role in many physiological conditions and various disease states [206]. They are attracting widespread attention as key biomarkers of disorders such as Alzheimer's [207], cancer [5], cardiovascular diseases [208] [209], cystic fibrosis [32], diabetes [210] and HIV [211]. The development of both sensitive and selective assays and sensors that monitor protease activity has therefore generated noticeable interest in recent years. According to Ong et al., it is possible to classify these methods into two main groups:

- homogeneous assays (that include those based on colorimetry, mass spectrometry and fluorescence resonance energy transfer)
- heterogeneous assays (that include those based on electrochemical techniques, surface-enhanced Raman scattering and surface plasmon resonance) [6].

In heterogeneous systems, the recognition elements (sensing probes) are typically immobilised onto solid surfaces, which provide a ready interrogation, signal generation and detection interface, when the target analyte is present in the neighbouring aqueous medium. In homogeneous systems, however, both probe and analyte are present in the same aqueous medium, which can result in contamination and detection challenges. The principle of detection for both assay systems is based mainly on the recognition and cleavage of a specific peptide sequence attached to various signal reporters (e.g. fluorophores, nanoparticles, quantum dots or redox tags) by a peptide-specific protease. Then the reporter generates an output signal following the interaction between the peptide and protease, providing analyte detection [212]–[215]. Amongst the various methods used for protease sensing, there has been a remarkable growth in reputation of electrochemical peptide-based biosensors, as they offer

- high sensitivity
- rapid response times
- ready multiplexing
- the use of cheap instrumentation
- ease of miniaturisation for point-of-care (PoC) applications [216].

Such electrochemical peptide-based biosensors typically use a specific substrate peptide attached to a redox tag as the selective recognition moiety and the protease as analyte. There

is extensive literature on protease detection using this approach [7], [8], [83], [196], [197], [217]–[229]. For example, Liu et al. described a method that allowed detection of matrix metalloproteinases (MMPs), whose proteolytic activities have close association with cancer progression, at very low concentrations with a limit of detection (LoD) of 3.4 pM [225]. An alternative approach was developed by Lee et al., who reported on the reference electrode-free sensing of MMP-9 using the self-gating effect on a concentric electrode system consisting of an island and an enclosing electrode [83]. More recently, Zheng et al. suggested a new strategy to amplify the sensor sensitivity resulting from multiple catalytic reactions triggered by palladium-polydopamine (Pd-PDA) nanocomposites. In this way they sensed MMP-7 with a very low concentration of 3.1 fg mL^{-1} [230]. In addition to these and other works targeting MMP type enzymes [231], there has been increased interest and activity in sensing other significant proteases such as β-Secretase (BACE1) [232], botulinum neurotoxin (BoNT) [233], caspase [234], cathepsin [235] and prostate specific antigen (PSA) [236]. Furthermore, researchers in the chemistry strand of the IMPACT project (detailed in Section 2.2.1), has previously proposed, produced, characterised and optimised a macroelectrode-based sensor system for the detection of trypsin activity using a peptide-based self-assembled monolayer (SAM) probe on an electrode surface [4], [7], [196], [197]. This sensor was translated successfully to the analysis of other proteases, e.g. human neutrophil elastase (HNE), allowing clinically relevant measurements of its activity in human blood [8]. Despite all these achievements in the area of protease sensing using electrochemical biosensors, most of these systems still use relatively large-scale electrodes which leads to limitations with respect to sensor performance as well as applicability to implantation. More specifically, as well as being smaller, with a less invasive footprint, microelectrodes offer other potential advantages over macroelectrodes that include more rapid diffusion (which can lead to shorter and more controlled response times through enhanced and more reproducible mass transport) and higher signal-to-noise which leads to higher sensitivities [180], [237]. This makes using microelectrodes an attractive route for electrochemical biosensors, in addition, miniaturised technologies offer advantages for biosensor design such as

- Integrated high-fidelity manufacturing with lower manufacturing costs per sensor
- The ability to work with small quantities of materials and samples
- Ease of multiplexed measurement options [102], [103].

Therefore, there are strong drivers for the development of miniaturised electrochemical systems for biosensors for the detection of proteases.

This chapter will describe the principle of detection for peptide-based electrochemical biosensors used for protease sensing. It will then cover some work consisting of step-by-step optimisation and characterisation of the proposed sensing system developed using gold macroelectrodes. This will also provide an understanding of the reason why a particular sensing probe was used through the rest of the work for characterisation of platinum macro- and microelectrodes. It will investigate the differences in sensor performance between macro- and microelectrode-based systems and how these differences could be explained in terms of the dissimilarities in the probe conformation on electrode surface, kinetics and thermodynamics of enzyme-substrate cleavage and the effects of non-specific binding.

4.2 Principle of Detection and Sensing Probes

The proposed electrochemical detection principle was based on the specific proteolytic cleavage of the redox-tagged peptide probes anchored onto the electrode surface by the target protease, which should lead to the release of the soluble redox-tagged peptide fragment and a corresponding decrease in the redox peak as measured by square wave voltammetry (SWV) technique (Figure 4.1). As a target enzyme, a serine protease trypsin was selected as a model, because it is widely researched and has important links to diseases such as pancreatitis [238] and colorectal cancer [239].

As details given in the synthesis and electrode preparation parts (Section 3.2 and Section 3.4), the sensing (recognition) layer consists of a mixed SAM; the probe with the target peptide tagged with methylene blue (MB) and attached to a thiol-terminated polyethylene-glycol (PEG)-6 spacer, backfilling with mercapto hexanol (MCH) to minimise pinholes in the SAM layer and co-adsorbent PEG-based dithiol (DT) molecules to support the orientation, specificity and accessibility of the probe on the electrode surface. Two different MB-labelled peptides were used, the L-amino acid sequence for trypsin-cleavable substrate or the D-amino acid sequence analogue as a trypsin-uncleavable control. The general sequence structure is depicted in Figure 4.2.

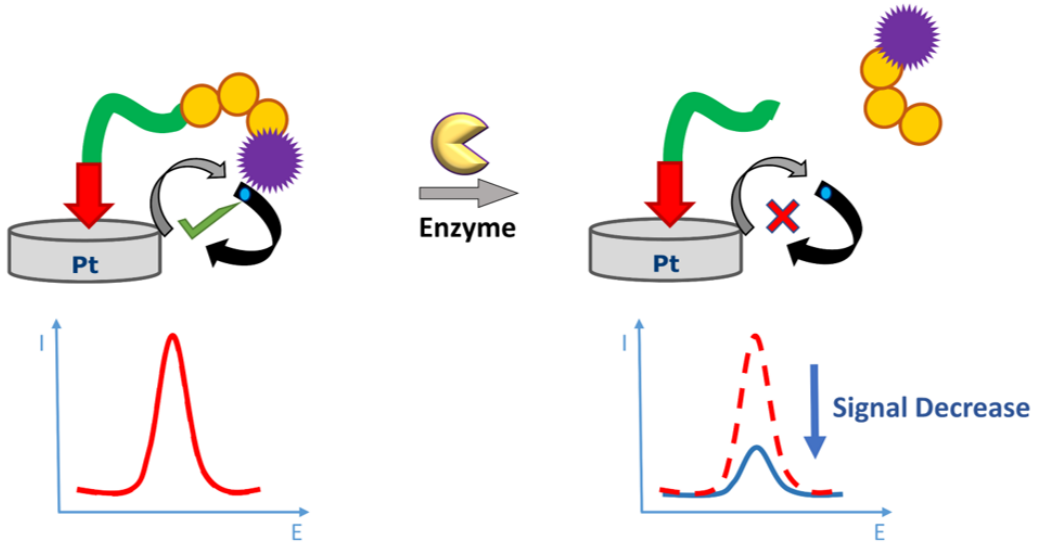

Figure 4-1: Principle of detection of the peptide-based electrochemical platform. The protease (trypsin) catalyses the cleavage of the immobilised redox-labelled peptide releasing the redox-containing fragment into solution and leading to a decrease of the electrochemical signal which is measured by SWV.

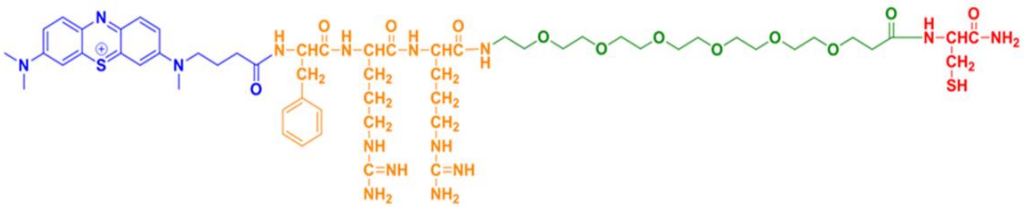

Figure 4-2: Chemical structure of the probe, containing methylene blue (blue) as the redox tag, Phenylalanine-Arginine-Arginine (orange) as the peptide sequence and PEG-6 (green) as the spacer and cysteine (red) as the anchor.

4.3 Optimisation of the Sensing Probes

The general sensing layer detailed in above section was the one mostly used throughout the work and this was the optimal design secured after various modifications [7], [196], [197]. This section will present a summary of these modifications developed by Dr. Eva Gonzalez-Fernandez and Dr. Matteo Staderini, through experiments performed using gold macroelectrodes. Different SAM models were designed, synthesised and characterised during this optimisation phase. These modifications consisted of spacer type (alkyl or PEG-based chain), SAM configuration (binary or ternary), redox tag (ferrocene or methylene blue), spacer length (PEG-x) and an anchor (mono or tri-branched).

4.3.1 Effect of the Spacer Type

Four analogous sensing layers were designed and synthesised, each having a spacer type of an alkyl (aminohexyl)-based (substrate-modified: L-amino acids or control-modified: D-amino acids) or a PEG-based chain (substrate-modified: L-amino acids or control-modified: D-amino acids) as the only difference in the probe (Figure 4.3). Each of the probe-modified gold macroelectrodes was then characterised in a 1x PBS solution by SWV measurements (Section 2.6.2) before and after the addition of trypsin. The rate of signal decrease recorded before and after enzyme was found to be similar (5-10% due to the change in redox signal with time) within experimental error for both substrate- and control-modified surfaces with the probe including the alkyl spacer [7]. This suggested that the enzyme was not able to bind the recognition site and release the redox-tagged fragment into solution. However, in the case of the probe containing the PEG-based spacer, a clear signal loss (25%) was observed for substrate-modified electrodes, whereas it was only about 5% for control-modified ones, confirming successful protease cleavage [7]. It suggested that a PEG type spacer was far better than an alkyl type spacer in terms of enabling effective protease cleavage. This is quite reasonable as PEG spacers are already known to increase the hydrophilicity of a surface as well as to create a less packed SAM layer, owing to their highly solvated nature, compared to the more packed SAMs which can be found in alkyl chain-included probes [240], [241]. This less packed SAM formation might have promoted the interchain enzyme accessibility and binding, which resulting in the cleavage of the peptide sequence.

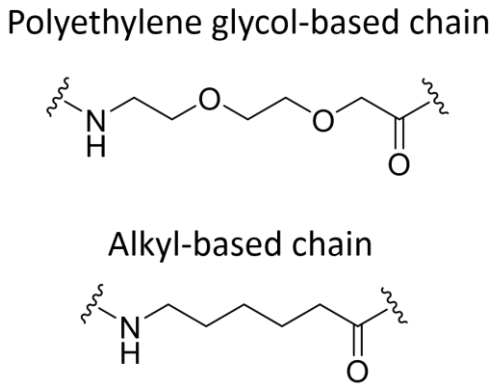

Figure 4-3: Chemical structures of two spacer types characterised during the optimisation phase, polyethylene glycol (PEG)- or alkyl-based.

4.3.2 Effect of the SAM Configuration

Four different SAM configurations were prepared and tested; B-SAM (substrate-modified or control-modified) and analogous T-SAM (substrate-modified or control-modified) as depicted in Figure 4.4. T-SAM was prepared by the introduction of DT as the third component. All electrodes modified with each sensing phases were subjected to SWV measurements in 1x PBS.

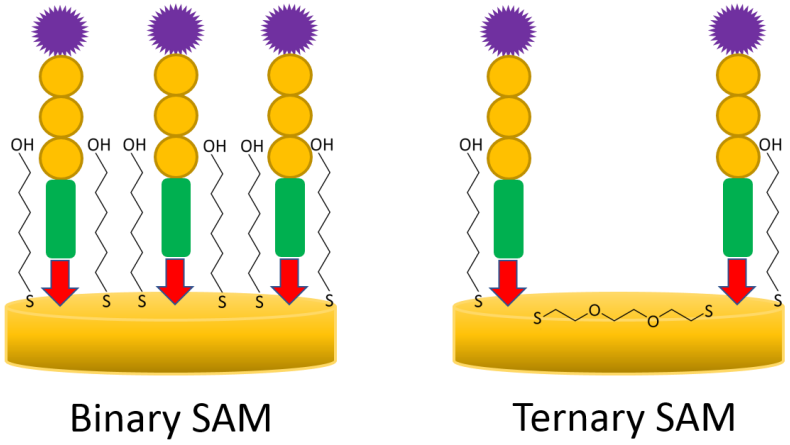

Figure 4-4: Two different SAM configurations used during the optimisation phase, binary (B-SAM) and an analogous ternary (T-SAM) structure which was prepared by the introduction of dithiol (DT) molecules as the third component.

As seen in Figure 4.5, both control- and substrate-modified T-SAM configurations did not show any signal loss until the enzyme addition which took place at time t = 20 min. On the other hand, a signal decrease of around 10% was registered for the substrate-modified B-SAM configuration before enzyme addition, which most probably indicates its lower background redox signal stability or inhibition of the electron transfer between the redox tag and the electrode. This might be due to the interchain interactions occurring between closer probe molecules in B-SAM orientation and/or the limited mobility of these molecules. After trypsin was added at min 20 and the signal was monitored for a further 70 min, a clear signal decrease of ~50% was recorded for substrate-modified T-SAM, while uncleavable control-modified T-SAM surfaces still did not show any significant signal change. It is worth noting that the signal decrease was only around 15% for the B-SAM configuration, even after 70 min incubation with the enzyme. The explanation for this enhanced amount of signal decrease observed for the T-SAM compared to the B-SAM configuration could be a more diluted SAM surface due to introduction of the DT molecules, because DT molecules are expected to increase the

spacing between the probes thus increasing enzyme accessibility and the total amount of probe cleavage. This can be achieved without a requirement to change the cleavage rate of each enzyme but only by increasing the proportion of cleavable probe on the surface [242], [243]. Because it was also reported by Buscher *et al.* that the surface coverage is significantly related to the intermolecular interactions and corresponding SAM orientation until a monolayer is formed [244]. However, in this case, increasing the DT concentration increased the percentage signal loss for concentrations below 150 µM, whereas there was little variation for the concentrations between 150 and 900 µM. 600 µM was selected as the optimum DT concentration added to the SAM deposition solutions [7].

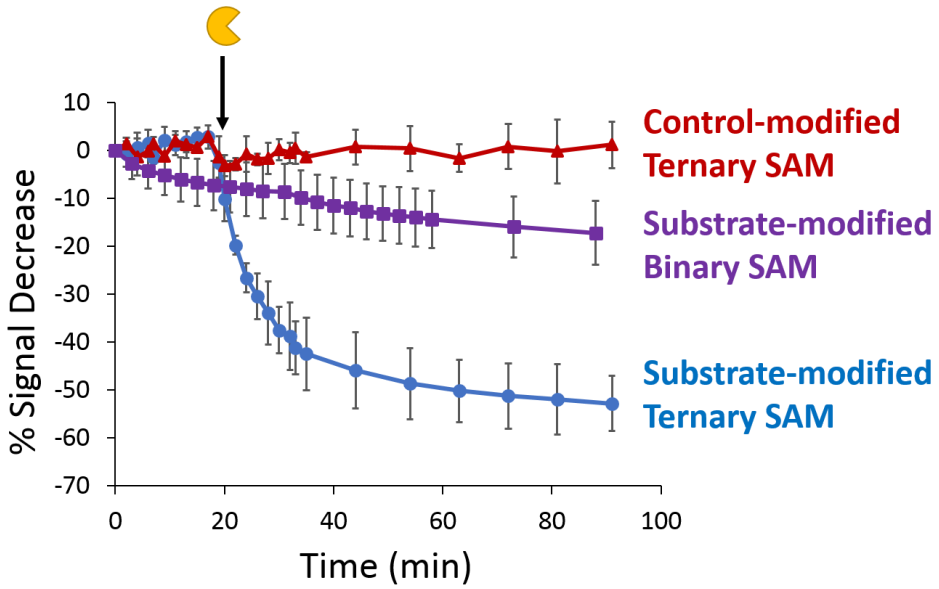

Figure 4-5: Percentage signal decrease registered upon trypsin addition (100 nM) for substrate-modified B-SAM (purple squares), control- (red triangles) and substrate-modified T-SAM (blue circles) in 1x PBS. The addition of trypsin (at time t = 20 min) is denoted by the yellow sector symbol. Average data and error bars are typically from 3 individual SAM sensing layers. Adapted from [7].

4.3.3 Effect of the Redox Tag

In order to analyse and optimise the redox tag included in the probe structure, analogous peptides were prepared and tagged with either ferrocene (Fc) or methylene blue (MB) molecules (Figure 4.6). Both substrate- and control-modified Fc-tagged peptides showed a steady decrease of the registered signal of ~10% until the time (t = 20 min) when the enzyme was introduced (Figure 4.7). On the other hand, the registered signal from MB-tagged peptides was constant within experimental error. Considering the strong Au-thiol bonding reported

previously [245] and identical anchors in all peptide types used for this characterisation, similar probe anchoring stability on electrode surfaces should be expected thus this difference cannot be justified as being due to any probe loss. In this case, any difference should be attributed to the stability of the redox tag, as it undergoes repeated electrochemical cycling during SWV measurements.

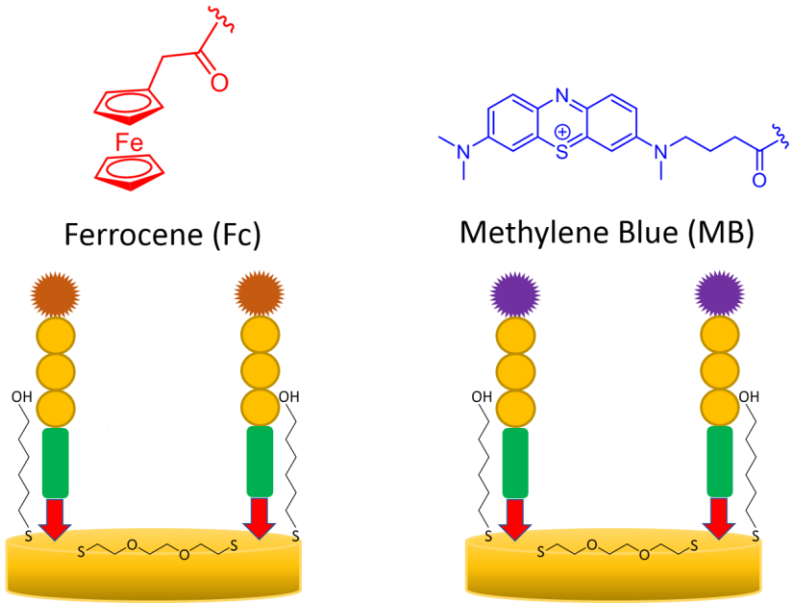

Figure 4-6: Representation of two different probe structures with different redox tags attached, ferrocene (Fc) and methylene blue (MB) as well as their chemical structures.

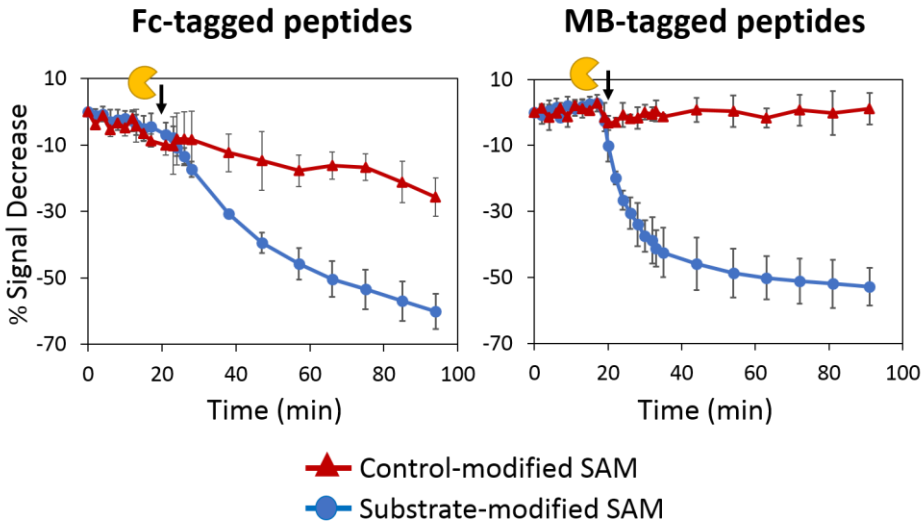

Figure 4-7: Percentage signal decrease registered upon trypsin addition (100 nM) for Fc-tagged and MB-tagged peptides in 1x PBS. Responses from control (red triangles) and substrate (blue circles)-modified SAMs are represented for both cases. Average data and error bars are typically from 3 individual SAM sensing layers. Adapted from [7].

Comparing the registered signal decreases from both control-modified Fc- and MB-tagged peptides, it can be suggested that use of MB significantly decreased the undesired background signal decrease which enables a more clear and reliable distinction from the substrate-modified probes, generating more robust and readily analysable data and developed detection sensitivity and selectivity. This observation was also found to be consistent with the literature where the relative lack of stability was attributed to the tendency of the oxidised form of ferrocene, ferrocinium (Fc^+) to undergo nucleophilic attack, followed by a ligand exchange, leading to an irreversible change in the redox activity [246].

4.3.4 Effect of the Spacer Length

As seen in the detailed probe structure in previous sections (Section 3.2 and Section 4.2), the spacer moiety plays a role as a bridge between the anchoring thiol group and the enzyme-specific peptide chain in promoting enzyme accessibility and probe flexibility. In order to analyse and define the optimum length and nature of the spacer, analogous peptides with varying PEG-based spacers (PEG-2, PEG-4, PEG-6, PEG-8 and PEG-12) and an alkyl-based spacer were synthesised (Figure 4.8) and interrogated by the addition of both a target enzyme, trypsin and non-specific binding protein, bovine serum albumin (BSA). All included MB as the redox tag and were prepared with the T-SAM configuration for which the parameters were already optimised and defined (Section 4.3.2). Firstly, all probes were evaluated in terms of their initial SWV signal in PBS. Initial peak currents of the two longest PEG-spacer lengths (PEG-8 and PEG-12) were found to be almost 2-fold lower than the three shorter spacers and PEG-2 had the highest peak SWV signal. This is expected considering that the longer spacer lengths lead to less efficient redox transfer between the redox tag and the electrode surface [247] Because the mechanism for electron transfer can change when the spacer length is altered. It was previously reported that electron tunnelling mechanism (where the electron tunnels through the large energy barrier between the donor and the acceptor via quantum mechanical effect by passing through virtual states of the molecular bridges) dominates for shorter chain oligoglycine spacers, whereas for longer chains, the electron transfer occurs via hopping mechanism (where the electron is temporarily found on the molecular bridge between the donor and acceptor, creates radical species and then transfers from the donor to the acceptor in different steps by passing the low energy barrier) [248] [249]. In addition, all peptides were also evaluated in terms of the specific (which occurs in the case of trypsin cleavage) as well as non-specific (which occurs in the case of any undesired enzyme or protein binding to the

probe, followed by restricted probe flexibility and signal loss due to the lack of efficient electron transfer) interactions. Their ability to deal with biofouling was assessed through comparative analysis by monitoring the electrochemical signal change upon addition of BSA and trypsin.

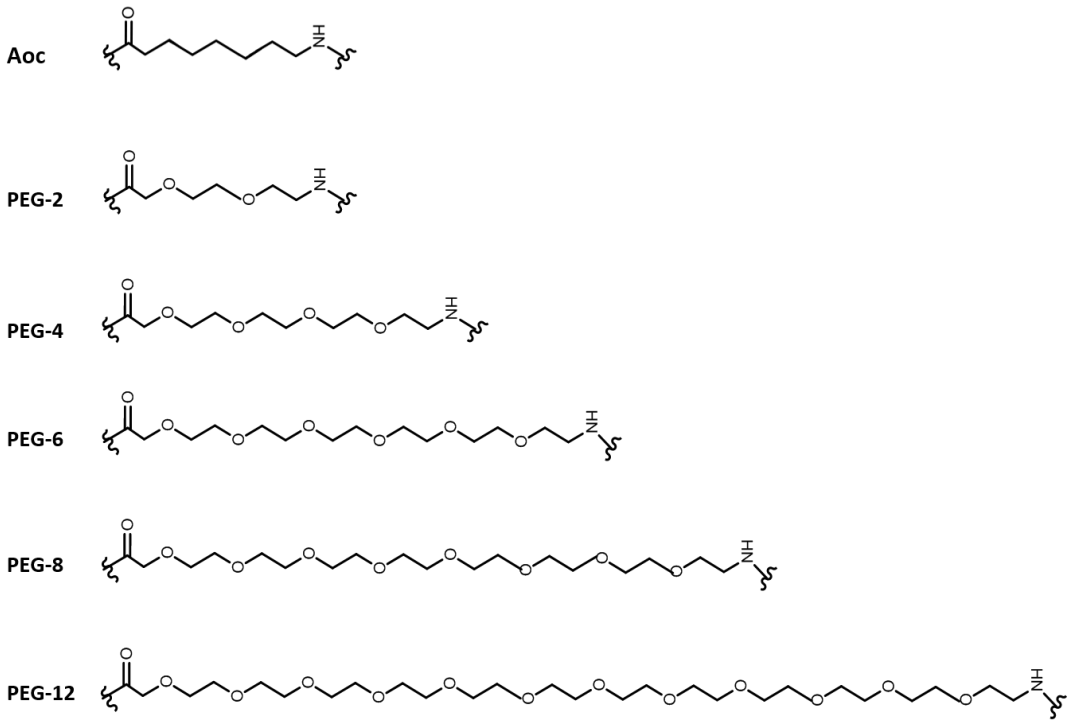

Figure 4-8: Chemical structures of the different PEG spacer lengths with the number of ethylene glycol (EG) units, denoted by PEG-x, and an alkyl-based spacer (8-aminooctanoic acid, Aoc).

Figure 4.9 presents the percentage signal change registered for substrate-modified surfaces for the specific interaction with 100 nM trypsin (green columns) compared to 100 nM BSA (orange columns). For all the different PEG-based and alkyl spacers tested, reassuringly the percentage signal change registered for the specific interaction was larger than for the non-specific interaction. The black line in Figure 4.9 shows the fraction of the specific versus non-specific registered signal, as a means of evaluating the degree of anti-fouling quantitatively for each spacer, PEG-6 was the best spacer length with highest specific versus non-specific ratio. This observation was also consistent with the analysis of the kinetics, where effective rate constants (k_{eff}) for specific and non-specific interactions were compared as illustrated in Figure 4.10. It is also worth noting that alkyl-based spacer showed the poorest anti-fouling properties, compared to the PEG-based spacers which further supports the argument discussed

in Section 4.3.1. This is most likely due to the hydrophilic nature of PEG molecules, as this hydrophilic nature has been thought to minimise the intermolecular interactions between the probe molecules and non-specific proteins, when they are not modified with any external effort [250], [251].

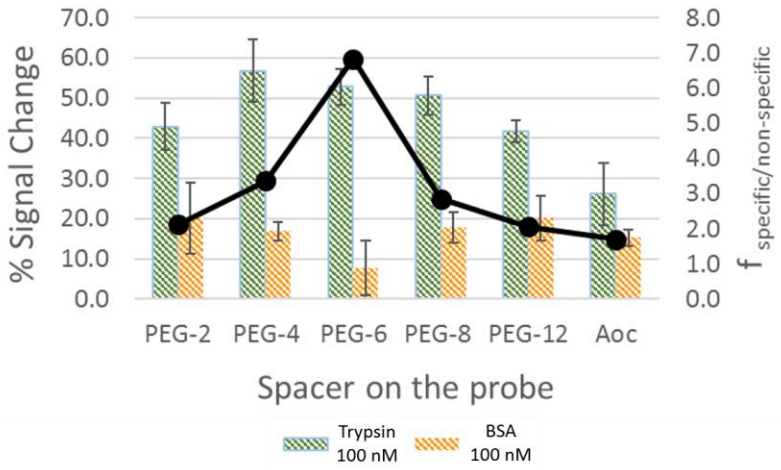

Figure 4-9: Percentage signal change for the specific interaction registered upon addition of trypsin 100 nM (green columns) or for the non-specific interaction with BSA 100 nM (orange columns) after 70 min incubation in 1x PBS. Black line represents the specific versus non-specific ratio of percentage signal change registered for each probe. Average data and error bars are typically from 3 individual SAM sensing layers. Adapted from [196].

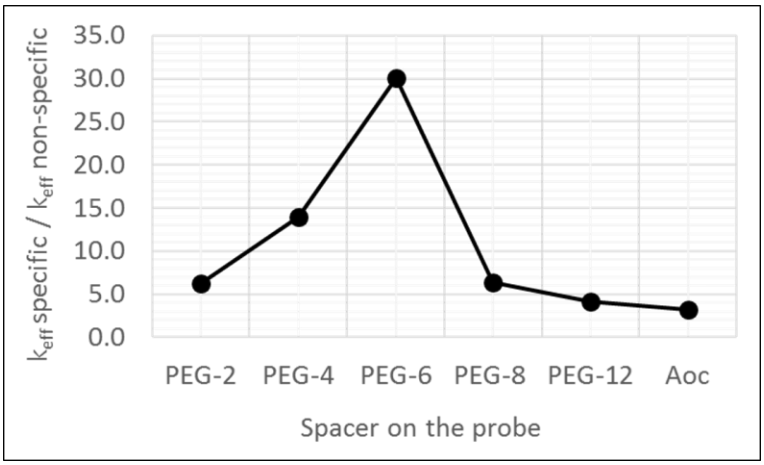

Figure 4-10: Ratio for the measured effective reaction rate constant, k_{eff} , for specific (trypsin 100 nM) versus non-specific (BSA 100 nM) binding. Adapted from [196].

4.3.5 Effect of the Anchor

It was mentioned in the previous sections that there is an interest in developing peptide-based electrochemical biosensors for many sensing applications and the immobilisation strategy of the recognition probes for these systems is mostly via SAM-based through a thiol group which can be strongly bonded to Au or Pt electrode surfaces. Therefore, unproblematic application and stability of this anchoring between the probe structure and the electrode is vital for reliable sensing, especially in complex biological media. For this reason, as a final optimisation parameter for macroelectrodes, the robustness and durability of a peptide probe tagged with a single or a tri-branched (tripod) thiol anchor (Figure 4.11) was investigated in terms of the performance, thermal and chemical stability. When the initial SWV signal was measured, they were found to be 1.9 ± 0.5 µA ($n = 19$) and 6.0 ± 2.0 µA ($n = 14$) for the mono-anchored and tripod-anchored probes, respectively. This is consistent with a higher amount of tripod-anchored probe being immobilised on the surface due to its enhanced and thus favoured binding energy (owing to the multiple thiol-Au bonding) relative to the backfilling MCH and DT molecules.

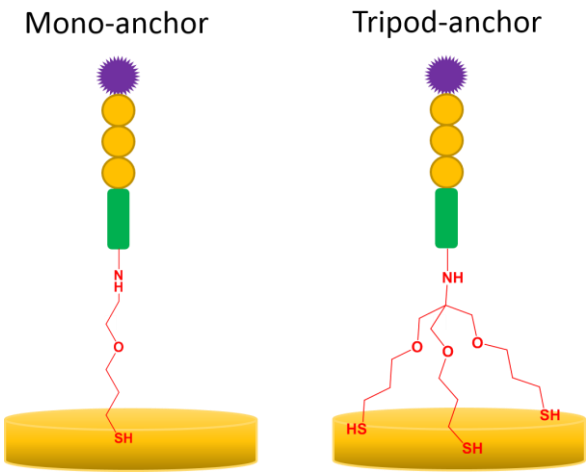

Figure 4-11: Representation of the mono- and triple (tripod)-anchor probes immobilised onto an electrode surface.

As depicted in Figure 4.12, the stability of the tripod-anchored probe was evaluated and compared to the analogous mono-anchored system. Figure 4.12A shows the assessment of their shelf life when the probes were stored at 4 °C in PBS for 30 days and periodically monitored with the SWV signal. An increased storage stability of tripod-anchored probes is clearly observable, as the signal loss was only about 25% after 30 days, whereas the signal

loss obtained for mono-anchored probes was about 55-60%. They were also evaluated in terms of thermal stability. For this purpose, they were immersed in PBS at 40 °C and the SWV signal was monitored over a time period of 2 hours (Figure 4.12B). Again, the stability of tripod-anchored probe was observed to be higher than mono-anchored probe. Furthermore, both anchor types were assessed in PBS containing 2 mM dithiothreitol (DTT) which is another thiol group-anchoring molecule often present, with the aim of challenging the anchors through competitive binding onto the electrode surface. Tripod-anchored probes again showed a greater stability, whereas the registered signal from mono-anchored probe was seen to continuously decrease. Overall, one can easily rely on multi-anchored strategy by considering these reproducible results that exhibited improved stability of tripod-anchor over mono-anchor under all tested conditions as well as similar multiple anchor studies reported for various applications [252]–[254]. However, the synthesis of tripod-anchored probes (Section 3.2) is challenging compared to the mono-anchored ones and unfortunately, they could not be obtained in large yields which hindered its use for most of the following performance characterisations of the protease sensors. Therefore, mono-anchored probes have been used instead unless otherwise is stated.

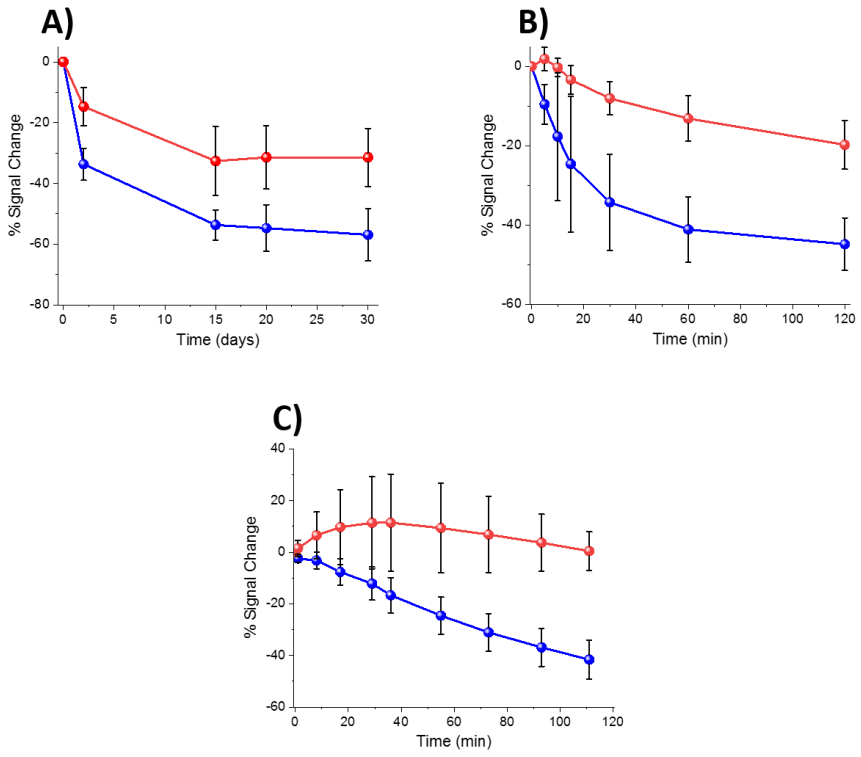

Figure 4-12: Percentage signal change registered for tripod- (red) and mono (blue)-anchored probes when (A) stored in 1x PBS at 4 °C for 30 days; (B) immersed in 1x PBS at 40 °C for 2 h; and (C) immersed in 1x PBS containing 2 mM DTT at room temperature. Average data and error bars are typically from 3 individual SAM sensing layers. Adapted from [197].

4.4 Analytical Performance of Gold Macroelectrodes

After the sensing probe was optimised, quantitative trypsin detection was evaluated and the analytical performance of a developed electrochemical sensors was assessed initially using gold macroelectrodes by Dr. Eva Gonzalez-Fernandez [7]. The optimised sensing probe (MB-tagged, PEG-6 spacer, T-SAM and mono-anchored) was therefore immersed in 1x PBS solutions containing varying trypsin concentrations (0.1–100 nM) for 70 mins. The addition of trypsin enzyme (at time t=0) caused the expected changes in signal for the macroelectrode when interrogated by SWV (Figure 4.13). This change was then plotted as a percentage signal decrease (Figure 4.14) as before as in Section 4.3. In addition to the varying trypsin concentrations incubated with substrate-modified probe, a negative control experiment was also performed by incubating the control-modified probe with 100 nM trypsin. As presented at the same figure, this negative control signal can be subtracted from the other data recorded for varying concentrations of trypsin, to emphasise the statistical differences between these concentrations.

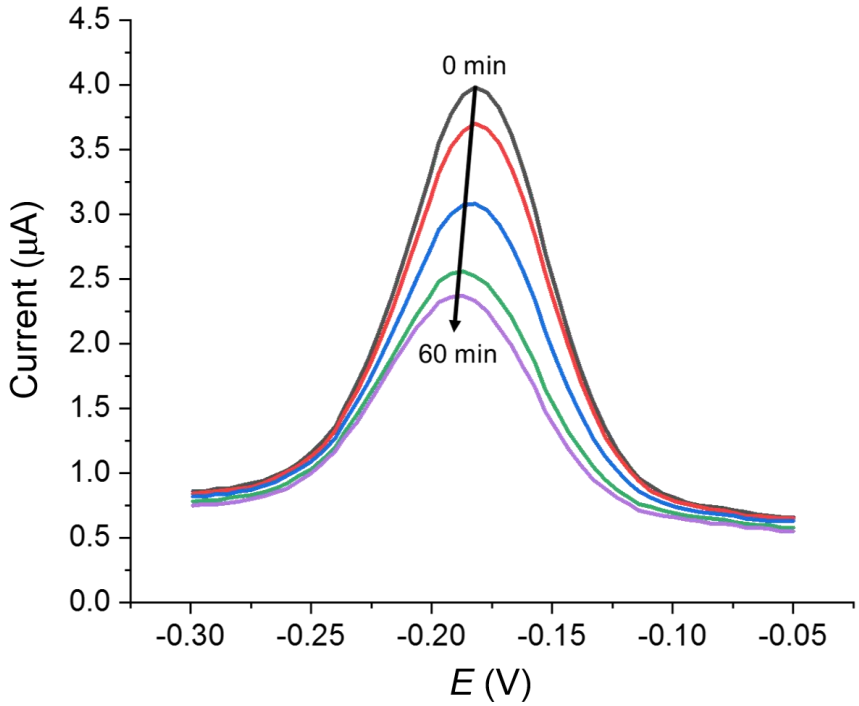

Figure 4-13: Typical background-subtracted SWV curves for a SAM-functionalised probe substrate immobilised onto Au macroelectrode registered for 100 nM trypsin at different incubation times (0, 5, 15, 35 and 60 min) in 1x PBS. Adapted from [7].

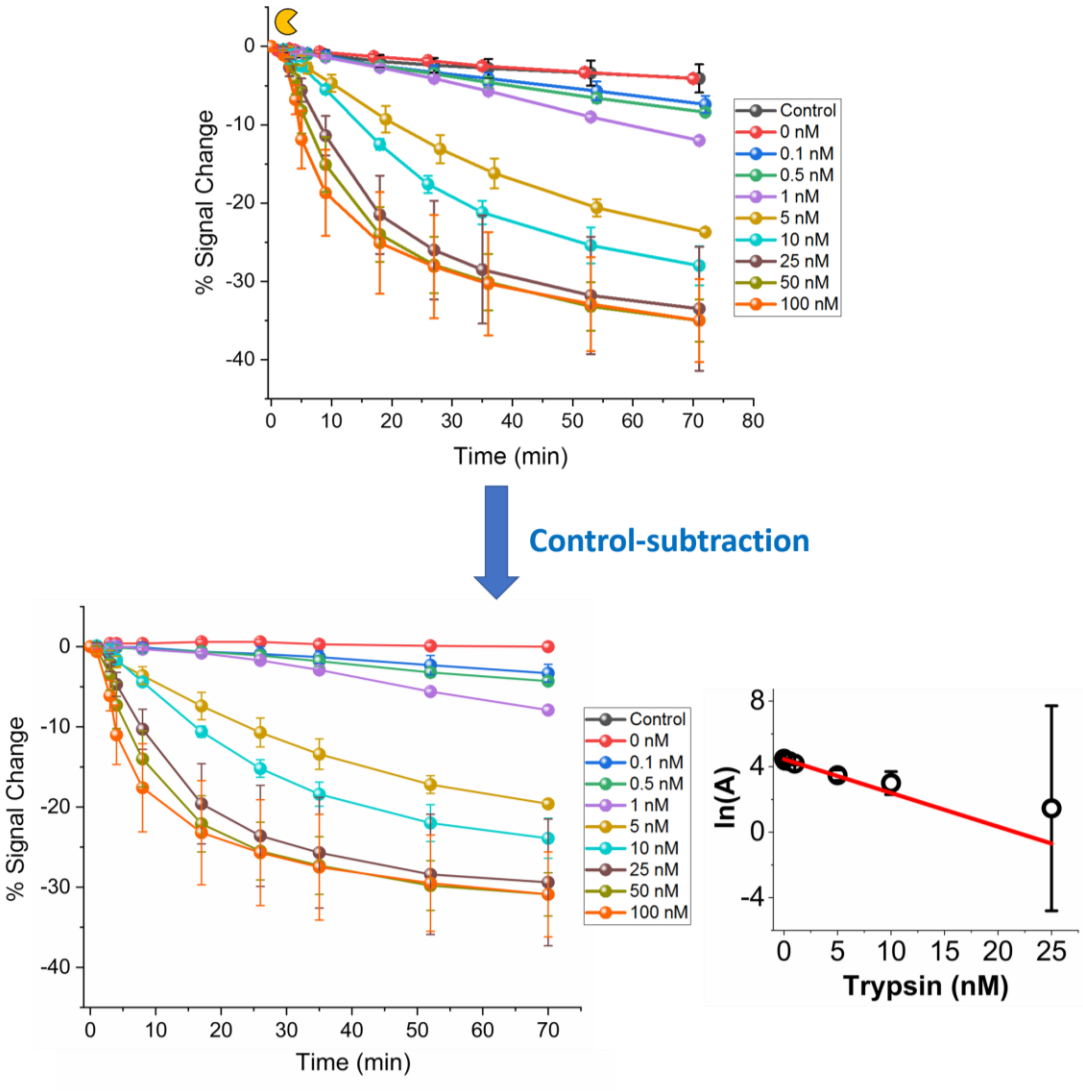

Figure 4-14: Top: Plot of % signal change vs time for SAM-functionalised probe immobilised onto Au macroelectrodes immersed in varying trypsin concentrations in PBS (0, 0.1, 0.5, 1, 5, 10, 25, 50, 100 nM for substrate probe and 100 nM for the negative control probe, containing D-amino acids). All data represent the average (and standard deviations) from (typically) 3 functionalised electrodes. Bottom left: The data recorded for the negative control subtracted from the others. Bottom right: Natural logarithm of A(%), after 70 min plotted against the concentration of trypsin. The straight line corresponds to the best linear regression fit (lnA =−0.21 [trypsin/nM] + 4.46; r2= 0.87). The points of [trypsin]= 50 and 100 nM were not included in the fit due to that A(t)=0 and having large replicate error compared to the other concentrations. Adapted from [7].

As expected, there was no statistically significant difference between the control and the blank (0 nM trypsin) experiments, expect a small, negligible decrease in the signal due to the loss of SAM. On the other hand, there was a marked difference between them and the lowest trypsin concentration (0.1 nM) used, which confirms the high sensitivity and selectivity of the sensing platform. In addition, it is worth noting that the higher the trypsin concentration in solution, the faster the % signal decrease. At low trypsin concentrations (up to 25 nM), there was a proportional relationship between the enzyme concentration incubated and the natural logarithm of the percentage signal decrease. However, it was seen that it reaches a saturation point at the concentrations above 25 nM. Given that this system has been shown to follow Langmuir kinetics, this is to be expected at relatively low concentrations of trypsin compared to the Michaelis constant, where the proportion of surface covered by the trypsin-protein complex is expected to be low and the resulting rate of proteolytic cleavage is determined by this and is proportional to the concentration of trypsin.

It is satisfying that, as predicted by the method previously developed [7], [8], A(t) can be defined as the percentage of signal left to change at time t, and calculated as;

$$\mathrm{A}(t) = \frac{(\%\ \mathrm{SC\ at}\ t)\ -\ (\%\ \mathrm{SC\ as}\ t\ \rightarrow\ \infty)}{(\%\ \mathrm{SC\ at}\ t = 0)\ -\ (\%\ \mathrm{SC\ as}\ t\ \rightarrow\ \infty\ \mathrm{and}\ [\mathrm{E}]\ \rightarrow\ \infty)} \times 100\% \qquad (4.1)$$

as % SC is the percentage signal change registered and [E] is the trypsin concentration. As plotted in Figure 4.14 Inset, the natural logarithm of A(t) is shown to be proportional to the trypsin concentration, [E] which is the confirmation of the first-order kinetics with respect to the trypsin concentration. It is also confirmed that this linear dependency is seen at only lower concentrations up to 25 nM, as it curved and reached saturation (for A(t)=0), with large replicate errors, at higher concentrations, 50 and 100 nM. This linear relationship allowed an estimation of the LoD as 250 pM for this Au macroelectrode-based sensor platform. This low LoD value is quite consistent with the values obtained using electrochemical, colorimetric and fluorescence-based techniques reported in literature [255]. It also successfully covers the clinically relevant range for trypsin levels in normal (5-15 nM) and chronic pancreatitis conditions (34-85 nM) [256], [257]. Additionally, the response of the sensor platform was evaluated upon exposure to enzyme followed by the enzyme inhibitor, Glycine wax, to further

confirm whether the source of the registered decrease was really due to selective enzyme cleavage.

Figure 4.15 shows the immersion of the probe into 1x PBS solution containing 100 nM trypsin and corresponding % signal decrease, represented as the increase in fraction of product, f_p with time. It shows the expected first order kinetics due to the trypsin cleavage. However, red line with triangles shows the inhibition of the cleavage reaction when initially it was immersed into the 1x PBS solution containing 100 nM trypsin, and then the introduction of 200 nM trypsin inhibitor (Glycine wax) after 10 min, where an almost stable signal registered afterwards. The hindering of the kinetics due to the enzyme inhibition in this way establishes the specificity of the sensor platform against the target enzyme.

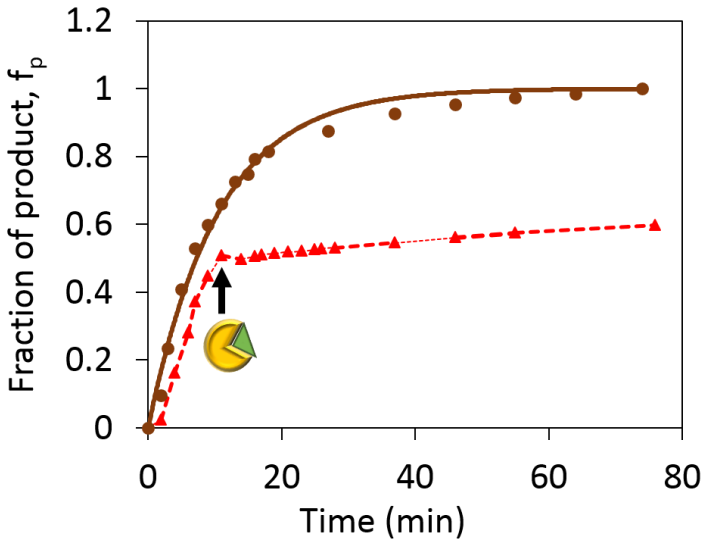

Figure 4-15: Fraction of products (fp or θ) vs time plot for probe immobilised-Au macroelectrodes responses upon addition of 100 nM trypsin (brown circles) or upon initial addition of 100 nM trypsin 100 nM (at time t=0), followed by the addition of trypsin inhibitor (200 nM Glycine wax) into the 1x PBS solution (at time t=10 min) (red triangles). Trypsin is denoted by the yellow sector symbol whereas the green triangle denotes trypsin inhibitor.

4.5 Analytical Performance of Platinum Macroelectrodes

In order to evaluate and compare the analytical characteristics offered by the gold and platinum macroelectrodes in protease sensing, platinum macroelectrode surfaces were identically modified with the mixed SAM as described in Section 3.4.2.1. They were then immersed in buffer (1x PBS) solutions containing varying concentrations of trypsin (1-100 nM) and the electrochemical signal was interrogated by SWV with time. Figure 4.16 shows typical SWV

signals obtained from the probe immobilised onto a Pt macroelectrode over a time period of 60 mins. The decrease in the signal (SWV peak height) is clearly observable after the addition of the enzyme (at time t=0). Also, the amount of this decrease observed per unit time (5 min) is higher initially after the enzyme addition (which means the higher amount of cleavage at the beginning), whereas it declines over time. In comparison to the typical SWV peaks obtained for the Au macroelectrode (Figure 4.13), it was found to be similar, in terms of the peak potential, height and also the approximate amount of decrease in signal after 60 min incubation with 100 nM trypsin. As only peaks obtained at 0, 5, 15, 35 and 60 min are given for Au macroelectrode, unlike Pt macroelectrode where all peaks are plotted in the figure, it seems like there was a difference in the amount of signal decrease per unit time. However, it was not the case when all of them has been analysed comparatively. It was again similar as observed in Au macroelectrodes, where the amount of the cleavage was found to be lowered with time again. This was quite advisable considering the cleavable probe amount has the highest level when enzyme is added, whereas this amount reduces over time and less amount of cleavable probe remains on the electrode surface, resulting in the experienced convergence.

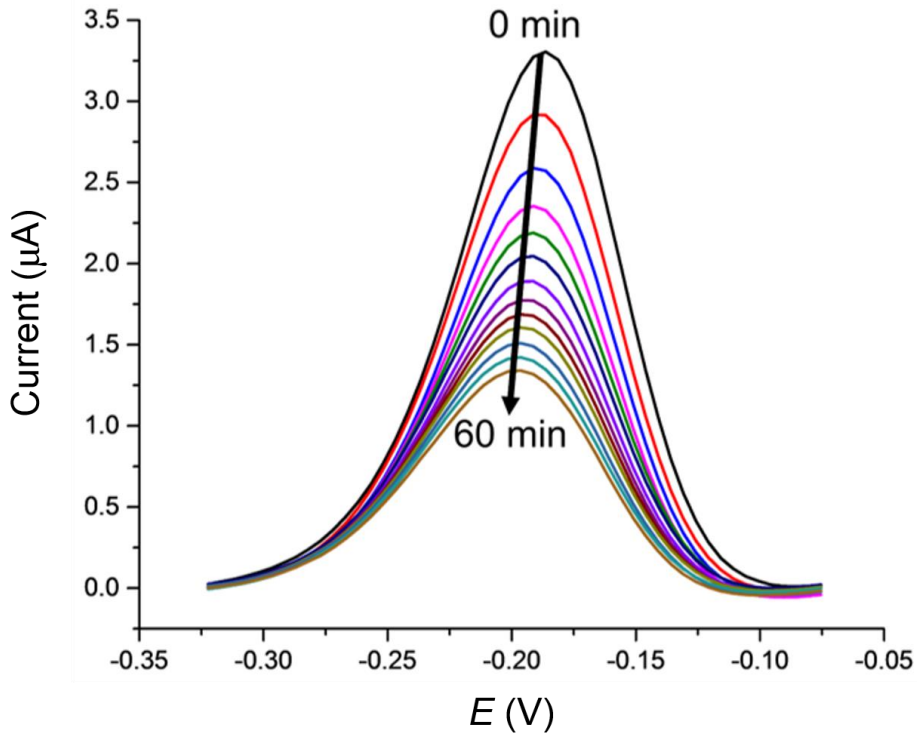

Figure 4-16: Typical background-subtracted SWV curves for a SAM-functionalised probe substrate immobilised onto Pt macroelectrode registered for 100 nM trypsin at different incubation times between 0 - 60 min (with intervals of 5 min) in 1x PBS.

Figure 4.17 shows the signal decrease amounts registered for probe-immobilised Pt macroelectrodes immersed in varying trypsin concentrations in 1x PBS for 92 min. This incubation time was slightly different than the one (70 min) used for Au macroelectrodes. However, this difference is not considered as significant because the percentage signal decrease was found to be constant after a while, due to the fact that all cleavable probes on the electrode surface were successfully cleaved. It should be noted that the percentage signal decreases registered for Pt macroelectrodes did not varied too much than Au macroelectrodes (for same concentrations incubated). There was a slight difference in terms of standard deviations observed in Au and Pt macroelectrodes. They were found to be larger in Pt especially for higher concentrations, which might be attributed to the poorer reproducibility. However, there is not any inspected confirmation of the reason for this. Apart from that, there was again a proportional relationship between the natural logarithm of the percentage signal decrease and trypsin concentrations, and the kinetics was shown to follow the Langmuir model as similar to Au macroelectrode findings. Again, it is shown by plotting the ln A(t) vs trypsin concentration, [E] as depicted in Figure 4.17 Inset, where this relationship was fitted to a linear fit. Using this observed linear dependency of ln A(t) to concentration, LoD for Pt macroelectrode-based trypsin sensor was determined as 2.5 nM for sensing up to 25 nM. Although this value is significantly higher than the earlier reported value obtained using Au macroelectrodes (250 pM), there is not any evidence to be convinced that it was caused by a fundamental distinction between Au and Pt as electrode material. Moreover, these LoD values are only estimations reached after a limited number of measurements/replicates per each concentration. Therefore, it is quite possible that they are vulnerable to variations in SAM probe formation or measurement conditions. In order to make sure that they completely reflect the actual reaction, enough measurements should be performed. Furthermore, taking additional concentrations (0.1 and 0.5 nM) tested for Au (unlike Pt macroelectrodes) into account might have been the main reason which has led to increasing the measurement range and corresponding different estimated value.

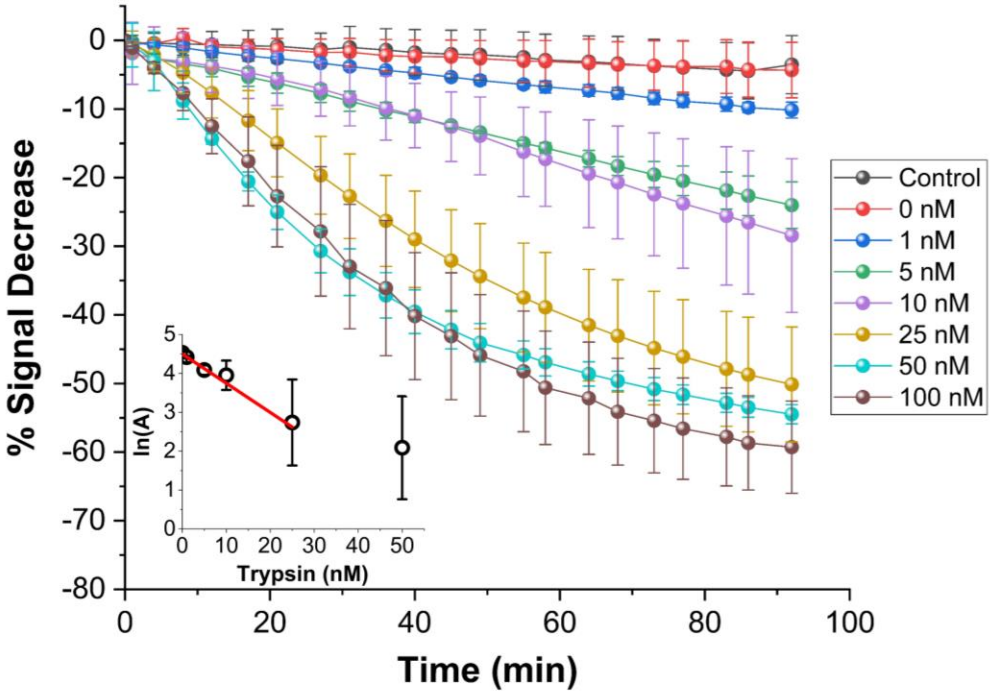

Figure 4-17: Plot of % signal change vs time for SAM-functionalised probe immobilised onto Pt macroelectrodes immersed in varying trypsin concentrations in PBS (0, 1, 5, 10, 25, 50, 100 nM for substrate probe and 100 nM for the negative control probe, containing D-amino acids). All data represent the average (and standard deviations) from (typically) 3 functionalised electrodes. Inset. Natural logarithm of the adjusted signal, A(%), after 92 min plotted against the concentration of trypsin. The straight line corresponds to the best linear regression fit (lnA =−0.075 [trypsin]/nM + 4.498; r2= 0.96). The point of [trypsin]=50 nM was not included in the fit due to having large replicate error compared to the other concentrations.

4.6 Further Optimisations of Microelectrodes

As significance of the design of the probe itself, all SAM-based components added to the probe solution plays an important role for the enzyme accessibility as well as electron transfer between the redox tag and electrode [258], [259]. It is also known that mass transport properties are different for macro- and microelectrodes. Enzyme cleavage and SAM film formation are normally faster for microelectrodes; however, it is valid only if they are under mass transport control. Therefore, optimising the self-assembled monolayers on electrode surfaces are vital, as the changes in surface chemistry and morphology have too much influence on diffusional properties. In addition, the optimal conditions should be used to avoid any possible undesired interaction between the charged/uncharged species or steric effects. For this purpose, further optimisations on microelectrodes were made in terms of backfilling substances (MCH) and third component (DT) molecules, keeping the same probe design,

concentration (40 µM) and protocols used for electrode preparation. Figure 4.18 shows both percentage signal decrease due to trypsin cleavage after 900 min as well as the initial probe signal before trypsin addition for Pt microelectrodes overnight-incubated with 40 µM probe + DT with varying concentrations of 50, 150, 300 and 600 µM.

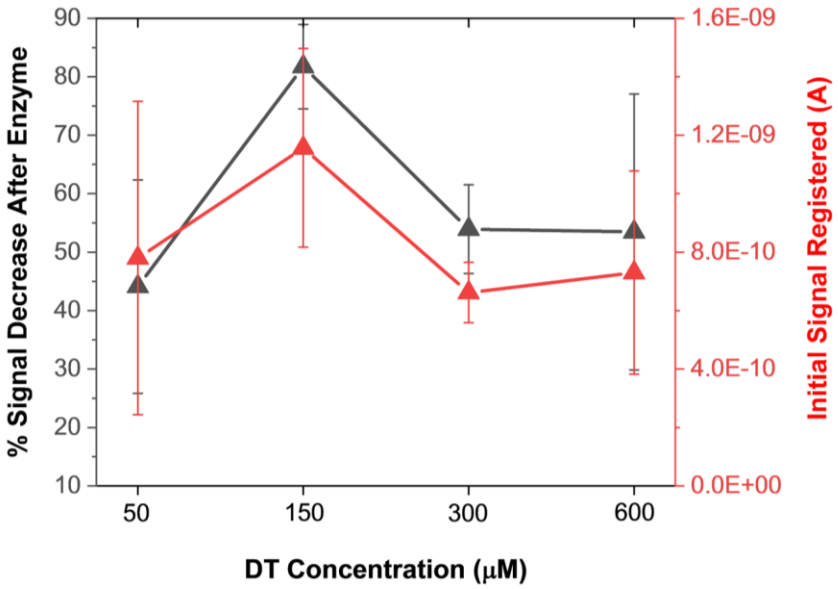

Figure 4-18: Registered % signal decrease (after trypsin incubation for 900 min) and initial currents (before any enzyme addition) for Pt microelectrodes following overnight incubation with 40 µM probe + DT in various concentrations (50, 150, 300 and 600 µM). All data represent the average (and standard deviations) from 3 replicates. SWV data used for the preparation of this figure can be found in Appendix-4.

% Signal decrease and initial currents registered were the same within experimental error for all DT concentrations. As given in Section 4.3.2, this was unsimilar to the macroelectrodes where increasing the DT concentration increased the percentage signal loss (for concentrations below 150 µM). This disparity in microelectrodes might be attributed to the possible formation of more close-packed probe layer immobilised on the surface prior to DT addition, thus leaving a limited space for DT molecules to get attached onto the surface, which might result in a less importance of the changes in concentrations above a threshold. As a result, 150 µM was selected as optimum DT concentration for further microelectrode experiments, because it at least has the highest mean value both in initial signals and % signal decrease registered.

In addition to the concentration of DT molecules used, backfilling MCH molecules were also optimised in terms of treatment duration. The backfilling molecules are of great significance

and thus required for SAM-based electrochemical biosensing [260]. Otherwise, the sensing layer can include some defects/pinholes on the surface, which would be exposed to any undesired interaction such as non-specific binding. Furthermore, sizes and numbers of these pinholes on the surface may alter SAM reorganisation process [261]. All these can induce detrimental changes in the electrochemical signal, which should be avoided. The optimised backfilling treatment used for macroelectrodes was 1 h in 1 mM ethanolic solution of MCH. Because its common concentration used in literature is 1 mM [154], [262]–[264], this was kept same but only the effect of treatment (incubation) time was analysed. Figure 4.19 shows comparative initial currents registered for non-treated and treated Pt microelectrodes with 1 mM MCH with varying treatment times (10, 30, 60, 1440 min) for both B-SAM (40 µM probe) and T-SAM (40 µM probe + readily optimised 150 µM DT) structures. Clearly, it suggests increasing MCH incubation time caused a decrease in the SWV signal registered for both B-SAM and T-SAM configurations. It is, of course, interesting that there was almost no signal for T-SAM configuration after overnight MCH treatment, whereas still some remaining redox activity was observed for B-SAM.

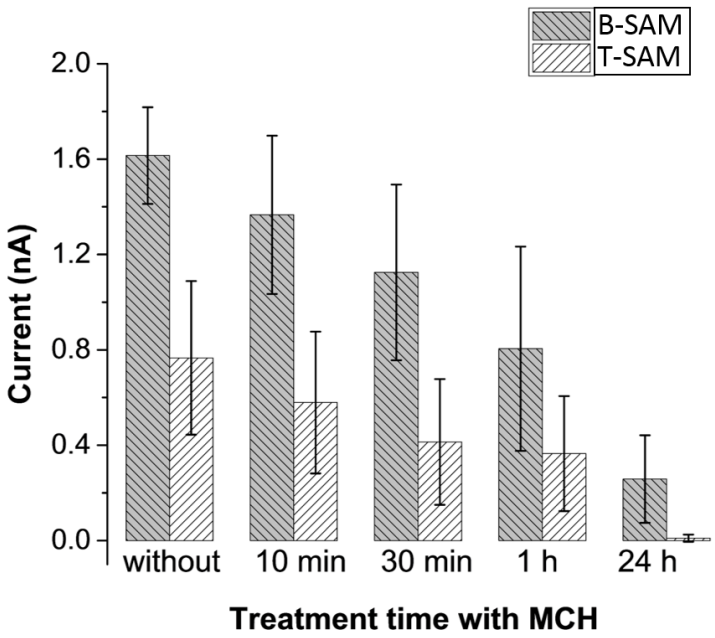

Figure 4-19: Comparative initial currents registered for non-treated and treated microelectrodes with 1 mM MCH using different treatment times for both B-SAM (40 µM probe, represented with dark columns) and T-SAM (40 µM probe + 150 µM DT, represented with light columns) configurations. All data represent the average (and standard deviations) from 9 functionalised electrodes.

It can be hypothesised that more diluted surface in T-SAM configuration, as previously discussed, can deliver more space to backfilling molecules which could be thermodynamically preferred over probe molecules, accordingly reorganised and replaced them overnight. However, when all probes were assessed also in terms of the % signal decrease after trypsin addition, these were observed to be in similar range within experimental errors. Since even well-ordered SAM layers are known to have surface defects [265], the backfilling and corresponding passivation of the pinholes are crucial for sensitivity purposes. Therefore, the shortest time tested for treatment, 10 min, was selected as optimal duration and used for the rest of the microelectrode work, although no evidence of treatment time-dependent change in the % signal decrease was observed so far.

4.7 Analytical Performance of Platinum Microelectrodes

After above mentioned optimisations in backfilling MCH and third component DT molecules have been completed, platinum microelectrode surfaces were modified with the mixed SAM using optimised concentrations and durations, then monitored with SWV in real time. Figure 4.20 shows typical SWV signals registered for the probe immobilised Pt microelectrode over a time period of 900 mins. The first difference to note was the amount of the signal, which was in the range of nanoamps (nA), whereas the signal recorded for macroelectrodes was usually in microamps (μA) range. This was expected and consistent with the electrode dimensions. As similar to Au or Pt macroelectrodes, the signal decreased after 100 nM trypsin addition (at time t=0). However, the decrease was explicitly slower for microelectrodes, compared to macroelectrodes. As seen in the figure, it was only around ~20-25% after an hour. In order to further investigate this, the electrodes were immersed into 1x PBS solutions with varying concentrations of trypsin, to check whether the response is similar. As depicted in Figure 4.21, the percentage signal decrease was slow for all trypsin concentrations incubated. In addition, microelectrodes were found to show different behaviour in terms of the amount of signal decrease. The maximum percentage signal decrease registered for Au and Pt macroelectrodes was, for example, ~35% (Figure 4.14, after 70 min) and ~55% (Figure 4.17, after 92 min), respectively, upon the addition of 100 nM trypsin. However, it was increased up to ~80% (after 900 min) for Pt microelectrodes. This observation was also valid for other high concentrations such as 25 and 50 nM. This means a change in the amount of the cleavable probes as well, which is not similar to macroelectrodes where no change of the proportion of cleavable/uncleavable probe amount was observed with increasing [E].

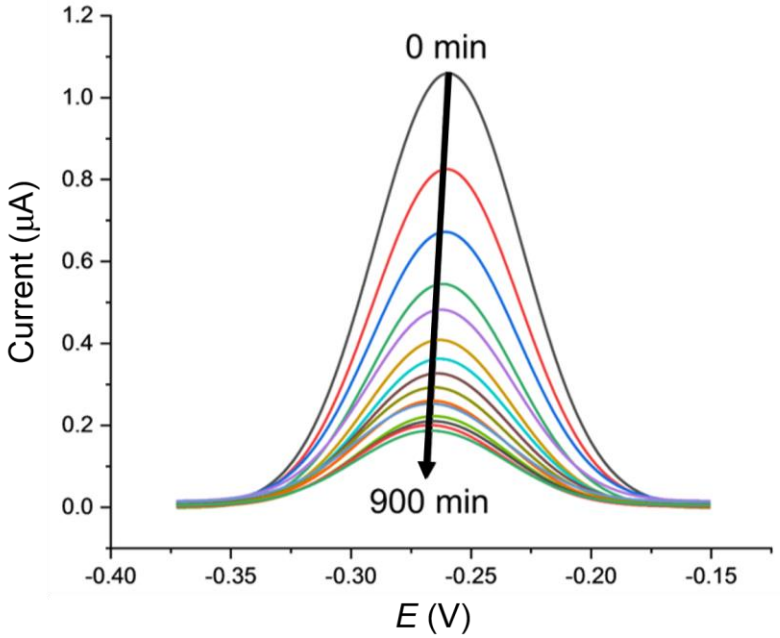

Figure 4-20: Typical background-subtracted SWV curves for a SAM-functionalised probe substrate immobilised onto Pt microelectrode registered for 100 nM trypsin at different incubation times between 0 - 900 min (with intervals of 60 min) in 1x PBS.

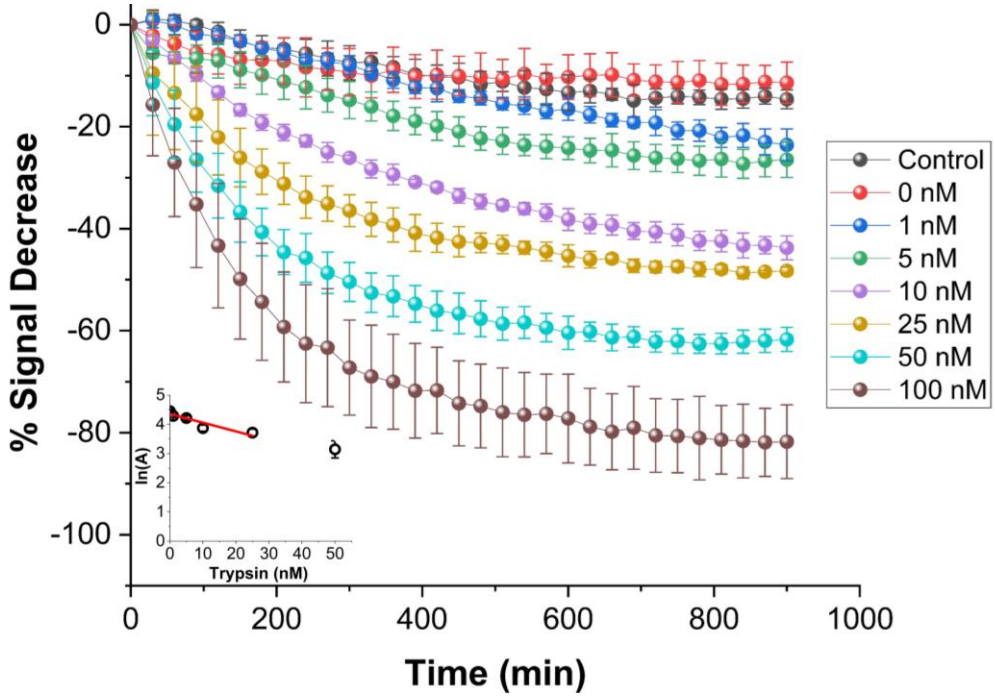

Figure 4-21: Plot of % signal decrease vs time for SAM-functionalised probe immobilised onto Pt microelectrodes immersed in varying trypsin concentrations in 1x PBS (0, 1, 5, 10, 25, 50, 100 nM for probe substrate and 100 nM for the negative control probe, containing D-amino acids). All data represent the average (and standard deviations) from (typically) 3 functionalised electrodes. Inset. Natural logarithm of A(%), after 900 min plotted against the concentration of trypsin. The straight line corresponds to the best linear regression fit (lnA =−0.030 [trypsin/nM] + 4.354; r2= 0.84). The point of [trypsin]=50 nM was not included again in the fit due to having large replicate error compared to the other concentrations.

Microelectrodes have been reported many times to show enhanced diffusional kinetics due to hemispherical diffusion compared to the linear diffusion observed for macroelectrodes as also given in Section 2.5.3 [266]. Therefore, it is clear from these observed cleavage rates that this difference in rate of proteolytic cleavage is not as a result of the rate of trypsin diffusion. Given that the rate must therefore be determined by surface reaction, it is likely that this difference results from the macro- and microelectrode surfaces having a different SAM structure and/or probe or target surface disposition. It was previously noted that macro- and microelectrodes might differ from each other regarding the deposition and disposition of SAMs on their surfaces, which could affect the resulting properties such as electron transfer [267]. Although the trypsin cleavage reaction is not under diffusional control, such differences could arise from differences in diffusional rates during SAM film formation (as previously noted in Section 4.6), and differences in uniformity of diffusion to macro and microelectrode surfaces when under diffusional control. Given this, it is interesting that there is a difference in the observed initial SWV peak potentials between macro and microelectrodes of around 70 mV which indicates a difference in average redox environment and overall film structure.

In spite of these variations in the rate and the cleavage amount, the proportional relationship between the natural logarithm of ln A(t) and trypsin concentration revealed that the cleavage kinetics is still first order (Figure 4.21 Inset). LoD for microelectrodes was again determined using this linear dependency and found as 2.9 nM which is a quite close value to the one obtained using Pt macroelectrodes. Although this is a single point measurement on only three electrode replicates and is therefore likely to be a conservative estimate of the LoD value, the calculated linear response range and values are in good agreement with those reported in the literature [215], [229], [268]–[270], and still successfully covers the clinically relevant range for trypsin levels.

4.8 Kinetic Analysis of Proteolytic Cleavage

Although single time point analysis and linear calibration is a facile method, time-dependent analysis of multiple data points is likely to be more robust and sensitive, and when combined with Michaelis-Menten kinetic analysis, which models the non-linearity of the response with [E], analysis should be possible over a wider trypsin concentration range. The measured % signal changes for varying trypsin concentrations were therefore analysed as a function of time using the previously established Michaelis-Menten kinetic model for similar heterogeneous

enzymatic assays [7], [215], [228], [271]. According to this model, the % signal change, A, is expressed as a variation in the fraction ($\theta(t) = 1 - A(t)$) of cleavable peptide which has been cleaved at any time, *t*. Data for each trypsin concentration are then fitted to the equation [7]:

$$\theta = 1 - e^{-k_{eff}t} \tag{4.2}$$

where θ is the fractional cleavage of the substrate on the surface, k_{eff} is the effective rate constant and *t* is the time. Although good fits were obtained to this equation for the Pt macroelectrode system, consistent with previous observations on Au macroelectrodes [7], this was not the case for the Pt microelectrode system. Inspection of Figure 4.21 indicates that this is likely due to an increase in the fraction of cleavable probe with increasing [E], as shown by the increasing maximum % signal change as $t \rightarrow \infty$. All data were therefore fitted to equation 4.3, which includes the additional concentration-dependent variable, *a*, which is the fraction of cleavable peptide that can be cleaved at each trypsin concentration, [E], (with $a \rightarrow 1$ and equation 4.3 $\rightarrow$ equation 4.2 as [E] $\rightarrow \infty$ and at all [E] for macroelectrodes):

$$\theta = a[1 - e^{-k_{eff}t}] \tag{4.3}$$

This simple equation was shown to fit well to all data and generally enabled the extraction of both *a* and k_{eff} values for each trypsin concentration (both Figure 4.22, for which $a = 1$ and equation 4.3 collapses to equation 4.2, and Figure 4.23). The only exception was for the lowest [E] in Figure 4.23, where over this measurement time range the product tk_{eff} was sufficiently small for equation 4.3 to become effectively linear and only a combined constant ak_{eff} could be determined.

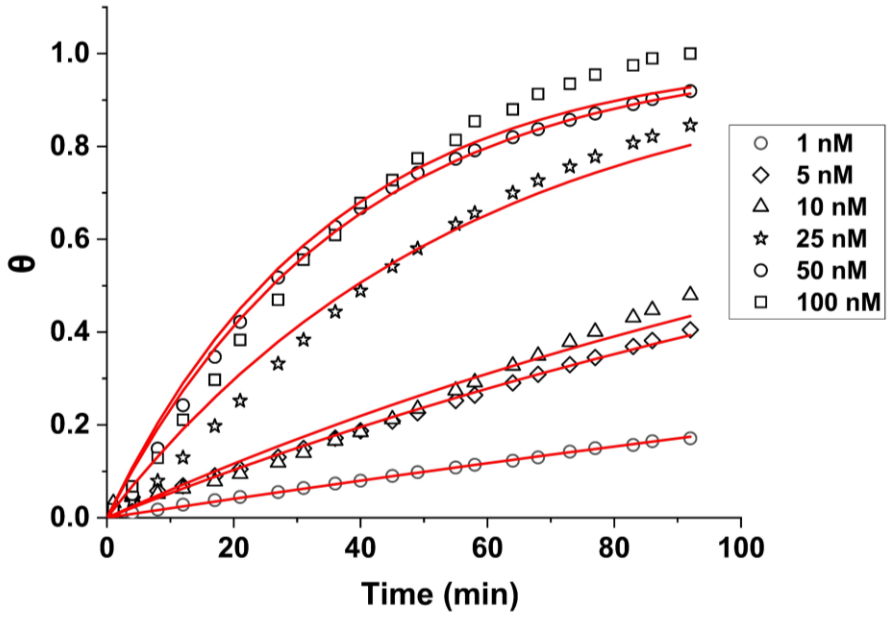

Figure 4-22: Calculated fractional cleavage, θ, vs time plots for data for Pt macroelectrode cleavage data from Fig. 4.17. The data points (from bottom to top) correspond to immersion in varying trypsin concentrations in 1x PBS (namely 1, 5, 10, 25, 50 and 100 nM), whilst each line shows the best fit to equation 4.2.

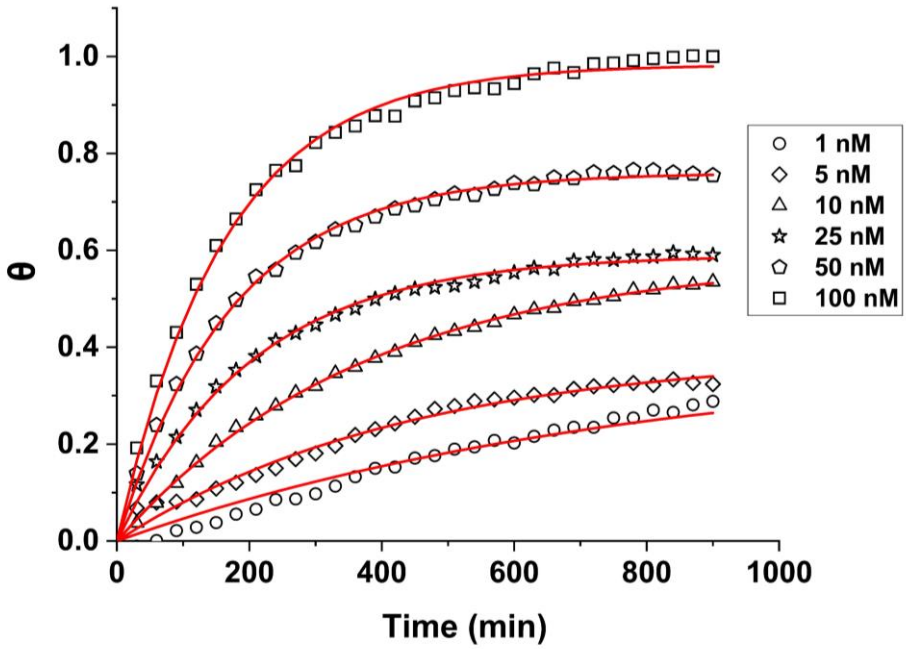

Figure 4-23: Calculated fractional cleavage, θ, vs time plots for data for Pt microelectrode cleavage data from Fig. 4.21. The data points (from bottom to top) correspond to immersion in varying trypsin concentrations in 1x PBS (namely 1, 5, 10, 25, 50 and 100 nM), whilst each line shows the best fit to equation 4.3 from which values of a = 0.39, 0.39, 0.58, 0.59, 0.76 and 0.98 respectively have been obtained.

For the estimation of k_{cat} (enzyme turn-over number) and K_M (Michaelis-Menten binding constant) values, these extracted k_{eff} values were plotted as a function of trypsin concentration (Figure 4.24 and 4.25) and fitted to the Michaelis-Menten enzyme cleavage model using the equation:

$$k_{eff} = k_{cat} / (1 + K_M / [\mathrm{E}]) \quad (4.4)$$

This non-linear fitting enabled the estimation of the values of k_{cat} and K_M as 0.035 min^{-1} and 19 ± 3 nM for Pt macroelectrodes and, 0.0075 min^{-1} and 15 ± 3 nM for Pt microelectrodes, respectively. Although there are significant differences in k_{cat} values, the calculated K_M values are comparable to each other and also to previously reported values by Anne et al. (~17 nM) [215] and also Au macroelectrode finding (28 ± 3 nM) [7]. All estimated values for Au and Pt macroelectrodes and Pt microelectrodes are presented in Table 2. Although k_{cat} values estimated for Au (0.102 min^{-1}) and Pt (0.035 min^{-1}) macroelectrode platforms were also found to be different, there is not enough evidence of any significance in this difference considering that they showed similar K_M values, SWV peak potentials, peak currents, current densities and thiol bonding strength.

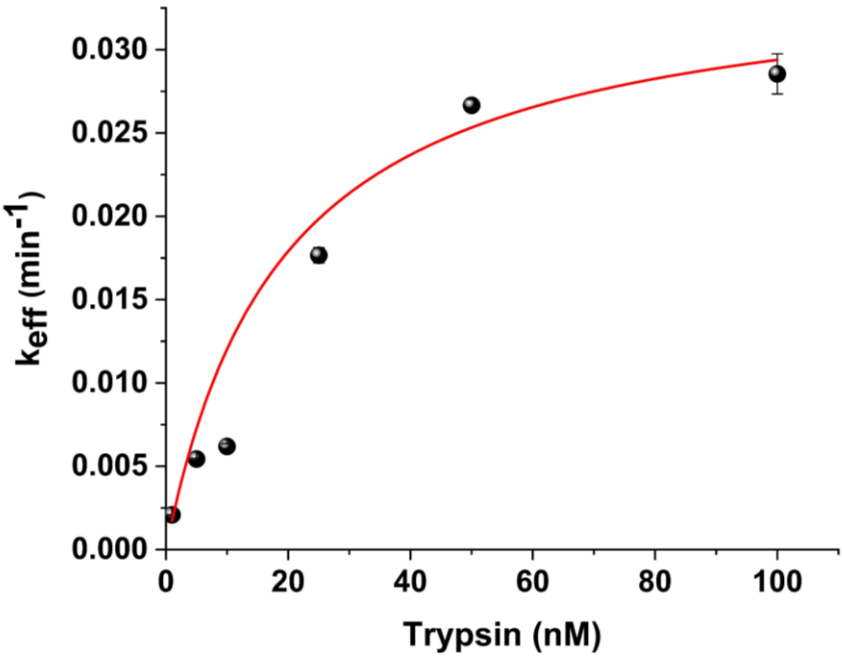

Figure 4-24: Effective rate constant, k_{eff}, as a function of the bulk trypsin solution concentration. Data represented by dots correspond to the experimental data obtained from the fits to the data in Fig. 4.22 and the solid red line shows the fitting processed according to equation 4.4.

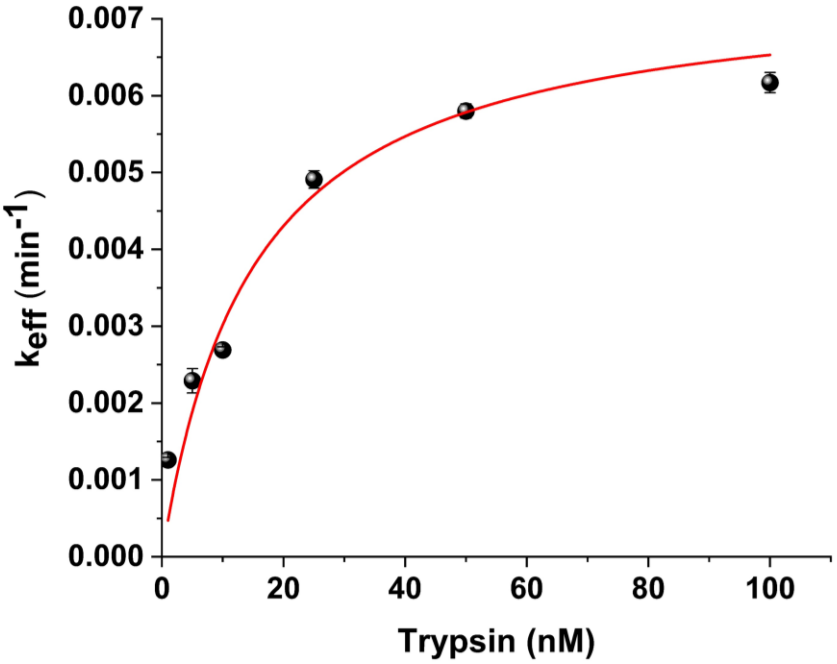

Figure 4-25: Effective rate constant, k_{eff}, as a function of the bulk trypsin solution concentration. Data represented by dots correspond to the experimental data obtained from the fit to the data in Fig. 4.23 and the solid red line shows the best iterative fit to equation 4.4.

Table 4-1: Summary of the extracted kinetics and SAM-based surface coverage-related values.

[trypsin / nM]	a	Langmuir (θ)	k_{eff} (min^{-1})	k_{cat} (min^{-1})	K_M (nM)	Current Density (A/m^2)
Macro Au				0.102	28 ± 3	0.95
0.1	1	0.21	0.00340 ± 0.00010			
0.5	1	0.24	0.00388 ± 0.00005			
1	1	0.34	0.00546 ± 0.00017			
5	1	0.68	0.01615 ± 0.00035			
10	1	0.80	0.02441 ± 0.00097			
25	1	0.96	0.04670 ± 0.00249			
50	1	1	0.05704 ± 0.00351			
100	1	1	0.06763 ± 0.00501			
Macro Pt				0.035	19 ± 3	1
1	1	0.17	0.00208 ± 0.00001			
5	1	0.40	0.00544 ± 0.00005			
10	1	0.48	0.00619 ± 0.00016			
25	1	0.85	0.01766 ± 0.00046			
50	1	0.92	0.02666 ± 0.00035			
100	1	1	0.02854 ± 0.00120			
Micro Pt				0.0075	15 ± 3	2.7
1	0.39	0.29	3.83E-04 ± 0.04E-04			
5	0.39	0.32	0.00229 ± 0.00002			
10	0.58	0.54	0.00269 ± 0.00004			
25	0.59	0.59	0.00491 ± 0.00011			
50	0.76	0.75	0.00580 ± 0.00009			
100	0.98	1	0.00617 ± 0.00013			

These comparable K_M values suggests that there is little difference between the thermodynamics of the trypsin binding to the probe substrate to form the enzyme-substrate complex in all cases. However, the markedly lower k_{cat} value indicates significantly lower kinetics of the reaction of this enzyme-substrate complex on the SAM-functionalised microelectrodes. This indicates that the catalytic efficiency (k_{cat}/K_M) of the enzyme is lower for this surface, and that although absolute and relative enzyme-substrate association and dissociation rates appear similar (which given the size and multiple interactions of the enzyme with the surface is likely to be reflective of more general enzyme-SAM surface association and dissociation) unlike the enzyme substrate reaction rates (which are likely to reflect differences in probe accessibility). Therefore, the rationale for slower proteolytic cleavage observed is lower probe accessibility to the enzyme active site at the microelectrode surface, which would result in lower probe reactivity. It is possible that this (and the fact that $a < 1$, equation 4.3 for microelectrodes) is due to the relative inaccessibility of the enhanced proportion of probe nearer the electrode edge, due to the dramatic increase in the amount and importance of edge per unit area on decreasing from the macro to the microelectrode dimension, as illustrated in Figure 4.26. This is in addition to the uncleavable subset of the immobilised peptides at all [E] for both electrode types, previously attributed to electrode roughness and probe orientation variation as sources of local site inaccessibility.

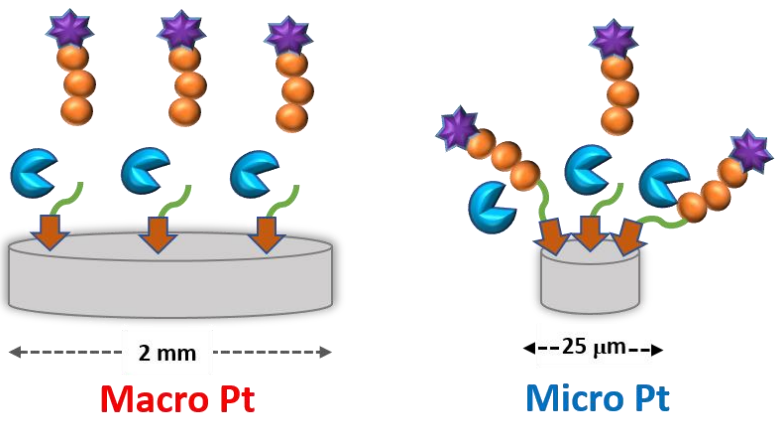

Figure 4-26: Representation of the dissimilar behaviour observed for macro- and microelectrodes due to the differences in the peptide film structure formation and their effect on the cleavage rate.

In order to further investigate and confirm the idea that SAM probe formation and structure on macro- and microelectrode surfaces is dissimilar, SAM surface coverage (Γ) for Au and Pt, macroelectrodes and microelectrodes, was calculated using the equation [176]:

$$i_{\mathrm{p}} = \frac{n^2 F^2}{4RT} vA\Gamma \tag{4.5}$$

where i_p is the peak current, n is the number of electrons transferred per mole of reaction (n=2 for methylene blue), F is the Faraday constant, R is the universal gas constant, T is the temperature, v is the scan rate and A is the surface area of electrode. In order to achieve this, cyclic voltammograms were recorded with various scan rates (Figure 4.27) and registered peak currents (the sum of oxidative and reductive) were linearly plotted against the scan rates (Figure 4.28).

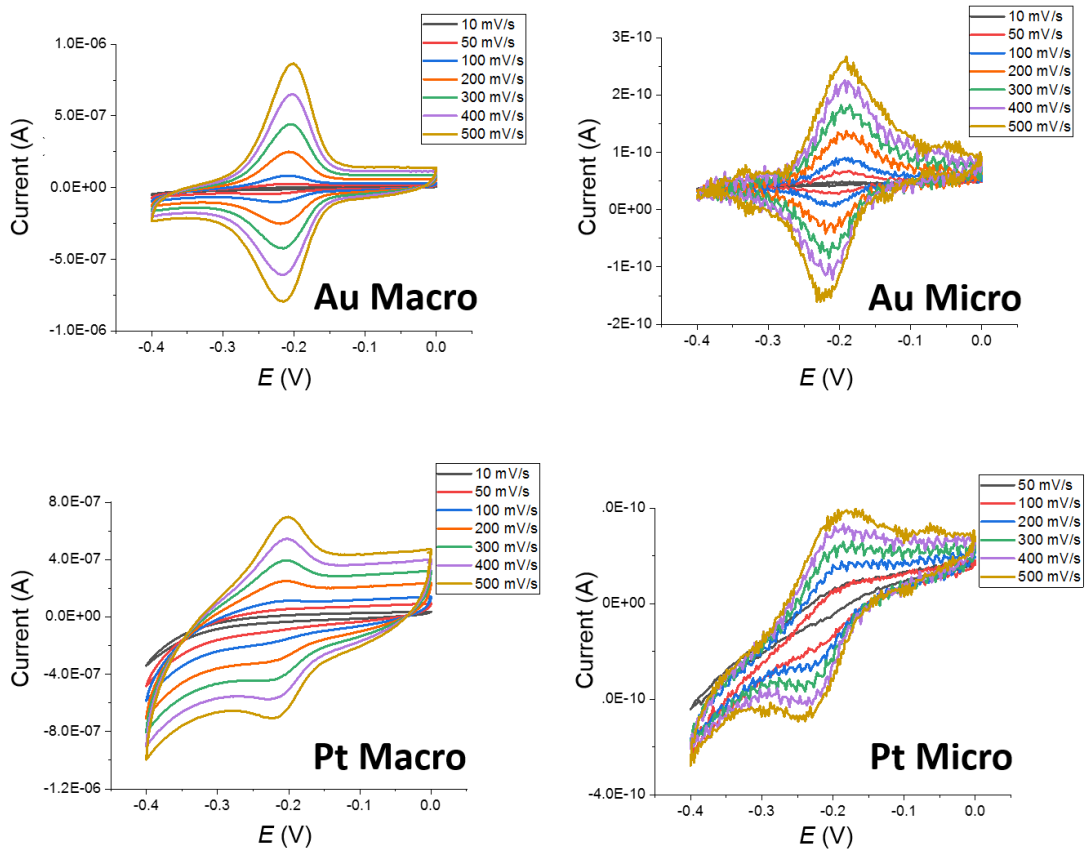

Figure 4-27: Cyclic voltammograms (CVs) recorded with varying scan rates of B-SAM probe-immobilised Au macro-, Au micro-, Pt macro- and Pt microelectrodes.

This linearity is also consistent with this electrochemical signal, due to surface-bound redox species, the MB-tagged peptide-based probes [197]. It was followed by the estimation of the surface coverage from the slopes of $i_p - v$ dependence using the above formula. These were calculated as 2.38 x 10^{-11} mol cm^{-2} for Au macroelectrodes, 4.00 x 10^{-11} mol cm^{-2} for Au microelectrodes, 2.11 x 10^{-11} mol cm^{-2} for Pt macroelectrodes and 3.94 x 10^{-11} mol cm^{-2} for Pt microelectrodes. Apparently, there are around a 2-fold larger values for microelectrodes compared to macroelectrodes, suggesting that more redox-active SAM probe exists per unit area on microelectrodes than on macroelectrodes. In addition, the average interchain spacings were estimated from the relation $(d=1/N\Gamma)^{1/2}$ (where d is the interchain spacing, N is the Avogadro constant and Γ is the surface coverage) [215] and found as 2.64 nm for Au macro-, 2.03 nm for Au micro-, 2.81 nm for Pt macro- and 2.05 nm for Pt microelectrodes. This might be another strong rationale for slower cleavage observed in microelectrodes, if peptide-chains are closely located, interpeptide interactions take place and the space for enzyme accessibility is thus further limited. This was also demonstrated by Wain et al. showing that SAM peptide chains can experience a restricted motion and reorganisation due to enhanced intermolecular interactions between the chains [177], [259].

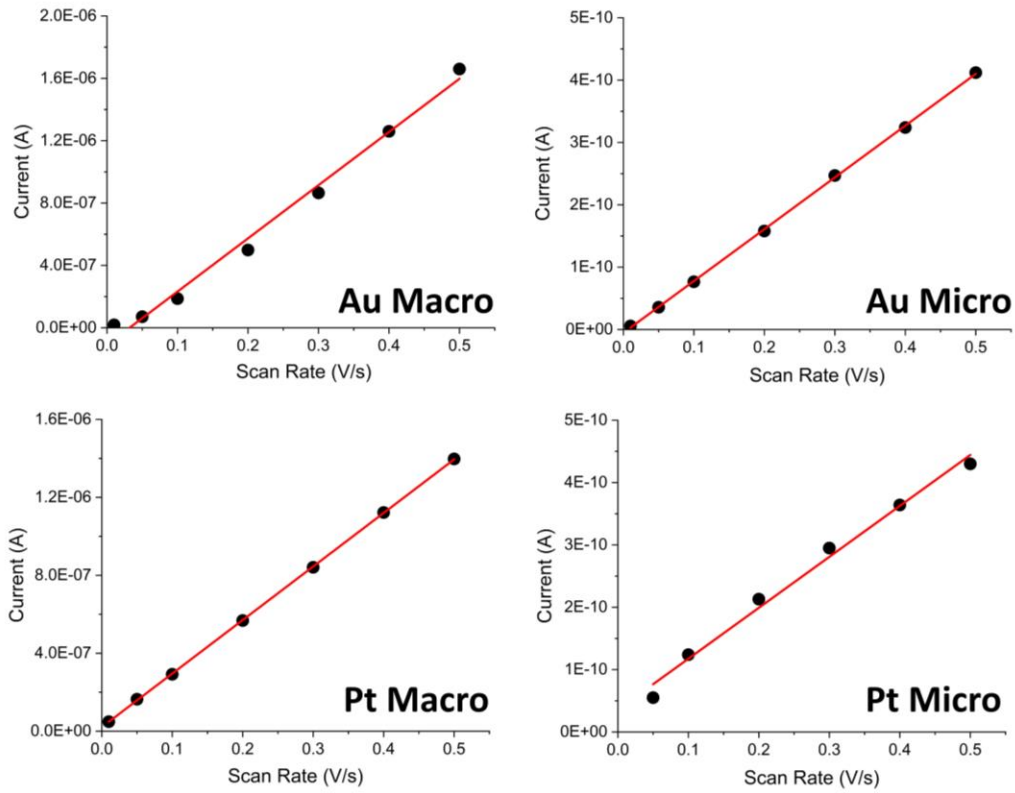

Figure 4-28: Linear correlation between i_p (anodic+cathodic) and scan rate for Au macro-, Au micro-, Pt macro- and Pt microelectrodes.

4.9 Characterisation of Response for Potential Interferents

In order to assess the selectivity of the macroelectrode and microelectrode-based (miniaturised) trypsin sensor, the modified electrodes were exposed to solutions containing potential interferents. Experiments for the selectivity assessment of Au macroelectrodes were performed previously by Dr. Eva Gonzalez-Fernandez [7].

The interferents, used in the assessment, consisted of BSA (100 nM), casein (100 nM), dopamine (1 nM) and Ca^{2+} (1 mM) for macroelectrodes (Figure 4.29) whereas of BSA (100 nM) and casein (100 nM) for microelectrodes (Figure 4.30). These interferents were specifically preferred for the selectivity studies, because BSA is a common protein used for the characterisation of non-specific binding [272], casein has a comparable size (~24 kDa) to trypsin and it is being used as substrate in protease assays [273], dopamine is an important substance for many physiological conditions and also it has been found to be related to tumour angiogenesis and growth [274], and Ca^{2+} signalling is very significant for tumour progression and thus monitoring of the anti-cancer therapy processes [275].

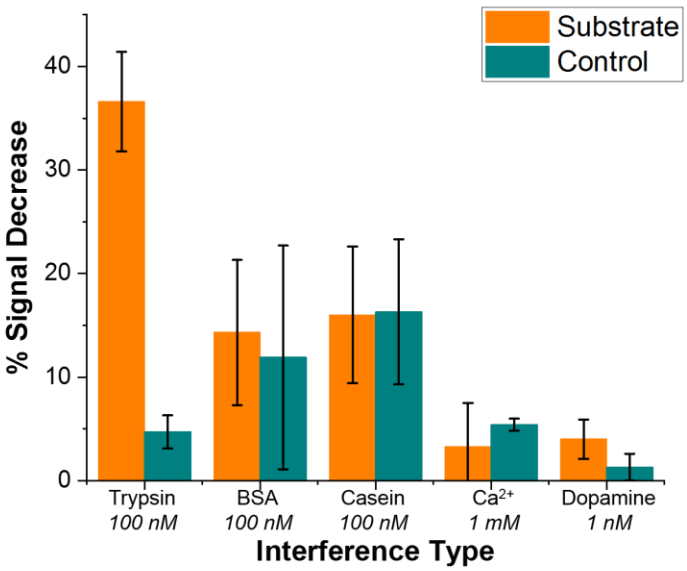

Figure 4-29: Comparative % signal decrease registered for SAM-functionalised macroelectrodes after 70 minutes upon the addition of trypsin (100 nM) or non-specific binding proteins; BSA (100 nM), casein (100 nM), Ca^{2+} (1 mM) and dopamine (1nM) for both substrate- (orange columns) and control-modified (cyan columns) sensing layers. Average data and error bars are typically from 3 individual SAM sensing layers. Adapted from [7].

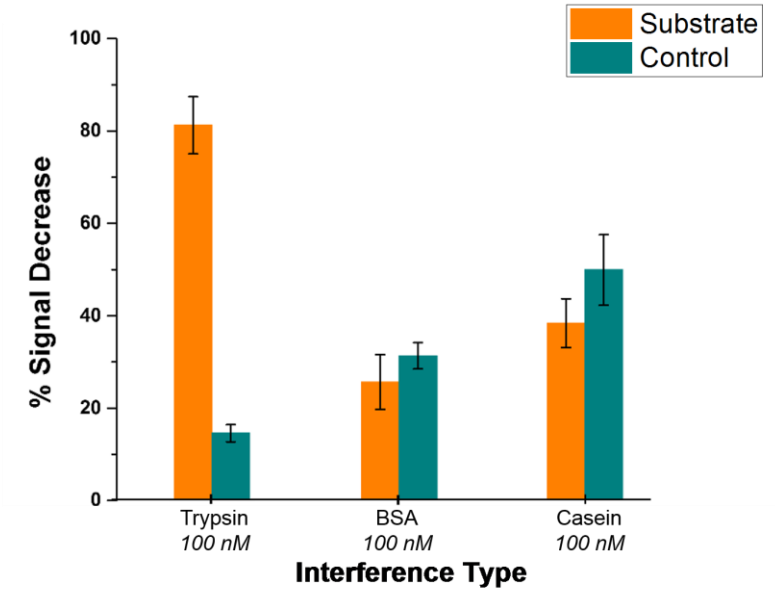

Figure 4-30: Comparative % signal decrease registered for SAM-functionalised microelectrodes after 900 minutes upon the addition of 100 nM trypsin or non-specific binding proteins; BSA and casein for both substrate- (orange) and control-modified (cyan) sensing layers. Average data and error bars are typically from 3 individual SAM sensing layers.

Both figures show the % signal decrease recorded from both the substrate (orange) and the control (cyan)-modified electrodes upon the addition of either the non-specific substances or the target enzyme trypsin. Because dopamine and Ca^{2+} have shown only a negligible effect on the signal decrease, they were not used as interferents to microelectrode response. However, BSA and casein were chosen as models for evaluating the potential for interference in real-world samples arising from non-specific binding of proteins and had an expected effect on the signal decrease recorded for the macro- and microelectrodes. This was expected because it is known that there are driving interactions between the peptide chains and proteins, which are governed by energetical pathways and functional conformations [276].

Although there was a significant amount of signal decrease recorded for BSA or casein, no statistically significant difference between the substrate and control probe responses were observed, which confirms that the signal decrease in both cases was most likely due to non-specific binding, occurring, presumably due to the reduction in probe flexibility that hinders the redox tag - electrode interaction and therefore, the redox activity. This is in contrast to, the maximum signal decrease of ~36% (for macroelectrodes) and ~80% (for microelectrodes) recorded for substrate-modified surfaces upon the addition of trypsin, which was markedly

and statistically different to the relatively smaller response of the control-modified probe surface.

Additionally, another selectivity test was performed which both macro- and microelectrodes were incubated with one of the non-specific binding protein and the target enzyme trypsin at the same time. As illustrated in Figure 4.31, both macroelectrode and microelectrode were immersed in 1x PBS solutions including a non-specific protein (BSA or casein) and the target enzyme, trypsin, at the same time in order assess the sensor selectivity in complex environments. Macroelectrode-based sensor exhibited a clear trypsin selectivity in the media consisting of casein in addition to trypsin. However, contrarily, trypsin selectivity of the microelectrode-based system was higher in the media including BSA as non-specific protein. Although casein had a larger effect than BSA on miniaturised system, contrary to macroelectrodes, this can be explained by the more close-packed conformation of SAM layer on microelectrodes, which might be more prone to casein (~24 kDa) than BSA (~66 kDa) due to casein's smaller size. Still, this highlights the fact that the proposed microelectrode-based sensing system is highly selective towards trypsin, and that a combination of substrate and control measurements offering potential for direct measurements in real-world samples containing proteins.

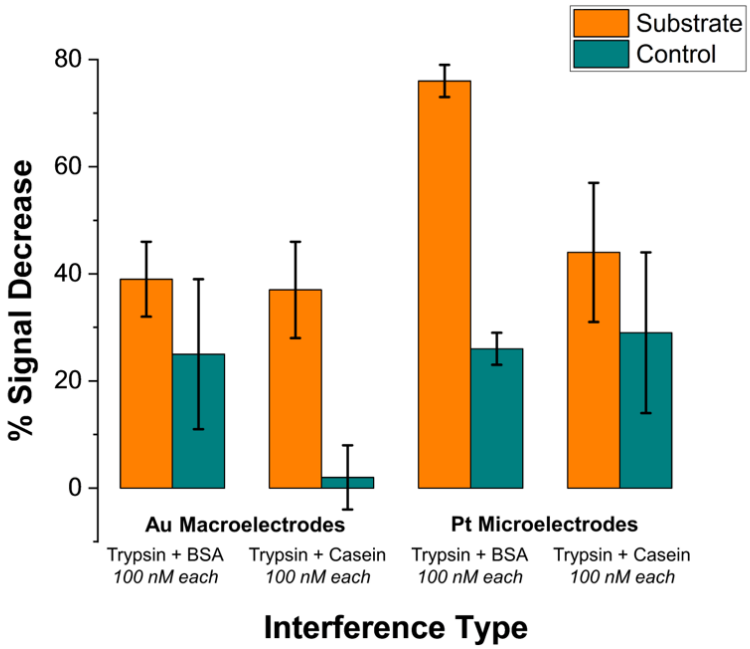

Figure 4-31: Comparative % signal decrease registered for SAM-functionalised Au macro- and Pt microelectrodes (after 70 min for macro and 900 min Pt micro) for upon the addition of 100 nM trypsin + non-specific binding protein; BSA or casein for both substrate- (orange) and control-modified (cyan) sensing layers. Average data and error bars are typically from 3 individual SAM sensing layers.

4.10 Effect of Temperature on SAM-functionalised Microelectrode Performance

It is known that temperature has an important role on the functional activity characteristics of most enzymes [277]. Therefore, the kinetics of proteolytic trypsin cleavage was determined on the microelectrode-based sensor not only at room temperature (25 °C) but also at the clinically relevant normal body temperature (37 °C). Figure 4.32A depicts the comparative signal decrease registered for both control- and substrate-modified microelectrodes at these temperatures with time. For both temperature cases, it is clearly seen that the signal decrease for the trypsin-cleavable substrate-modified electrodes is higher than the control-modified electrodes, which again demonstrates the trypsin selectivity of the sensor.

A higher rate of signal decrease (~30% after 200 min) was observed for the control-modified surfaces at 37 °C, compared to that (~10% after 200 min) registered at 25 °C, indicative of an enhanced detachment and loss of probe from the surface at these elevated temperatures. This is an additional process also present in the substrate-modified surfaces which, like trypsin cleavage, results in probe signal loss shown by subtracting the time dependent control-modified electrode response from that of the substrate-modified electrode. This was then converted to fractional cleavage, θ and A(t) following the same process as previously detailed in Section 4.8, but in this case normalised to the signal for these data as $t \rightarrow \infty$ at this value of [E] (Figure 4.32B). This shows the expected characteristic change in signal with time due only to probe loss arising from trypsin cleavage, as shown by the good fit to equation 4.3 (which is equivalent to equation 4.2, as this normalisation by definition fixes a as 1 in equation 4.3) (Figure 4.32B). This fit gives k_{eff} = 0.082 ± 0.004 min^{-1} at 37 ^{o}C, which is around four-times larger than the 0.021 ± 0.002 min^{-1} obtained at 25 ^{o}C. Using these values and the modified Arrhenius equation;

$$ln\left(\frac{k_{eff,\ T_2}}{k_{eff,\ T_1}}\right) = -\frac{E_a}{R}\left(\frac{1}{T_2} - \frac{1}{T_1}\right) \quad (4.6)$$

where k_{eff} is the effective rate constant, for T_1 or T_2 which are temperatures in Kelvin, R is the universal gas constant and E_a is the apparent activation energy of the reaction. E_a for this system was estimated as 87.2 ± 6.9 kJ/mol. This estimated value is comparable to the one determined for the BSA-trypsin model system, E_a = 64.8 kJ/mol [278], which also shows that reliable and consistent data can be recorded using this sensor platform. In addition, the enhancement in kinetics with increasing temperature is consistent with previously reported

work [279] and indicates the potential for markedly faster trypsin measurement in vivo on implanted microelectrodes.

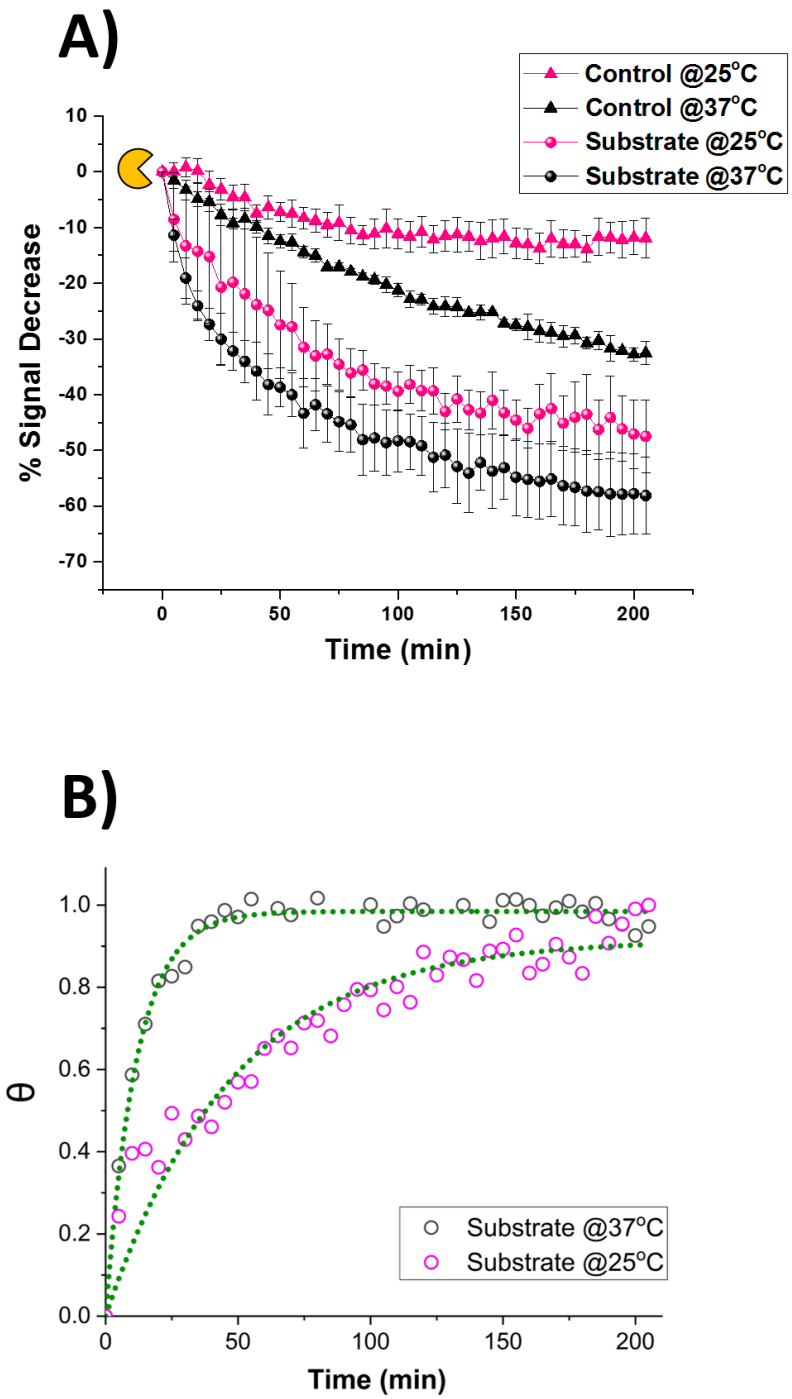

Figure 4-32: (A) Comparative signal decrease vs time curves registered for the miniaturised sensor upon the addition of 100 nM trypsin in 1x PBS at 25 °C (pink) and 37 °C (black) for both control- (triangle) and substrate-modified (circle) microelectrodes. (B) Calculated fractional cleavage, θ, vs time plots for control-subtracted substrate data from (A). The data points correspond to temperatures of 25 °C (magenta) and 37 °C (black) whilst the green dotted lines show the best iterative fits to equation (1) with k_{eff} = 0.021 ± 0.002 min^{-1} and 0.082 ± 0.004 min^{-1} respectively.

In addition to the enhancement in kinetics by controlling temperature, it should be noted that that uncontrolled temperature of the measurement environment might also influence the signal amount registered. Figure 4.33 illustrates the long-term stability of the tripod-anchored probes which have been immobilised on Pt microelectrodes. In order to investigate the effect of ambient temperature in the long-term stability of the probe-modified electrodes, two identical commercial Pt microelectrodes were modified with tripod-anchored substrate probes and interrogated with SWV for ~3 days (66 hours) after immersion into 1x PBS solution, without addition of any enzyme or other non-specific proteins. The temperature was recorded using a commercial data logger over the course of measurements. As depicted in Figure 4.33A, there was some difference in the initial signals registered for electrode-1 (~7.9 x 10^{-10} A) and electrode-2 (~4.6 x 10^{-10} A), although similar responses/currents were recorded during their electrochemical cleaning and then they were identically modified at the same time. However, it was not surprising as there was frequently a variation in the signals registered for identically prepared electrodes, which is attributed to the ambiguous nature of SAM formation. However, it is always possible to overcome this issue, by reporting the change in the signal as percentage, instead of its actual value, as presented in Figure 4.33B. By this means, lower deviations can be secured between the replicates. That is why the change in the signal has been reported as percentage value for all analyses presented through this thesis.

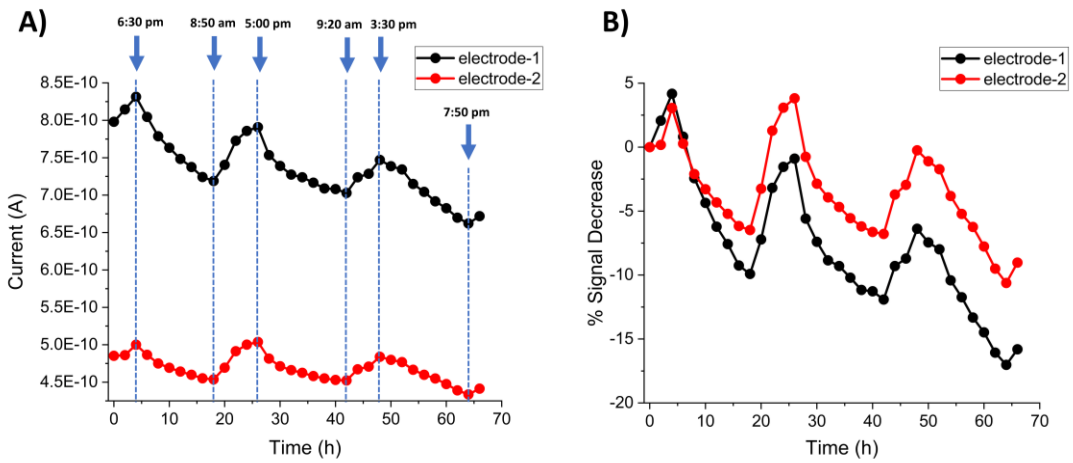

Figure 4-33: Long-term time-temperature-dependency of SWV signal recorded for probe-immobilised electrodes: A) SWV signal vs time and B) % signal change vs time registered for tripod-anchored probes immobilised onto two individual Pt microelectrodes (electrode-1 given in black circles and electrode-2 given in red circles), for ~3-day measurement. Blue dotted lines and arrows illustrates the transition points between signal increase-decrease fluctuations and corresponding times.

As explicitly produced by both identical electrodes, there were time-dependent fluctuations in the recorded signal. It was revealed that the signal consistently decreased at night and then increased during the day. It should be remarked at this point, the signal increase (during the day) was lower than the decrease (at night) for both electrodes, which resulted in an overall decrease of around 15%.

There was no external stimulator under ambient laboratory conditions except the temperature, which could result in these fluctuations. Therefore, the corresponding temperature data, which were recorded using the data logger placed inside the Faraday cage, was compared to the variations in the percentage signal. Although the data logger could not be located inside the buffer solution because of its non-waterproof characteristic, it was found that there is only a negligible difference between the buffer solution and the Faraday cage medium. Figure 4.34 shows a good correlation between the temperature and % signal decrease was observed and this confirmed that even the tripod-anchored probes which was previously characterised and found to have an improved stability against thermal, chemical and storage conditions [197], can face some issues related to stability/durability on electrode surfaces under uncontrolled measurement conditions. This exhibits the significance of controlled measurement parameters and it should be regarded as a motivation for the enhanced electrode development.

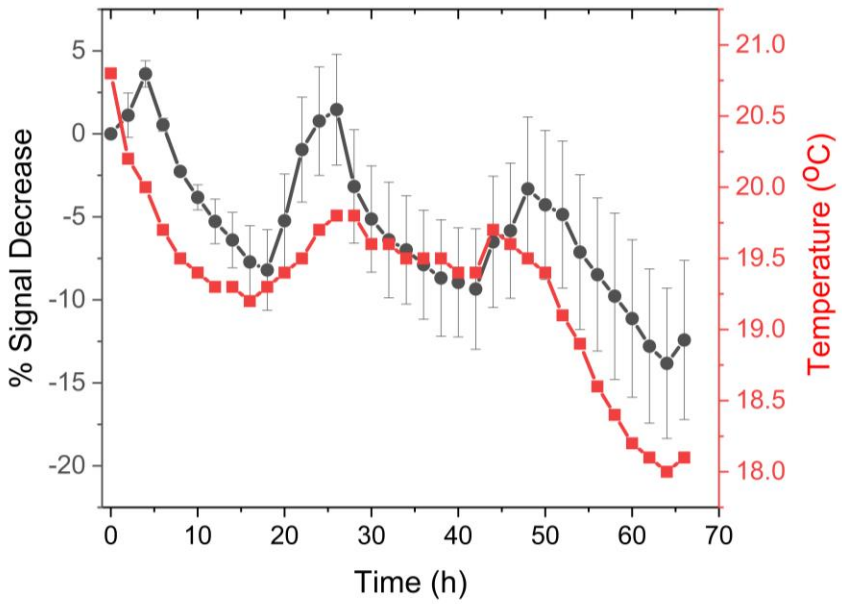

Figure 4-34: Long-term time-temperature-dependency of SWV signal recorded for probe-immobilised electrodes: % signal change vs temperature (°C) recorded over time using data logger for tripod-anchored probes immobilised onto Pt microelectrodes for ~3-day measurement. Average data and error bars are from 2 individual SAM sensing layers (electrode-1 and electrode-2).

4.11 Summary

In this chapter, the miniaturisation of a peptide-based electrochemical biosensor platform for protease detection using platinum microelectrodes is presented in comparison to the macroelectrode-based sensing. Using a previously developed detection mechanism based on the signal change due to the proteolytic cleavage of a peptide sequence followed by the removal of the redox tag by the enzyme, trypsin, some background work focusing on the probe optimisation has been step-by-step summarised. Then, analytical quantitative performances obtained for gold macro-, platinum macro- and platinum microelectrodes were evaluated, especially concentrating on the effect of miniaturisation on sensor performance. The ability of the proposed miniaturised electrode to support efficient trypsin detection was assessed and compared to the previously reported gold and new platinum results registered for macroelectrodes. These comparisons demonstrated the feasibility of using microelectrodes for these platforms as comparable analytical performance has been observed in terms of target accessibility and specificity, as well as insensitivity to the non-specific adsorption of proteins. The proposed system was also shown to give a quantitative response across the entire measured concentration range and fit well to a Michaelis–Menten surface cleavage model which enabled the estimation of global k_{cat} and K_M values. A LoD value of 2.9 nM was determined confirming that this sensing platform operates in a clinically relevant range for trypsin and suggests that this approach can be further applied to a wide range of proteases. The insensitivity of the sensor system to two potential interferent proteins shows its potential for measurement in complex media. The increase in temperature enhanced the kinetics and resulted in faster trypsin detection, although it caused a slight decrease in the surface stability of the probe. However, it is worth noting that the undesirable need for control data subtraction arising from the observed enhancement of probe loss at normal body temperature can be addressed by the use of a stronger tri-branched thiol anchor. Some important subjects for next chapters will be investigating the translation of these findings to electrode-on-silicon chips (in-house made) and the different methods which could be utilised for probe immobilisation onto the electrode surfaces.

Chapter 5

Translation to In-house Built Electrodes for Protease Sensing

5.1 Introduction

The background and main motivations of the biosensor miniaturisation were given in detail in Section 2.2.2. As part of this evolution, advancements in fabrication techniques have led to research activities in the miniaturising of the components of electrochemical devices such as electrodes. The advantageous reasons for this transition to smaller transducers are their higher sensitivity and selectivity as well as integration with electronics and their construction as implantable biosensors to enable *in vivo* measurements [280]. Also, decreasing electrode dimensions from mm to the µm or nm range offers enhancements such as increasing signal-to-noise ratios. Analyte LoDs which are measured using miniaturised electrodes are enhanced or at least comparable to those obtained using commercial macroelectrodes [281]. That is why both micro- and nanoelectrodes are being used in a wide range of applications in many fields of analytical sciences today.

Reproducible microelectrode fabrication has improved over time due to the emerging photolithographic methods used in the semiconductor industry. These improvements have been extremely important in producing high-fidelity and reproducible electrodes with well-defined shapes and dimensions [282]. This has enabled microelectrodes to be fabricated with various geometries such as cylinders, discs, cones, bands and hemispheres. Among all these different geometries, metal disc electrodes which are encapsulated in insulator materials (such as glass/plastic) are the most favoured because of their ease of production and established quantitative analytical response [283]. Some examples of areas where microelectrodes have been used are sensors [284], biosensors [285], scanning electrochemical microscopy (SECM) [286], microfluidic devices [287] and liquid chromatography [288]. As a local example, the IMPACT team at the University of Edinburgh (Section 2.2.1) has recently measured dynamic intestinal oxygenation changes, in real-time, in a rodent model using a miniaturised oxygen sensor which consists of a three-electrode cell with a platinum working and counter-electrodes and a silver/silver chloride reference electrode on a silicon chip [109].

Following these successes, there has been a need for the preparation of more sensitive, new generation electrodes which could be able to detect very small members of molecules, and this constitutes the main driving force for the development of nanoelectrodes [289]. They offer even more advantages over microelectrodes in terms of improved mass transport, signal-to-noise ratio and sensitivity as detailed in Section 2.5.3. In addition, they do not typically include surrounding materials unlike glassy commercial bulk electrodes which restrain their use in defined spaces, and which is a vital limitation for localised *in vivo* measurement

compatibilities. It has been also suggested that they are more preferable platforms than commercial macroelectrodes because of enhancing accessibility to analytes, and not being limited by time-dependent planar diffusion [283]. Reproducible and robust nanoelectrode fabrication is more challenging and is not fully established, but they have been widely used and sufficiently well-understood. They are much more sensitive to even small variations in their geometry, size, shape and surface chemistry [289]. Therefore, a person who targets a particular nanoelectrode application should be careful and specific when considering the fabrication process.

There are various methods existing for fabrication. The first type of nanoelectrode was fabricated as a nanoband (with widths between 2 - 50 nm and lengths between 0.5 - 1 cm) in 1987, by Au/Pt metal evaporation [290]. Typical nanoelectrode preparation techniques include photolithographic fabrication, electroless/electrochemical metal deposition, templated production, laser-assisted pipette pulling and many others [291]. In templated production, nano-porous solid structures can be used as templates for the deposition of metallic layers which can then serve as nanoelectrodes and nanoelectrode ensembles where their dimensions can be controlled by the pore sizes [291]. Some examples of previously employed templates include polycarbonate and polyester membranes [292] [293], anodic aluminium oxide [294], zinc oxide [295], carbon nanotubes [296] and tetraethoxysilane sol-gel films [297]. In parallel with these expanded production practices, there are many different applications within the range of nanoelectrode utilisation such as the detection of neurological diseases by using neurochemical sensors [298], hypertension monitoring [299], DNA [300] and glucose [301] detection as well as *in vitro* analysis of the cell medium for reactive oxygen and nitrogen species [302]. Moreover, the Mount Research Group at the University of Edinburgh has also developed experience in the photolithographic fabrication and fundamental understanding of analysis of microcavity nanoband edge electrode arrays (MNEE) which offer similar but enhanced reproducible steady-state response to nanoelectrodes [187], [203], [303]–[306].

Of course, there are some possible drawbacks with downscaling in electrode dimensions. These include (i) smaller amounts of current generated, (ii) potential of (liquid) probe/sample evaporation during preparation/analysis because of their reduced volumes if nanolitres used and (iii) the risks of inaccessibility of analyte resulting from geometrical restrictions [283]. In order to resolve these problems, most of the micro- and nanoelectrode architectures are fabricated in arrays, instead of individual electrodes. Thus, they can generate higher signals by combining each array response in parallel as well as reducing evaporation and inaccessibility risks owing to the enlargement in the sensing (array of electrode) region.

However, it is important in this case to preserve the enhanced mass transport characteristics while multiplying the number of electrodes. Controlling and finding the optimum interelectrode spacing is quite significant here, to avoid any overlapping of diffusion layers whilst maximising signal. Therefore, photolithography is typically easier compared to the templated production such as utilisation through pores which makes it hard to control.

Although there are some examples of the use of microelectrodes [228] and nanoelectrodes [307] in peptide-based protease sensing, the literature still lacks a systematic study of the effects of miniaturisation. Peptide-based sensing probes used throughout this work have been attached onto electrode surfaces as SAMs. Considering that the characteristics of SAMs might have deleterious effects on the biosensors performance [308] and the influence may be much more important on a miniaturised system than on a commercial macro-scale sensor, understanding the miniaturisation effects in terms of SAM formation and the effects on resulting response is crucial.

This chapter seeks to address these questions, by investigating how an electrode type or dimension effects the preparation and performance of a peptide-based electrochemical protease sensor. As a follow-up of the work on sensor miniaturisation using commercial bulk microelectrodes in Chapter-4, this will cover various established platinum in-house built designs (as thin films on a silicon substrate) such as single microelectrodes with thin (TT) and superthin (STT) contact tracks, microelectrode arrays (MEA), microcavity nanoband edge electrode arrays (MNEE) and macro-scale metal films. It will analyse any observed difference between all these electrode designs or dimensions in terms of electrochemical response against either common redox agents (bare electrodes) or trypsin enzyme (target protease) (SAM probe-modified electrodes). Altogether, the aim of this chapter will be to produce a systematic study of these effects to inform the sensing strategies based on miniaturised electrodes.

5.2 Thin Track and Superthin Track Single Microelectrodes

In order to translate findings achieved for commercial platinum microelectrodes given in the previous chapter to in-house built platinum electrodes, initially two designs were fabricated and characterised in terms of cleaning, preparation and protease detection performance. They were single disc microelectrodes of varying diameters, with thin (TT) and superthin (STT) contact tracks. Although there is no different fabrication process step involved in their production, they might be expected to show different track resistances (which should be

greater for STT compared to the TT microelectrodes) between the electrodes and the contact pads, due to having this particular contact track arising from the different masks used for photolithography during fabrication. However, differences between them in terms of characterisation (as bare electrodes) and performance (as functionalised biosensors) should not be expected, because exposed electrode surfaces are expected to be identical. Their fabrication process chain and all other details of involved steps are given in Section 3.3.2 and Appendix-1.

5.2.1 Cleaning

Comprehensive cleaning of electrode surfaces is very important in electrochemistry, to achieve reproducible and consistent measurements. That is why a fresh electrode surface which is free of any residue is needed before any individual measurement. Typically, a three-step cleaning process is used for commercial (plastic or glass insulator-encapsulated) macro- or microelectrodes, consisting of

(i) concentrated acid treatment
(ii) mechanical polishing with alumina slurries
(iii) electrochemical cleaning in a dilute acidic solution

as these have been shown to avoid any impurities on an electrode surface [309]. Specifically, applying a cycle of potentials repetitively in electrochemical cleaning in acidic solutions was reported to activate the surface due to the formation and reduction of metal oxide films, local pH changes (oxidation/reduction) as well as the mechanical act of the bubbles of gases produced, H_2 and O_2 [182]. Unfortunately, some of these steps such as mechanical polishing or concentrated acid treatment are inappropriate for microfabricated thin film electrodes as they are sensitive to rough treatment and strong acid/base solutions [310]. For example, only a thin (~500 nm) silicon nitride layer is formed as the passivation layer in TT and STT single microelectrodes, which might be easily cracked or worn when mechanically polished. Besides, immersing them into concentrated acids for 10 min might change their surface chemistry significantly and irreversibly. Therefore, electrochemical cleaning was considered the best option to clean a microfabricated electrode surface.

Cyclic voltammograms (CVs) of platinum TT and STT single microelectrodes of various sizes recorded in 0.1 M sulfuric acid are shown in Figure 5-1. Each individual CV shows the 20^{th} in

a set number of repetitive CV scans and for a specific type (TT or STT) and diameter (20, 50 or 100 µm) disc electrode. In general, each cleaning CV were seen to be comparable to each other in terms of previously seen characteristic features for commercial platinum microelectrodes (Section 3.4.1). The first significant feature to note is the oxygen formation (as surface-adsorbed and/or platinum oxide) peak around +1.55 V which increases for electrodes with successively larger areas, as expected. Interestingly, the oxygen formation peak of TT 100 µm electrode was not significantly larger than TT 50 µm and was not similar to STT 100 µm. However, there was the expected correlation between the electrode size and intensity of the oxygen reduction wave at ~0.30 V for both STT and TT microelectrodes.

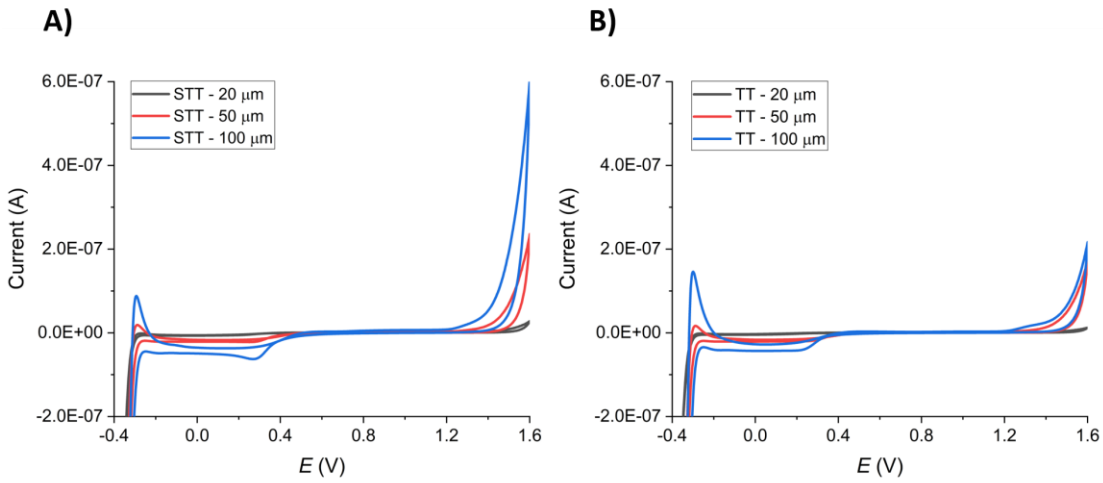

Figure 5-1: CVs of Pt A) superthin track (STT) and B) thin track (TT) microelectrodes of various sizes recorded in 0.1 M H_2SO_4 between -0.35 and +1.6 V at a scan rate of 100 $mV.s^{-1}$. Each scan corresponds to the 20^{th} cycle of electrochemical cleaning.

One possibility is that an electrode surface could be qualified as clean if there is no further change in the heights/areas of these characteristic peaks as the scans progress. Figure 5-2 presents the 20^{th} and 1000^{th} CVs, in comparison, of a TT 20 µm microelectrode recorded in 0.1 M H_2SO_4. It is seen that there is an almost three-fold difference in the height of oxygen evolution peaks obtained after 20^{th} and 1000^{th} scans, as well as an additional peak around +1.35 V after 1000 scans. This can be attributed to the electrode roughness which increased with time. Because, the re-formation mechanism of Pt from Pt oxide results in an expansion and increase in Pt surface area. Adsorption is determined by this peak. However, it should be emphasised that oxygen reduction peak at ~0.30 V was similar even after 1000 scans. Because there was no increase in geometric (cross-sectional) area, which determines mass transport. Considering this dependency on the electroactive area of the electrode, the necessity for longer

time cycling becomes questionable. In addition, keeping the electrode surface in acidic solution, even it is diluted, more than enough is a high potential of causing surface roughness to increase which would not be preferred for most of the probe-based biosensing applications. It should be also noted that 1000 scans take approximately 11 h to complete at a scan rate of 100 $mV.s^{-1}$, whereas 20 scans take 13 minutes. This makes 20 CV scans more preferable for electrochemical cleaning and thus typically applied for the rest of the study, because a clean electrode with constant surface roughness was intended.

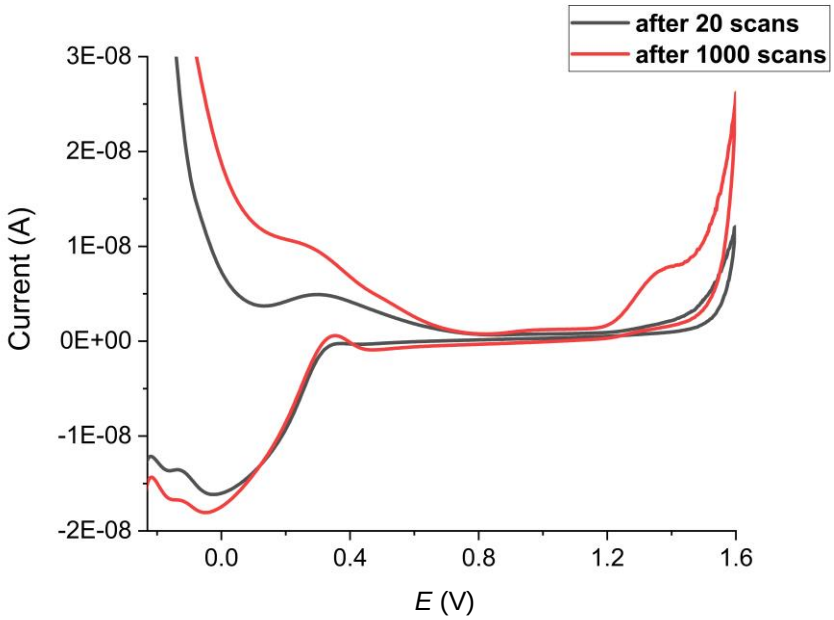

Figure 5-2: Comparative cleaning CVs of Pt TT 20 µm recorded after 20 (black line) or 1000 (red line) scans in 0.1 M H_2SO_4 between -0.35 and +1.6 V at a scan rate of 100 $mV.s^{-1}$.

5.2.2 Characterisation

The best way to characterise a clean bare electrode is to obtain a cyclic voltammogram using a common redox agent which can be reduced and oxidized reproducibly on an electrode surface. The shape of the recorded voltammograms using micro- or nanoelectrodes which have much smaller sizes typically differ from the ones obtained for macroelectrodes which are in the mm range. Usually a characteristic sigmoidal shape is obtained for micro- or nanoelectrodes whereas peaks are obtained for macroelectrodes. The reason for this difference and its relation to mass transport and diffusion are explained in Section 2.5.3.

Cyclic voltammograms for commercial bulk and STT platinum microelectrodes of varying diameters recorded in 5 mM potassium ferri/ferrocyanide in PBS at a scan rate of 100 $mV.s^{-1}$ is given in Figure 5-3. As clearly seen, there is the expected correlation between current and electrode size. Also, the current obtained for 30 µm-diameter STT electrodes is the same with the commercial bulk electrode which has a diameter of 25 µm, which shows that in-house built electrodes can present similar electrochemical performances to commercially-available electrodes.

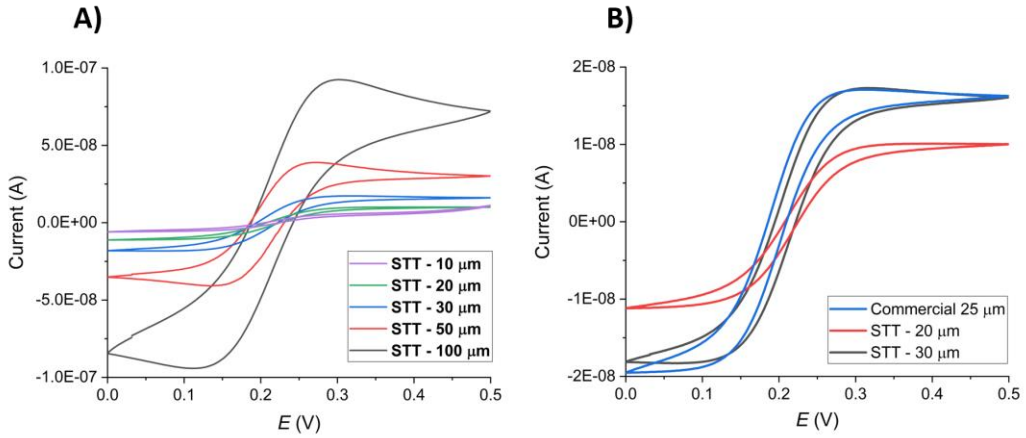

Figure 5-3: CVs of various Pt microelectrodes of different diameters recorded in 5 mM potassium ferri/ferrocyanide in 1x PBS between 0 and +0.5 V at a scan rate of 100 $mV.s^{-1}$: A) STT (10, 20, 30, 50 and 100 µm) and B) commercial (25 µm) and STT (20 µm and 30 µm).

When STT and TT microelectrodes were compared, it was observed that they exhibited the same responses within experimental errors, in terms of voltammogram shape and currents registered. This was also consistent with the electrochemical cleaning observations. This was attributed to identical electroactive areas of comparable STT and TT microelectrodes. In addition, characteristic waves were observed for all electrodes and most of the sizes except STT 50 and 100 µm. This was already expected for microelectrodes due to hemispherical diffusion and enhanced mass transport. The reason why voltammograms of STT 50 and 100 µm showed peaks instead of waves was their larger electrode areas compared to others, which resulted in partially macroelectrode response at these scan rates.

In order to check how the current responses and CV shapes change with respect to the scan rate, STT 100 µm was subjected to the cyclic voltammograms recorded at varying scan rates of 10, 50, 100, 200, 300, 400 and 500 $mV.s^{-1}$, as depicted in Figure 5-4. Again, mostly peaks were observed only except the voltammogram recorded at 10 $mV.s^{-1}$ which was more like a

sigmoidal response. It was expected because of that slower scan rates promotes the hemispherical (radial) diffusion and steady-state behaviours to be seen, whereas the linear (planar) diffusion is favoured under higher scan rate conditions [184]. In addition, the investigation of the dependence existing between the recorded peak current and the scan rate, revealed that the mass transport for STT 100 µm was dominated largely by planar diffusion.

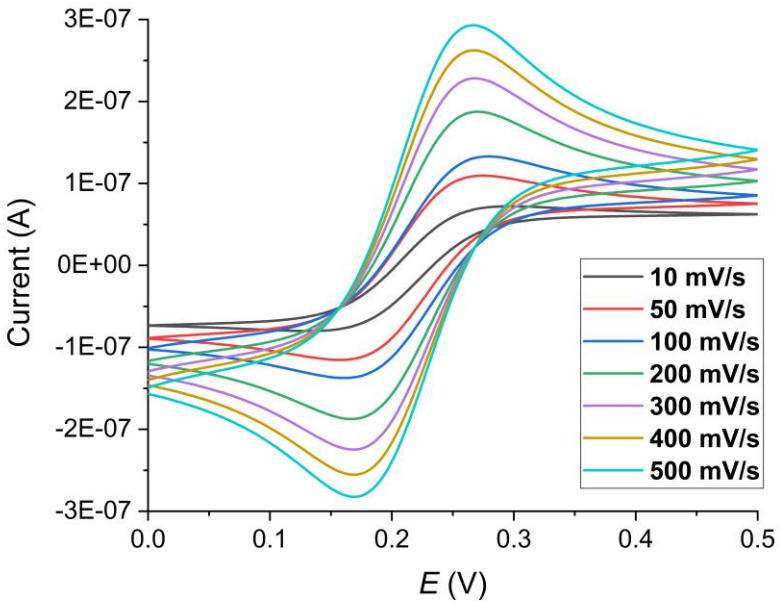

Figure 5-4: : CVs of STT 100 µm recorded with varying scan rates (10, 50, 100, 200, 300, 400 and 500 $mV.s^{-1}$) in 5 mM potassium ferri/ferrocyanide in 1x PBS between 0 and +0.5 V.

To make a quantitative evaluation using these electrodes, Saito equations [283], [311] (Section 2.6.1) were used to calculate the experimental diffusion coefficient of potassium ferri/ferrocyanide in 1x PBS, for a disc-shaped (used for in-house built STT) and hemisphere-shaped (used for commercial) microelectrodes, respectively;

$$i_L = 4nFDCr \tag{5.1}$$

$$i_L = 2\pi nFDCr \tag{5.2}$$

where *n* is the number of electrons (which is equal to 1 for ferri/ferrocyanide), *F* is the Faraday constant, *D* is the diffusion coefficient (cm^2/s), *C* is the concentration (mol/cm^3) for redox molecule (ferri/ferrocyanide) in the solution and *r* is the radius (cm) for the electrode. Using these two equations (Equation 5.1 for in-house built and Equation 5.2 for commercial bulk microelectrodes), experimental diffusion coefficients of potassium ferri/ferrocyanide were

found to be 6 x 10^{-6} cm^2/s for STT 10 µm, 6 x 10^{-6} cm^2/s for STT 20 µm, 6 x 10^{-6} cm^2/s for STT 30 µm, 8 x 10^{-6} cm^2/s for STT 50 µm, 10 x 10^{-6} cm^2/s for STT 100 µm and 7 x 10^{-6} cm^2/s for commercial (25 µm) microelectrodes. In comparison to its literature value reported as D = 7 x 10^{-6} cm^2/s at ambient temperature [312], it can be suggested that all gave the comparable results to the previously estimated value with little differences which most likely resulted from the variations in uncontrolled temperature of measurement environment.

All these demonstrate that in-house built single microelectrodes exhibit expected characteristic features which are comparable to commercial microelectrodes. Therefore, they are ready for performance characterisation in the detection of proteases.

5.2.3 Performance in Protease Detection

5.2.3.1 Experimental

In order to evaluate the analytical performance offered by the in-house built single microelectrodes in protease sensing, four individual electrodes (STT 20 µm, STT 50 µm, STT 100 µm and TT 100 µm) were selected and modified with the mixed SAM layer as previously described. However, the mixed SAM probe layer was incubated on the electrode surfaces by drop-casting in this case, instead of dip coating, because of that the electrode geometry was created as a Pt thin film on a planar Si chip which is significantly larger in area than commercial bulk microelectrodes (See Section 3.3). Also, by this means, probe solution volumes could be reduced, saving probes for future trials and thus allowing more experiments. In preliminary tests, it was found that the probe solution prepared in ethanol, as used for commercial electrodes (Section 3.4.2.1), evaporated over time during an overnight incubation, leaving a dried liquid mark on the in-house built electrode surfaces. This was not observed for commercial electrodes, because they were dip coated into solution inside parafilm-sealed tubes, but this would lead to excessive consumption of probe for in-house electrode designs, as these designs are not cylindrical, the electrode is not located at the bottom of the chips and thus would require more solution to fill the tube to cover the whole electrode surface during dip coating. Therefore, the probe solutions were prepared in 1x PBS, instead of ethanol, to avoid this evaporation. Control tests on commercial microelectrodes showed that the SWV signals recorded for the electrodes incubated with probe solutions prepared in PBS were in a similar current range to the electrodes prepared with ethanolic solutions, confirming that change of the solvent had no apparent effect on the formation of self-assembled monolayers

in this case. There was not any other change in protocol except this. The molecules used and the concentrations present in the mixed SAM solution used for commercial microelectrodes (Section 4.6) were kept the same for these electrodes.

5.2.3.2 Response

Figure 5-5 shows the percentage signal changes for STT 20 µm, STT 50 µm, STT 100 µm and TT 100 µm electrodes after they were SAM modified with either the substrate or the control probe, immersed in buffer (1x PBS) solution containing 100 nM trypsin and interrogated by SWV with time. It is clearly noticeable with that none of the electrodes modified with the control probe gave the expected stability with time. The initial rapid signal decrease for the control-modified STT 20 µm and TT 100 µm was ~90-100%, whereas it was around 30% for STT 50 µm and STT 100 µm which increased with time, up to ~60-90%. Unexpectedly, the signal decrease observed for control-modified STT 20 µm, STT 100 µm and TT 100 µm was higher than for substrate-modified analogues. Although the expected response (the signal decrease recorded for control-modified electrodes was lower than substrate-modified ones) was observed for STT 50 µm, the difference after 900 min was only around 15-20%.

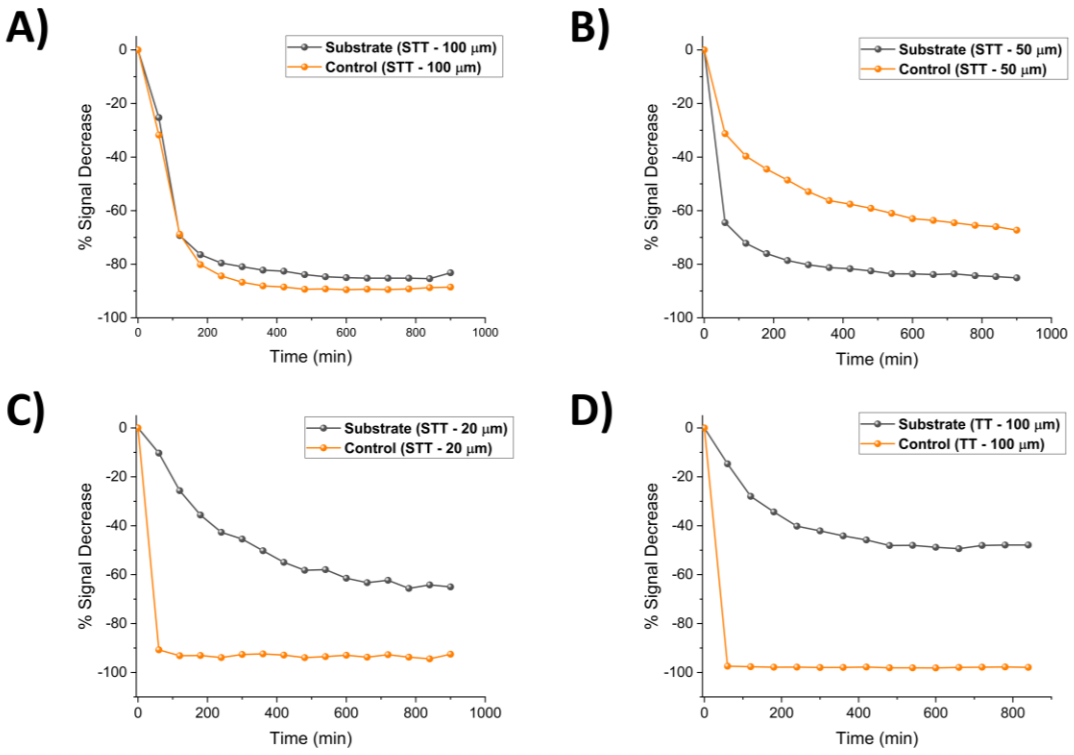

Figure 5-5: Plots of % signal change vs time upon addition of trypsin 100 nM (at time = 0) for SAM-functionalised substrate (black circles) and control (orange circles) probes immobilised onto Pt microelectrodes: A) STT 100 µm, B) STT 50 µm, C) STT 20 µm and D) TT 100 µm. SWV data used for the preparation of this figure can be found in Appendix-4.

This was very low in comparison to the difference (~70%, Figure 4-21) obtained when using a commercial Pt microelectrode and these, of course, raises an issue with the robustness/stability of the sensor system when utilising these types of electrodes.

In order to understand the underlying problem, a similar experiment was designed after preparing and conditioning the electrodes. This time no trypsin was added into the 1x PBS solution. As illustrated in Figure 5-6, there was again an almost immediate decrease in the signal recorded for the control-modified STT 100 µm. Though it was not as immediate, and more gradual, it was still significant at around 50-60% for the control-modified STT 50 µm and TT 100 µm. Also, the total decreases recorded for three electrodes when modified with the substrate probe were found to be between 40% and 60%. Given this is not correlated with enzyme cleavage, the most likely reason is loss of the probes from the surface. The behaviour observed for STT 20 µm was dissimilar to the others. The signal decreases shown for both the control-modified and the substrate-modified analogue STT 20 µm electrodes fluctuated over time, but did not drop significantly. In fact, in this case, even an increase in the signal was observed for a time course of ~200 min for the control-modified electrode, which was very likely due to the ongoing reorganisation of self-assembling structures on the surface.

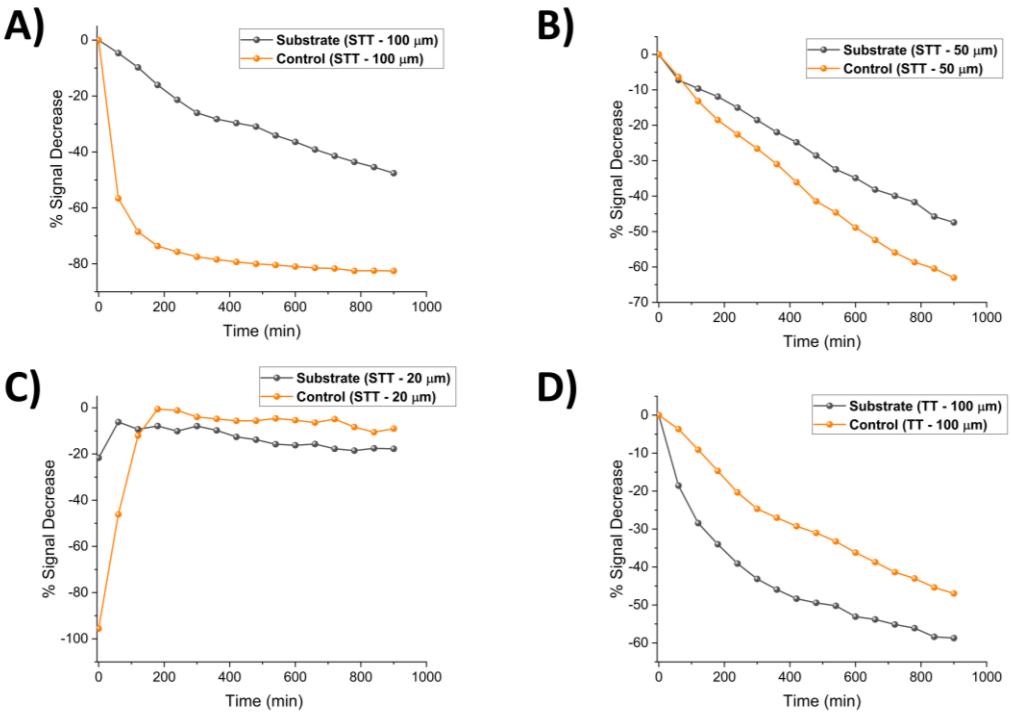

Figure 5-6: Plots of % signal change vs time with no addition of trypsin for SAM-functionalised substrate (black circles) and control (orange circles) probes immobilised onto Pt microelectrodes: A) STT 100 µm, B) STT 50 µm, C) STT 20 µm and D) TT 100 µm. SWV data used for the preparation of this figure can be found in Appendix-4.

The comparative analysis of two experiment sets demonstrated that the signals did not go down only because of the protease cleavage. In a nutshell the major signal stability problem arose either from the probe or the electrode surface, given that the real expectation for this test performed without an enzyme was to see a stable, constant signal, independent of SWV interrogation time.

Figure 5-7 shows the optical images taken from STT 20 µm, STT 50 µm, STT 100 µm and TT 100 µm electrode surfaces respectively, after experiments which included the 900 min-trypsin incubation. As can clearly be seen in the figure, there were some different features on the surfaces, and it was thought that they might have played a role in the durability problems encountered. First, the upper side of the electrode region of STT 20 µm showed some metal loss, which was spread in smaller pieces. For STT 100 µm, although the electrode itself has not been damaged, there was a thin delamination on the perimeter of the insulator, which might have expanded the electrode size and it thus gave a macroelectrode response some time later even if it was not at the time when images taken. STT 50 µm and STT 100 µm electrodes also showed some minor hollows in little speckles, however it can be seen they were already existing even prior to use, in Figure 3-9. They are thought to be inevitable features which are sporadically observed after the etching process in microfabrication. In addition, some fibre-shaped features have been found on STT 50 µm and TT 100 µm surfaces.

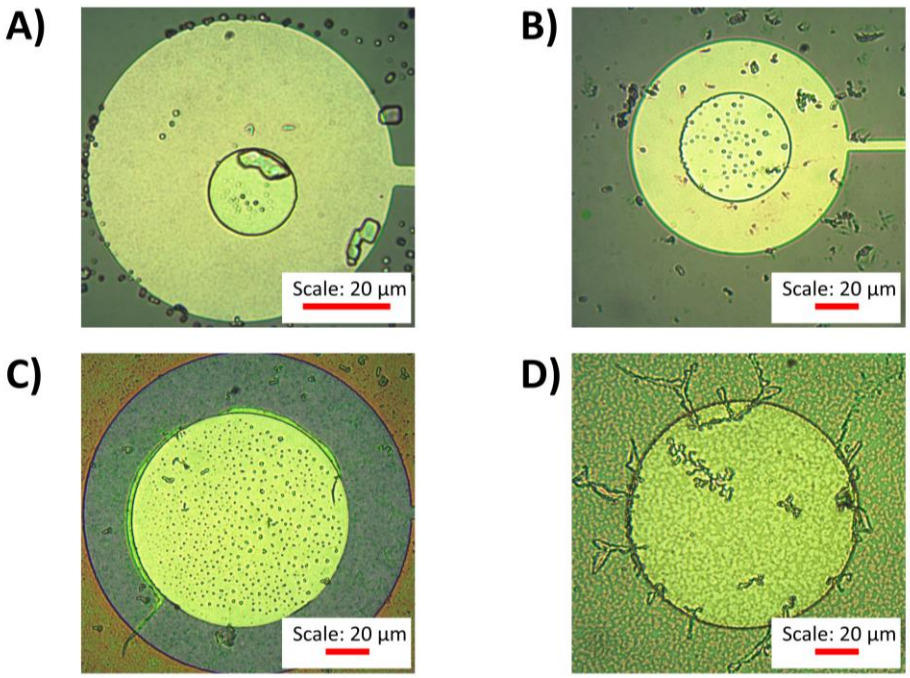

Figure 5-7: Optical microscope images of Pt microelectrodes: A) STT 20 µm, B) STT 50 µm, C) STT 100 µm and D) TT 100 µm following the immobilisation with SAM-functionalised probes, incubation with 100 nM trypsin for 900 min and electrochemical cleaning in H_2SO_4 afterwards.

As these electrodes were cleaned electrochemically before SAM probe deposition, and then washed with PBS and water after trypsin experiments, they cannot be dust or individual probe molecules either, considering the low resolution of the current optical microscopy. Because they were located on the insulator just outside the electrodes, it is likely that some of them might be clusters of thiol-based residues, which could not be electrochemically cleaned and thus accumulated over time. Briefly, some of these effects may have happened during initial electrochemical cleaning, and some of them during SAM formation. All these can positively contribute to the thought of electrode-related adverse effect on SAM probe stability.

In order to fully characterise the performance of in-house electrodes in protease sensing and investigate the advantages and drawbacks, electrode types tested were broadened using different alternatives. IMPACT miniaturised three-electrode on-chip design was one of these alternatives. As illustrated in Figure 5-8A and 5-8B, it consists of all the working, the reference and the counter electrodes (in order from inside to outside) patterned on the chip. There was no major difference in the fabrication protocols of this three-electrode chip and single microelectrodes. Only the working electrode (WE, with a diameter of 50 µm) was used for the characterisation, using an external Pt counter and an external Ag/AgCl reference electrode as usual, to make a fair comparison between the performances of electrodes characterised within the scope of this chapter. Therefore, the reference electrode was patterned but not fabricated on this chip, although it could be successfully fabricated for *in vivo* applications by first silver plating and then chlorination processes [109]. Besides, mixed SAM probe solution was drop-cast on all electrodes inevitably since there was no any protecting layer on top of the reference and counter electrodes. It did not pose any problem in this case as only WE was used. However, in a real implanted biosensor application, counter and reference electrodes should be protected by coating and patterning a solution-etchable layer (photoresist etc.) on top of them prior the probe immobilisation and then removed and activated afterwards, not to alter surface chemistry of the reference electrode and/or block the counter electrode. Cyclic voltammograms recorded in 0.1 H_2SO_4 for electrochemical cleaning of the electrode, prior to immobilisation with the probe, were consistent in comparison to the characteristic voltammogram of a commercial Pt microelectrode, given in Figure 3-11. The two-fold differences between their diameters (25 µm for commercial microelectrode and 50 µm for this electrode) lead to an increase in the oxygen evolution peak at ~1.55 V to nearly 4-fold, as expected. Figure 5-8D shows the performance of the WE of this device for protease sensing, by concentrating on the analysis of the substrate-modified and the control-modified analogue with incubation with 100 nM trypsin (added at time = 0), as well as a substrate-modified analogue without the addition of trypsin. The signal decrease for the substrate-modified

electrode after incubation with trypsin for 900 min was found to be 85%, whereas it was around 60% for the control-modified analogous. This difference clearly offers the selectivity of the substrate-modified electrodes against trypsin. However, the recorded signal decrease for the control sample was again above the expectation. It was significant to understand if this was due to either a degree of non-specific binding of trypsin enzyme to D-amino acids in the control probe or a recurring stability issue. The additional data gathered without any trypsin showed a signal decrease of ~40% for a substrate-modified electrode and revealed that the effect of the stability problem was more severe than non-specific binding, although non-specific binding also should be borne in mind as a point in question since the decrease (60%) recorded for control probes with enzyme found to be higher than 40%.

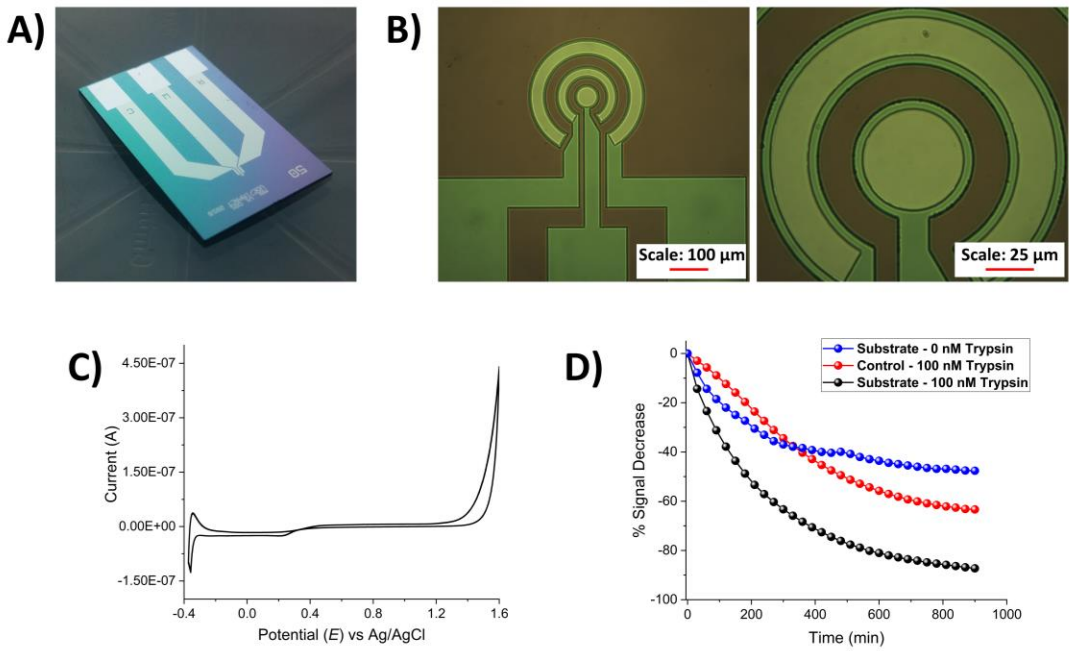

Figure 5-8: Conformance testing of the working electrode (WE) of the miniaturised three-electrode system on-chip with usual electrode preparation protocol and trypsin sensing. A) Macroscopic image of the miniaturised three-electrode system on-chip with WE of 50 µm-diameter. B) Optical microscope images showing the region for the electrodes on the chip. C) Electrochemical cleaning CV of WE in 0.1 M H_2SO_4 between -0.35 and +1.6 V at a scan rate of 100 $mV.s^{-1}$. D) Percentage signal change registered upon addition of trypsin 100 nM for substrate (black circles) and control-modified (red circles) probe immobilised electrodes, as well as substrate-modified probe immobilised electrodes with no addition of trypsin represented in blue circles.

The characterisation of this different electrode type e.g. WE of the miniaturised three-electrode system on-chip in terms of the response against trypsin showed that the experience of stability issue was not only for the STT or TT single microelectrodes as a one-off, production batch-induced issue. Also, it cannot be attributed to the electrode size as well, because it was experienced for various diameters of 20, 50 and 100 µm. Instead, this should be considered as a serious problem which needs to be resolved to successfully translate SAM-based biosensing into the silicon-on-chip technologies.

5.2.4 Effect of Increasing Anchor Strength: Tripod-Anchored Probes

As previously reported [197], [253], [313] and also discussed in Section 4.3.5, multiplied anchors can improve the stability/durability of probe molecules on electrode surfaces. For this reason, the effect of using a tripod-anchored analogous probes instead of the mono-anchored ones was investigated on STT 50 µm, STT 100 µm and TT 100 µm electrodes, as shown in Figure 5-9. The data labelled here as mono-anchor were discussed in Figure 5-6. This experiment was also performed without an enzyme, to focus solely on potential stability improvements and avoid any effect of non-specific binding or proteolytic cleavage. In all three individual electrodes, the tripod-anchored probes provided slightly improved stability in comparison to the mono-anchor materials. Still, there was a similar immediate decrease of at least ~20% in the signals registered for all three electrodes. This further confirmed and established the stability problem even if the anchoring capabilities of the probe structures have been enhanced. It is also worth noting that the signal decrease recorded for tripod-anchored probe was observed over different time points, which were ~200 min for STT 50 µm and TT 100 µm, and ~400 min for STT 100 µm. The decreases after these time points were negligible for the tripod-anchored probes, whereas the decreases in the signals were continuous until the final time points for the experiments for the mono-anchored probes. Interestingly, the signal recorded for TT 100 µm went down over ~200 min and then increased after this time. This can be explained by the orientation and/or re-organisation of the anchor(s) in the multi-dentate probe onto the surface, which might have inhibited the electron transfer between the methylene blue and the electrode for a while. This may have resulted in the signal decreasing until a time point when stabilisation on the surface was complete and the electron transfer was recovered. In addition to these, comparison of the responses observed for TT 100 µm and STT 100 µm revealed a significant variation between the electrodes, whereas they are expected to be identical.

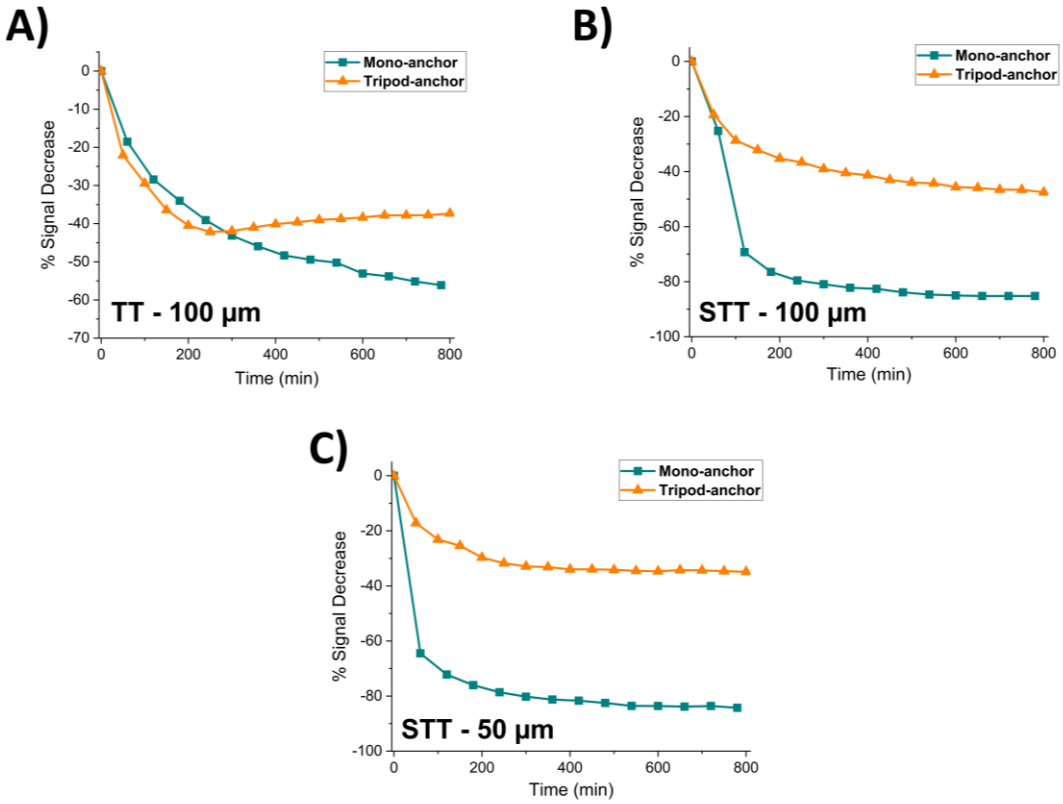

Figure 5-9: Percentage signal change registered for mono- (cyan) and tripod (orange)-anchored probes when immobilised onto A) thin track (100 µm-diameter), B) superthin track (100 µm-diameter) and C) superthin track (50 µm-diameter) electrodes and interrogated with SWV in 1x PBS for 800 min to check and compare the stability.

Although some of the above-mentioned results taken from tripod-anchored probes might be seen as promising, the recorded signal decreases for the in-house electrodes were still higher than commercial microelectrodes when they were modified with the same tripod-anchored probes. Figure 5-10 shows that the signal decrease observed for commercial microelectrodes was only around 10% after 800 min SWV interrogation and were almost stable after 50th min over the same experiment. This suggests that they can be used effectively to enhance the stability on the commercial electrodes, but not effectively on the in-house built electrodes. Given the fact that more or less stability problems were experienced regardless of the improvements in the probe, it was established that the source of the problem is substantially electrode-based and further advancements/changes in their fabrication are needed to overcome these drawbacks.

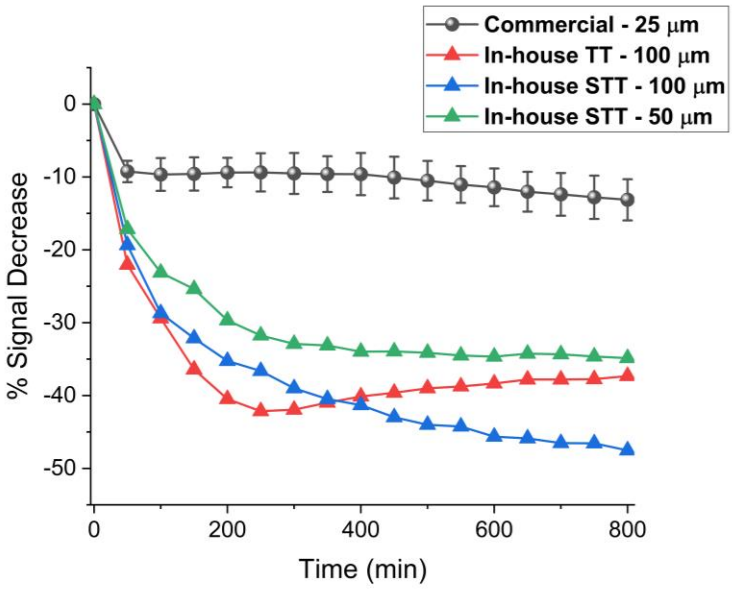

Figure 5-10: Percentage signal change registered for tripod-anchored probes when immobilised onto commercial bulk microelectrodes (black line and circles), compared to the stability of thin track and superthin track microelectrodes shown in Figure 5-9, and interrogated with SWV in 1x PBS for 800 min.

5.2.5 Effect of Increasing Platinum Film Thickness

In the previous section, it was emphasised that the stability of SAM-based probes was found to be better for commercial bulk electrodes, compared to the in-house built, thin film electrodes. Considering they are significantly different in terms of the amount and metal layer thickness of the Pt electrode material; this difference was proposed to be an important parameter effecting the stability/durability of the electrodes. Therefore, thicker films with a Pt layer thickness of 200 nm were fabricated in-house and characterised, as an alternative to TT or STT microelectrodes (which include a Pt layer of 50 nm-thickness).

As depicted in Figure 5-11A, these electrodes were fabricated by depositing adhesion (Ti) and electrode metal (Pt) blanket layers onto Si chips (with dimensions of 35 mm x 7.50 mm x 0.55 mm). They are named as "Pt blanket films" for the rest of this work. In contrast to the TT and STT microelectrodes, the size of the electrode region was not defined, because they were not patterned (using photolithography) or coated with an insulator silicon nitride layer in order to simplify the fabrication process.

Figure 5-11B shows that all three identical Pt blanket replicates consistently exhibited characteristic Pt features when they were electrochemically cycled (cleaned) in 0.1 M sulfuric acid. A sharp metal oxide reduction peak near +0.4 V (instead of the typical oxygen wave

characteristic of microelectrodes) and hydrogen absorption/desorption peaks below 0 V illustrate typical macroelectrode characteristics, as expected. After each was successively cleaned in this way, they were modified with the tripod-anchored probes overnight by drop-casting (approximately the same area of ~1 cm^2) for each film. They were then assessed in terms of the SWV signal stability over time. There were only small and negligible difference between the recorded initial currents obtained (for the three replicates), confirming that the similar sizes of surface area (drop-cast) with the probe solutions. Figure 5-11C shows percentage signal changes registered for these probe-modified three individual replicates (green, blue and purple triangles) when interrogated with SWV in 1x PBS for 800 min. The signal decrease recorded was around 75-80% after 800 min, similar for all three replicates. For ease of comparison, they are plotted together with the previously presented data (Figure 5-10) showing the response of commercial (black circles) and average in-house TT and STT microelectrodes (red squares). This clearly reveals that the probe stability on the Pt blanket film surfaces were no better and made worse. Thicker films could be expected to cause the layer to act more like bulk metal as in commercial macro- or microelectrodes, instead of a microfabricated thin films. However, these results showed that thickness was not the main reason of stability problem.

When the film surfaces were analysed with an optical microscope afterwards, it was interesting that many fractures and cracks were present on all three electrodes (Figure 5-11D). It should be noted that these features were observed across the whole blanket film, not just the probe-modified region. Given the surfaces were found not to include any of these features when they were optically monitored after fabrication, prior to use, this might indicate surface re-organisation due to stress based on insertion into solution. This is consistent with the observed positive correlation between the internal stress and the Pt deposit thickness (up to the values ~500 nm Pt on ~2500 nm Cu substrate) which has been reported in literature, after electrodeposition of Pt onto Ni or Cu surfaces [314]. It was also shown that the structural damage (cracks) on the Pt deposits were produced by this increased internal stress, which was suggested as being due to the strong forces at the substrate surface with corresponding formation of strain and fracture in the deposited material [314]. Another study [315] suggested that 150 nm-thick Pt films e-beam evaporated onto silicon oxide substrates showed tensile stresses of 230 MPa at a deposition rate of 0.1 nm s^{-1} and 847 MPa at 0.7 nm s^{-1}, due to the correlation between the deposition rate and the size of intergranular porosities, resulting in an increase in internal stress. The lack of the passivation layer on top of the Pt film should be also considered as they were shown to be able to reduce the substrate stress [316]. Therefore, it is suggested that that these effects might have together provoked the formation of surface

cracking following the fabrication, during immersion into solution and either electrode cleaning or stability measurements.

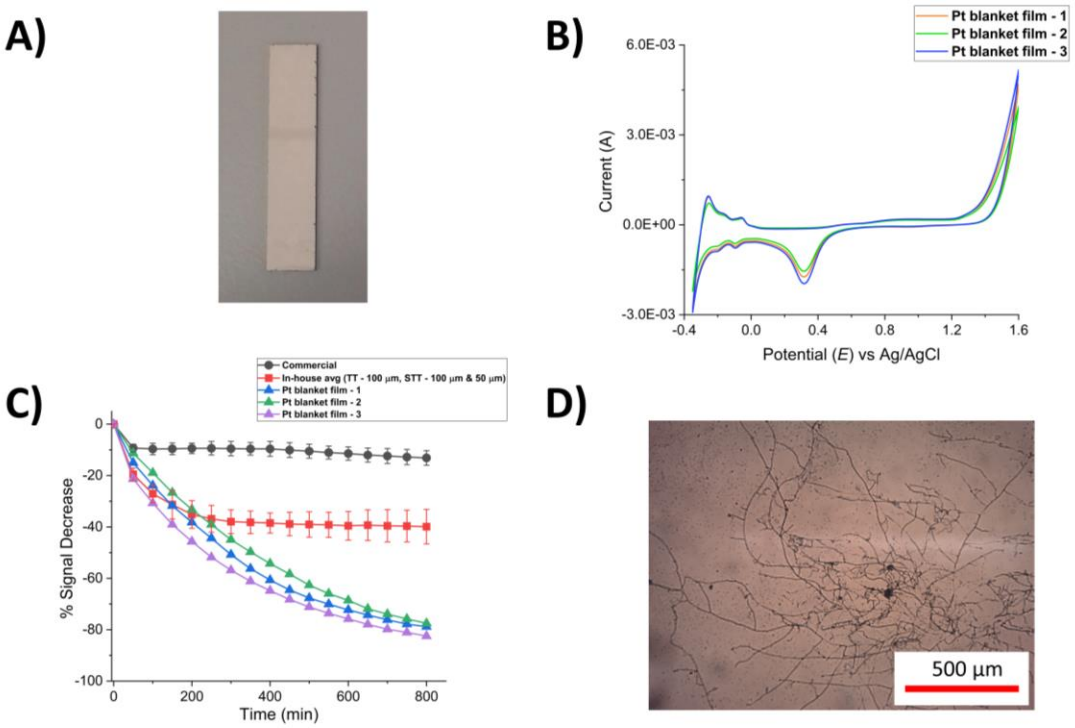

Figure 5-11: Stability of tripod-anchored probes on 200 nm-thick Pt blanket films (electrodes). A) Macroscopic image of the 200 nm-thick Pt film coated on SiO_2/Si chip (35 mm x 3.75 mm). B) Electrochemical cleaning CVs of three individual films in 0.1 M H_2SO_4 between -0.35 and +1.6 V at a scan rate of 100 $mV.s^{-1}$. C) Percentage signal change registered for tripod-anchored probes when immobilised onto three individual 200 nm-thick Pt films (green, blue and purple triangles) and interrogated with SWV in 1x PBS for 800 min. compared to the stability of commercial bulk (black circles) and in-house built TT and STT (red squares) which were given in Figure 5-10. D) Optical microscope image of the probe-immobilised region of the film has shown many fractures and cracks following the stability tests given in C).

5.2.6 Effect of Annealing Platinum Films

In the previous section, it was thought that fabrication of thicker platinum films might have led to an increase in the internal film stress and this might have caused the formation of surface cracking as presented in optical microscope images and an increased propensity for probe loss through metal debonding. Post-annealing of thin films is a commonly used technique to alter film microstructure [317]. This also helps to reduce internal film stress and control surface morphology (roughness) when applied under optimised conditions [318].

In order to investigate whether post-annealing might reduce stress and increase SAM film stability, two sets of Pt blanket films, each including three identical replicates of 50 nm-thick Pt layer, were fabricated and one set was post-annealed, for 10 hours at 500 ^{o}C in N_2. This was followed by the established mono-anchored probe immobilisation step (Section 3.4.2.1) and a comparative investigation of the stability in 1x PBS over time.

As shown in Figure 5-12A, the deposited materials and their thicknesses used in two sets were slightly different. The Pt blanket films used in the annealed set included a thicker adhesion Ti layer compared to the other set, as well as an additional Si_3N_4 insulator layer. This can be accounted for by the fact that this set of Pt blanket films (which were then exposed to annealing) were already available as they had been previously fabricated for a different application. However, it was presumed this should not make any substantial difference between the two sets as the top Pt layer thickness is similar for each set. To confirm this, optical images obtained before and after probe immobilisation on both unannealed and annealed blanket films did not exhibit any variation or any kind of surface defects, such as delamination (Figure 5-12B).

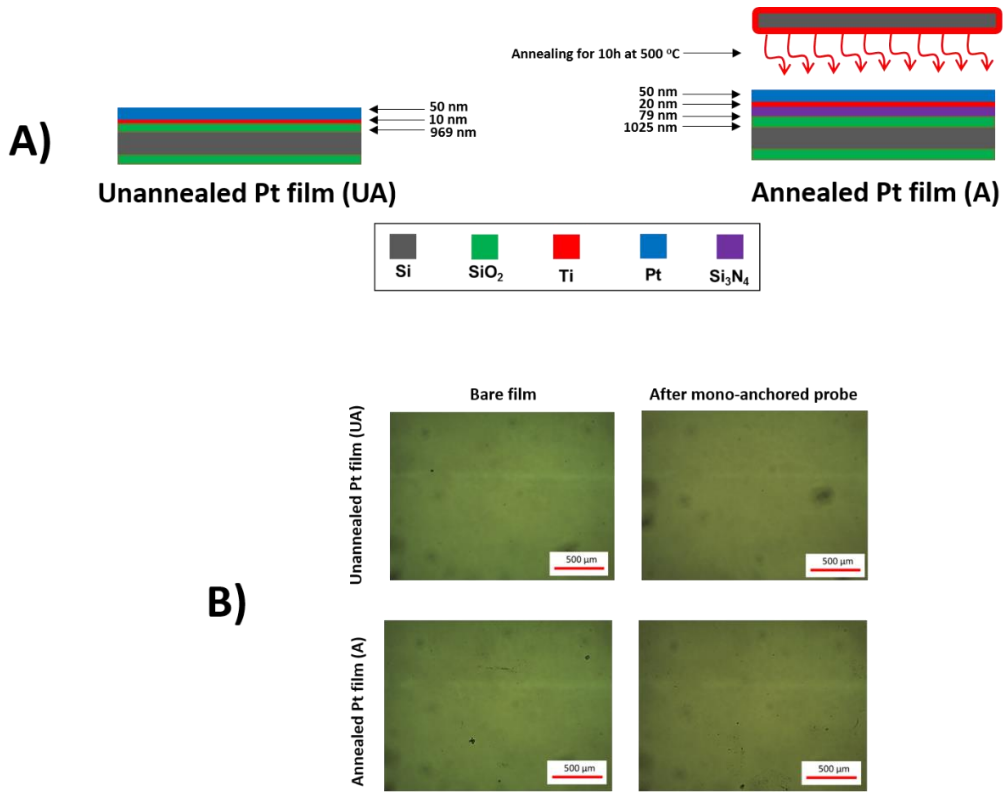

Figure 5-12: Stability of mono-anchored probes on unannealed (UA) vs annealed (A) 50 nm-thick Pt blanket films (electrodes). A) Cross-sectional schematic diagrams (not to scale) of the layers with thicknesses for unannealed and annealed films. (B) Optical microscope images of both unannealed and annealed films before or after, mono-anchored probe immobilisation.

Figure 5-13 presents the percentage signal change registered for mono-anchored probes immobilised onto unannealed and annealed Pt blanket films (each consisting of 3 replicates) which were immersed to 1x PBS and interrogated for 500 min. There is a clear difference between the responses of these unannealed and annealed films. A significant immediate signal decrease, around 90%, was registered for all unannealed blanket films just after 250 min they have been placed into buffer solution. This signal loss was comparable but quicker than the amount of signal loss registered for unannealed 200 nm-thick Pt blanket films with tripod-anchored probes, as given in Figure 5-11. Also, in both experiments, a perfect consistency between the replicates of unannealed blanket films was experienced and this further confirms the recurrence and reproducibility of the stability problem, regardless of the fabrication batch or the nature of the probe.

Interestingly, the stability of mono-anchored probe molecules immobilised onto annealed films was found to be very different. The signal initially rose which was attributed to the ongoing reorganisation of the film up to a time point (~100-150 min). This suggested that the post-annealing has decreased the rate of signal loss, although the annealing protocols were not optimised and there were some variation between the replicates in terms of the amount and the rate of experienced probe loss. However, this increased signal due to film reorganisation is balanced by SAM film loss, which limits the potential of post-annealing to recover film stability.

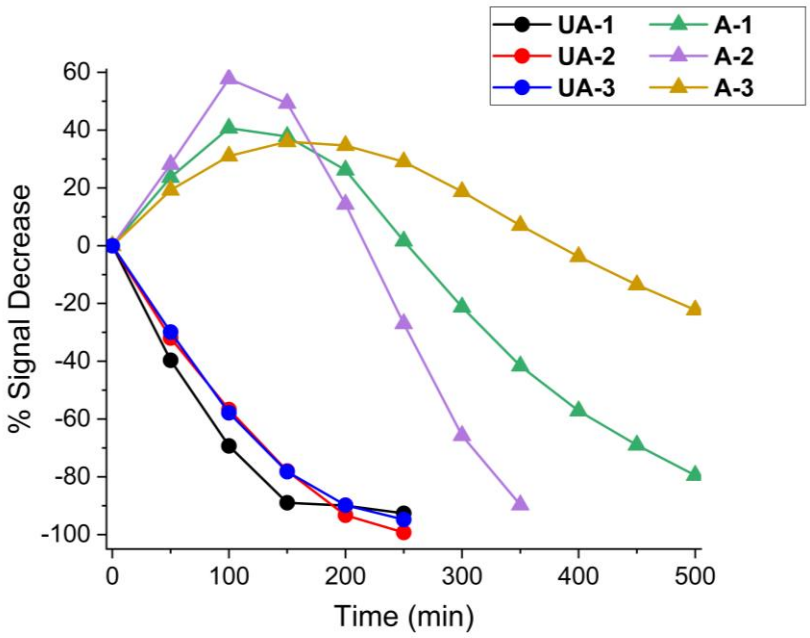

Figure 5-13: Percentage signal change registered for mono-anchored probes when immobilised onto three individual of each unannealed (black, red and blue circles) or annealed (green, purple and yellow triangles) 50 nm-thick Pt films and interrogated with SWV in 1x PBS for 500 min.

As consistent with the experienced stability issue, platinum microelectrodes has been also found to be susceptible to chemical and morphological changes when they were exposed to electric fields (6 V_{pp}/175 µm AC and ±3 V/175 µm DC field) in various biological buffer solutions such as PBS, HEPES or Tris buffered saline [319]. These changes consisted of platinum oxidation, dissolution, re-deposition as well as potassium and/or chloride formation depending on a buffer solution used, and these changes were observed to be more effective under DC electric fields than in AC fields [319]. Another study revealed that the products of the dissolution/corrosion can have some cytotoxic effects in the long term, focusing on the Pt-induced death of murine fibroblast (NIH 3T3) and human neuroblastoma (SH-SY5Y) cell lines [320]. This is not surprising when it is considered that cisplatin is widely used to treat cancer [321].

Luckily, there have been a few successful attempts to avoid (or minimise at least) this drawback of platinum. For example, de Haro *et al.* reported that the lower rate of dissolution (7.8 ng/C) was obtained for electroplated Pt microelectrodes, whereas it was observed to be 38.8 ng/C for thin film microelectrodes, with this improvement attributed to the good adhesion of electroplated Pt onto substrate Pt thin film due to an initial surface pre-treatment process [322]. Also, Park *et al.* showed that the Pt microelectrodes with fractal designs exhibited better charge transfer characteristics than the ones with circular designs, but they suffered from a significantly faster neurostimulation-induced Pt dissolution [323]. However, a single layer of graphene coating was shown to decrease the dissolution rate by almost ~97% without deteriorating the charge transfer [323]. As a relieving finding in addition to these, platinum dissolution was observed to be slower in solutions including proteins, which inhibit any release and/or accumulation into tissues and thus promoting their use for in vivo biosensing applications [324].

Although some efforts e.g. using stronger anchoring, increased film thickness, post-annealing, have been given to improve the SAM film (probe) stability on platinum thin film single microelectrodes, the problem could not be resolved entirely. It was thought that this might have resulted from the employed cleaning method based on electrochemical oxidation/reduction in the acidic solution that might have led to increased Pt surface roughness. Therefore, the feasibility of its replacement with a simpler and less aggressive cleaning technique was investigated in the next sections, using the arrays of microelectrodes (MEA) and microcavity nanoband edge electrodes (MNEE) in order to increase the set of data and resulting currents.

5.3 Microelectrode Arrays (MEAs)

In addition to the single microelectrodes analysed in the former section, arrays of microelectrodes were also produced, cleaned and assessed. For this purpose, two electrodes with a similar size (20 µm) and shape (circular) to commercial electrodes were selected. As presented in Figure 5-14B and C, they have the same diameter and shape, but different interelectrode spacings (2D and 4D) to characterise the effect arising from the interelectrode distance on sensor performances. Accordingly, they will be abbreviated as MEA 20µm-2D and MEA 20µm-4D from now on (Section 3.3.3 and Figure 5-14A).

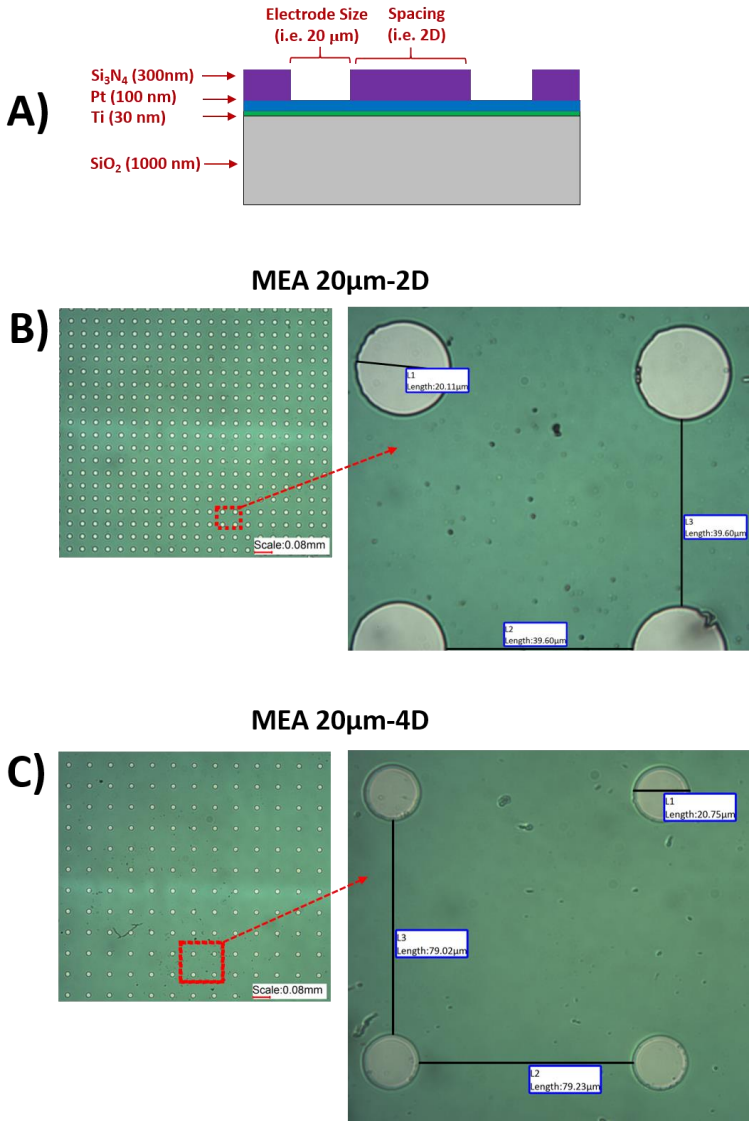

Figure 5-14: A) Cross-sectional schematic diagram (not to scale) with constituent materials layer thicknesses of a microelectrode array (MEA) with an electrode diameter/edge length of 20 µm and the separation of 2D (40 µm) as well as optical microscope images of B) MEA 20µm-2D and C) MEA 20µm-4D.

5.3.1 Cleaning

As suggested in the previous section, typical electrochemical cleaning in dilute acidic solutions (0.1 M H_2SO_4) was not successful to result in high fidelity reproducible SAM probe films on in-house built Pt thin film single microelectrodes. This stability problem was most likely due to loss of probes with weakened bonding to roughened electrode surfaces because of the progressive effect of formation and re-reduction of Pt oxide at positive solvent limit. Because microfabricated electrodes are already sufficiently clean, there is no need for such an aggressive cleaning technique. Therefore, an alternative method, electrochemical reduction [325]–[327] which has been shown to break gold-sulphur bonds, leading to the reductive desorption of SAM-based molecules from the substrate and thus cleaning the electrode surface could be used. Moreover, this method was not limited to gold electrodes, as it has been shown to be extendable to platinum and palladium substrates as well [328]. These redox reactions for reductive thiol desorption and the oxidative thiol adsorption can be given respectively, where RSH shows free thiol molecules and RS–M shows metal surface-adsorbed thiol molecules [329]:

$$\text{(i)} \qquad \text{RS–M} + e^- \longrightarrow \text{M} + \text{RS}^-$$

$$\text{(ii)} \qquad \text{RSH} + \text{M} \longrightarrow \text{RS–M} + H^+ + e^-$$

If such a cleaning protocol was to be effective, it would also be useful to see it such cleaning was effective for electrode arrays. Therefore, microelectrode arrays, MEA 20µm-2D and MEA 20µm-4D, were assessed in terms of the usefulness of the reductive cleaning method. Figure 5-15 shows typical CVs (1st, 20th, 40th, 60th, 80th and 100th scans) recorded for MEA 20µm-2D after modified with mono-anchored SAM probe and then cycled between -1.1 and +0.25 V vs Ag/AgCl reference electrode, at a scan rate of 100 mV/s in 1 mM potassium ferri/ferrocyanide and 0.1 M KCl. As expected, the first CV scan recorded after the overnight modification of the electrode with the probe solution showed inhibition of the redox reaction of the ferri/ferrocyanide redox couple due to the blocking SAM layer on the electrode surface. However, it can be seen in the succeeding cycles, the redox reaction of the external agents was reinstated and the currents increased, confirming the desorption of thiols from the surface. The importance of using a fresh buffer solution and replacing it after each 10 min intervals was mentioned in other studies, because the process is reversible and re-adsorption of thiols (which desorbed from the surface and released into the buffer) can take place at oxidative potentials [201]. However, the buffer replacement was avoided in this work, limiting the oxidative

potential at only +0.25 V, instead of +0.45 V which was the oxidative potential limit used in the previous work. No evidence of SAM re-adsorption was seen within the potential range used for this study.

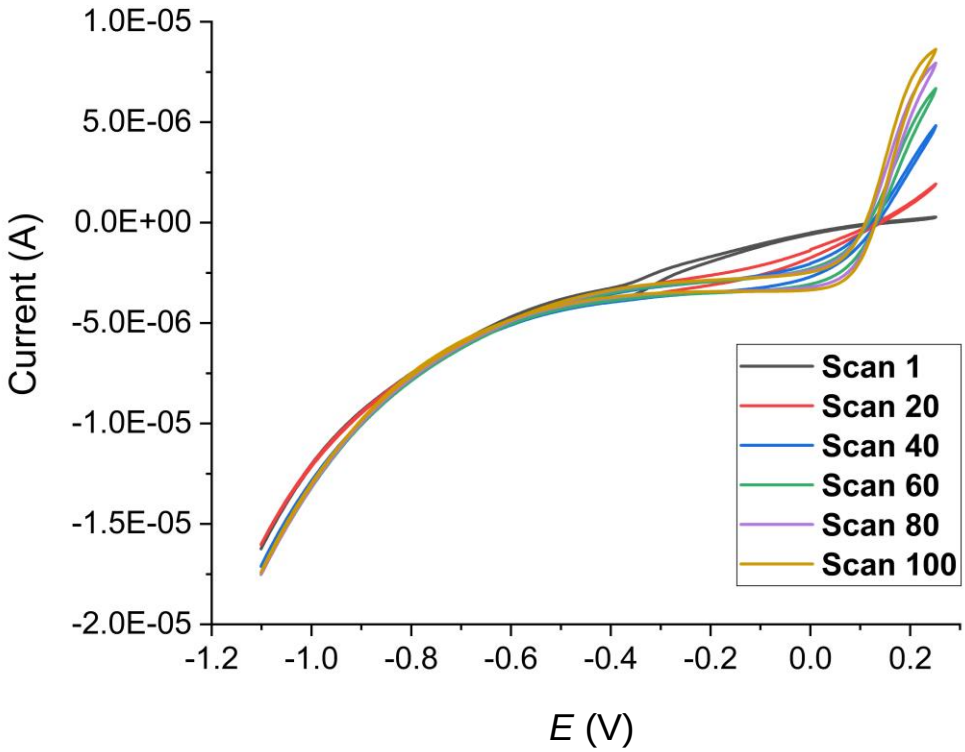

Figure 5-15: Reductive electrochemical removal of SAM-functionalised probes: Typical CVs (1st, 20th, 40th, 60th, 80th and 100th scans) of a MEA 20µm-2D recorded between -1.1 and +0.25 V at a scan rate of 100 $mV.s^{-1}$ in an aqueous solution of 1 mM potassium ferri/ferrocyanide and 0.1 M KCl.

Figure 5-16 presents voltammograms of MEA 20µm-2D and MEA 20µm-4D electrodes before and after this reductive electrochemical cleaning process. For both electrodes, as expected there is a clear difference which is compared to the uncleaned condition, even after 20 cycles of reductive cleaning. Although this is further improved with 80 more cycles, it was seen there was little difference between the voltammograms of MEA 20µm-2D registered after 20 and 100 cycles, unlike MEA 20µm-4D. This means that even a few cycles of electrochemical reduction can be sufficient to generate a fresh surface for an array of electrodes. A statistical evaluation of the registered currents revealed that all electrodes found in arrays can be successfully cleaned after sufficient time of cycling depending on the extent of SAM coverage and number of electrodes (depending on electrode size and interelectrode spacing). The most significant advantage of this cleaning technique over electrochemical

cleaning with acidic solution, is an opportunity of real time monitoring of the electrode surface, as enabled by the external redox agent present in the buffer solution. This also enables better quantitative control on electrode morphology, as the cycling can be stopped when the monitored limiting current reaches the target value of a clean electrode determined by previous experiments.

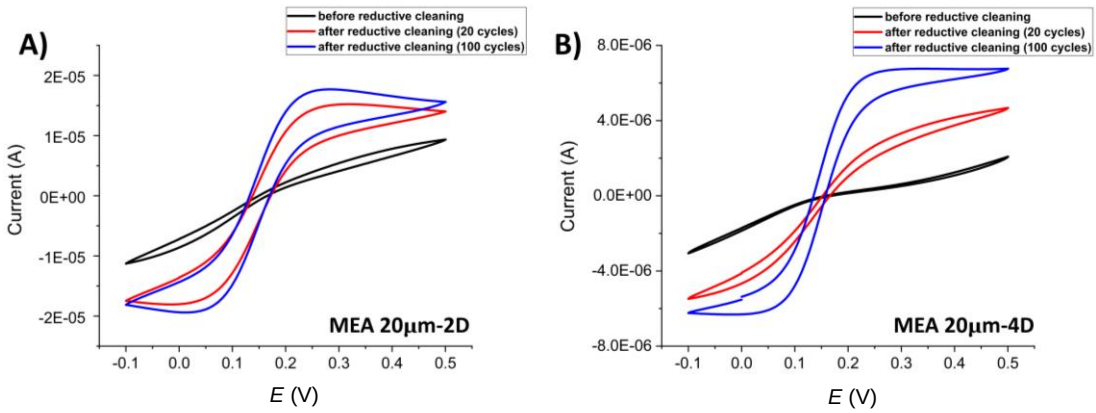

Figure 5-16: Reductive electrochemical removal of SAM-functionalised probes: CVs of a A) MEA 20µm-2D and B) MEA 20µm-4D recorded between -0.1 and +0.5 V at a scan rate of 100 $mV.s^{-1}$ in an aqueous solution of 1 mM potassium ferri/ferrocyanide and 0.1 M KCl vs Ag/AgCl reference electrode, before reductive cleaning (black line) or after 20 cycles of reductive cleaning (red line) or after 100 cycles of reductive cleaning (blue line).

5.3.2 Characterisation of Clean MEAs

Typical clean cyclic voltammograms of MEA 20µm-2D and MEA 20µm-4D are given in Figure 5-17A. There was around 2.5-fold difference in limiting currents, which were found to be higher for MEA 20µm-2D. This was the expected correlation, because 2500 individual electrodes are patterned on MEA 20µm-4D design, whereas MEA 20µm-2D consists of 6889 individual single microelectrodes (See Appendix-2). The ratio of electrode number (the number of electrodes found in MEA 20µm-2D design divided by the number of electrodes found in MEA 20µm-4D design) is 2.76 which is slightly higher than the observed difference. Although, both array devices showed the expected sigmoidal, or near sigmoidal response characteristic of the hemispherical diffusion (Section 2.6.1), it was seen that MEA 20µm-4D had a more sigmoidal shape, compared to the MEA 20µm-2D which has a more peak-like response at this scan rate (100 $mV.s^{-1}$). This is consistent with the fact that the individual electrodes are closer to each other for MEA 20µm-2D, which results in an overlap of the neighbouring diffusion layers.

Figure 5-17B therefore shows cyclic voltammograms of MEA 20µm-2D recorded at varying scan rates of 10, 50, 100, 200, 300, 400 and 500 mV.s^{-1}. It was seen that a progressively more peak-like shape occurred at lower scan rates, which was especially observable for 10 mV.s^{-1}. This was not surprising as it is known that the decrease in the scan rate causes the diffusion fields of the array electrodes to overlap and, correspondingly, resulting in the mass transport to each electrode becoming less efficient. At higher scan rates, however, this overlap is not seen due to the limited diffusion time, and each electrode in the array is able to respond as an individual microelectrode. This lays emphasis on the selection of the fastest scan rate (which should be enough to promote electrodes to respond individually) while a target limiting current is to be determined for an array [201]. In order to make a quantitative evaluation for MEA 20µm-2D, Equation 5.1 was used to determine the experimental diffusion coefficient of ferri/ferrocyanide redox couple. The limiting current, i_L of an individual microelectrode in the array was calculated by dividing the total limiting current obtained at the fastest scan rate (500 mV.s^{-1}) by the number of electrodes (N=6889). The diffusion coefficient was found to be D = 6 x 10^{-6} cm^2/s, which was very close to the literature value of 7 x 10^{-6} cm^2/s [312], consistent with the variation in temperature. This confirms that the electrodes located in these fabricated MEAs are electroactive and they exhibit quantitative performance under redox conditions, thus they are expected to be successfully used for protease sensing as well.

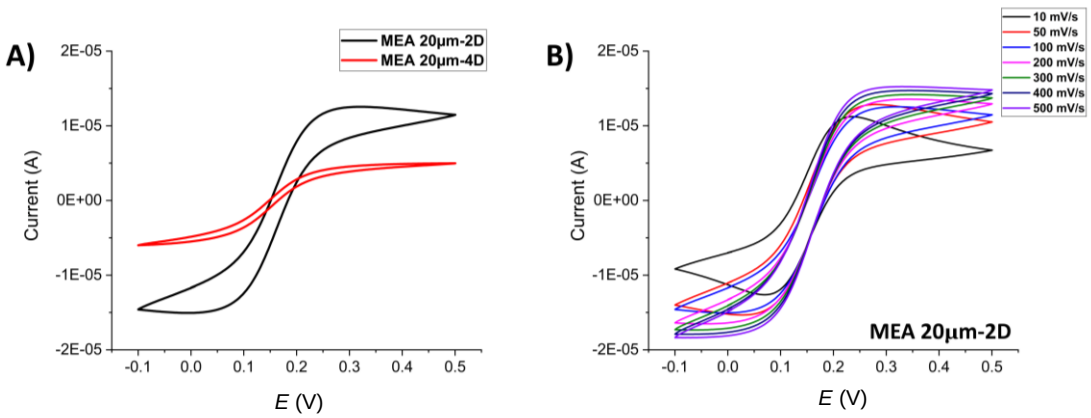

Figure 5-17: A) Typical CVs of a MEA 20µm-2D (black line) and MEA 20µm-4D (red line) recorded between -0.1 and +0.5 V at a scan rate of 100 mV.s^{-1} in an aqueous solution of 1 mM potassium ferri/ferrocyanide and 0.1 M KCl. B) CVs of a MEA 20µm-2D with varying scan rates (10, 50, 100, 200, 300, 400 and 500 mV.s^{-1}) using the same buffer solution and conditions.

5.3.3 Performance in Protease Detection

In order to evaluate the analytical performance of MEAs in protease sensing, MEA 20µm-2D and MEA 20µm-4D were modified with the mixed SAM layer by drop-casting as previously described (See Section 3.4.2.1). In order to assess them in terms of trypsin selectivity, MEA 20µm-2D was modified with the substrate probe, whereas control probes were immobilised onto MEA 20µm-4D; and then they were replaced for the second analogous experiment to check whether an interelectrode spacing has any effect on the performance. SWV peaks (right, Figure 5-18) registered for both control and substrate probe modified arrays were analysed using a simple MATLAB code (Appendix-3) this time, whereas the peaks were normally analysed by fitting to a Gaussian curve in the Origin software. Because, Gaussian fitting has been found to be significantly time consuming for a large number of scans. Therefore, the MATLAB code was created to simply find a background for the given peak and then calculate the peak height. Reassuringly, the peak height values obtained using both methods were compared and found to give the same results with experimental errors. Consequently, the SWV data obtained were analysed using the MATLAB code, unless other peak parameters (such as full width at half maximum, FWHM) were needed for analysis. As an initial SWV signal, MEA 20µm-2D (6889 electrodes) device gave ~2 µA whereas it was around 0.5 µA for MEA 20µm-4D (2500 electrodes). The currents given by a single microelectrode in both arrays were thus found to be comparable to the currents (~10^{-10} A) registered with single microelectrodes (with comparable diameters).

Figure 5-18 shows the percentage signal change for both arrays immersed in buffer solution, 1x PBS before and after the addition of 100 nM trypsin (at time t=100 min). The most significant finding to note here was the improved stability of the microelectrode arrays for probe molecules. Until the time when enzyme was added into solution, both substrate and control modified arrays showed a similar and more stable background than TT and STT microelectrodes, only decreasing by ~10%. This was of course significant considering the major stability problem experienced with single TT and STT microelectrodes, which sometimes caused at least ~50% signal decrease within the first 100 min. This improvement can be attributed to the feasibility of reductive cleaning used for MEAs.

Following trypsin addition at 100 min, the signal was monitored for a further 175 min and a clear signal decrease of 70% was recorded for substrate-modified MEA 20µm-2D while control modified MEA 20µm-4D device still did not present any significant signal change afterwards. There was only a little change which was attributed to the background decrease

due to the stability, because the rate of this decrease was similar to the one which was observed before enzyme addition. This background signal change recorded with control probes was then subtracted from the trypsin-induced signal change recorded for substrate modified electrode. Afterwards, the effective rate constant was calculated as detailed before (Section 4.8) and found to be 0.01864 ± 0.00047 min^{-1}. Despite being a bit lower than the one recorded for commercial Pt macroelectrode (0.02854 ± 0.00120 min^{-1}), surprisingly it was 3-fold faster than the one estimated for commercial Pt microelectrode (0.00617 ± 0.00013 min^{-1}).

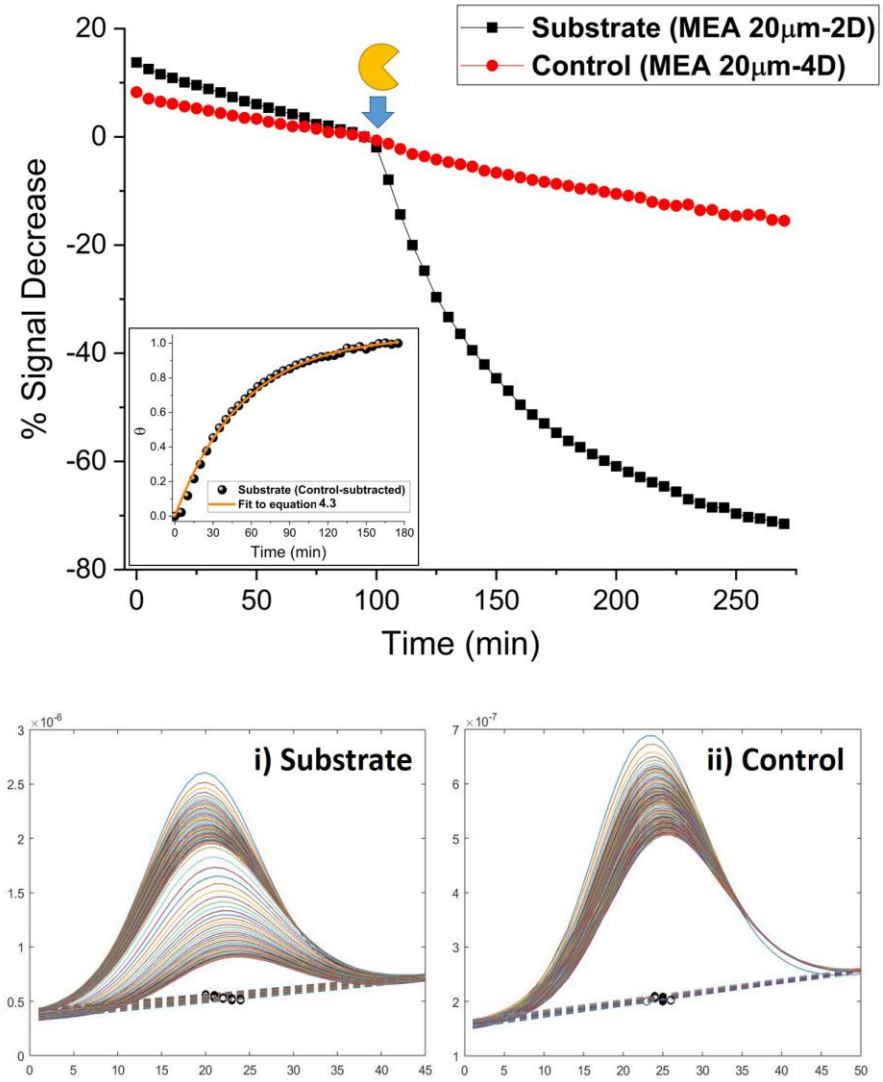

Figure 5-18: Top: Plot of % signal decrease vs time for SAM-functionalised mono-anchored probe immobilised onto Pt microelectrode arrays (Substrate-modified: MEA 20µm-2D, Control-modified: MEA 20µm-4D) upon the addition (at time t = 100 min) of 100 nM trypsin in 1x PBS. Inset. Calculated fractional cleavage, θ, vs time plot for the control-subtracted substrate data, where its fit to equation 4.3 gives a k_{eff} value of 0.01864 ± 0.00047 min^{-1}. Bottom: Typical SWV curves and their peak height calculations using a MATLAB code for SAM-functionalised i) substrate and ii) control-modified probes immobilised onto MEAs at different incubation times (between 0 - 275 min) with 100 nM trypsin are also given.

In order to assess whether the estimated rate constants are reproducible, the arrays were again cleaned with electrochemical reduction until the target limiting currents were obtained. They are then modified with probe, but the other way around this time; MEA 20µm-4D was modified with the substrate probe and MEA 20µm-2D was modified with the control probe. Initial signals were again comparable, confirming the reproducibility of reductive cleaning for creating a fresh electroactive surface. Although there has been a quite similar and stable background (~5%) for both arrays until trypsin addition (at time t = 100 min), the rate of trypsin cleavage was notably slower, with a decrease of 60 – 65% after 900 min of incubation (Figure 5-19). This was also presented by the k_{eff} value for this experiment, which was estimated as 0.00344 ± 0.00064 min^{-1}. It was interesting because this rate was too slow to be affected by mass transport, and there should have thus been no difference. There might have been some differences between these two electrodes such as (i) the amount of cleavable substrate probe molecules (anticipated to be higher for MEA 20µm-2D due to the larger total area) and (ii) possible macroelectrode-like behaviour for MEA 20µm-2D, arising from the overlapping of diffusion fields. However, any of them was typically expected not to affect the rate.

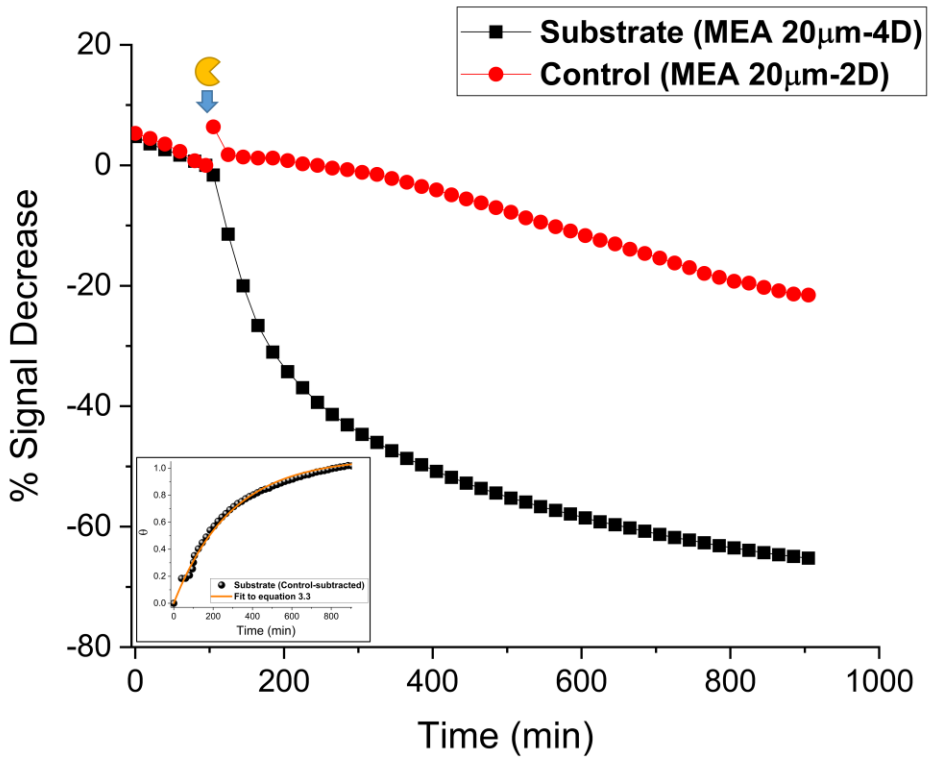

Figure 5-19: Plot of % signal decrease vs time for SAM-functionalised mono-anchored probe immobilised onto Pt microelectrode arrays (Substrate-modified: MEA 20µm-4D, Control-modified: MEA 20µm-2D contrarily to given in Figure 5-18) upon the addition (at time = 100 min) of 100 nM trypsin in 1x PBS. Inset. Calculated fractional cleavage, θ, vs time plot for the control-subtracted substrate data, where its fit to equation 4.3 gives a k_{eff} value of 0.00344 ± 0.00064 min^{-1}.

To make sure that the rate of trypsin cleavage specific to this MEA 20µm-4D was reproducible, the same array device was reductively cleaned, modified with the substrate probe and incubated with varying trypsin concentrations (0, 25 and 100 nM) at ambient (25 °C) and body temperature (37 °C). As depicted in Figure 5-20, the array-based platform gave different amounts of percentage signal change for varying concentrations. Also, it was seen to be quite stable when incubated with only buffer solutions, which did not include any trypsin (0 nM). It was interesting that the stability was even seen to be higher this time, compared to the previous experiments presented in Figure 5-18 and 5-19. This confirms the trypsin sensitivity of the array-based sensor platform. Also, increasing the temperature up to 37 °C resulted in an increase in the rate in shorter time period, losing its effect in longer terms. Most likely, this increase was lower than ~4-fold which was obtained for commercial microelectrodes. It is also worth noting that the standard deviations for the replicates of the experiment performed at 37 °C were the lowest compared to all other data obtained at 25 °C. This offers further improved consistency regarding clinical measurement conditions.

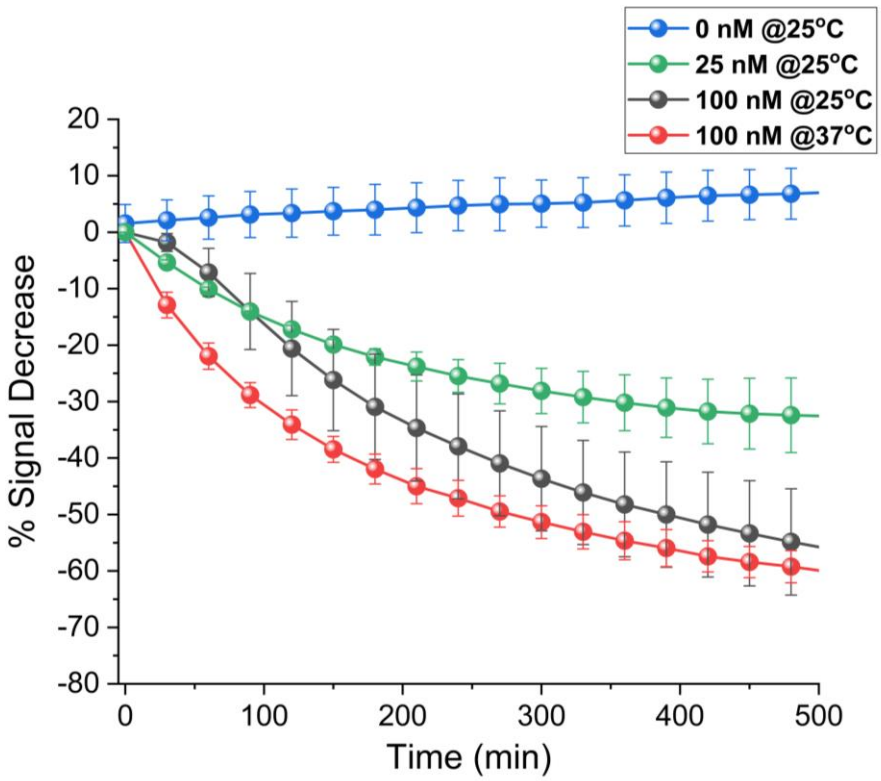

Figure 5-20: Plot of % signal decrease vs time for SAM-functionalised mono-anchored substrate-modified probe immobilised onto Pt microelectrode arrays (MEA 20µm-4D) immersed in varying trypsin concentrations in 1x PBS: 0 nM (blue circles), 25 nM (green circles) and 100 nM (at 25 °C, black circles or at 37 °C, red circles). All data represent the average and error bars from 3 functionalised electrodes.

5.4 Microcavity Nanoband Edge Electrode Arrays (MNEEs)

Although nanoelectrodes have attracted significant interest in lots of fields in the recent years [291], their use in protease detection is very limited. Existing works have mainly focused on the utilisation of nanoelectrode arrays for understanding the proteolytic activities of cathepsin B and/or legumain in buffer solutions, tissue and cancer cell lysates [84], [235], [307], [330]. However, their fabrication were based on the encapsulation of vertically aligned carbon nanofibers (VACNFs) into SiO_2 substrates, and they are not thus convenient platforms for SAM molecules which requires a thiol bonding to immobilise onto the substrates. This necessitates for Au- or Pt-based nanoelectrodes which can allow metal-thiol bonding. Therefore, two types (i. in-house built and ii. commercially available) of microcavity Pt nanoband edge electrode array (MNEE) devices were used to characterise their performance in protease sensing. For both commercial and in-house MNEEs, electrochemical reductive cleaning was successfully used and achieved reproducible surface cleanliness similar to MEA findings.

5.4.1 NanoFlex MNEEs

The first type of MNEE electrodes was commercially available and supplied by NanoFlex Ltd, UK with a brand name of CAVIARE™ (CAVIty ARray Electrode). This array includes square (30 x 30 µm) cavities with a 50 nm Pt band at the edges, as shown in Figure 5-21B and C. The type used here consisted of dual contact pads where both connected to the array of electrodes in the same way, but only one of the contact pads was used for connection. Figure 5-21A presents two individual identical NanoFlex MNEEs drop-cast with the solution of substrate probe molecules.

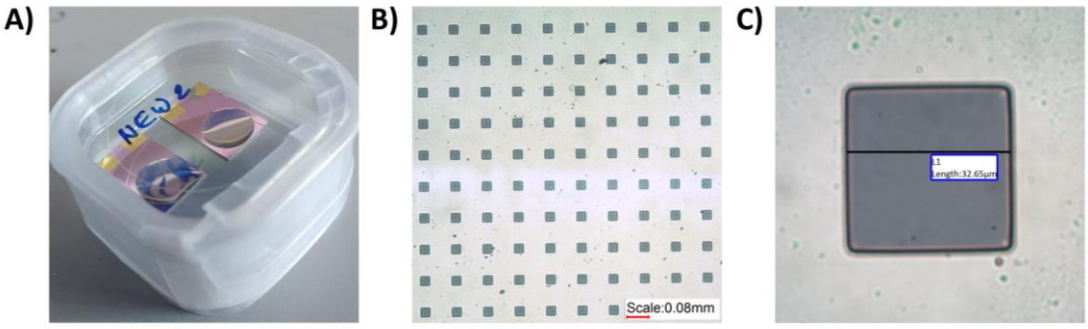

Figure 5-21: A) Macroscopic image of two individual and identical (left: Electrode-1, right: Electrode-2) NanoFlex Microcavity Nanoband Edge Electrode (MNEE) arrays incubated with 40 µM of probe solution by drop-casting. Optical microscope images show B) the array of 10 x 10 electrodes and C) a single microsquare cavity of 30 µm x 30 µm and a 50 nm Pt nanoband at the edge of the cavity.

As depicted in Figure 5-22(i), limiting currents and redox reaction of both MNEEs were significantly enhanced after successfully cleaned via 100 cycles of reductive cleaning between -1.1 and +0.25 V. This was as anticipated, as any production-induced adsorbates were reductively desorbed from the Pt nanoband surface. However, the shapes of the voltammograms were slightly different from each other, which were found to be interesting as they are identical electrodes and the same behaviour was expected.

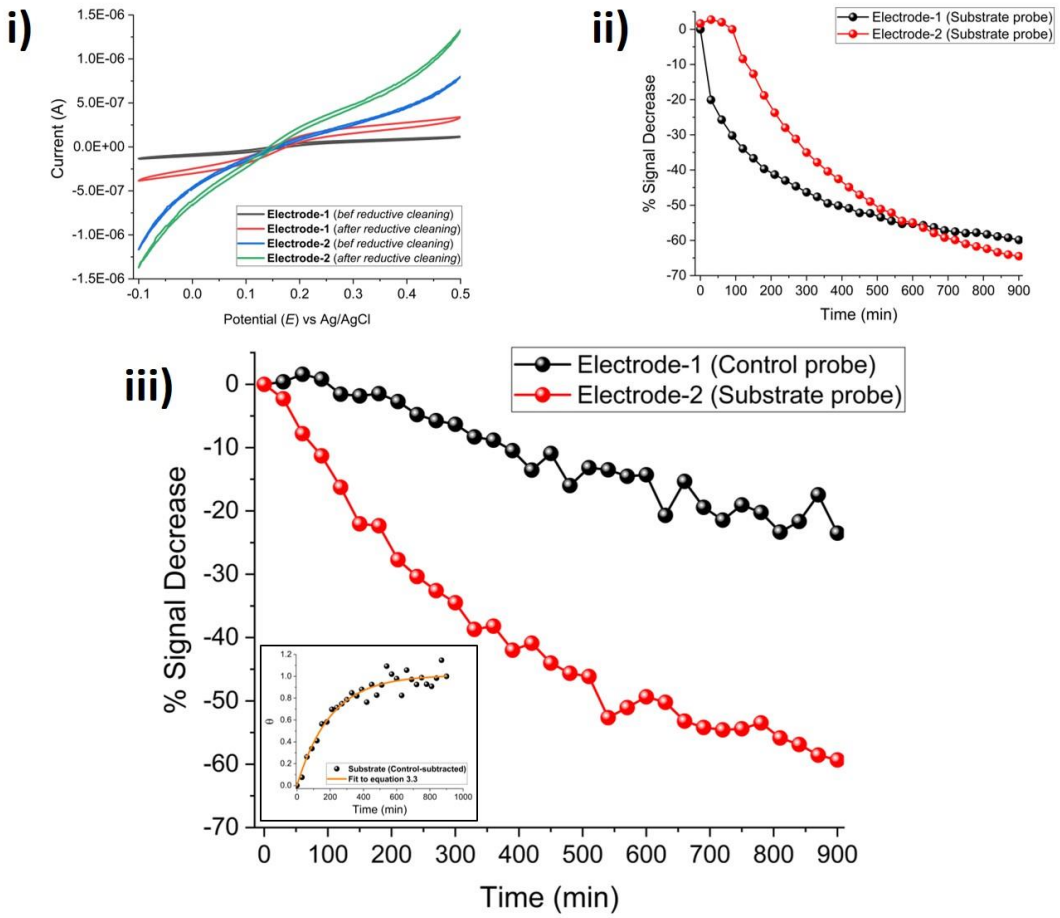

Figure 5-22: Using NanoFlex MNEE arrays for trypsin sensing. i) Electrochemical reductive cleaning with 100 cycles of CVs between -1.1 and +0.25 V at a scan rate of 100 $mV.s^{-1}$ in an aqueous solution of 1 mM potassium ferri/ferrocyanide and 0.1 M KCl. ii) Plot of % signal decrease vs time for SAM-functionalised mono-anchored probe immobilised onto NanoFlex MNEE arrays (both Electrode-1 and 2 substrate-modified) upon the addition (at time = 0 min) of 100 nM trypsin in 1x PBS. iii) Plot of % signal decrease vs time for second performance characterisation with SAM-functionalised mono-anchored probe immobilised onto NanoFlex MNEE arrays (Control-modified: Electrode-1, Substrate-modified: Electrode-2 this time) upon the addition (at time = 0 min) of 100 nM trypsin in 1x PBS, with calculated fractional cleavage, θ, vs time plot (Inset) for the control-subtracted substrate data, where its fit to equation 4.3 gives a k_{eff} value of 0.00490 ± 0.00041 min^{-1}.

These devices were then immobilised with substrate probe molecules exhibited ~60-65% signal decrease over 900 min, after the addition of 100 nM trypsin (at time t=0 min) (Figure 5-22(ii)). Although the registered decreases in the percentage signals obtained from both replicates were similar after 900 min, the initial response of Electrode-2 was markedly different than Electrode-1. A difference was also seen in variation in their initial peak currents, recorded as 87 nA for Electrode-1 and 44 nA for Electrode-2.

In order to estimate the efficient rate constant and analyse whether they were similar to the ones recorded for microelectrode arrays, they were modified with the substrate (Electrode-2) and control (Electrode-1) probes. Closer values were obtained as initial signals this time, which are 95 nA for Electrode-1 and 73 nA for Electrode-2. A clear difference between the percentage signal decreases calculated for control (~20%) and substrate modified (~60%) nanoelectrodes was seen after 900 min incubation of 100 nM trypsin (Figure 5-22(iii)). In addition, the effective rate constant was calculated as 0.00490 ± 0.00041 min^{-1} for this cleavage - not much different from the k_{eff} reported for MEAs (0.00344 ± 0.00064 min^{-1}, where substrate: MEA 20µm-4D, control: 20µm-2D). This simply suggests that commercial Pt MNEEs were sensitive against trypsin and this motivated the fabrication of similar architecture MNEE devices in-house.

5.4.2 In-house MNEEs

After it was seen that the commercial MNEE sensing platform has shown successful probe deposition and trypsin cleavage (sensitivity), corresponding MNEE devices were fabricated in-house in SMC (as detailed in [201]) as an alternative to commercially available version, and then characterised in terms of protease detection, as similarly. Again, two designs, MNEE 20µm-1D and MNEE 20µm-2D, due to fact that they are comparable with previously analysed electrodes in terms of size and shape, were selected for characterisations, although it is possible to fabricate them in any size and any shape.

5.4.2.1 Characterisation

Cyclic voltammograms of MNEE 20µm-1D and MNEE 20µm-2D recorded between -0.1 and +0.5 V at varying scan rates in an aqueous buffer solution of 0.5 mM ferrocene methanol (FcMeOH) and 0.1 M KCl are given in Figure 5-23. There is an about 2-fold difference when

MNEE 20µm-1D and MNEE 20µm-2D are compared in terms of the limiting currents obtained in their CVs recorded at the same scan rate. Again, similarly to the comparison of MEA devices, this was consistent with the ratio of electroactive area (Appendix-2, MNEE 20µm-1D: 15625 cavities and MNEE 20µm-2D: 6889 cavities) on the arrays. The voltammogram shapes were observed to be more sigmoidal compared to the MEAs and single microelectrodes, due to the enhanced hemispherical diffusion. When CVs taken at 10 $mV.s^{-1}$ are compared, MNEE 20µm-1D seems slightly less sigmoidal than in MNEE 20µm-2D, which again attributed to the overlapping of the diffusion fields. This, of course, disappeared at faster scan rates for both devices, as overlapping of the diffusion fields at neighbour electrodes does not exist. The experimental diffusion coefficient of ferrocene methanol was calculated at fast scan rate using the equation [192];

$$i_L = 0.956nNFDCr \tag{5.3}$$

where n is the number of electrons (which is equal to 1 for ferrocene methanol), N is the number of electrodes in the array, F is the Faraday constant, D is the diffusion coefficient (cm^2/s), C is the concentration (mol/cm^3) for redox molecule in the solution and r is the radius (cm) of an individual electrode in the array.

The diffusion coefficient was found to be D = 6 x 10^{-6} cm^2/s using both MNEE 20µm-1D and MNEE 20µm-2D. These given values are the same as each other and the literature (D = 7 x 10^{-6} cm^2/s) [331] within experimental error.

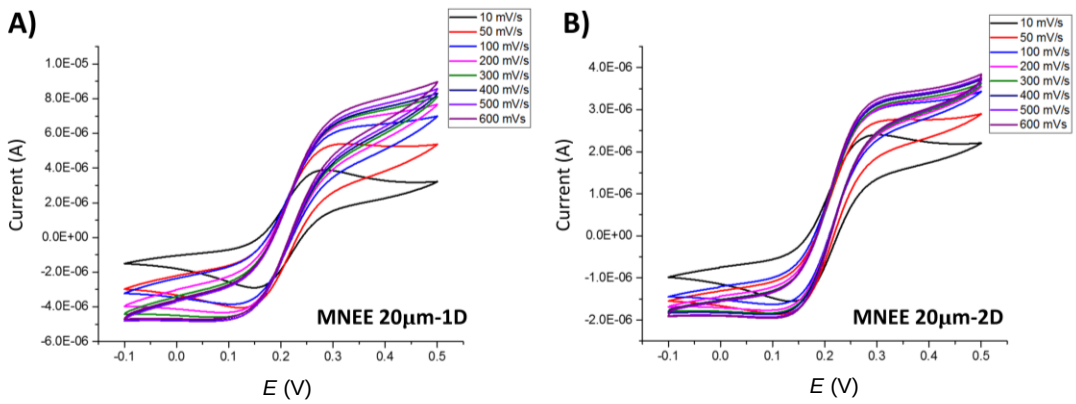

Figure 5-23: A) Typical CVs of in-house built A) MNEE 20µm-1D and B) MNEE 20µm-2D recorded between -0.1 and +0.5 V at varying scan rates (10, 50, 100, 200, 300, 400, 500 and 600 $mV.s^{-1}$) in an aqueous solution of 0.5 mM ferrocene methanol and 0.1 M KCl.

5.4.2.2 Performance in Protease Detection

Both MNEE 20µm-1D and MNEE 20µm-2D devices were cleaned using the same electrochemical reduction method prior to the probe immobilisation. Afterwards, MNEE 20µm-1D was modified with the substrate probe, whereas control probes were immobilised onto MNEE 20µm-2D. The initial SWV signals were observed as ~0.7 µA for MNEE 20µm-1D and ~0.4 µA for MNEE 20µm-2D. The ratio was consistent with the number of electrodes in the arrays, and these signal amounts were significantly higher than single microelectrodes tested up to now. The current densities of probe modified TT & STT single microelectrodes, MEAs and MNEEs were calculated for further analysis, and given in Table 5-1. They were also compared to the commercial Pt single microelectrodes. In-house STT single microelectrodes gave similar values within experimental errors to the commercial microelectrodes. The current density values calculated for all STT single microelectrodes (20µm, 50µm and 100µm) were found to be the same with each other. In addition, the current densities of MEAs also found as smaller than expected. They were observed to be same with STT single microelectrodes within errors. The highest current densities were recorded using MNEE devices, by almost 10-fold superior numbers than other in-house built devices. This is a significant finding that MNEE electrodes can offer the best signal-to-noise ratio for SAM-based redox probes of all the miniaturised electrodes in this study.

When MNEE 20µm-1D (substrate) and MNEE 20µm-2D (control) were incubated with 100 nM trypsin (added at time t=0 min) for 900 min, this resulted in a clear difference between substrate- and control-modified electrodes, as shown by Figure 5.24. The control probe only showed a decrease around 25%, where the change for substrate probe was found as ~70%. These signal decreases were observed to be quite reproducible when other tests were carried out. The effective rate constant was calculated as 0.01302 ± 0.00127 min^{-1} for the cleavage (Figure 5-24 Inset). This value was found to be comparable with the first k_{eff}, 0.01864 ± 0.00047 min^{-1}, reported using MEAs (where MEA 20µm-2D: substrate modified and MEA 20µm-4D: control modified). Also, it is worth noting that it was ~2-fold faster than commercial Pt microelectrodes (0.00617 ± 0.00013 min^{-1}). On the other hand, all k_{eff} values reported, through this chapter, estimated for MEAs as well as commercial and in-house MNEEs have been smaller than the values given by Au and Pt commercial macroelectrodes (See Table 4-1). This further confirms the suggestion of similar and valid findings for all tested miniaturised electrodes, in terms of SAM film variations compared to macroelectrodes, partial

inaccessibility of enzyme and slower proteolytic cleavage, in accordance with the discussion in Section 4-8.

Table 5-1: Summary of calculated current densities for various Pt electrodes.

Electrode (Type, Diameter/Edge Length)	Average Output Signal (A) (n>3)	Total Area ($x10^{-8}$ m^2)	Current Density J (A/m^2)
Single Bulk Microelectrode (Commercial, 25µm)	1.3 ± 0.4 ($x10^{-9}$)	0.0491	**2.7 ± 0.8**
Single Microelectrode (STT, 20µm)	5.2 ± 1.1 ($x10^{-10}$)	0.0314	**1.7 ± 0.4**
Single Microelectrode (STT, 50µm)	3.4 ± 0.5 ($x10^{-9}$)	0.1963	**1.7 ± 0.3**
Single Microelectrode (STT, 100µm)	1.3 ± 0.3 ($x10^{-8}$)	0.7854	**1.7 ± 0.4**
Single Microelectrode (TT, 100µm)	2.7 ± 0.6 ($x10^{-9}$)	0.7854	**0.3 ± 0.1**
MEA (20µm-1D)	5.7 ± 1.7 ($x10^{-6}$)	491	**1.2 ± 0.3**
MEA (20µm-2D)	2.9 ± 0.8 ($x10^{-6}$)	216	**1.3 ± 0.4**
MEA (20µm-4D)	0.8 ± 0.2 ($x10^{-6}$)	79	**1.0 ± 0.3**
MNEE (20µm-1D)	6.7 ± 0.9 ($x10^{-7}$)	4.91	**13.6 ± 1.8**
MNEE (20µm-2D)	3.1 ± 1.3 ($x10^{-7}$)	2.16	**14.4 ± 6.0**

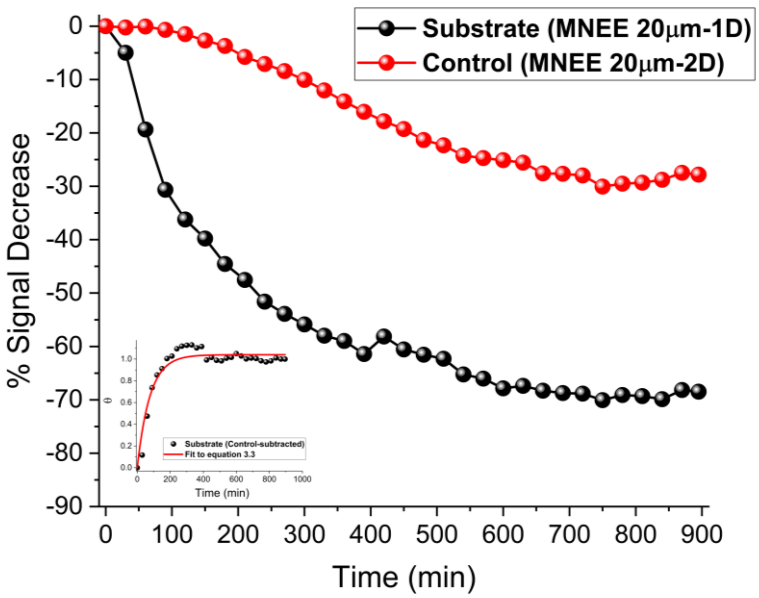

Figure 5-24: Using in-house built MNEE arrays for trypsin sensing. Plot of % signal decrease vs time for SAM-functionalised mono-anchored probe immobilised onto in-house built MNEE arrays (Substrate-modified: MNEE 20µm-1D and Control-modified: MNEE 20µm-2D) upon the addition (at time = 0 min) of 100 nM trypsin in 1x PBS. Inset. Calculated fractional cleavage, θ, vs time plot (Inset) for the control-subtracted substrate data, where its fit to equation 4.3 gives a k_{eff} value of as 0.01302 ± 0.00127 min^{-1}.

5.4.2.3 Issues with Reproducible Measurement using MNEEs

Although MNEE devices have displayed encouraging performance for protease sensing, some issues were experienced during the measurements and they might constitute future challenges if not addressed. Therefore, the problems and possible solutions were investigated, in collaboration with Mr. Daniel Dewar under the programme of EPSRC Vacation Bursary Undergraduate Project.

The first challenge experienced by MNEE-based sensors was due to the sensitivity of nanoelectrodes to the presence of O_2 in buffer solution. As depicted in Figure 5-25, in most of the cases, there is an elevation at the lower potential side of the background due to the O_2 reduction, whereas it should be ideally a Gaussian curve which is centred around $\Delta E_{1/2}$ of the usual potential range for methylene blue. The same situation is sometimes faced during the microelectrode measurements as well, due to the improved sensitivity of miniaturised systems. The presence of this elevated background requires longer analysis times, as background subtraction is usually needed prior to fitting of the data according to Gaussian distribution.

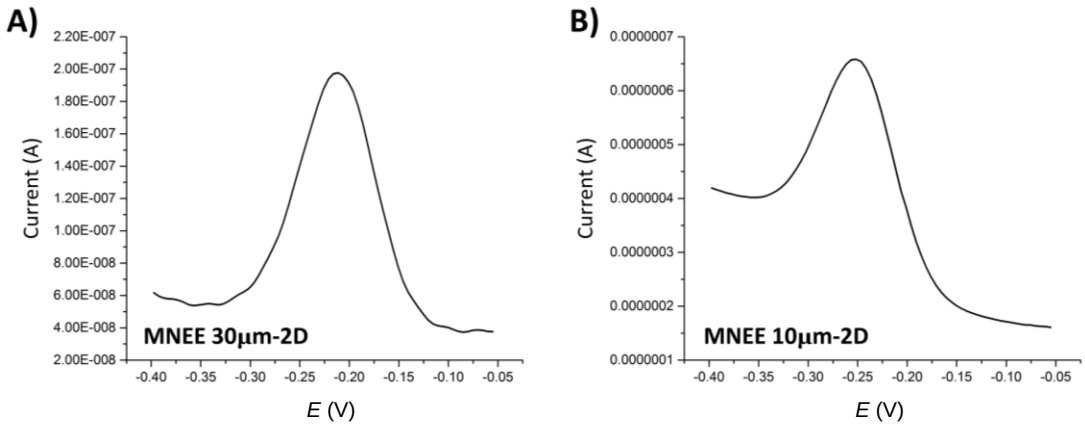

Figure 5-25: A) Ideal SWV curve of a methylene blue-tagged probe where clear Gaussian distribution is centred around $\Delta E_{1/2}$ of the usual potential range for methylene blue. B) However frequently observed SWV response of the probe immobilised onto MNEE arrays shows an elevation at the lower potential side due to the reduction of oxygen in PBS solution.

Moreover, the background does not remain constant and changes over the course of experiments due to the same reason. Figure 5-26A shows SWV data consisting of 240 individual scans recorded with 5 min intervals for an experiment performed overnight, without the addition of the enzyme. As illustrated in Figure 5-26B, five individual scans recorded at varying times of the experiment course were selected from data set and plotted, in order to

exhibit the drastic background change at negative end of the potential window. This drawback of MNEE devices hinders the possibility of automated analysis (peak fitting) of all data using the same algorithm and thus significantly effects the time and effort spent for the extraction of the real MB redox peak.

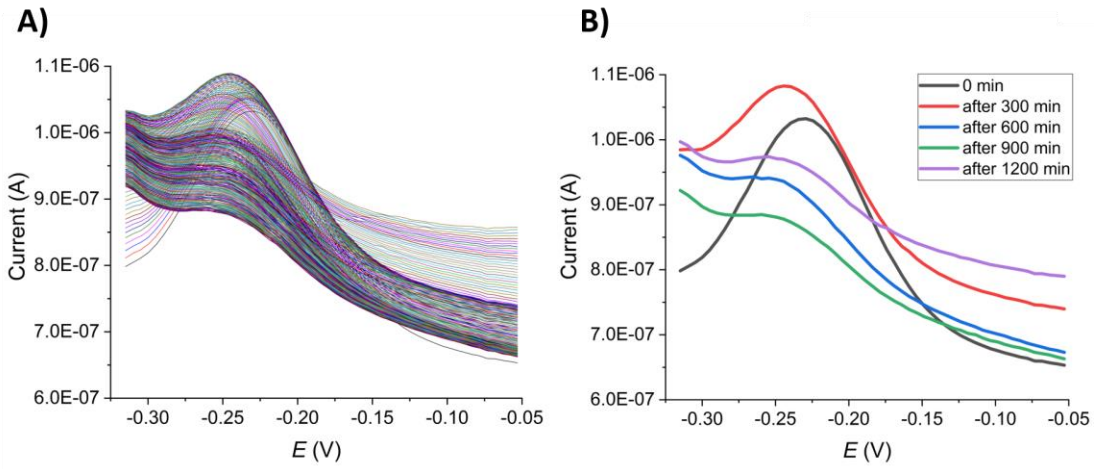

Figure 5-26: A) Typical SWV data (240 scans with intervals of 5 min) which belongs to the substrate-modified probe immobilised onto a MNEE array for an experiment performed overnight, where no enzyme was added. B) Five selected SWV curves over this long experiment period demonstrates how the oxygen background varies over time.

A SWV scan recorded over a wider potential window (from -0.7 V to +0.1 V) can show the peak corresponding to O_2 reduction at -0.6 V and this illustrates how an increase in the amount of this peak effects the background of the MB redox peak (Figure 5-27). As also depicted in the same plot, degassing of the solution with an inert gas such as N_2 or Ar can decrease this background considerably. Because degassing results in a decrease in the amount of O_2 dissolved in the buffer solution, which accordingly provides an easier and reliable data analysis. However, this can only be a temporary solution which can be benefited for bench measurements. Because the future work aims these sensing platforms to be implanted into the body, there is a need for other approaches which can be applicable from a lab-on-a-chip technology, as degassing cannot be a final answer in this case.

Changing the SWV sweep direction was used as another method in order to decrease the amount of background change due to O_2 reduction. SWV scans are normally scanned towards the reductive side, where the sweep goes from 0 V to -0.4 V. The potential is held at 0 V for two seconds to ensure that the MB is returned to the oxidised state prior to its later reduction. However, applying a potential of -0.4 V and then sweeping the potential towards 0 V was

found to reduce the amount of background change over the course of measurements (Figure 5-28). The reason is attributed to the possible depletion of reducible O_2 near the electrode surface, which is most likely due to holding the potential at -0.4 V initially, which should be reducing enough to decrease the available local oxygen.

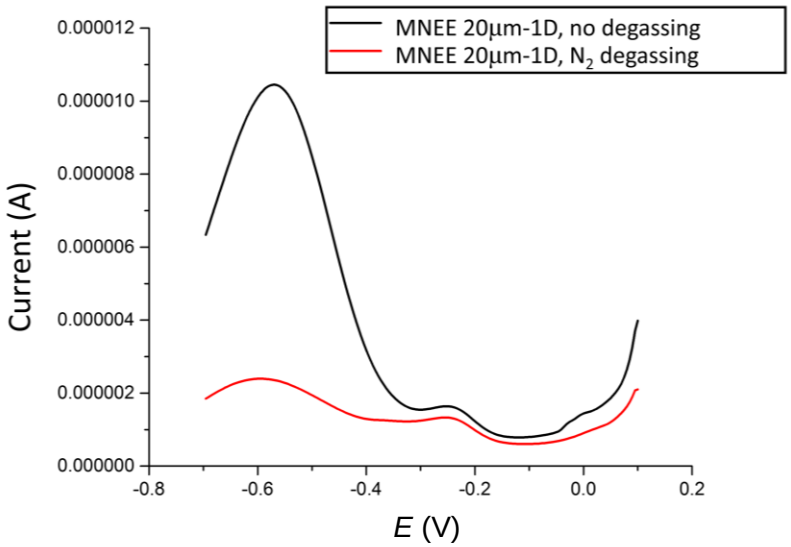

Figure 5-27: Typical SWVs with an extended potential window (-0.7 to +0.1 V) for substrate-modified probe immobilised MNEE 20µm-1D before and after degassing 1x PBS solution with N_2.

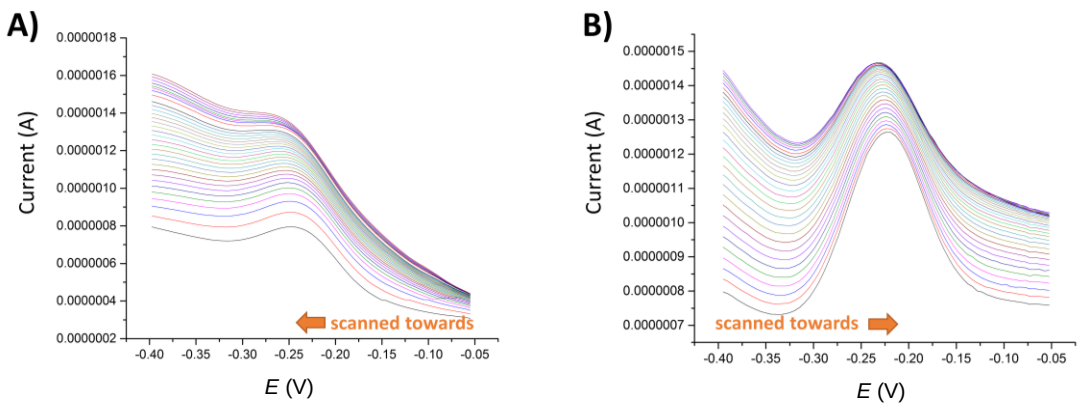

Figure 5-28: A) Typical SWVs performed in the reductive direction (from -0.05 V towards -0.4 V), with the potential being held at -0.05 V for 2s before starting the sweep, compared to the B) SWV curves scanned in the oxidative direction (from -0.4 V towards -0.05 V), with the potential being held at -0.4 V for 2s before starting the sweep, and it has been observed that magnitude of the background decreased dramatically for curves scanned in the oxidative direction.

5.5 Summary

In this chapter, further miniaturisation of the peptide-based protease sensing platform was investigated. This was approached by translating commercial (conventional) bulk macro- and microelectrodes to in-house built Pt thin film electrodes on silicon chips. These electrodes have been grouped with respect to their size and structure and then individually assessed, as single microelectrodes, microelectrode arrays (MEAs) and microcavity nanoband edge electrode arrays (MNEEs). The cleaning procedures and characterisation were primary features which have been discussed for each group, before the evaluation of their performance in trypsin detection, together with encountered problems and possible solutions.

Investigation of superthin track (STT) and thin track (TT) single microelectrodes discovered a major stability problem which significantly limited the detection of trypsin. Optical microscope images of electrode surfaces presented several defects and evidences of metal removal, consistently with the experienced problem. Although the effects of different treatments such as using probes with stronger anchors (tripod-), increasing the metal film thickness and post-fabrication annealing were assessed, any of them could not completely recover the in-house single microelectrode stability. An increased surface roughness due to the electrochemical oxidation and reduction in the acidic cleaning solution was thought to be responsible for the problem, because of the possible Pt surface reconstruction after oxide formation and removal. Therefore, acidic cleaning was replaced with a less-aggressive reductive cleaning technique, which was found to increase MEAs stability and reproducibility. Although MEA findings revealed very promising advances in protease sensing (i.e. easier and reproducible cleaning, improved probe stability, rapid sensing depending on an array structure, enhanced consistency) compared to in-house single microelectrodes, the addition of other concentrations and the characterisation of non-specific binding should be included in future work, for complete analytical evaluation. Also, similar cleavage rates and significantly enhanced electrode current densities were obtained using MNEEs, although some additional drawbacks related to increased background due to O_2 reduction were found. As a result, in-house fabricated electrodes can be designed and used as suitable platforms for the development of peptide-based protease biosensors with enhanced signal-to-noise ratio and sensitivity.

Chapter 6

==========

Potential-Controlled Deposition of SAM-Functionalised Protease Sensors

6.1 Introduction

Self-assembled monolayers (SAMs) have long been an interest of many researchers because of their ready formation and their successful employment in several applications, as detailed in Section 2.4. Typical SAM structures consist of functionalised tails and thiol head groups which can strongly bind to Au/Pt substrate atoms, as previously illustrated in Figure 2-9. The mechanism and kinetics of SAM formation have also attracted attention. It has been found that the initial adsorption and subsequent re-organisation processes and kinetics can be affected by changes in parameters such as temperature, bulk solution concentration, type and chain length of SAMs, and substrate surface cleanliness, morphology and chemistry [147]. This is why, although SAM formation has been widely studied and is established, deconvolution of the effects of surface processes and the resulting SAM film structural variety can quite easily become challenging. SAMs are commonly deposited using incubation of a clean gold substrate with an organic-based solvent including SAM-forming molecules. It is often found that initial adsorption rapidly results in 80-90% of surface coverage within second to minutes, dependent on concentration, with further coverage continuing at a slower rate thereafter [332]. For example, an evaporated Au film surface was seen to be almost completely covered with dodecanethiol (2 μM in hexane solution) within the first 5 min [333]. In another study [11], the initial and fastest step of SAM formation was related to the strong chemisorption of the headgroup onto the substrate surface, which is followed by chain straightening in a 3-4 times slower second step and further chain re-organisation in a 35-70 times slower final step. Therefore, it has been claimed that typical high fidelity SAM coverage can take hours and even days [334].

Controlling SAM adsorption kinetics and mechanism as well as decreasing these required timescales is considered vital in order to enhance their applicability and to create preferentially-patterned substrates [335]. Given that the gold metal surfaces typically have uncontrolled potentials (and hence surface charges and energies), fixed by the likely variable redox composition and potential of the SAM deposition solution, this has led to studies focused on potentiostatic (potential-controlled) selective SAM adsorption and desorption. For example, Riepl *et al.* have performed capacitive monitoring of SAM thiols (mercapto-hexanoic acid and octadecanethiol) which were found to be chemisorbed onto Au microelectrode arrays at +0.3 V vs SCE, but only physisorbed when the applied electrode potential was -1.4 V after 100-200 min [336]. In similar work, +0.4 V vs SCE applied over 5 min was found to result in the best film integrity when forming a *n*-dodecanethiol SAM [337]. Ma *et al.* deposited C_{16} RS SAMs onto Au substrates from a 5 mM solution in only 15 min

applying potentials between +0.2 and 0.6 V vs Ag/AgCl [338]. In addition to these thiol studies, the effect of potential in controlling SAM adsorption/desorption and film formation was also studied when using different types of SAM head groups (thiol, dithiolane, thioester, disulfide and thiosulfanate) [339] and different substrates (Au, Pt and Pd) [328]. A combination of applied anodic and cathodic potentials was found to enable the selective deposition of one of two different redox tag (ferrocene)-labelled SAM molecules from the same bulk solution each onto two individual electrodes [329]. This was then extended to the immobilisation of single-stranded DNA on Au surfaces by employing potential pulses for 15 min [340].

Accordingly, the proof of concept work presented in this chapter aims to analyse the applicability and feasibility of an active, potential-controlled technique in creating enhanced probe-modified surfaces in comparison to the ones provided by passive overnight incubation.

6.2 Effect of Potential on SAM Probe Deposition

Commercially available (Metrohm Dropsens UK, Section 3.3) screen-printed electrodes (SPEs) were used for the experimental work in Chapter 6 and Chapter 7. Due to the differences between the commercial SPEs (formed from a screen printed gold ink) and in-house microfabricated electrodes (formed from deposition of pure platinum films), some significant differences for these SPEs in e.g. electrode material composition and/or distribution, electrochemically-active area, surface cleanliness might be expected. This has been observed previously [341], and in order to mitigate this, the SPEs were cleaned using the protocol developed in [341]. This involved cycling the potential (performing 10 cyclic voltammograms) between 0 and +1.6 V at 100 mV/s in 0.1 M H_2SO_4. Although the size of the peaks per unit area in these cleaning CVs were sometimes different across SPE batches and compared to microfabricated electrodes, they were found to be similar and self-consistent within the same SPE batch following cleaning. Still, in order to avoid any remaining issues which may arise from such peak size variations, the changes in the resulting signals were always defined as the normalised percentage, where possible, instead of the actual current values. This followed the approach in [341] and was thought to be reasonable as such percentage changes should be insensitive to any differences in electro-active area.

In order to measure the effect of applying a potential to the gold working electrode when depositing SAM-functionalised probe, 100 µl of 40 µM mono-anchored substrate probe

(Section 4.2) in 1x PBS was drop-cast onto a horizontally oriented and electrochemically-cleaned (see Section 3.4.1 for protocol) Au screen printed three electrode system with a Au working electrode of 4 mm-diameter whilst a constant DC potential was applied for 10 min using a chronoamperometry (See Section 2.6.3). The internal Ag pseudo reference electrode and Au counter electrode were used as this volume was sufficient to ensure coverage of all three electrodes and electrochemical control. Although the reference potentials of pseudo REs are typically unknown and highly dependent on the solution, the difference between the internal SPE pseudo RE used here and an external Ag/AgCl (3M KCl) was measured as only ~18 mV in 1x PBS. After 10 min, each electrode was immersed in 1x PBS solutions to washing off any weakly or non-adsorbed SAM molecules. In order to analyse the amount of adsorbed SAM probe at each applied potential, they were then interrogated with SWV in 1x PBS in the established potential range for peak methylene blue detection (-0.4 V – 0 V, See Section 3.4.3) because each SAM-functionalised substrate probes in the SAM was covalently attached to a methylene blue redox-tag.

Figure 6-1 shows the resulting methylene blue SWV average peak currents registered for 3 replicates, versus applied electrode potential (vs the internal Ag pseudo RE). Although these average peak current values unexpectedly seemed to show an increasing trend when shifting the applied potential to more cathodic potentials, the variation reflected in the error limits was found to increase markedly at and below 0V, such the difference in average values were not statistically significant. These larger deviations can be attributed to variation caused by physisorption at these negative potentials, which would be consistent with the literature findings [329], that thiol SAMS were typically observed to be physisorbed at cathodic potentials, instead of chemically adsorbed. This is consistent with the fact that the most negative potential applied was chosen to be -1.0 V since it was shown that -1.1 V resulted in the reductive cleaning of the electrode surface of SAM molecules (See Section 5.3.1). In contrast, the peak currents were found to be similar and with much reduced experimental errors between +0.2 V and +0.6 V. This we attribute to a region where stronger adsorption, potentially chemisorption is occurring. Moreover, at larger anodic values e.g. +0.8 and +1.0 V, there was a progressive decrease in the signal obtained. Only negligible signals were registered, consistently for all replicates, which was most likely due to Au oxidation resulting in the progressive change of the surface to Au-O and decrease in SAM sorption strength. Consistent average peak current values and high reproducibility within the replicates obtained at +0.2, +0.4 and +0.6 V therefore indicate that this potential range is preferable for potential-controlled SAM probe deposition.

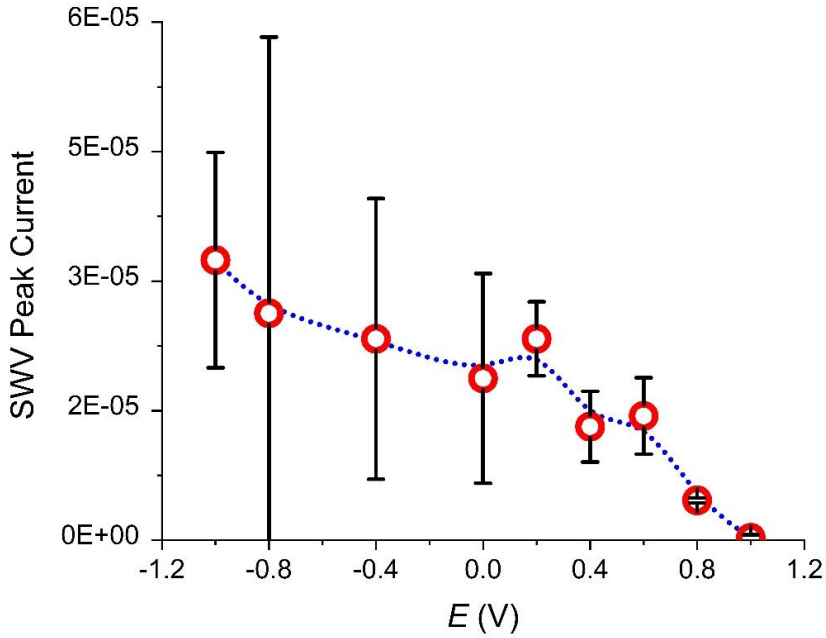

Figure 6-1: The dependence of the methylene blue SWV peak current on the electrode potential applied to the Au SPEs over 10 min of SAM probe deposition. All data points typically represent the average and standard deviation for 3 replicates.

As well as determining surface coverage from the relative number of probe molecules electrochemically detectable, given the relatively short deposition time, the degree of surface electrode blocking is another related parameter which should be characterised, as this should be independent of probe orientation and electrode accessibility. In order to do this, an electrode coverage test was carried out by using the soluble redox couple ferri/ferrocyanide. Figure 6-2 shows cyclic voltammograms of bare and probe-modified (overnight passive incubation, -1.0 V, +0.2 V and +0.6 V) electrodes recorded in 5 mM potassium ferri/ferrocyanide in 1x PBS between potentials of -0.2 and +0.5 V at a scan rate of 100 mV/s. The bare electrode showed the expected and characteristic macroelectrode response for a reversible redox reaction. For all probe-modified electrodes, although there were also oxidation and reduction peaks which are indicative of electrode redox reaction, they were decreased in height and more separated. This confirms that SAM-functionalised probe molecules have not completely passivated the electrode surface but clearly affected the reversibility of the electron transfer reaction. This effect was largest for the probe deposited with the potential at +0.6, followed by the non-potential controlled overnight incubation, -1.0V and +0.2 V. Although this data on its own does not establish an optimum deposition method, since more surface coverage might not indicate the best orientation and performance for trypsin cleavage, it is interesting that

potential controlled deposition at +0.6 V for 10 minutes produces a greater response than overnight, non-potential controlled functionalisation.

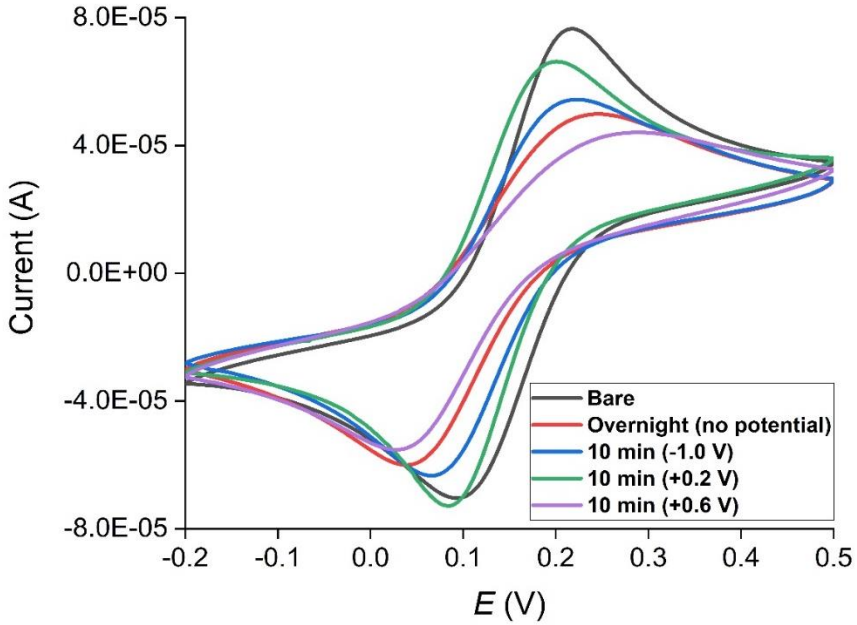

Figure 6-2: Cyclic voltammograms at electrodes which are bare (black), and have undergone overnight non potential controlled SAM deposition (red) and potential-assisted SAM deposition (at -1.0 V: blue, at +0.2 V: green, at +0.6 V: purple) in 5 mM potassium ferri/ferrocyanide in 1x PBS between potentials of -0.2 and +0.5 V at a scan rate of 100 mV/s.

6.3 Trypsin Sensing Performance of Deposited SAM Probes

The best way to understand the feasibility of potential-assisted deposition technique was to perform an experiment to analyse the trypsin sensing performance of deposited probes. Figure 6-3 presents background-subtracted SWV curves registered for overnight deposited and potential-controlled (at +0.2 V) deposited probes before addition of the enzyme as well as the percentage signal decrease against 100 nM trypsin registered for the overnight incubated probes in comparison to the potential-assisted deposited probes at -1.0 V and +0.2 V. It is interesting that the variation in percentage signal decrease between the replicates of overnight incubated probes was higher than the short time potential-controlled SAM deposition. Also, higher SWV peak height registered for 10 mins at +0.2V compared to overnight with non-potential control is worth noting. These confirm that a more reproducible SAM film has resulted in a more reproducible trypsin performance. It is interesting that the mean percentage signal decreases for all of these data were found to be the same within experimental error.

That's why the fractional cleavage (Figure 6-3 Inset) of the probes and the effective rate constants were calculated using equation 4.3 and found to be 0.0083 ± 0.0002 min^{-1} for overnight incubation, 0.0085 ± 0.0002 min^{-1} for -1.0 V and 0.0083 ± 0.0001 min^{-1} for +0.2 V applied potential. It has been found that these calculated effective rate constants were the same with each other (within experimental errors) as in their average percentage signal decreases recorded. This suggested that the extent of the probe molecules deposited onto electrode surface might not be much effective on the cleavage rate, unless the surface is dilute enough so as not to hinder either redox tag-electrode interactions or trypsin binding and proteolytic cleavage. As a result, non-potential deposition runs overnight and produces more variation, whereas potential-controlled technique takes ten minutes and results in less variation with similar cleavage kinetics. These findings thus confirmed the feasibility of using potential-assisted SAM adsorption technique in the development of SAM-based biosensor systems.

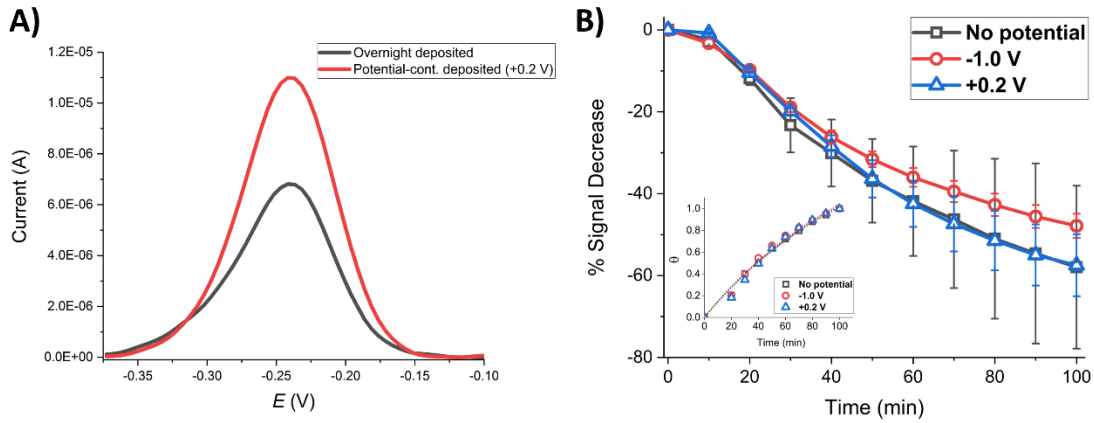

Figure 6-3: Characterisation of the trypsin sensitivity after potential-assisted probe deposition onto Au SPEs in comparison to overnight incubation: A) Background-subtracted SWV curves registered for overnight deposited and potential-controlled (at +0.2 V) deposited probes before addition of the enzyme. B) Percentage signal change registered for overnight deposited (No potential, black squares) and potential-controlled deposited probes (at -1.0 V for 10 min: red circles or at +0.2 V for 10 min: blue triangles) after the addition of 100 nM trypsin at time = 0 in 1x PBS. All data points typically represent the average and standard deviation for 3 replicates. Inset: Calculated fractional cleavage, θ, vs time plots for the same data.

6.4 Summary

Potential-controlled SAM deposition technique was investigated in a comparative manner to the commonly used probe incubation method. Preliminary proof of concept results revealed that potential-controlled deposition can provide faster SAM immobilisation onto surfaces, more reproducible SWV peak currents and same biosensing performance. All probes deposited on the electrode surfaces via applied potentials (between +0.2 and +0.6) under the shorter deposition times were found to be redox-active, trypsin-accessible and cleavable to the same extent as those prepared using the usual overnight incubation, which clearly highlights the usefulness of this proposed technique. Combination of this method and reductive cleaning can selectively functionalise individual electrodes in an array on the 10 minute timescale, which will open a way for practical SAM deposition and selective functionalisation with different control and non-control protease sensor SAMs on different electrodes.

Chapter 7

Dissolvable Polymeric Coatings for Protection of SAM-functionalised pH and Protease Sensors

7.1 Introduction

The applicability of electrochemical biosensors integrated with wearable [342], [343] or implantable [344], [345] platforms for the detection of many different analytes, both *in vitro* and *in vivo*, has attracted widespread attention owing to the many advantages detailed in Section 2.2. However, foreign body response is still a major challenge for implantable electrochemical sensing devices. Specifically, if an implanted device needs to be used for long periods of time, biofouling can cause the sensor transducer (electrode) surface to become passivated by fibrous capsules and non-specific proteins (See Section 2.3.2). This significantly limits the potential of *in vivo* electrochemical biosensing in complex biological media [127].

Accordingly, there is growing research interest in order to avoid biofouling by minimising material-tissue interactions and/or protecting the implantable sensing systems. Some of these are shown in Figure 2-8, and include a variety of approaches based on polymers, hydrogels, SAMs, MEMS and even fluidic systems [346].

Polymers have been widely used in medical devices and implants due to their easily-controllable chemical, electrical and thermal properties [347]. Mostly because of this ease of control, they are often synthesised/fabricated as biocompatible materials unlike other alternatives such as the metals and ceramics used in packaging. Also, polymers are typically soft materials due to their lower Young's modulus values and thus can be fabricated in any size or shape on demand [348]. There are different groups of polymers which can be coated on electrode surfaces to minimise biofouling, largely by reducing interactions between the electrode surface and proteins/cells [138]. For example, hydrophilic polymers like polyethylene glycol (PEG) form a hydration layer which has been found to act as a physical barrier for protein adsorption [349]. Also, zwitterionic polymers were shown to have some additional advantages over hydrophilic polymers, such as the ability to form stronger hydration layers, biodegradability and lower immunogenicity [350]. Conducting polymers can be also used to reduce biofouling [351]. For example, polypyrrole (PPy) and polyaniline (PANI), when combined with PEG, were shown to significantly enhance the fouling resistance against BSA adsorption [352]. Another study suggested the development of an antifouling electrochemical dopamine sensor, where glassy carbon electrodes were modified with a conducting polymer, poly(3,4-ethylenedioxythiophene) (PEDOT) doped with a water insoluble ionic liquid, 1-ethyl-3-methylimidazolium bis(trifluoromethylsulfonyl)imide [353]. This enabled the detection of dopamine with a LoD of 33 nM in the presence of several proteins and in human serum. Despite not being studied as commonly as other types,

hydrophobic polymers might also hold significant potential for antifouling coatings. Xue *et al.* showed that fluorinated methacrylate molecules fabricated on poly(ethylene terephthalate) (PET) fabrics via surface-initiated atom transfer radical polymerization, with alterations of their wettability based on polymerisation time, were effective in improving surface antifouling properties [354]. In addition to these approaches, there are other polymeric coatings like Nafion [355], polyvinyl chloride (PVC) [356], poly(1,3,5-tris(3-indolcarbonyl)benzene) (PTICBL) [357] and copolymers of a poly(vinylidene fluoride) (PVDF) and poly(oxyethylene methacrylate) (POEM) [358] who act as selective membranes by allowing only the target analytes to permeate to the electrode surface and blocking the transport of other non-specific macromolecules, thus minimising the onset of biofouling.

Recently, Montiel *et al.* reported delayed activation and the enhancement of the anti-biofouling characteristics of bare and enzyme (glucose oxidase)-embedded carbon paste electrodes through coating the surfaces with biocompatible, methacrylate-based pH-responsive transient polymers [359]. The capability of these polymeric coatings was characterised in undiluted blood and saliva samples in terms of the delayed activation and the anti-biofouling enhancement of glucose sensing [359]. This approach was then translated into sensing in other biologically relevant media such as gastric (pH ~ 1.5) and intestinal (pH ~ 6.5) fluids [360].

Based on these advancements, the development of such transient polymeric coatings could be applicable to other biosensing platforms. Therefore, in this chapter, the delayed activation and anti-biofouling characteristics of Eudragit® S100 (Evonik Industries) commercial pH-responsive polymers coated on gold screen printed electrodes (Au SPEs) were investigated. Building on the desirability of compatibility with the new pH [361] and protease (trypsin) sensor system developed in this thesis (Chapter 4), enabled by self-assembled monolayer (SAM)-functionalised recognition probe system studies, results will be presented concerning the optimisation and performance of these coatings both on bare and SAM-functionalised electrodes, along with a discussion of the applicability of this work to *in vivo* biosensing.

7.2 pH-Activated Polymeric Coatings: Eudragit®

Poly(meth)acrylate-based polymer formulations have been commercialised, produced and distributed under the Eudragit® brand of Evonik (Nutrition & Care GMBH) Industries since 1954 [362]. They are used for drug release, mainly for three types which are: (i) immediate,

(ii) delayed and (iii) time-controlled (sustained), which are controlled by the formulation (chemical structure) of the respective polymer as shown in Figure 7-1.

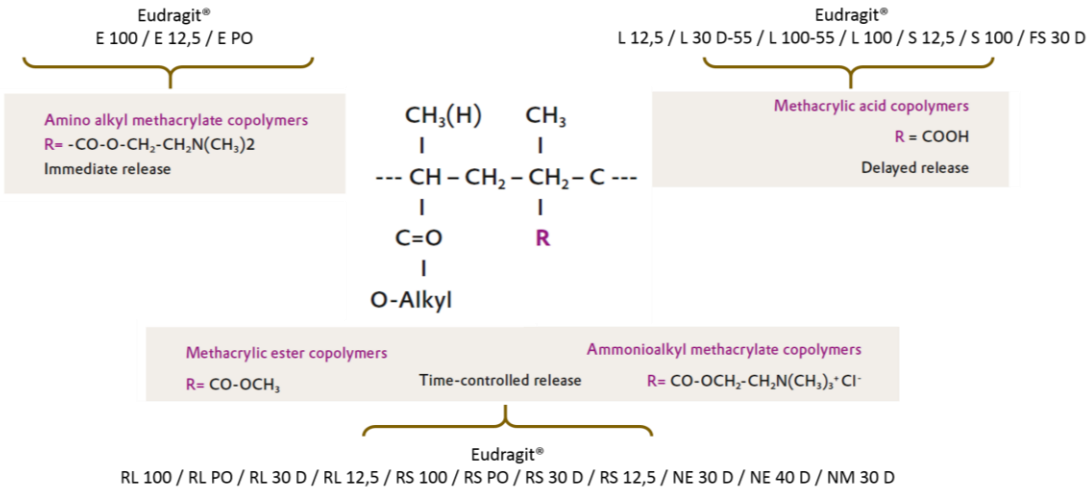

Figure 7-1: Chemical structures of Eudragit® polymers and their enabling of various types of drug release. Adapted from [362].

Eudragit® L and S type polymers (L12,5 / L 30 D-55 / L100-55 / L100 / S 12,5 / S100 / FS30 D) which provide delayed release are typically preferred for the drugs targeted toward gastrointestinal (GI) systems, as the stomach is a highly acidic environment which would decrease the efficiency of some drugs if they were not protected [363]. Also, as delivery to different locations in the GI system might be required for targeted clinical purposes, a family of Eudragit® polymers has been produced which achieve delayed release by becoming activated and dissolving above a specific pH value; e.g. Eudragit® L100-55 (powder form) and Eudragit® L30 D-55 (aqueous dispersion form) dissolve in the duodenum above pH 5.5, Eudragit® L100 (powder form) and Eudragit® L12,5 (organic solution form) dissolve in the jejunum around pH 6.0-7.0, Eudragit® S100 (powder form), Eudragit® S12,5 (organic solution form) and Eudragit® FS30 D (aqueous dispersion form) dissolve in the ileum above pH 7.0 [362]. Here Eudragit® S100 (powder form) was selected for the studies found in this chapter with PBS used as a buffer solution for majority of the experiments since its pH of 7.4 was already high enough to cleave the polymer, leading to activation and dissolution.

Eudragit® S100 (molecular weight, MW ~ 125 kDa) is a solid, anionic copolymer consisting of methacrylic acid and methyl methacrylate in a ratio of approximately 1:2, (Figure 7-2) [364].

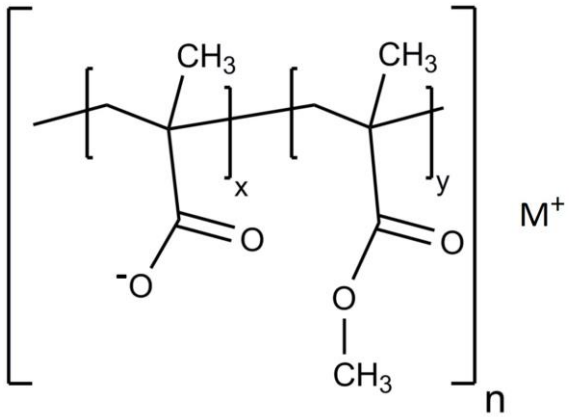

Figure 7-2: Chemical structure of Eudragit® polymer. The ratio (x:y) of methacrylic acid and methyl methacrylate units is approximately 1:2 for Eudragit® S100, whereas n shows the degree of polymerization. Counter ion, M, can be a sodium or a potassium ion found in PBS. Adapted from [364].

The mechanism behind the pH-dependent dissolution of Eudragit® S100 polymers was explained by Nguyen *et al.* as occurring in five main steps [365]:

i. H_2O and -OH diffuse into the polymer matrix and form a gel layer
ii. polymer chains in the gel layer become ionised
iii. chains start to disentangle from the gel layer and move to the polymer-bulk solution interface
iv. polymer chains at this interface are further ionised
v. disentangled polymer chains diffuse from the interface and dissolve into the bulk solution.

Accordingly, the main reason behind the pH-responsivity of Eudragit® S100 polymer is the presence of weakly acidic carboxyl groups which are initially uncharged in the acidic environments and then become charged at values greater than their pKa ~ 4 and start to disentangle and diffuse into bulk solution, as suggested by Vinner *et al.* and illustrated in Figure 7-3 [366]. In addition, in higher pH values, the hydrolysis product of ester groups can produce negatively charged carboxylate groups, which can enhance the rate of disentangling.

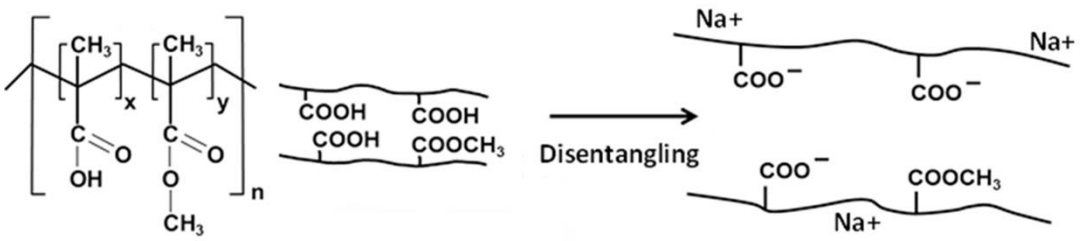

Figure 7-3: Mechanism for Eudragit® S100 dissociation due to weakly acidic functional groups, followed by electrostatic repulsion and polymer swelling. Adapted from [366].

7.3 Characterisation of Polymer Dissolution

The protocol of polymer modification on bare or probe-modified Au SPEs was detailed in Section 3.5. Briefly, 10 μL of Eudragit® S100 polymer powder was dissolved in isopropanol (IPA) at specific concentrations (8, 16 or 32% (w/v)) and was drop-cast onto a modified or an unmodified (bare) electrode surface, either as a single layer or successive deposition of consecutive layers (1-layer, 2-layers or 3-layers) of 10 μL following evaporation. After the solvent IPA was evaporated at room temperature, polymer-coated electrodes were incubated in solution (5 mM ferri/ferrocyanide in 1x PBS for bare electrodes, or 1x PBS for probe-modified electrodes, or DMEM-FBS mixture for anti-biofouling characterisation) and subjected to electrochemical characterisation with time using CV and/or SWV measurements in order to monitor the dissolution of the coated polymer layers.

In order to check whether polymer modification of electrodes was achieved, a polymer layer integrity test was performed by recording CVs between -0.1 and +0.4 V at a scan rate of 100 mV/s in 5 mM ferri/ferrocyanide in 1x PBS (Figure 7-4). Comparison of the bare and polymer-coated electrodes showed a significant difference in their responses. The expected complete hindrance of the redox reaction of the external redox agent (ferri/ferrocyanide) was observed with the polymer-coated electrodes, whereas characteristic (peaked) voltammogram responses were obtained for the uncoated bare electrode. This confirmed the successful modification and integrity of the blocking polymer layer coated on these electrode surfaces. It is therefore expected in the following characterisations that all probe-modified electrodes coated with even a single layer of transient polymer should exhibit a zero current initially, since the redox environment underneath the blocking layer will not be solvated before polymer dissolution starts to take place.

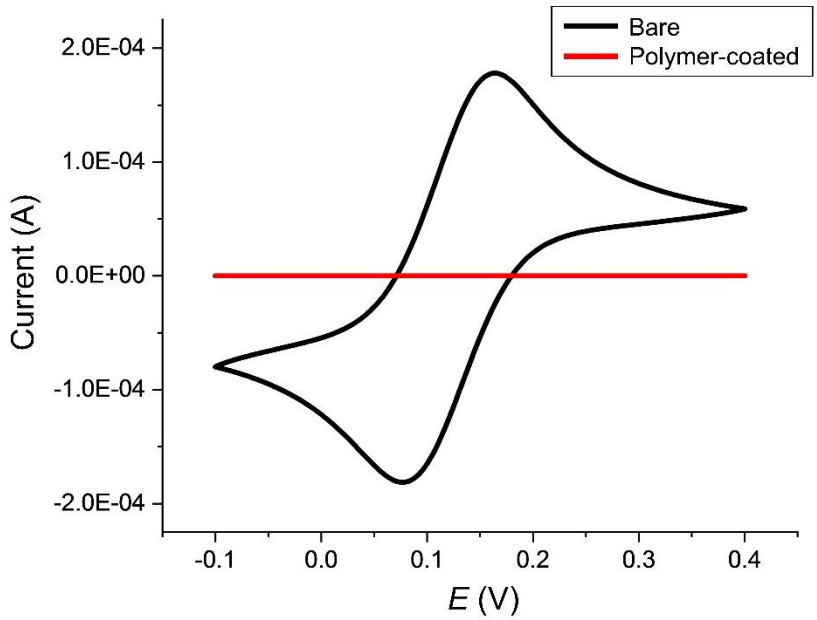

Figure 7-4: CVs of Au SPE recorded in 5 mM potassium ferri/ferrocyanide in 1x PBS, before (black) and after (red) coated with a single layer of 16% Eudragit® S100. CVs were recorded between potentials of -0.1 and +0.4 V at a scan rate of 100 mV/s.

When the modified electrode is immersed into a solution which has a higher pH value than a specific activation pH of the polymer, e.g. 1x PBS with pH 7.4, dissolution should be immediately initiated by diffusion of water and hydroxyl ions directly into the polymer matrix and the change of the solid polymer layer into a gel, by the established mechanism mentioned above. This should promote the progressive and time-dependent activation of passivated (blocked) electrode surfaces until each is completely exposed.

Figure 7-5 shows the voltammograms of a gold SPE coated with a single layer of 16% Eudragit® S100 subjected to potential cycles between -0.1 and +0.5 V at a scan rate of 100 mV/s after immersion in 5 mM potassium ferri/ferrocyanide in 1x PBS at different measurement times between 0 - 180 min at intervals of ~18 min. As expected, the first scan (0 min) registered following the immersion of the polymer-coated electrode into redox solution did not show any peaks attributable to a redox reaction at electrode surface. However, there was a clear difference between the first and second voltammogram recorded after 18 min, which shows redox reaction occurring at electrode surface due to transport of ferri/ferrocyanide redox couple to the underlying electrode surface, most likely through pores formed due to polymer layer dissolution. This redox current then increased with the time which the electrode was incubated in this solution. After 3 hours of incubation, the shape and current

magnitudes of the voltammograms were still not the same as the response observed for the bare electrode in Figure 7-4; the oxidation and reduction voltammogram peak current heights were around 35 µA after 3 hours of dissolution, compared to ~175 µA for the bare surface. Considering that peak current is proportional to electrode area, it can be suggested that only ~20% of the area of polymer-coated electrode was activated in this case. Also, more widely separated peaks in comparison to the bare electrode were seen due to resistance and this suggested that the holes were not completely exposed and the electrode surface was not fully activated. However, less resistive film was generally and progressively obtained due to the solvent (and redox couple) ingress. Of course, it should be noted that these two individual electrode surfaces might not be identical. In addition, there is a significant possibility that polymer coating might be non-uniform due to the simple nature of drop-casting method. Furthermore, it was mentioned before (Section 4.10) that SAM-functionalised probes also exhibited some variations in SWV peak currents, likely caused by the differences in their surface conformations. In order to avoid variations based on any of these, the redox current was monitored until it reached a stable value which is expressed as 100%, and then the relative change (% signal change) were evaluated and plotted versus time, in most of the subsequent experiments unless otherwise stated.

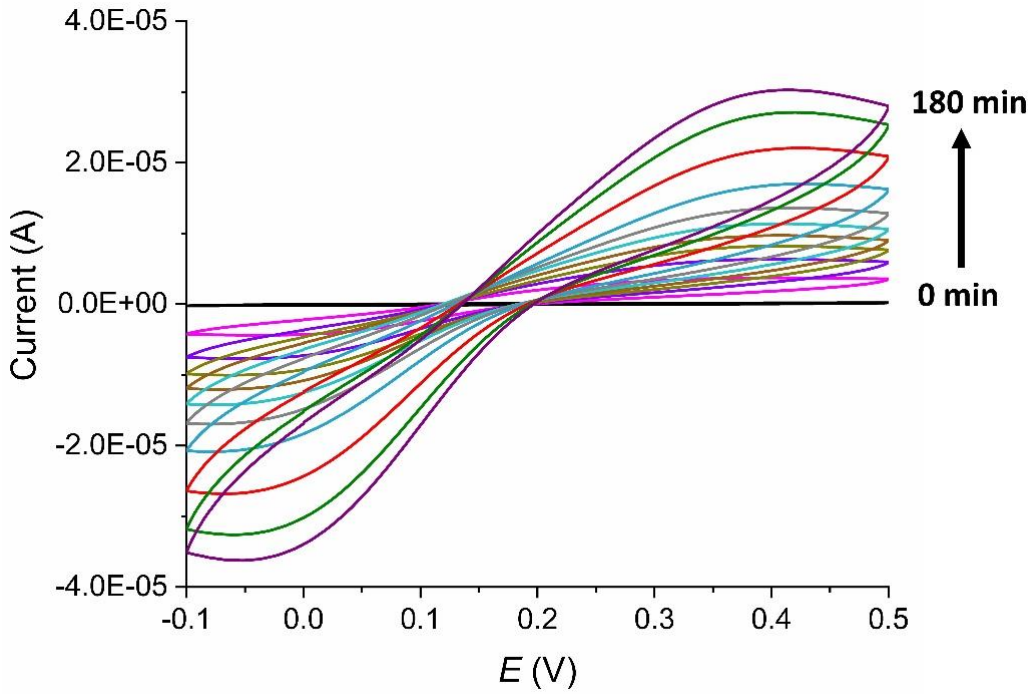

Figure 7-5: CVs of Au SPE coated with a single layer of 16% Eudragit® S100 recorded in 5 mM potassium ferri/ferrocyanide in 1x PBS at different incubation times between 0 - 180 min (with intervals of ~18 min). CVs were recorded between potentials of -0.1 and +0.5 V at a scan rate of 100 mV/s.

In order to check the pH specificity of Eudragit® S100 polymer coatings, two Au SPEs were identically modified with Probe-1 as detailed in Section 3.4.2.1 and Section 7.4, before they were coated with three consecutive layers of 16% Eudragit® S100 and then subjected to SWV characterisation between 0 and -0.4 V (the methylene blue redox potential window) in PBS solutions (i) pH 5.6 and (ii) pH 7.4 for 1000 min. As illustrated in Figure 7-6, there was not any redox signal at all observed for the electrode immersed at pH 5.6, whereas the current for the other electrode immersed in pH 7.4 continuously increased over 1000 min. This was consistent with the previous findings where it was reported that any combination (of L100-S100 mixtures in w/w such as 1:1, 2:3, 1:4, 1:5, 0:1) including 50% or more S100 coating did not release any amount of tested model drug, mesalazine in pH 6.5 phosphate buffer [367]. Eudragit® S100 was already shown to dissolve above pH 7.0 and is employed for drug release in the colon for the treatment of particular diseases such as ulcerative colitis, Crohn's disease, and irritable bowel syndrome [368]; this result further confirms that its activation/dissolution is highly specific to the pH value.

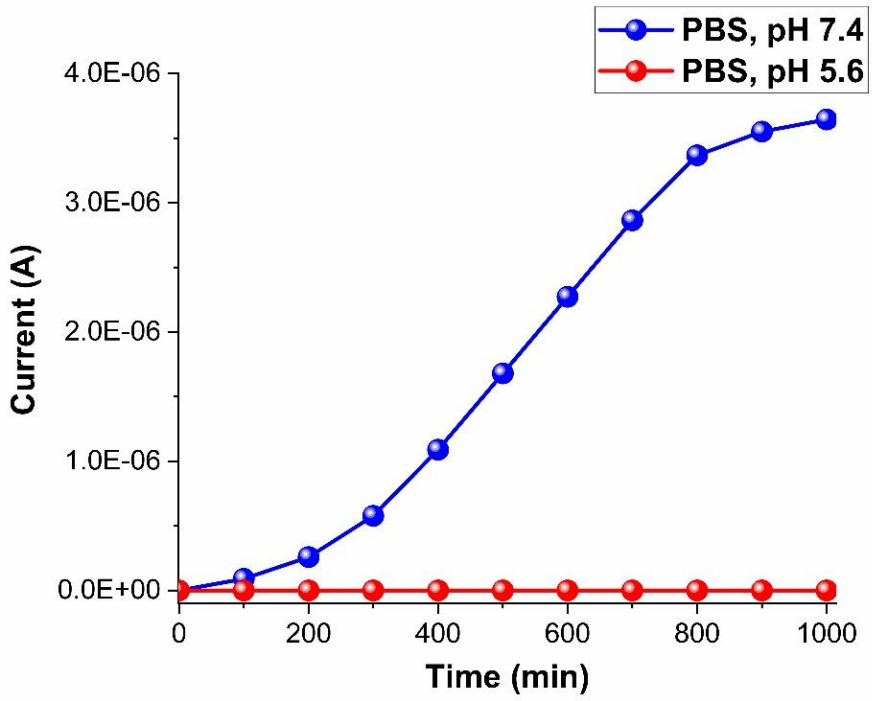

Figure 7-6: SWV peak current vs time registered for Au SPE modified with Probe-1 and then coated with three layers of 16% Eudragit® S100 when incubated in PBS at pH 5.6 (red) and at pH 7.4 (blue) for 1000 mins.

7.4 Applicability to SAM Biosensor Probes

This chapter has been aimed at enhancing the anti-biofouling characteristics of the protease (trypsin) and pH sensor systems, in which SAM-functionalised recognition probes were employed. Therefore, these two different sensing probes (Probe-1 for pH sensing or Probe-2 for trypsin sensing) were also used here to optimise and characterise the performance of polymeric coatings with respect to integration and feasibility of use with SAM-based biosensors (Figure 7-7). The details of the procedures used for chemical synthesis can be found elsewhere [7], [361]. Typically, Probe-1 was employed in the experiments performed for polymer coating optimisations (Section 7.5), because it is already shown in the previous chapters that the tripod-anchor was more robust and stable as an anchor than the mono-anchor. However, Probe-2 was also used, in order to test the feasibility of the approach for trypsin sensing, which can be found in Section 7.6.2.

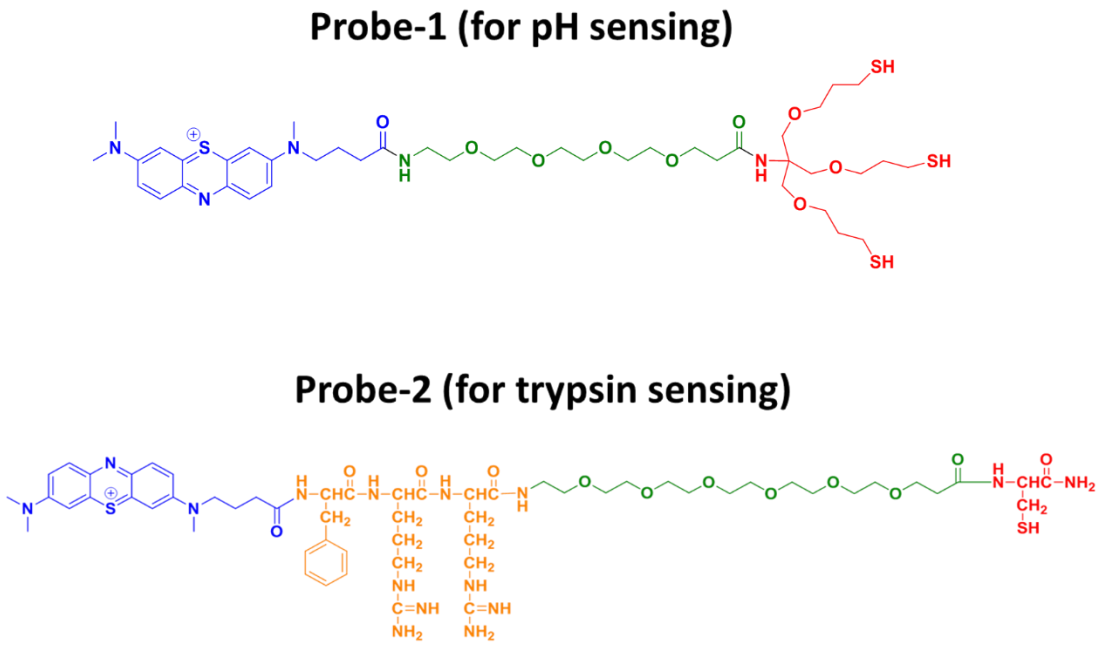

Figure 7-7: Chemical structures of the probes used for pH (Probe-1) and trypsin (Probe-2) sensing. Probe-1 contains methylene blue (blue) as the redox tag, PEG-4 as the spacer and tripod anchor (red) [361]. As detailed in Section 4-2, Probe-2 contains methylene blue (blue) as the redox tag, attached to Phenylalanine-Arginine-Arginine (orange) as the peptide sequence and PEG-6 (green) as the spacer and cysteine (red) as the anchor.

Figure 7-8 shows SWV curves registered for an Au SPE which was modified with the pH sensing probe (Probe-1) by drop-casting overnight and then coated with a single layer of 16% Eudragit® S100, before immersion in 1x PBS solution for 150 min. As clearly seen, the SWV peak current (purple curve) was ~1.1 µA before the polymer layer was drop-cast. However, this decreased to zero as shown by the first scan after the polymer was coated on top of the probe-modified electrode surface. This confirmed that the polymer layer also completely blocked the SAM-modified surface and hindered the redox reaction of surface-bound redox tags in addition to the external redox couples found in bulk solution as observed for bare electrodes. This was attributed to the effects of the resistive surface layer in blocking the electron transfer by stopping counterion and proton transport to the MB from solution and stopping probe flexibility and bending towards the electrode surface.

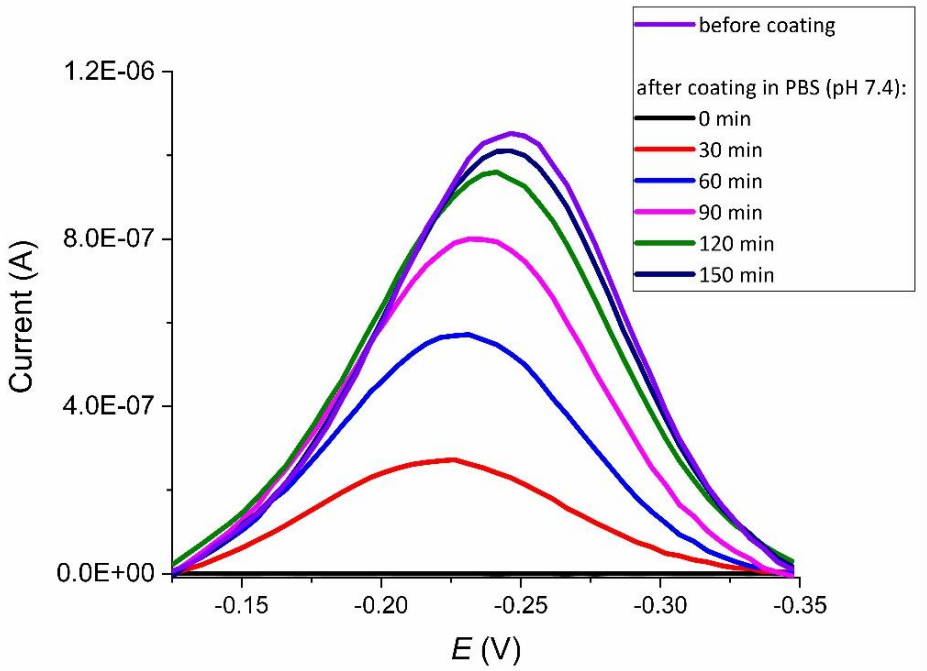

Figure 7-8: SWV curves recorded for an Au SPE modified with the Probe-1 and then coated with a single layer of the 16% Eudragit® followed by its immersion in 1x PBS.

As expected, the signal then increased with time due to dissolution of the polymer layer but unlike previous experiments with redox species in solution, the shape of the redox signal was restored and the blocking characteristics disappeared. It was seen that the registered signal almost returned to the initial, uncoated value within 150 min, suggesting ~95-100% dissolution. It was also observed the dissolution rate was faster initially and converged over time. A difference of ~30 mV in the SWV peak potentials between uncoated electrode and the

coated electrode (red line, after 30 min dissolution) suggests a clear difference in their redox environment. This difference in peak potentials disappeared when the polymer dissolved over time, which might be thus attributed to the local pH change or electron transfer alterations due to changes in the local solvation environment and/or conformational changes in SAM-based probes.

7.5 Optimisation

Dissolution time could change depending on factors such as the thickness of the coating layers and the concentration of the drop-cast polymer solution. The effects of these two factors on the transiency behaviour of polymeric coatings have been investigated previously, when bare carbon SPEs were drop-cast with a single layer (3 μL of 4, 8 or 16% (w/v)) or consecutive layers (3 μL of 16% (w/v)) of polymeric solution onto the electrode surface [359]. However, this had not been done for any SAM-modified sensor electrodes systems. Therefore, it was important to understand how thickness and concentration affected the polymer dissolution time and performance in this order to optimise and control these parameters for future *in vivo* SAM-based biosensor protection applications.

7.5.1 Layer Thickness

The influence of the thickness on polymer dissolution time was examined after modified Au SPE surfaces with Probe-1 were coated with a number of layers using 16% (w/v) solution. Figure 7-9 presents optical microscope images of a region of the coated area for each electrode (1-layer, 2-layer or 3-layer). As clearly seen in the figure, increasing layer thickness resulted in a more uniform polymer coating, which can be suggested by the reduced number of surface defects such as holes and hillocks. Although these images were taken from randomly chosen areas, it was confirmed that they were representative and comparable across the whole surfaces of each electrode.

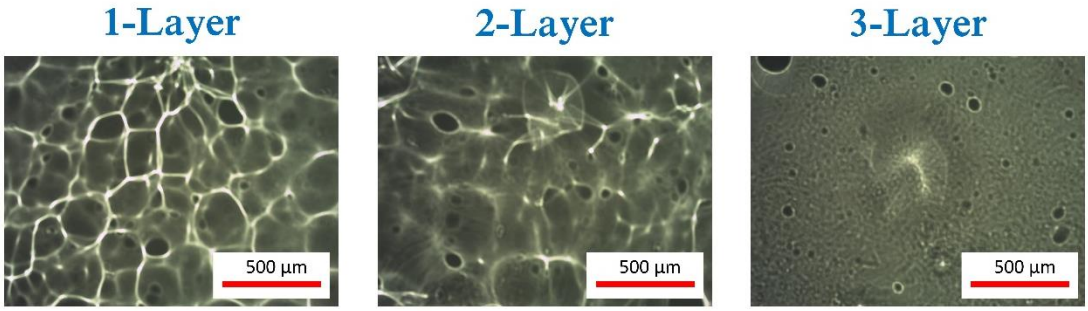

Figure 7-9: Optical microscope images of Au SPEs drop-cast with consecutive layers (1-Layer, 2-Layer and 3-Layer) using 10 µL of 16% (w/v)) of the Eudragit® S100 polymeric solution for each layer.

Figure 7-10 shows the percentage signal changes vs time registered for these different Au SPEs modified with Probe-1 and the number of (1, 2, and 3) layers of the 16% coating. It can be easily seen that polymer dissolution (electrode activation) can be delayed by more than 20 hours when using 3 layers of the polymeric coating, while one layer of coating exposes the sensor surface within 2-8 hours. However, there is a significant variation between identically prepared electrodes, especially the ones coated with 1 or 2 layers. This was attributed to that the films included variable defects which were non-uniformly distributed on the electrode surfaces, as also represented by optical images above. This variability was, however, reduced for the electrode modified with three layers of the coating, most likely due to the filling of the defects in underlying films by the subsequent layers.

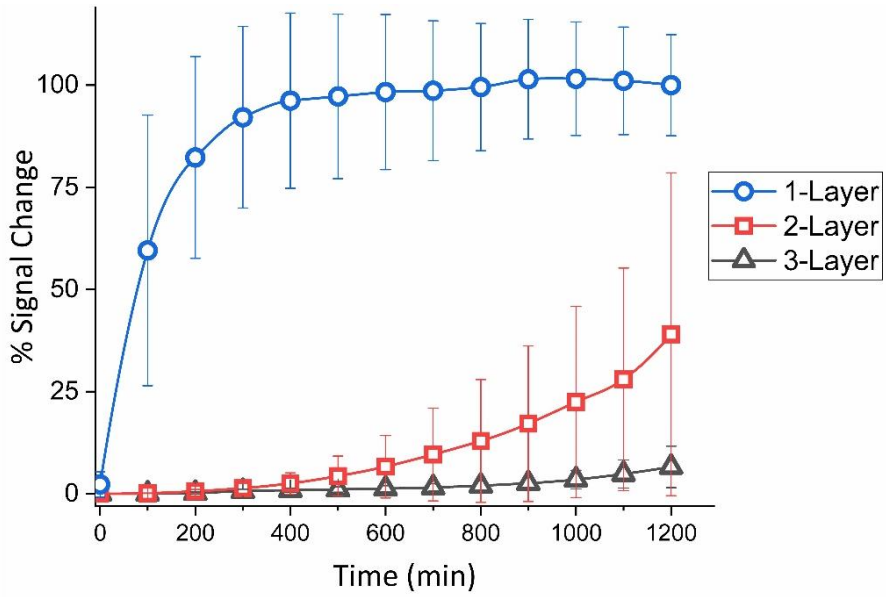

Figure 7-10: The relationship between % signal change (referred to polymer dissolution time) and layer thickness, examined by the redox signal registered for Probe-1 modified Au SPEs coated with different numbers of layers (1, 2 or 3-L) of a 16% solution and immersed in 1x PBS over 1200 min and interrogated with SWV. The averages and error bars are for three replicates.

7.5.2 Concentration

The influence of the polymer layer concentration was analysed by employing different Au SPEs each identically modified with Probe-1 and then coated with single layers which contain different weight to volume percentages (8%, 16% or 32%) of the S100 polymer. Figure 7-11 exhibits the dependency of the resulting polymer dissolution time on the concentration, which seems to be an inversely proportional relationship as the volume drop-cast was fixed. Especially for the concentrations of 8% and 16%, exposure rate was observed to be linear within experimental errors, which might suggest that changing concentration is more controllable than multiple layer deposition. It was observed that the polymer layers coated from solution with concentration of 8% completely dissolved in only 30 minutes, with almost no variation between the responses of replicates. The signal decrease of around 20% after full exposure in 30 min was interesting and statistically significant, but was only experienced in this case. It may indicate longer term changes in redox probe environment in this solution alone, but more measurements would be required to confirm this. It was observed that although both 16% and 32% coatings were both fully exposed in around 3 hours the initial activation rate was markedly slower for 32%.

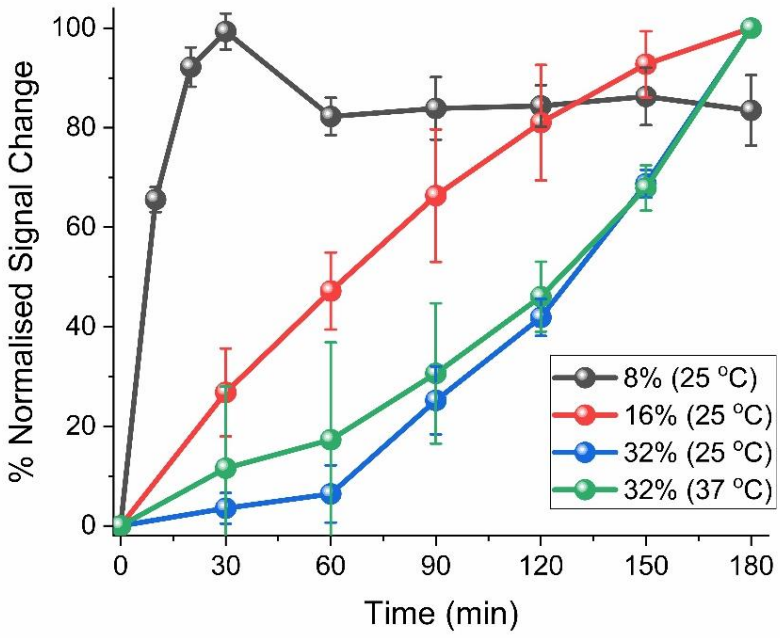

Figure 7-11: The relationship between % normalised signal change (referred to polymer dissolution time) and concentration, examined by the redox signal registered for Probe-1 modified Au SPEs (three replicates for each) drop-cast with a single layer of Eudragit® solution in different concentrations (8%, 16% or 32%) followed by immersion to 1x PBS over 3 hours and interrogation with SWV. The averages and error bars are for three replicates.

In addition, another three replicates were prepared with 32% coating and tested at 37 °C in order to understand whether temperature has an effect on the dissolution rate. Although the increase in temperature might have resulted in the enhanced dissolution rate in first 60 min, it was not as effective as expected in long time points, showing the same percentage signal changes within experimental errors. It is, however, worth noting that larger variations were seen between replicates compared to the ones characterised at 25 °C, particularly for early time points. In summary, these results were promising in terms of the potential to control polymer dissolution times (and corresponding extent of delay in sensor activation) by fine-tuning of the preparation/fabrication parameters.

7.6 Biofouling Protection

After demonstrating the ability to control delayed sensor activation, the anti-biofouling protection characteristics of these polymeric coatings were investigated. To achieve this, polymer-coated (or uncoated as a control) pH and trypsin sensors were prepared on Au SPEs and tested at 37 °C in Dulbecco's Modified Eagle Medium (DMEM) including 10% fetal bovine serum (FBS) which mainly consists of proteins such as BSA and growth factors, and is commonly used for *in vitro* biofouling characterisation [369]. The anti-biofouling protective properties (Figure 7-12) were evaluated by comparing electrochemical signal from polymer-coated and uncoated samples with time, and then determining the pH or trypsin sensing performance of polymer-coated sensors after sufficient time to expect complete polymer dissolution.

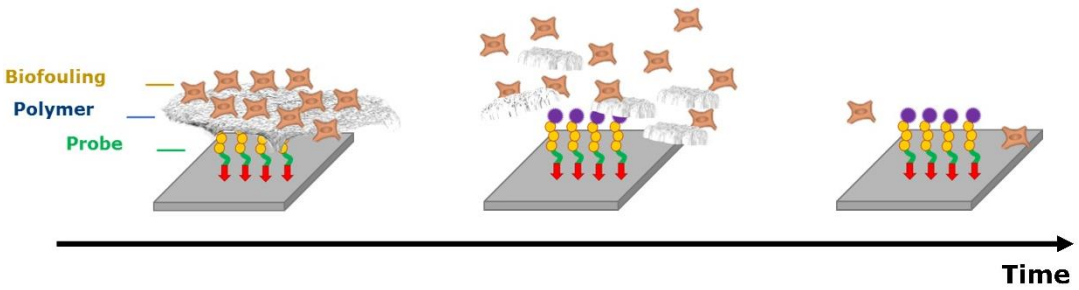

Figure 7-12: Illustration of the determination of the anti-biofouling protection of the SAM-based sensors through the dissolution of the polymeric coatings.

7.6.1 pH Sensor Protection

The development as well as *in vitro* and *in vivo* characterisation of MB-based pH sensors can be found elsewhere [361]. Briefly, the sensor was developed by depositing a SAM-functionalised film of probe molecules (Probe-1) onto microfabricated three-electrode chips packaged with a biocompatible epoxy in order to monitor tumour microenvironment pH in real-time based on the established pH-specific variation of the redox behaviour of MB [370]. In vitro test results exhibited a linear dependency between the peak potential of the MB reduction and the pH, giving -26 mV/pH; the expected Nernstian behaviour for a 2 e- / 1 H+ redox process. Some of the chips also included Nafion as a top layer on these probe-modified electrodes given that it is a widely used cation-exchange polymeric membrane. The use of Nafion resulted in a better pH sensitivity, showing larger than two-fold change in the calibration line, which was -68.0 mV/pH. This was attributed to Nernstian behaviour for a 2 e- / 2 H+ redox process due to a shift in the pKa of reduced MB arising from the negatively charged nature of Nafion membrane. Although the sensor system also exhibited very promising results when tested *in vivo* through implantation into ovine pulmonary adenocarcinoma (OPA) cases, it was established that better anti-biofouling protection approaches are needed for long term measurements. This is why the feasibility of transient polymeric coatings were now investigated.

Figure 7-13 shows the relative changes in the SWV peak current of the polymer-coated and uncoated pH sensors over 1100 min. The signal registered for the uncoated sensors decreased rapidly by 65-70% within this time range consistent with non-specific binding reducing the electrochemical signal, whereas the polymer coated sensors showed a signal which continuously and reproducibly increased with time, without ever decreasing. Because the polymer-coated sensors are not likely to anywhere near fully exposed at 1100 mins according to the finding (less than 10% of signal recorded for 3 layers after 1200 min) as shown in Figure 7-10, the relative signal changes was normalised with respect to the final measured signal, instead of the expected 100% signal. This means that the polymer is still on top of the probe molecules without fully exposure but with some opened channels providing the redox interactions. While the dissolution is still occurring, the fact there was not any indication of signal decrease due to non-specific protein binding onto these coated surfaces on this timescale clearly suggests enhanced anti-biofouling is provided by these transient polymeric coatings.

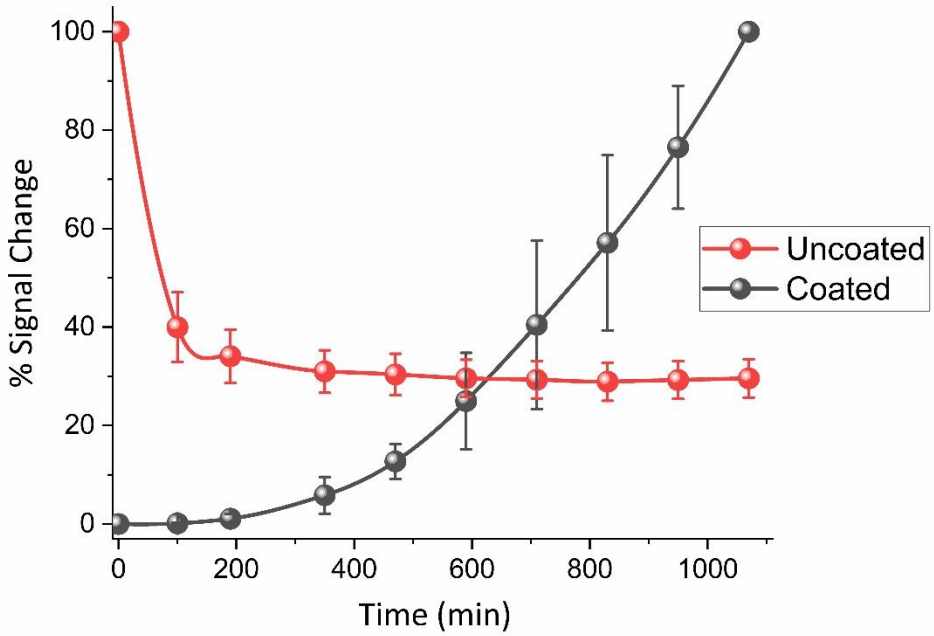

Figure 7-13: % Signal changes registered for the polymer-coated (three consecutive layers of 16% Eudragit®) and uncoated pH sensors (Au SPEs modified with Probe-1) in DMEM inc. 10% FBS (pH = ~7.2). The averages and error bars are for three replicates.

It was of course significant for protected and activated sensor systems to show comparable sensing performances after the polymer was dissolved. Therefore, another experiment was performed to check the pH sensitivity of the exposed sensors, using the same method as previously reported [361]. As shown in Figure 7-14A, Nafion-coated and uncoated pH sensors were placed in phosphate buffers with varying pH's (5.8, 6.2, 6.8, 7.2 and 7.6) and interrogated with SWV. Afterwards, the peak potential of MB redox signal was plotted against pH to create a calibration line for pH response (Figure 7-14B). This resulted in pH sensitivities of 36 ± 2 mV/pH for Nafion-uncoated and 39 ± 4 mV/pH for Nafion-coated sensors. It was interesting that Nafion did not show any significant difference in potential-pH sensitivity this time rather a difference in potential offset, and that the slope observed was midway between $2e^-$ 2H+ and $2e^-$ $1H^+$ behaviour. Although there is not any evidence to confirm, this might be an indication of possible interaction between Nafion and Eudragit® S100 polymers which might have altered the redox behaviour of MB.

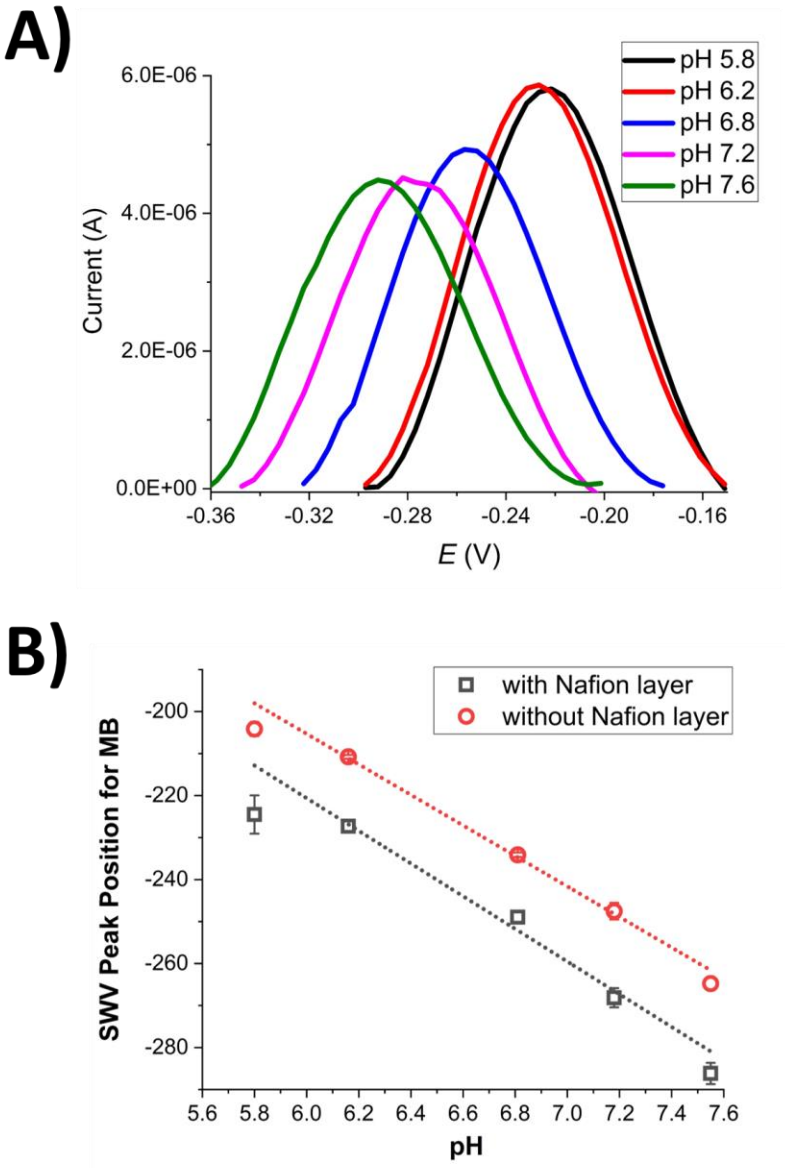

Figure 7-14: Characterisation of the pH sensitivity after complete polymer dissolution. A) Square wave voltammograms registered for Nafion-coated pH sensors immersed in phosphate buffered solutions with varying pHs: 5.8 (black), 6.2 (red), 6.8 (blue), 7.2 (magenta) and 7.6 (green). B) Calibration line of MB redox (average of reduction and oxidation) potentials registered for Nafion-coated and uncoated sensors versus the solution pHs. All data points typically represent the average and standard deviation for 3 replicates and straight lines correspond to the best linear fits.

7.6.2 Trypsin Sensor Protection

Similar to anti-biofouling characterisations performed for pH sensors, trypsin sensors were also prepared (modifying Au SPEs with Probe-2 and either coated with a single layer of 16% Eudragit® on top or uncoated for control) and subjected to SWV measurements in DMEM including 10% FBS. Figure 7-15 shows the relative changes in the SWV peak current of the polymer-coated and uncoated trypsin sensors over 250 min. The reason why less incubation time was used this time is that a single layer of polymer was coated instead of three consecutive layers in this case and it was shown in the optimisation section that ~3-4 hours would be enough to obtain an exposed surface (Figure 7-11). The signal registered for the uncoated sensors decreased by 70-75% after 250 min whereas a continuous increase was observed for the coated surfaces again. The signal decrease of ~60% obtained in first 100 min for uncoated sensors was consistent and similar for both pH and trypsin sensor experiments, suggesting that most of the non-specific protein adsorption takes place in this period. As expected, the signal registered for the polymer-coated trypsin sensors increased over 250 min although there are some variations between the replicates. These variations are similar in magnitude (Figure 7-9) and can again be related to non-uniformity of the single polymer layer, which might have caused an inhomogeneous dissolution of the layer surface. Even so, this further confirmed that dissolvable polymeric coatings also improve anti-biofouling characteristics of these sensors.

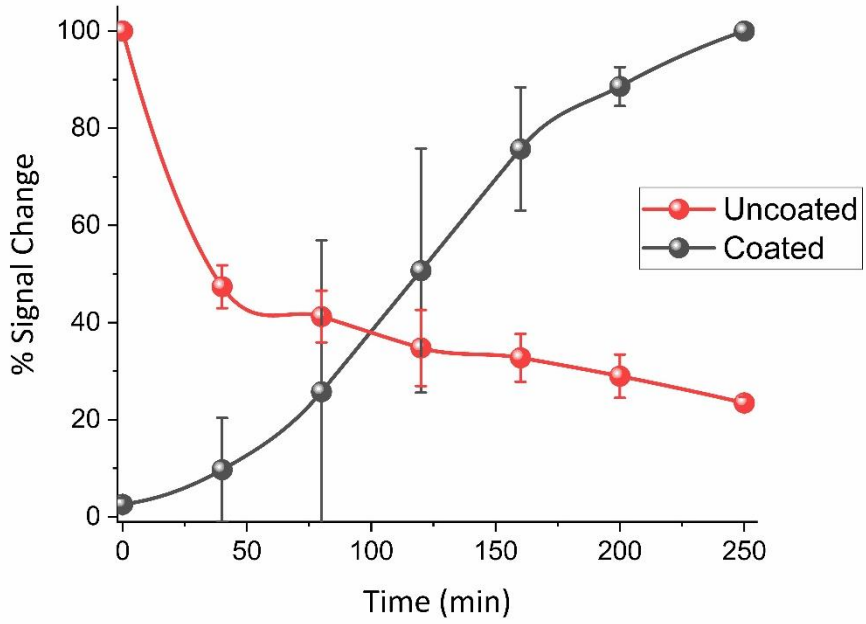

Figure 7-15: % Signal changes registered for the polymer-coated (with a single layer of 16% Eudragit®) and uncoated trypsin sensors (Au SPEs modified with Probe-2) in DMEM inc. 10% FBS.

As shown in Figure 7-16, the percentage signal decrease registered for the polymer coated trypsin sensor against 100 nM trypsin was measured and compared to a typical trypsin sensor response which was not coated with polymer. Although they presented comparable signal decreases of around 55% after ~90 min of incubation with 100 nM trypsin enzyme, it can also be seen that the rate was slightly slower and have more variation for the polymer-coated system. It was found to be 0.026 min^{-1} when calculated using the same method detailed in Chapter 4, whereas the typical uncoated sensor gave 0.058 min^{-1}. Despite the fact that the polymer-coated sensors were left in 1x PBS for a day before this experiment to secure complete dissolution, some polymeric residues could be still present in close proximity to SAM-functionalised probe molecules, which might have resulted in this variation and reduced rate constant. In the future other trypsin concentrations should also be investigated in order to better understand the effect of polymer coating integrity and dissolution on the kinetics of protease cleavage on the exposed SAM film.

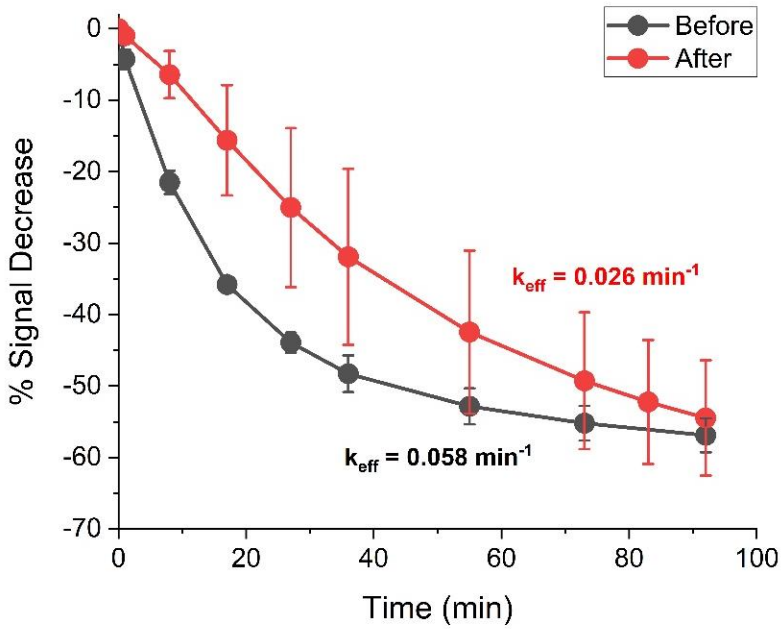

Figure 7-16: Characterisation of the trypsin sensitivity after complete polymer dissolution. Percentage signal change registered for uncoated (Before, black line and data points) and polymer-coated (After, red line and data points) trypsin sensors after the addition of 100 nM trypsin at time = 0 in 1x PBS. All data points typically represent the average and standard deviation for 3 replicates.

7.7 Summary

In this chapter, the applicability of adding dissolvable pH-activated commercial polymeric coatings onto our already established trypsin and new pH sensors was evaluated in terms of their anti-biofouling characteristics. The enhancement in the anti-biofouling properties of both sensing platforms, particularly at short times within the first 100 mins was observed when they were tested in biologically relevant medium. The delay in sensor exposure and activation was found to be vital for avoiding the effects of rapid non-specific protein adsorption. By optimising the thickness and concentration of coated polymeric layers, delay times were shown to be increased to up to 20 hours with a potential of further increases. Analytical performance of polymer-coated SAM sensors (both pH and trypsin) were comparatively characterised before and after complete polymer dissolution. Although the sensitivity of Nafion-coated pH sensors apparently slightly decreased and the apparent rate constant for 100 nM trypsin detection reduced, all sensor platforms were still redox-active and sensitive to the target analytes. Together, these promising findings offer potential for translation to *in vivo* biosensing. Future work will focus on ways to further increase and control delay times and to integrate these coatings with in-house built devices.

Chapter 8

==========

Conclusions & Future Work

8.1 Summary

This thesis has presented research on the development and miniaturisation of an electrochemical peptide-based protease sensor along with a study to determine and potentially enhance anti-biofouling properties. The sensing principle was recently established and is based on the signal change due to the proteolytic cleavage by trypsin (a model protease used previously and in this study) of a SAM-functionalised peptide sequence, leading to the removal of the labelled redox tag, methylene blue.

This biosensor platform was previously optimised and characterised by employing commercial Au macroelectrodes; however, the use of this metal is problematic when using microfabrication to design and fabricate integrated micro and nanoelectrode systems such as those studied in this thesis. As even trace gold is known to affect microelectronic device performance, gold is typically prohibited within microelectronic fabrication centres such as the Scottish Microelectronics Centre. Therefore, the first part of this research focused on the development of the same platform on commercial Pt macroelectrodes, building as far as possible on the gold surface optimisations which have been outlined in detail. The results indicated that both macroelectrode platforms behave comparably; they exhibit quite similar SWV peak potentials (~ -0.20 V), peak currents (3-4 μA) and current density values (~1 A/m^2) which suggests no effect of changing the electrode metal in terms of SAM-functionalised probe film formation. This is important, and consistent with the fact that both Au-S and Pt-S bonds are strong. To assess the potential for sensor miniaturisation, this was then followed by the assessment of the protease sensing performance of these SAM films on both commercial Pt microelectrodes and Pt macroelectrodes. Despite a few further microelectrode-specific optimisations (regarding the treatment time of the backfilling MCH and concentration of the third component, DT), the probe design, probe concentration and protocols were kept unchanged. The characterisation and analysis of the response demonstrated that comparable analytical performance to Pt macroelectrodes was observed with commercial platinum microelectrodes, with respect to the trypsin accessibility and specificity, with a comparable K_M of (15 ± 3 nM) from a Michaelis-Menten surface cleavage model, which suggests a comparable surface binding energy. It was interesting that there was less variations between electrode response compared to macroelectrodes, which suggests more reproducible SAM probe film formation and conformation for microelectrodes. In addition, microelectrode-based sensing system gave a quantitative response covering the clinically relevant trypsin concentration range for both normal and disease states. However, the kinetics of enzyme cleavage, also analysed according to the Michaelis-Menten model was found to be k_{cat} (0.0075

min^{-1}) at 25 °C, which is lower than that observed on Pt macroelectrodes of k_{cat} (0.035 min^{-1}). Although this proteolytic cleavage rate was significantly slower for microelectrodes at room temperature, it was observed to be markedly increased at the normal body temperature (37 °C) applicable to implantation. Some interesting differences were found between macroelectrode- and microelectrode-based platforms. The SWV peak potential for microelectrodes was found to be around -0.27 V which is ~70 mV lower than macroelectrodes. Comparable binding constants suggested that there should not have been any difference in the cleavage rates, unless the enzyme accessibility to probe molecules have been satisfied. Therefore, the differences in peak potentials and cleavage rates were attributed to the distinctions between macro- and microelectrodes in terms of SAM film structures. This was suggested by the lower catalytic efficiency (k_{cat}/K_M) observed for microelectrodes, likely resulting from less probe accessibility to the active site of the enzyme and thus leading to decreased probe reactivity, although absolute and relative enzyme-substrate association and dissociation rates appeared similar for both electrodes. This accessibility difference could be resulted from geometric and/or orientational reasons e.g. enzymes bound near microelectrode edge interact with less probe molecules which are able to interact with the active site. Furthermore, microelectrode-based sensing system was shown to be relatively insensitive to the adsorption of non-specific proteins, which opens up the prospect of measurement in complex biological media.

In order to further develop the implantability of this biosensor platform and assess the effect of moving from micro to nanoelectrodes, Pt thin film electrodes were fabricated in-house on silicon chips. These included thin track (TT) and super thin track (STT) single microelectrodes, microelectrode arrays (MEAs) and microcavity nanoband edge electrode arrays (MNEEs). The addition of arrays for analysis was in order to increase the data set of electrodes for wider assessment and also to increase the overall currents through combining the response of many electrodes. For each group of electrodes, they were initially electrochemically-cleaned, characterised with external (freely diffusing in solution) redox couples and finally modified with sensing probes and analysed in terms of trypsin detection performance. Investigation of TT and STT single microelectrodes discovered a major stability problem which hindered proper trypsin detection, because signal decreases were observed for both substrate and control probes, even without added enzyme. Optical microscopy revealed some surface defects and metal loss, which correlating with the problem. In order to enhance the probe film stability, different treatments e.g. more strongly (tripod-) anchored probes, increasing the metal film thickness and metal film post-deposition annealing were tried. These could not completely recover the in-house microelectrode stability, although post-annealing in particular helped a little. The main underlying problem leading to this issue was attributed

to the increased surface roughness due to the electrochemical oxidation and reduction in the acidic cleaning solution, through surface reconstruction driven by Pt oxide formation and removal. This was confirmed by replacing this with a simpler reductive cleaning technique which also enabled real-time monitoring of the surface cleanliness through an external redox couple included in solution. Reductively cleaned MEAs then exhibited increased stability, reproducibility and comparable trypsin sensitivity. Comparable cleavage rates and enhanced electrode current densities were obtained using MNEEs, but the background due to O_2 reduction significantly increased which made the data analysis more difficult. Therefore, there was no additional advantage in using MNEEs, instead of MEAs. Overall, this systematic study confirmed the feasibility of in-house microfabricated electrodes as platforms for peptide-based SAM-functionalised probes and protease detection.

Given the observed dependency of conditions on SAM film formation and response, and the likely effect of an electrode potential on this, it is interesting that later, promising results were obtained which showed that applying a controlled potential to the working Au electrode can promote more reproducible SAM probe film formation (compared to standard overnight incubation) in a shorter timescale of 10 min. Although all probes deposited at a wide potential range were observed to be trypsin sensitive with similar cleavage rates, slight anodic potentials (+0.2, +0.4 and +0.6 vs Ag pseudo RE) were seen to give more consistent and reproducible signals.

The second aspect of this work was to focus on the creation of biofouling protection for the sensor platform. In order to achieve this, commercial biocompatible polymers developed for controlled release drug delivery purposes and triggered by pH selective dissolution, were assessed with a view to incorporating these into our biosensors. Two biosensors platforms were used; the trypsin sensor (detailed throughout this thesis) and recently developed pH sensor which employs the pH dependency of a thiol-terminated methylene blue redox tag as a SAM film. Initial experiments varying the thickness and concentration of the polymeric coatings showed the possibility of 20 hours and more delay in complete sensor exposure, and variation of the length and reproducibility of this delay with control of surface thickness and deposition method. Comparative evaluation of polymer-coated and uncoated trypsin and pH sensor samples in biologically relevant medium revealed the detrimental effects of non-specific protein binding within first 100 mins on uncoated electrodes, which were found to be markedly reduced on polymer-coated sensors. Post-dissolution performance tests confirmed that both polymer coated sensor platforms were still redox-active and sensitive against trypsin and pH.

Together, this PhD research has demonstrated progress towards the development, miniaturisation and biofouling protection of this peptide-based SAM-functionalised electrochemical biosensor system for trypsin, which has been demonstrated to be able to sense trypsin concentration across the whole clinically relevant range. In this way, the biosensor capabilities have been enhanced as a step towards implantation into solid tumours to monitor real-time changes in biomarker quantity and activity, which would lead to the personalisation of cancer treatment. Although this development was largely designed for protease (trypsin) detection here, the need for miniaturisation and protection is more universally applicable and, as the biofouling pH studies indicate, these results can be applied to other analytes. This emphasises a wider contribution to the biosensing field. Combining with the future work suggested below, this could enable the move to clinical trials and *in vivo* biosensing.

8.2 Future Work

8.2.1 Translation to Detection of Other Proteases

Trypsin enzyme was chosen as a model protease in this work because it is widely studied enzyme with well-understood properties. Also, it plays vital roles in digestion and has links to some diseases including pancreatitis, cystic fibrosis and cancer. However, there are other significant proteases e.g. MMPs, caspases and cathepsins which have clear links to many cancer processes, as discussed in Chapter 2. Although there are several works in the literature showing their electrochemical peptide-based detection, most of these have employed macroelectrodes. Therefore, the miniaturisation strategy presented here could also be applied to detect these proteases, which can be enabled by changing the peptide sequence used here (Phe-Arg-Arg) to another sequence which is specific to a target protease. Of course, if the binding sequence were longer than three amino acids (and even if it weren't), such changes might affect the SAM formation mechanism and structure as well as cleavage kinetics. In this case, the experimental protocols might require some additional optimisations.

8.2.2 Enhancing the Development of Array-Based Sensing

Although microelectrode arrays (MEA) and microcavity nanoband edge electrode (MNEE) arrays have been briefly shown to be convenient for protease sensing in addition, it would be useful if, as with the commercial screen printed electrode systems, they could be fabricated as a three-electrode system with on-chip reference (Ag/AgCl) and counter electrodes (Pt), because external electrodes could be used with a finalised implanted device. Following this, to assess the potential for multiparameter binding, potential-assisted deposition should be investigated for these array systems. If an array is divided into some parts including electrodes and these parts are connected to different individual working electrode contact pads, they can be separately and selectively modified with different types of probes (substrate vs control, or specific for different proteases) using potential-assisted deposition technique (e.g. by applying a negative potential for desorption/avoiding adsorption or positive potentials for adsorption).

8.2.3 Controlling Surface Chemistry to Avoid or Promote Protein/Cell Adhesion

Even if the biosensor is incorporated with pH-triggered dissolving polymeric coating, biofouling of electrodes and/or system surfaces can still occur, after complete coating dissolution, in the complex medium experienced by an implanted sensor. One aspect to consider is the altering and controlling the charge and wettability characteristics and thus cell/protein adhesion on these surfaces. Given that SAM molecules with varying functionalised end groups e.g. -OH, $-NH_2$, -COOH, $-CH_3$ can exhibit different surface wettability and charge, these can be used to enhance anti-biofouling properties of the biosensor systems. Specifically, the advancements in the potential-assisted SAM deposition technique can enable their selective patterning onto electrode surfaces and/or surrounding locations in order to control protein/cell surface attachment and biofouling which would be of benefit in progressing towards implantation.

List of Figures

List of Tables

Glossary

Variables and Constants

A(t): Percentage of signal left to change at time t
a: Concentration-dependent variable
A: Electrode area
C: Concentration
D: Diameter/Diffusion constant
E: Potential
E_a: Activation energy
F: Faraday constant

f: Frequency
f_p or θ: Fraction of product
i: Current
k: Rate constant
k_{cat}: Turnover number
k_{eff}: Effective rate constant
K_M: Michaelis-Menten constant
N: Number of electrodes
n: Number of electrons
r: Radius
R: Universal gas constant
SD: Signal decrease
T: Temperature
t: Time
V: Voltage
Γ: Surface coverage
v: Scan rate
υ_{max}: Maximum rate (velocity)
Ψ: Dimensionless parameter

Acronyms / Abbreviations

BSA: Bovine Serum Albumin
CA: Chronoamperometry
CE: Counter (Auxiliary Electrode)
CV: Cyclic Voltammetry
DMEM: Dulbecco's Modified Eagle Medium
DT: 2,2′-(ethylenedioxy)diethanethiol
EIS: Electrochemical Impedance Spectroscopy
FBGC: Foreign Body Giant Cells
FBR: Foreign Body Response
FBS: Fetal Bovine Serum
Fc: Ferrocene
FFC: Ferri/Ferro Cyanide
HNE: Human Neutrophil Elastase
ISO: International Organisation for Standardisation
LMB: Leuco-Methylene Blue
LoD: Limit of Detection
MB: Methylene Blue
MCH: 6-Mercaptohexanol
MEA: Microelectrode Arrays
MEMS: Micro Electro Mechanical System
MMP: Matrix metalloproteinase
MNEE: Microcavity Nanoband Edge Electrode

MW: Molecular Weight
NO: Nitric Oxide
PBS: Phosphate-Buffered Saline
PEG: Polyethylene Glycol
PPy: Polypyrrole
PSA: Prostate-Specific Antigen
RE: Reference Electrode
Redox: Reduction-Oxidation
SAM: Self-Assembled Monolayers
SECM: Scanning Electrochemical Microscopy
SERS: Surface-Enhanced Raman Scattering
SPE: Screen-Printed Electrodes
STT: Super Thin Track
SWV: Square Wave Voltammetry
TT: Thin Track
vdW: van der Waals
WE: Working Electrode

List of Amino Acids

Alanine: Ala, A
Arginine: Arg, R
Asparagine: Asn, N
Aspartic acid: Asp, D
Cysteine: Cys, C
Glutamic acid: Glu, E
Glutamine: Gln, Q
Glycine: Gly, G
Histidine: His, H
Isoleucine: Ile, I
Leucine: Leu, L
Lysine: Lys, K
Methionine: Met, M
Phenylalanine: Phe, F
Proline: Pro, P
Serine: Ser, S
Threonine: Thr, T
Tryptophan: Trp, W
Tyrosine: Tyr, Y
Valine: Val, V

Bibliography

[1] N. H. S. England, “Improving outcomes through personalised medicine: working at the cutting edge of science to improve patients’ lives.” NHSE, 2016.

[2] S. E. Jackson and J. D. Chester, “Personalised cancer medicine,” *Int. J. cancer*, vol. 137, no. 2, pp. 262–266, 2015.

[3] Cancer.Net, “What Is Personalized Cancer Medicine?,” 2018. [Online]. Available: https://www.cancer.net/navigating-cancer-care/how-cancer-treated/personalized-and-targeted-therapies/what-personalized-cancer-medicine. [Accessed: 05-Jan-2020].

[4] J. R. K. Marland *et al.*, “Implantable microsystems for personalised anticancer therapy,” in *CMOS Circuits for Biological Sensing and Processing*, Springer, 2018, pp. 259–286.

[5] J. S. Dudani, A. D. Warren, and S. N. Bhatia, “Harnessing Protease Activity to Improve Cancer Care,” *Annu. Rev. Cancer Biol.*, vol. 2, no. 1, pp. 353–376, 2018.

[6] I. L. H. Ong and K.-L. Yang, “Recent developments in protease activity assays and sensors,” *Analyst*, vol. 142, no. 11, pp. 1867–1881, 2017.

[7] E. González-Fernández, N. Avlonitis, A. F. Murray, A. R. Mount, and M. Bradley, “Methylene blue not ferrocene: Optimal reporters for electrochemical detection of protease activity,” *Biosens. Bioelectron.*, vol. 84, pp. 82–88, 2016.

[8] E. González-Fernández *et al.*, “Electrochemical sensing of human neutrophil elastase and polymorphonuclear neutrophil activity,” *Biosens. Bioelectron.*, vol. 119, pp. 209–214, 2018.

[9] K. Bazaka and M. Jacob, “Implantable devices: issues and challenges,” *Electronics*, vol. 2, no. 1, pp. 1–34, 2013.

[10] F. Zang *et al.*, “Scale-down effects: Towards miniaturization of an electrochemical sensor using biomolecules,” in *SENSORS, 2013 IEEE*, 2013, pp. 1–4.

[11] C. Vericat, M. E. Vela, G. Benitez, P. Carro, and R. C. Salvarezza, “Self-assembled monolayers of thiols and dithiols on gold: new challenges for a well-known system,” *Chem. Soc. Rev.*, vol. 39, no. 5, pp. 1805–1834, 2010.

[12] S. Nazarpour, *Thin films and coatings in biology*. Springer, 2013.

[13] A. Inmann and D. Hodgins, *Implantable sensor systems for medical applications*. Elsevier, 2013.

[14] B. W. Stewart and C. P. Wild, “World Cancer Report 2014. International Agency for Research on Cancer,” 2014.

[15] A. S. Ahmad, N. Ormiston-Smith, and P. D. Sasieni, “Trends in the lifetime risk of developing cancer in Great Britain: comparison of risk for those born from 1930 to 1960,” *Br. J. Cancer*, vol. 112, no. 5, pp. 943–947, 2015.

[16] “Cancer Facts & Figures 2019,” *Am. Cancer Soc. Atlanta, GA, USA*, 2019.

[17] E. M. Ward *et al.*, “Annual Report to the Nation on the Status of Cancer, Featuring Cancer in Men and Women Age 20–49 Years,” *JNCI J. Natl. Cancer Inst.*, 2019.

[18] D. Hanahan and R. A. Weinberg, “The hallmarks of cancer,” *Cell*, vol. 100, no. 1, pp. 57–70, 2000.

[19] D. Hanahan and R. A. Weinberg, “Hallmarks of cancer: the next generation,” *Cell*, vol. 144, no. 5, pp. 646–674, 2011.

[20] M. C. Brahimi-Horn, J. Chiche, and J. Pouysségur, “Hypoxia and cancer,” *J. Mol. Med.*, vol. 85, no. 12, pp. 1301–1307, 2007.

[21] M. Gray *et al.*, “Implantable biosensors and their contribution to the future of precision medicine,” *Vet. J.*, vol. 239, pp. 21–29, 2018.

[22] M. Nordsmark *et al.*, “Prognostic value of tumor oxygenation in 397 head and neck tumors after primary radiation therapy. An international multi-center study,” *Radiother. Oncol.*, vol. 77, no. 1, pp. 18–24, 2005.

[23] I. F. Tannock and D. Rotin, “Acid pH in tumors and its potential for therapeutic exploitation,” *Cancer Res.*, vol. 49, no. 16, pp. 4373–4384, 1989.

[24] T. Henning, M. Kraus, M. Brischwein, A. M. Otto, and B. Wolf, “Relevance of tumor microenvironment for progression, therapy and drug development,” *Anticancer. Drugs*, vol. 15, no. 1, 2004.

[25] X. Xu, M. C. Farach-Carson, and X. Jia, “Three-dimensional in vitro tumor models for cancer research and drug evaluation,” *Biotechnol. Adv.*, vol. 32, no. 7, pp. 1256–1268, 2014.

[26] J. A. Joyce and J. W. Pollard, “Microenvironmental regulation of metastasis,” *Nat. Rev. cancer*, vol. 9, no. 4, p. 239, 2009.

[27] C. López-Otín and J. S. Bond, “Proteases: multifunctional enzymes in life and disease,” *J. Biol. Chem.*, vol. 283, no. 45, pp. 30433–30437, 2008.

[28] S. D. Mason and J. A. Joyce, “Proteolytic networks in cancer,” *Trends Cell Biol.*, vol. 21, no. 4, pp. 228–237, 2011.

[29] A. G. Porter and R. U. Jänicke, “Emerging roles of caspase-3 in apoptosis,” *Cell Death Differ.*, vol. 6, no. 2, p. 99, 1999.

[30] B. F. Sloane, “Cathepsin B and cystatins: evidence for a role in cancer progression.,” in *Seminars in cancer biology*, 1990, vol. 1, no. 2, pp. 137–152.

[31] A. K. Tandon, G. M. Clark, G. C. Chamness, J. M. Chirgwin, and W. L. McGuire, “Cathepsin D and prognosis in breast cancer,” *N. Engl. J. Med.*, vol. 322, no. 5, pp. 297–302, 1990.

[32] R. D. A. Wilkinson, R. Williams, C. J. Scott, and R. E. Burden, “Cathepsin S: Therapeutic, diagnostic, and prognostic potential,” *Biol. Chem.*, vol. 396, no. 8, pp.

867–882, 2015.

[33] C. M. Overall and C. López-Otín, “Strategies for MMP inhibition in cancer: innovations for the post-trial era,” *Nat. Rev. Cancer*, vol. 2, no. 9, p. 657, 2002.

[34] J. Jankun, S. H. Selman, R. Swiercz, and E. Skrzypczak-Jankun, “Why drinking green tea could prevent cancer,” *Nature*, vol. 387, no. 6633, p. 561, 1997.

[35] J. Jankun, R. W. Keck, E. Skrzypczak-Jankun, and R. Swiercz, “Inhibitors of urokinase reduce size of prostate cancer xenografts in severe combined immunodeficient mice,” *Cancer Res.*, vol. 57, no. 4, pp. 559–563, 1997.

[36] S. Rakash, F. Rana, S. Rafiq, A. Masood, and S. Amin, “Role of proteases in cancer: A review,” *Biotechnol. Mol. Biol. Rev.*, vol. 7, no. 4, pp. 90–101, 2012.

[37] C. López-Otín and L. M. Matrisian, “Emerging roles of proteases in tumour suppression,” *Nat. Rev. cancer*, vol. 7, no. 10, p. 800, 2007.

[38] J. A. Joyce, “Therapeutic targeting of the tumor microenvironment,” *Cancer Cell*, vol. 7, no. 6, pp. 513–520, 2005.

[39] F. Chen *et al.*, “New horizons in tumor microenvironment biology: challenges and opportunities,” *BMC Med.*, vol. 13, no. 1, p. 1, 2015.

[40] F.-G. Banica, *Chemical sensors and biosensors: fundamentals and applications*. John Wiley & Sons, 2012.

[41] J. L. Hammond, N. Formisano, P. Estrela, S. Carrara, and J. Tkac, “Electrochemical biosensors and nanobiosensors,” *Essays Biochem.*, vol. 60, no. 1, pp. 69–80, 2016.

[42] S. Patel, R. Nanda, S. Sahoo, and E. Mohapatra, “Biosensors in health care: the milestones achieved in their development towards lab-on-chip-analysis,” *Biochem. Res. Int.*, vol. 2016, 2016.

[43] S. Rodriguez-Mozaz, M. J. L. de Alda, M.-P. Marco, and D. Barceló, “Biosensors for environmental monitoring: A global perspective,” *Talanta*, vol. 65, no. 2, pp. 291–297, 2005.

[44] D. Yu, B. Blankert, J. Viré, and J. Kauffmann, “Biosensors in drug discovery and drug analysis,” *Anal. Lett.*, vol. 38, no. 11, pp. 1687–1701, 2005.

[45] E. C. Alocilja and S. M. Radke, “Market analysis of biosensors for food safety,” *Biosens. Bioelectron.*, vol. 18, no. 5–6, pp. 841–846, 2003.

[46] A. Bentley, A. Atkinson, J. Jezek, and D. M. Rawson, “Whole cell biosensors—electrochemical and optical approaches to ecotoxicity testing,” *Toxicol. Vitr.*, vol. 15, no. 4–5, pp. 469–475, 2001.

[47] A. Syahir, K. Usui, K. Tomizaki, K. Kajikawa, and H. Mihara, “Label and label-free detection techniques for protein microarrays,” *Microarrays*, vol. 4, no. 2, pp. 228–244, 2015.

[48] M. J. Schöning and A. Poghossian, *Label-free biosensing: advanced materials, devices*

and applications, vol. 16. Springer, 2018.

[49] E. S. Kolosovas-Machuca, G. Vera-Reveles, M. C. Rodríguez-Aranda, L. C. Ortiz-Dosal, E. Segura-Cardenas, and F. J. Gonzalez, "Resistance-Based Biosensor of Multi-Walled Carbon Nanotubes," *J. Immunoass. Immunochem.*, vol. 36, no. 2, pp. 142–148, 2015.

[50] I. Bontidean *et al.*, "Novel synthetic phytochelatin-based capacitive biosensor for heavy metal ion detection," *Biosens. Bioelectron.*, vol. 18, no. 5–6, pp. 547–553, 2003.

[51] R. W. Cattrall, *Chemical sensors*. Oxford University Press, 1997.

[52] P. Skládal, "Piezoelectric biosensors," *TrAC Trends Anal. Chem.*, vol. 79, pp. 127–133, 2016.

[53] Y. Wang, R. Hu, G. Lin, I. Roy, and K.-T. Yong, "Functionalized quantum dots for biosensing and bioimaging and concerns on toxicity," *ACS Appl. Mater. Interfaces*, vol. 5, no. 8, pp. 2786–2799, 2013.

[54] Z. Zhu, "An overview of carbon nanotubes and graphene for biosensing applications," *Nano-micro Lett.*, vol. 9, no. 3, p. 25, 2017.

[55] C. Parolo and A. Merkoçi, "Paper-based nanobiosensors for diagnostics," *Chem. Soc. Rev.*, vol. 42, no. 2, pp. 450–457, 2013.

[56] A. Brecht and G. Gauglitz, "Recent developments in optical transducers for chemical or biochemical applications," *Sensors Actuators B Chem.*, vol. 38, no. 1–3, pp. 1–7, 1997.

[57] G. Zanchetta, R. Lanfranco, F. Giavazzi, T. Bellini, and M. Buscaglia, "Emerging applications of label-free optical biosensors," *Nanophotonics*, vol. 6, no. 4, pp. 627–645, 2017.

[58] V. S. A. Jayanthi, A. B. Das, and U. Saxena, "Recent advances in biosensor development for the detection of cancer biomarkers," *Biosens. Bioelectron.*, vol. 91, pp. 15–23, 2017.

[59] N. J. Ronkainen, H. B. Halsall, and W. R. Heineman, "Electrochemical biosensors," *Chem. Soc. Rev.*, vol. 39, no. 5, pp. 1747–1763, 2010.

[60] J. D. Newman and A. P. F. Turner, "Home blood glucose biosensors: a commercial perspective," *Biosens. Bioelectron.*, vol. 20, no. 12, pp. 2435–2453, 2005.

[61] W. H. Organization, "WHO Global report on diabetes," 2016. [Online]. Available: https://www.who.int/diabetes/global-report/en/.

[62] MarketsandMarkets, "Biosensors Market Report," 2019. [Online]. Available: https://www.marketsandmarkets.com/Market-Reports/biosensors-market-798.html. [Accessed: 09-Dec-2019].

[63] L. Rassaei, W. Olthuis, S. Tsujimura, E. J. R. Sudhölter, and A. van den Berg, "Lactate biosensors: current status and outlook," *Anal. Bioanal. Chem.*, vol. 406, no. 1, pp. 123–137, 2014.

[64] E. B. Bahadır and M. K. Sezgintürk, “Applications of commercial biosensors in clinical, food, environmental, and biothreat/biowarfare analyses,” *Anal. Biochem.*, vol. 478, pp. 107–120, 2015.

[65] N. Bhalla, P. Jolly, N. Formisano, and P. Estrela, “Introduction to biosensors,” *Essays Biochem.*, vol. 60, no. 1, pp. 1–8, Jun. 2016.

[66] A. Potti, R. L. Schilsky, and J. R. Nevins, “Refocusing the War on Cancer: The Critical Role of Personalized Treatment,” *Sci. Transl. Med.*, vol. 2, no. 28, pp. 28cm13 LP-28cm13, Apr. 2010.

[67] S. N. Topkaya, M. Azimzadeh, and M. Ozsoz, “Electrochemical Biosensors for Cancer Biomarkers Detection: Recent Advances and Challenges,” *Electroanalysis*, vol. 28, no. 7, pp. 1402–1419, 2016.

[68] A. Kirwan, M. Utratna, M. E. O. Dwyer, L. Joshi, and M. Kilcoyne, “Glycosylation-Based Serum Biomarkers for Cancer Diagnostics and Prognostics,” *Biomed Res. Int.*, vol. 2015, p. Article ID 490531, 2015.

[69] B. Bohunicky and S. A. Mousa, “Biosensors: the new wave in cancer diagnosis,” *Nanotechnol. Sci. Appl.*, vol. 4, pp. 1–10, Dec. 2010.

[70] Y. Wan *et al.*, “Carbon nanotube-based ultrasensitive multiplexing electrochemical immunosensor for cancer biomarkers,” *Biosens. Bioelectron.*, vol. 30, no. 1, pp. 93–99, 2011.

[71] Z. Changrong, D. Lin, J. Wu, L. Ding, H. Ju, and F. Yan, “Nanogold-Enriched Carbon Nanohorn Label for Sensitive Electrochemical Detection of Biomarker on a Disposable Immunosensor,” *Electroanalysis*, vol. 25, no. 4, pp. 1044–1049, 2013.

[72] Y. Ding, J. Liu, H. Wang, G. Shen, and R. Yu, “A piezoelectric immunosensor for the detection of α-fetoprotein using an interface of gold/hydroxyapatite hybrid nanomaterial,” *Biomaterials*, vol. 28, no. 12, pp. 2147–2154, 2007.

[73] S.-F. Chou, W.-L. Hsu, J.-M. Hwang, and C.-Y. Chen, “Development of an immunosensor for human ferritin, a nonspecific tumor marker, based on a quartz crystal microbalance,” *Anal. Chim. Acta*, vol. 453, no. 2, pp. 181–189, 2002.

[74] E. Hamidi-Asl, J. B. Raoof, R. Ojani, and M. S. Hejazi, “Indigo Carmine as New Label in PNA Biosensor for Detection of Short Sequence of p53 Tumor Suppressor Gene,” *Electroanalysis*, vol. 25, no. 9, pp. 2075–2083, 2013.

[75] H. Li, L. Shi, D. Sun, P. Li, and Z. Liu, “Fluorescence resonance energy transfer biosensor between upconverting nanoparticles and palladium nanoparticles for ultrasensitive CEA detection,” *Biosens. Bioelectron.*, vol. 86, pp. 791–798, 2016.

[76] M. Hao and Z. Ma, “An Ultrasensitive Chemiluminescence Biosensor for Carcinoembryonic Antigen Based on Autocatalytic Enlargement of Immunogold Nanoprobes,” *Sensors*, vol. 12, no. 12, pp. 17320–17329, 2012.

[77] S. Qu *et al.*, “A rapid and highly sensitive portable chemiluminescent immunosensor of carcinoembryonic antigen based on immunomagnetic separation in human serum,” *Anal. Chim. Acta*, vol. 766, pp. 94–99, 2013.

[78] J. Yuan, R. Duan, H. Yang, X. Luo, and M. Xi, “Detection of serum human epididymis secretory protein 4 in patients with ovarian cancer using a label-free biosensor based on localized surface plasmon resonance.,” *Int. J. Nanomedicine*, vol. 7, pp. 2921–2928, 2012.

[79] H. Li, J. He, S. Li, and A. P. F. Turner, “Electrochemical immunosensor with N-doped graphene-modified electrode for label-free detection of the breast cancer biomarker CA 15-3,” *Biosens. Bioelectron.*, vol. 43, pp. 25–29, 2013.

[80] Y. Pang, C. Wang, J. Wang, Z. Sun, R. Xiao, and S. Wang, “Fe3O4@Ag magnetic nanoparticles for microRNA capture and duplex-specific nuclease signal amplification based SERS detection in cancer cells,” *Biosens. Bioelectron.*, vol. 79, pp. 574–580, 2016.

[81] F. J. Gruhl and K. Länge, “Surface modification of an acoustic biosensor allowing the detection of low concentrations of cancer markers,” *Anal. Biochem.*, vol. 420, no. 2, pp. 188–190, 2012.

[82] Z. Wang *et al.*, “Acoustofluidic Salivary Exosome Isolation: A Liquid Biopsy Compatible Approach for Human Papillomavirus–Associated Oropharyngeal Cancer Detection,” *J. Mol. Diagnostics*, 2019.

[83] J. W. Lee *et al.*, “A reference electrode-free electrochemical biosensor for detecting MMP-9 using a concentric electrode device,” *Sensors Actuators B Chem.*, vol. 240, pp. 735–741, 2017.

[84] L. Z. Swisher, A. M. Prior, S. Shishido, T. A. Nguyen, D. H. Hua, and J. Li, “Quantitative electrochemical detection of cathepsin B activity in complex tissue lysates using enhanced AC voltammetry at carbon nanofiber nanoelectrode arrays,” *Biosens. Bioelectron.*, vol. 56, pp. 129–136, 2014.

[85] H. Fan *et al.*, “Sensitive proteolysis assay based on the detection of a highly characteristic solid-state process,” *RSC Adv.*, vol. 5, no. 60, pp. 48893–48897, 2015.

[86] E. D. Matayoshi, G. T. Wang, G. A. Krafft, and J. Erickson, “Novel fluorogenic substrates for assaying retroviral proteases by resonance energy transfer,” *Science (80-.).*, vol. 247, no. 4945, pp. 954–958, 1990.

[87] H. Dacres, M. M. Dumancic, I. Horne, and S. C. Trowell, “Direct comparison of fluorescence-and bioluminescence-based resonance energy transfer methods for real-time monitoring of thrombin-catalysed proteolytic cleavage,” *Biosens. Bioelectron.*, vol. 24, no. 5, pp. 1164–1170, 2009.

[88] P. Chen, R. Selegård, D. Aili, and B. Liedberg, “Peptide functionalized gold nanoparticles for colorimetric detection of matrilysin (MMP-7) activity,” *Nanoscale*, vol. 5, no. 19, pp. 8973–8976, 2013.

[89] S. Schuerle, J. S. Dudani, M. G. Christiansen, P. Anikeeva, and S. N. Bhatia, “Magnetically Actuated Protease Sensors for in Vivo Tumor Profiling.,” *Nano Lett.*, vol. 16, no. 10, pp. 6303–6310, Oct. 2016.

[90] H. Chen *et al.*, “Fabrication of a protease sensor for caspase-3 activity detection based on surface plasmon resonance,” *Analyst*, vol. 138, no. 19, pp. 5757–5761, 2013.

[91] L. Hu, S. Han, S. Parveen, Y. Yuan, L. Zhang, and G. Xu, "Highly sensitive fluorescent detection of trypsin based on BSA-stabilized gold nanoclusters," *Biosens. Bioelectron.*, vol. 32, no. 1, pp. 297–299, 2012.

[92] L. Yang, T. Wu, C. Fu, G. Chen, S. Xu, and W. Xu, "SERS determination of protease through a particle-on-a-film configuration constructed by electrostatic assembly in an enzymatic hydrolysis reaction," *RSC Adv.*, vol. 6, no. 93, pp. 90120–90125, 2016.

[93] X. Ding and K. Yang, "Enzymatic deposition of silver particles for detecting protease activity," *Part. Part. Syst. Charact.*, vol. 31, no. 12, pp. 1300–1306, 2014.

[94] C.-H. Chen and K.-L. Yang, "Oligopeptide immobilization strategy for improving stability and sensitivity of liquid-crystal protease assays," *Sensors Actuators B Chem.*, vol. 204, pp. 734–740, 2014.

[95] IMPACT, "Implantable Microsystems for Personalised Anti-Cancer Therapy." [Online]. Available: https://www.impact.eng.ed.ac.uk/research. [Accessed: 14-Dec-2019].

[96] A. Rios, A. Escarpa, and B. Simonet, *Miniaturization of analytical systems: principles, designs and applications*. John Wiley & Sons Totowa, NJ, 2009.

[97] D. R. Reyes, D. Iossifidis, P.-A. Auroux, and A. Manz, "Micro total analysis systems. 1. Introduction, theory, and technology," *Anal. Chem.*, vol. 74, no. 12, pp. 2623–2636, 2002.

[98] A. Manz, N. Graber, and H. áM Widmer, "Miniaturized total chemical analysis systems: a novel concept for chemical sensing," *Sensors actuators B Chem.*, vol. 1, no. 1–6, pp. 244–248, 1990.

[99] L. C. Clark JR, R. Wolf, D. Granger, and Z. Taylor, "Continuous recording of blood oxygen tensions by polarography," *J. Appl. Physiol.*, vol. 6, no. 3, pp. 189–193, 1953.

[100] L. M. Bellan, D. Wu, and R. S. Langer, "Current trends in nanobiosensor technology," *Wiley Interdiscip. Rev. Nanomedicine Nanobiotechnology*, vol. 3, no. 3, pp. 229–246, 2011.

[101] A. Koyun, E. Ahlatcolu, Y. Koca, and S. Kara, "Biosensors and their principles," *A Roadmap Biomed. Eng. Milestones*, pp. 117–142, 2012.

[102] B. Derkus, "Applying the miniaturization technologies for biosensor design," *Biosens. Bioelectron.*, vol. 79, pp. 901–913, 2016.

[103] L. Soleymani and F. Li, "Mechanistic Challenges and Advantages of Biosensor Miniaturization into the Nanoscale," *ACS Sensors*, vol. 2, no. 4, pp. 458–467, 2017.

[104] E. Katz, "Implantable Bioelectronics – Editorial Introduction," in *Implantable Bioelectronics*, John Wiley & Sons, Ltd, 2014, pp. 1–5.

[105] T. M. Gross *et al.*, "Performance evaluation of the MiniMed® continuous glucose monitoring system during patient home use," *Diabetes Technol. Ther.*, vol. 2, no. 1, pp. 49–56, 2000.

[106] J. Kropff *et al.*, "Accuracy and longevity of an implantable continuous glucose sensor in the PRECISE study: a 180-day, prospective, multicenter, pivotal trial," *Diabetes Care*, vol. 40, no. 1, pp. 63–68, 2017.

[107] B. Venkatesh, T. H. Glutton-Brock, and S. P. Hendry, "Continuous measurement of blood gases using a combined electrochemical and spectrophotometric sensor," *J. Med. Eng. Technol.*, vol. 18, no. 5, pp. 165–168, 1994.

[108] C. A. Cordeiro, M. G. de Vries, W. Ngabi, P. E. Oomen, T. Cremers, and B. H. C. Westerink, "In vivo continuous and simultaneous monitoring of brain energy substrates with a multiplex amperometric enzyme-based biosensor device," *Biosens. Bioelectron.*, vol. 67, pp. 677–686, 2015.

[109] M. E. Gray *et al.*, "In vivo validation of a miniaturised electrochemical oxygen sensor for measuring intestinal oxygen tension," *Am. J. Physiol. Liver Physiol.*, 2019.

[110] S.-K. Kang *et al.*, "Bioresorbable silicon electronic sensors for the brain," *Nature*, vol. 530, no. 7588, p. 71, 2016.

[111] K. D. Daniel *et al.*, "Implantable diagnostic device for cancer monitoring," *Biosens. Bioelectron.*, vol. 24, no. 11, pp. 3252–3257, 2009.

[112] J. T. Santini, M. J. Cima, and R. Langer, "A controlled-release microchip," *Nature*, vol. 397, no. 6717, pp. 335–338, 1999.

[113] F. N. Pirmoradi, J. K. Jackson, H. M. Burt, and M. Chiao, "On-demand controlled release of docetaxel from a battery-less MEMS drug delivery device," *Lab Chip*, vol. 11, no. 16, pp. 2744–2752, 2011.

[114] S. H. Lee *et al.*, "Implantable batteryless device for on-demand and pulsatile insulin administration," *Nat. Commun.*, vol. 8, p. 15032, 2017.

[115] R. Farra *et al.*, "First-in-human testing of a wirelessly controlled drug delivery microchip," *Sci. Transl. Med.*, vol. 4, no. 122, pp. 122ra21-122ra21, 2012.

[116] A. Cobo, R. Sheybani, and E. Meng, "MEMS: enabled drug delivery systems," *Adv. Healthc. Mater.*, vol. 4, no. 7, pp. 969–982, 2015.

[117] A. Santos, M. S. Aw, M. Bariana, T. Kumeria, Y. Wang, and D. Losic, "Drug-releasing implants: current progress, challenges and perspectives," *J. Mater. Chem. B*, vol. 2, no. 37, pp. 6157–6182, 2014.

[118] T. Traitel, Y. Cohen, and J. Kost, "Characterization of glucose-sensitive insulin release systems in simulated in vivo conditions," *Biomaterials*, vol. 21, no. 16, pp. 1679–1687, 2000.

[119] H. A. Tsai, E. A. Moschou, S. Daunert, M. Madou, and L. Kulinsky, "Integrating Biosensors and Drug Delivery: A Step Closer Toward Scalable Responsive Drug-Delivery Systems," *Adv. Mater.*, vol. 21, no. 6, pp. 656–660, 2009.

[120] J. M. Anderson, "Mechanisms of inflammation and infection with implanted devices," *Cardiovasc. Pathol.*, vol. 2, no. 3, pp. 33–41, 1993.

[121] Y. Onuki, U. Bhardwaj, F. Papadimitrakopoulos, and D. J. Burgess, “A review of the biocompatibility of implantable devices: current challenges to overcome foreign body response,” *J. Diabetes Sci. Technol.*, vol. 2, no. 6, pp. 1003–1015, 2008.

[122] ISO, “ISO 10993 Biological evaluation of medical devices,” *2018*. [Online]. Available: https://www.iso.org/standard/68936.html. [Accessed: 16-Dec-2019].

[123] J. M. Anderson and S. Jiang, “Implications of the acute and chronic inflammatory response and the foreign body reaction to the immune response of implanted biomaterials,” in *The Immune Response to Implanted Materials and Devices*, Springer, 2017, pp. 15–36.

[124] J. M. Anderson, A. Rodriguez, and D. T. Chang, “Foreign body reaction to biomaterials,” *Semin. Immunol.*, vol. 20, no. 2, pp. 86–100, 2008.

[125] O. Veiseh *et al.*, “Size- and shape-dependent foreign body immune response to materials implanted in rodents and non-human primates,” *Nat. Mater.*, vol. 14, no. 6, pp. 643–651, 2015.

[126] D. Gurera, B. Bhushan, and N. Kumar, “Lessons from mosquitoes’ painless piercing,” *J. Mech. Behav. Biomed. Mater.*, vol. 84, pp. 178–187, 2018.

[127] N. Wisniewski, F. Moussy, and W. M. Reichert, “Characterization of implantable biosensor membrane biofouling,” *Fresenius. J. Anal. Chem.*, vol. 366, no. 6–7, pp. 611–621, 2000.

[128] M. J. Mahoney and J. Leighton, “The inflammatory response to a foreign body within transplantable tumors,” *Cancer Res.*, vol. 22, no. 3, pp. 334–338, 1962.

[129] M. E. Gray *et al.*, “Biocompatibility of common implantable sensor materials in a tumor xenograft model,” *J. Biomed. Mater. Res. Part B Appl. Biomater.*, vol. 107B, no. 5, pp. 1620–1633, 2019.

[130] T. Ishizaki, N. Saito, and O. Takai, “Correlation of Cell Adhesive Behaviors on Superhydrophobic, Superhydrophilic, and Micropatterned Superhydrophobic/Superhydrophilic Surfaces to Their Surface Chemistry,” *Langmuir*, vol. 26, no. 11, pp. 8147–8154, Jun. 2010.

[131] E. D. Daneshvar and E. Smela, “Characterization of conjugated polymer actuation under cerebral physiological conditions,” *Adv. Healthc. Mater.*, vol. 3, no. 7, pp. 1026–1035, 2014.

[132] A. Than *et al.*, “Self-implantable double-layered micro-drug-reservoirs for efficient and controlled ocular drug delivery,” *Nat. Commun.*, vol. 9, no. 1, p. 4433, 2018.

[133] J. H. Shin and M. H. Schoenfisch, “Improving the biocompatibility of in vivo sensors via nitric oxide release,” *Analyst*, vol. 131, no. 5, pp. 609–615, 2006.

[134] R. J. Soto, B. J. Privett, and M. H. Schoenfisch, “In vivo analytical performance of nitric oxide-releasing glucose biosensors,” *Anal. Chem.*, vol. 86, no. 14, pp. 7141–7149, 2014.

[135] T. R. R. Singh, G. Laverty, and R. Donnelly, *Hydrogels: design, synthesis and*

application in drug delivery and regenerative medicine. CRC Press, 2018.

[136] B. Yu *et al.*, "Use of hydrogel coating to improve the performance of implanted glucose sensors," *Biosens. Bioelectron.*, vol. 23, no. 8, pp. 1278–1284, 2008.

[137] F. Robotti *et al.*, "Microengineered biosynthesized cellulose as anti-fibrotic in vivo protection for cardiac implantable electronic devices," *Biomaterials*, vol. 229, p. 119583, 2020.

[138] S. Campuzano, M. Pedrero, P. Yáñez-Sedeño, and J. M. Pingarrón, "Antifouling (Bio) materials for Electrochemical (Bio) sensing," *Int. J. Mol. Sci.*, vol. 20, no. 2, p. 423, 2019.

[139] I. Langmuir, "The constitution and fundamental properties of solids and liquids. II. Liquids.," *J. Am. Chem. Soc.*, vol. 39, no. 9, pp. 1848–1906, 1917.

[140] W. C. Bigelow, D. L. Pickett, and W. A. Zisman, "Oleophobic monolayers: I. Films adsorbed from solution in non-polar liquids," *J. Colloid Sci.*, vol. 1, no. 6, pp. 513–538, 1946.

[141] S. Flink, F. C. J. M. van Veggel, and D. N. Reinhoudt, "Sensor functionalities in self-assembled monolayers," *Adv. Mater.*, vol. 12, no. 18, pp. 1315–1328, 2000.

[142] K. B. Blodgett, "Films built by depositing successive monomolecular layers on a solid surface," *J. Am. Chem. Soc.*, vol. 57, no. 6, pp. 1007–1022, 1935.

[143] J. C. Love, L. A. Estroff, J. K. Kriebel, R. G. Nuzzo, and G. M. Whitesides, "Self-assembled monolayers of thiolates on metals as a form of nanotechnology," *Chem. Rev.*, vol. 105, no. 4, pp. 1103–1170, 2005.

[144] J. Sagiv, "Organized monolayers by adsorption. 1. Formation and structure of oleophobic mixed monolayers on solid surfaces," *J. Am. Chem. Soc.*, vol. 102, no. 1, pp. 92–98, 1980.

[145] M. Wang, K. M. Liechti, Q. Wang, and J. M. White, "Self-assembled silane monolayers: fabrication with nanoscale uniformity," *Langmuir*, vol. 21, no. 5, pp. 1848–1857, 2005.

[146] J. P. Folkers, C. B. Gorman, P. E. Laibinis, S. Buchholz, G. M. Whitesides, and R. G. Nuzzo, "Self-assembled monolayers of long-chain hydroxamic acids on the native oxide of metals," *Langmuir*, vol. 11, no. 3, pp. 813–824, 1995.

[147] D. K. Schwartz, "Mechanisms and kinetics of self-assembled monolayer formation," *Annu. Rev. Phys. Chem.*, vol. 52, no. 1, pp. 107–137, 2001.

[148] C. Carraro, O. W. Yauw, M. M. Sung, and R. Maboudian, "Observation of three growth mechanisms in self-assembled monolayers," *J. Phys. Chem. B*, vol. 102, no. 23, pp. 4441–4445, 1998.

[149] C. Messerschmidt and D. K. Schwartz, "Growth mechanisms of octadecylphosphonic acid self-assembled monolayers on sapphire (corundum): Evidence for a quasi-equilibrium triple point," *Langmuir*, vol. 17, no. 2, pp. 462–467, 2001.

[150] C. D. Bain, E. B. Troughton, Y. T. Tao, J. Evall, G. M. Whitesides, and R. G. Nuzzo, "Formation of monolayer films by the spontaneous assembly of organic thiols from solution onto gold," *J. Am. Chem. Soc.*, vol. 111, no. 1, pp. 321–335, 1989.

[151] T. W. Schneider and D. A. Buttry, "Electrochemical quartz crystal microbalance studies of adsorption and desorption of self-assembled monolayers of alkyl thiols on gold," *J. Am. Chem. Soc.*, vol. 115, no. 26, pp. 12391–12397, 1993.

[152] D. Losic, J. G. Shapter, and J. J. Gooding, "Mapping of defects in self-assembled monolayers by polymer decoration," *J. Solid State Electrochem.*, vol. 9, no. 7, pp. 512–519, 2005.

[153] M. Himmelhaus, F. Eisert, M. Buck, and M. Grunze, "Self-Assembly of n-Alkanethiol Monolayers. A Study by IR− Visible Sum Frequency Spectroscopy (SFG)," *J. Phys. Chem. B*, vol. 104, no. 3, pp. 576–584, 2000.

[154] D. Corrigan *et al.*, "A microelectrode array with reproducible performance shows loss of consistency following functionalization with a self-assembled 6-mercapto-1-hexanol layer," *Sensors*, vol. 18, no. 6, p. 1891, 2018.

[155] X.-L. Su and Y. Li, "A self-assembled monolayer-based piezoelectric immunosensor for rapid detection of Escherichia coli O157: H7," *Biosens. Bioelectron.*, vol. 19, no. 6, pp. 563–574, 2004.

[156] C. P. Tripp and M. L. Hair, "Direct observation of the surface bonds between self-assembled monolayers of octadecyltrichlorosilane and silica surfaces: a low-frequency IR study at the solid/liquid interface," *Langmuir*, vol. 11, no. 4, pp. 1215–1219, 1995.

[157] G. Kalyuzhny, A. Vaskevich, G. Ashkenasy, A. Shanzer, and I. Rubinstein, "UV/Vis spectroscopy of metalloporphyrin and metallophthalocyanine monolayers self-assembled on ultrathin gold films," *J. Phys. Chem. B*, vol. 104, no. 34, pp. 8238–8244, 2000.

[158] S. H. Chen and C. W. Frank, "Infrared and fluorescence spectroscopic studies of self-assembled n-alkanoic acid monolayers," *Langmuir*, vol. 5, no. 4, pp. 978–987, 1989.

[159] M. Prato *et al.*, "Optical characterization of thiolate self-assembled monolayers on Au (111)," *J. Phys. Chem. C*, vol. 112, no. 10, pp. 3899–3906, 2008.

[160] X. Yao, J. Wang, F. Zhou, J. Wang, and N. Tao, "Quantification of redox-induced thickness changes of 11-ferrocenylundecanethiol self-assembled monolayers by electrochemical surface plasmon resonance," *J. Phys. Chem. B*, vol. 108, no. 22, pp. 7206–7212, 2004.

[161] C. D. Bain and G. M. Whitesides, "Modeling organic surfaces with self-assembled monolayers," *Angew. Chemie*, vol. 101, no. 4, pp. 522–528, 1989.

[162] N. Faucheux, R. Schweiss, K. Lützow, C. Werner, and T. Groth, "Self-assembled monolayers with different terminating groups as model substrates for cell adhesion studies," *Biomaterials*, vol. 25, no. 14, pp. 2721–2730, 2004.

[163] K. Tamada, M. Hara, H. Sasabe, and W. Knoll, "Surface phase behavior of n-alkanethiol self-assembled monolayers adsorbed on Au (111): An atomic force

microscope study," *Langmuir*, vol. 13, no. 6, pp. 1558–1566, 1997.

[164] J. Lü, E. Delamarche, L. Eng, R. Bennewitz, E. Meyer, and H.-J. Güntherodt, "Kelvin probe force microscopy on surfaces: Investigation of the surface potential of self-assembled monolayers on gold," *Langmuir*, vol. 15, no. 23, pp. 8184–8188, 1999.

[165] S. Datta, W. Tian, S. Hong, R. Reifenberger, J. I. Henderson, and C. P. Kubiak, "Current-voltage characteristics of self-assembled monolayers by scanning tunneling microscopy," *Phys. Rev. Lett.*, vol. 79, no. 13, p. 2530, 1997.

[166] B. Liu, A. J. Bard, M. V Mirkin, and S. E. Creager, "Electron transfer at self-assembled monolayers measured by scanning electrochemical microscopy," *J. Am. Chem. Soc.*, vol. 126, no. 5, pp. 1485–1492, 2004.

[167] S. V Kalinin and A. Gruverman, *Scanning probe microscopy: electrical and electromechanical phenomena at the nanoscale*, vol. 1. Springer Science & Business Media, 2007.

[168] A.-S. Duwez, "Exploiting electron spectroscopies to probe the structure and organization of self-assembled monolayers: a review," *J. Electron Spectros. Relat. Phenomena*, vol. 134, no. 2–3, pp. 97–138, 2004.

[169] S. Wang *et al.*, "Manipulation of surface wettability between superhydrophobicity and superhydrophilicity on copper films," *ChemPhysChem*, vol. 6, no. 8, pp. 1475–1478, 2005.

[170] J. J. Hickman, D. Ofer, P. E. Laibinis, G. M. Whitesides, and M. S. Wrighton, "Molecular self-assembly of two-terminal, voltammetric microsensors with internal references," *Science (80-.).*, vol. 252, no. 5006, pp. 688–691, 1991.

[171] H.-Y. Chang *et al.*, "Effect of surface potential on epithelial cell adhesion, proliferation and morphology," *Colloids Surfaces B Biointerfaces*, vol. 141, pp. 179–186, 2016.

[172] A. S. Widge, M. Jeffries-El, X. Cui, C. F. Lagenaur, and Y. Matsuoka, "Self-assembled monolayers of polythiophene conductive polymers improve biocompatibility and electrical impedance of neural electrodes," *Biosens. Bioelectron.*, vol. 22, no. 8, pp. 1723–1732, 2007.

[173] L. Zuo, Y. Xiong, X. Xie, and X. Xiao, "Enhanced lubricity in mixed alkanethiol monolayers," *J. Phys. Chem. B*, vol. 109, no. 48, pp. 22971–22975, 2005.

[174] Y. Yamamoto, H. Nishihara, and K. Aramaki, "Self-Assembled Layers of Alkanethiols on Copper for Protection Against Corrosion," *J. Electrochem. Soc.*, vol. 140, no. 2, pp. 436–443, 1993.

[175] N. K. Chaki and K. Vijayamohanan, "Self-assembled monolayers as a tunable platform for biosensor applications," *Biosens. Bioelectron.*, vol. 17, no. 1–2, pp. 1–12, 2002.

[176] A. L. Eckermann, D. J. Feld, J. A. Shaw, and T. J. Meade, "Electrochemistry of redox-active self-assembled monolayers," *Coord. Chem. Rev.*, vol. 254, no. 15–16, pp. 1769–1802, 2010.

[177] E. Gatto and M. Venanzi, "Self-assembled monolayers formed by helical peptide

building blocks: a new tool for bioinspired nanotechnology," *Polym. J.*, vol. 45, no. 5, p. 468, 2013.

[178] D. Pletcher, R. Greff, R. Peat, L. M. Peter, and J. Robinson, *Instrumental methods in electrochemistry*. Elsevier, 2001.

[179] P. W. Atkins, J. De Paula, and J. Keeler, *Atkins' physical chemistry*. Oxford university press, 2018.

[180] J. Heinze, "Ultramicroelectrodes in Electrochemistry," *Angew. Chemie Int. Ed. English*, vol. 32, no. 9, pp. 1268–1288, 1993.

[181] C. Amatore, C. Pebay, L. Thouin, A. Wang, and J.-S. Warkocz, "Difference between Ultramicroelectrodes and Microelectrodes: Influence of Natural Convection," *Anal. Chem.*, vol. 82, no. 16, pp. 6933–6939, Aug. 2010.

[182] C. L. Brady, "Development and characterisation of microelectrodes for extreme environments," 2013.

[183] E. O. Blair, "Optimisation and characterisation of durable microelectrodes for electroanalysis in molten salt," 2017.

[184] R. G. Compton and C. E. Banks, *Understanding voltammetry*. World Scientific, 2011.

[185] I. Schmüser, "Design, fabrication and characterisation of nanoelectrodes for electrochemical sensing," 2015.

[186] A. Delcourt-Lancon, "Electrochemical analysis supported by macro and microelectrode array." Durham University, 2011.

[187] M. Falk, R. Sultana, M. J. Swann, A. R. Mount, and N. J. Freeman, "Nanoband array electrode as a platform for high sensitivity enzyme-based glucose biosensing," *Bioelectrochemistry*, vol. 112, pp. 100–105, 2016.

[188] A. E. Cohen and R. R. Kunz, "Large-area interdigitated array microelectrodes for electrochemical sensing," *Sensors Actuators B Chem.*, vol. 62, no. 1, pp. 23–29, 2000.

[189] C. M. A. Brett and A. M. O. Brett, *Electroanalysis*. Oxford: Oxford Univ. Press, 1998.

[190] N. Elgrishi, K. J. Rountree, B. D. McCarthy, E. S. Rountree, T. T. Eisenhart, and J. L. Dempsey, "A Practical Beginner's Guide to Cyclic Voltammetry," *J. Chem. Educ.*, vol. 95, no. 2, pp. 197–206, Feb. 2018.

[191] A. J. Bard, L. R. Faulkner, J. Leddy, and C. G. Zoski, *Electrochemical methods: fundamentals and applications*, vol. 2. wiley New York, 1980.

[192] I. Schmueser, A. J. Walton, J. G. Terry, H. L. Woodvine, N. J. Freeman, and A. R. Mount, "A systematic study of the influence of nanoelectrode dimensions on electrode performance and the implications for electroanalysis and sensing," *Faraday Discuss.*, vol. 164, pp. 295–314, 2013.

[193] V. Mirceski, S. Skrzypek, and L. Stojanov, "Square-wave voltammetry," *ChemTexts*, vol. 4, no. 4, p. 17, 2018.

[194] B. Alberts *et al.*, “Molecular biology of the cell, 6th edn New York,” *NY WW Nort. Co.*, 2014.

[195] G. M. Cooper, R. E. Hausman, and R. E. Hausman, *The cell: a molecular approach. The Central Role of Enzymes as Biological Catalyst*, vol. 10. ASM press Washington, DC, 2000.

[196] E. González-Fernández, M. Staderini, N. Avlonitis, A. F. Murray, A. R. Mount, and M. Bradley, “Effect of spacer length on the performance of peptide-based electrochemical biosensors for protease detection,” *Sensors Actuators B Chem.*, vol. 255, pp. 3040–3046, 2018.

[197] M. Staderini, E. González-Fernández, A. F. Murray, A. R. Mount, and M. Bradley, “A tripod anchor offers improved robustness of peptide-based electrochemical biosensors,” *Sensors Actuators B Chem.*, vol. 274, pp. 662–667, 2018.

[198] C. G. Pheeney and J. K. Barton, “DNA electrochemistry with tethered methylene blue,” *Langmuir*, vol. 28, no. 17, pp. 7063–7070, 2012.

[199] S. J. Wagner, A. Skripchenko, D. Robinette, J. W. Foley, and L. Cincotta, “Factors affecting virus photoinactivation by a series of phenothiazine dyes,” *Photochem. Photobiol.*, vol. 67, no. 3, pp. 343–349, 1998.

[200] E. Kaiser, R. L. Colescott, C. D. Bossinger, and P. I. Cook, “Color test for detection of free terminal amino groups in the solid-phase synthesis of peptides,” *Anal. Biochem.*, vol. 34, no. 2, pp. 595–598, 1970.

[201] A. Piper, “Electrochemical characterisation of microsquare nanoband edge electrode (MNEE) arrays and their use as biosensors,” 2017.

[202] H. L. Woodvine, J. G. Terry, A. J. Walton, and A. R. Mount, “The development and characterisation of square microfabricated electrode systems,” *Analyst*, vol. 135, no. 5, pp. 1058–1065, 2010.

[203] J. G. Terry *et al.*, “Nanoscale electrode arrays produced with microscale lithographic techniques for use in biomedical sensing applications,” *IET nanobiotechnology*, vol. 7, no. 4, pp. 125–134, 2013.

[204] W. Ma *et al.*, “Investigating electron-transfer processes using a biomimetic hybrid bilayer membrane system,” *Nat. Protoc.*, vol. 8, no. 3, p. 439, 2013.

[205] L. Jacobse, S. J. Raaijman, and M. T. M. Koper, “The reactivity of platinum microelectrodes,” *Phys. Chem. Chem. Phys.*, vol. 18, no. 41, pp. 28451–28457, 2016.

[206] H. Neurath and K. A. Walsh, “Role of proteolytic enzymes in biological regulation (a review).,” *Proc. Natl. Acad. Sci. U. S. A.*, vol. 73, no. 11, pp. 3825–32, 1976.

[207] J. Yuan and B. A. Yankner, “Apoptosis in the nervous system,” *Nature*, vol. 407, no. 6805, pp. 802–809, 2000.

[208] Y. Hua and S. Nair, “Proteases in cardiometabolic diseases: Pathophysiology, molecular mechanisms and clinical applications,” *Biochim. Biophys. Acta - Mol. Basis Dis.*, vol. 1852, no. 2, pp. 195–208, 2015.

[209] J. Ji, J. Gan, J. Kong, P. Yang, B. Liu, and C. Ji, “Electrochemical detection of the activities of thrombin and its inhibitor,” *Electrochem. commun.*, vol. 16, no. 1, pp. 53–56, 2012.

[210] S. H. Havale and M. Pal, “Medicinal chemistry approaches to the inhibition of dipeptidyl peptidase-4 for the treatment of type 2 diabetes,” *Bioorganic Med. Chem.*, vol. 17, no. 5, pp. 1783–1802, 2009.

[211] H. Haim, I. Salas, and J. Sodroski, “Proteolytic Processing of the Human Immunodeficiency Virus Envelope Glycoprotein Precursor Decreases Conformational Flexibility,” *J. Virol.*, vol. 87, no. 3, pp. 1884–1889, 2013.

[212] E. Pazos, O. Vázquez, J. L. Mascareñas, and M. Eugenio Vázquez, “Peptide-based fluorescent biosensors,” *Chem. Soc. Rev.*, vol. 38, no. 12, p. 3348, 2009.

[213] T. Zeng *et al.*, “Compact, Programmable, and Stable Biofunctionalized Upconversion Nanoparticles Prepared through Peptide-Mediated Phase Transfer for High-Sensitive Protease Sensing and in Vivo Apoptosis Imaging,” *ACS Appl. Mater. Interfaces*, vol. 7, no. 22, pp. 11849–11856, 2015.

[214] S. B. Lowe, J. A. G. Dick, B. E. Cohen, and M. M. Stevens, “Multiplex sensing of protease and kinase enzyme activity via orthogonal coupling of quantum dot-peptide conjugates,” *ACS Nano*, vol. 6, no. 1, pp. 851–857, 2012.

[215] A. Anne, A. Chovin, and C. Demaille, “Optimizing electrode-attached redox-peptide systems for kinetic characterization of protease action on immobilized substrates. observation of dissimilar behavior of trypsin and thrombin enzymes,” *Langmuir*, vol. 28, no. 23, pp. 8804–8813, 2012.

[216] M. Puiu and C. Bala, “Peptide-based biosensors: From self-assembled interfaces to molecular probes in electrochemical assays,” *Bioelectrochemistry*, vol. 120, pp. 66–75, 2018.

[217] H. Wu, S. Liu, J. Jiang, G. Shen, and R. Yu, “A novel electrochemical biosensor for highly selective detection of protease biomarker from Bacillus licheniformis with D-amino acid containing peptide,” *Analyst*, vol. 137, no. 20, pp. 4829–4833, 2012.

[218] M. A. Sowole and H.-B. Kraatz, “Electrochemical detection of hepatitis C viral NS3-4A protease,” *Analyst*, vol. 137, no. 5, pp. 1120–1124, 2012.

[219] D. Deng, Y. Shi, H. Feng, Q. Chen, D. Li, and L. Liu, “Label-free electrochemical sensing platform for the detection of protease,” *Int. J. Electrochem. Sci*, vol. 8, pp. 6933–6940, 2013.

[220] Y. Cao, J. Yu, B. Bo, Y. Shu, and G. Li, “A simple and general approach to assay protease activity with electrochemical technique,” *Biosens. Bioelectron.*, vol. 45, pp. 1–5, 2013.

[221] R.-P. Liang, X.-C. Tian, P. Qiu, and J.-D. Qiu, “Multiplexed electrochemical detection of trypsin and chymotrypsin based on distinguishable signal nanoprobes,” *Anal. Chem.*, vol. 86, no. 18, pp. 9256–9263, 2014.

[222] J. Zhang, Y. Liu, J. Lv, Y. Cao, and G. Li, “Dipeptidyl peptidase-IV activity assay and

inhibitor screening using a gold nanoparticle-modified gold electrode with an immobilized enzyme substrate," *Microchim. Acta*, vol. 182, no. 1–2, pp. 281–288, 2015.

[223] M. La, X.-Y. Zhao, Q.-L. Peng, C.-D. Chen, and G.-Q. Zhao, "Electrochemical Biosensors for Probing of Protease Activity and Screening of Protease Inhibitors," *Int. J. Electrochem. Sci*, vol. 10, pp. 3329–3339, 2015.

[224] H. Chen *et al.*, "Sensitive cell apoptosis assay based on caspase-3 activity detection with graphene oxide-assisted electrochemical signal amplification," *Biosens. Bioelectron.*, vol. 68, pp. 777–782, 2015.

[225] G. Liu, J. Wang, D. S. Wunschel, and Y. Lin, "Electrochemical proteolytic beacon for detection of matrix metalloproteinase activities," *J. Am. Chem. Soc.*, vol. 128, no. 38, pp. 12382–12383, 2006.

[226] H. Xiao, L. Liu, F. Meng, J. Huang, and G. Li, "Electrochemical Approach To Detect Apoptosis," *Anal. Chem.*, vol. 80, no. 13, pp. 5272–5275, 2008.

[227] N. Zhao *et al.*, "Electrochemical assay of active prostate-specific antigen (PSA) using ferrocene-functionalized peptide probes," *Electrochem. commun.*, vol. 12, no. 3, pp. 471–474, 2010.

[228] D.-S. Shin, Y. Liu, Y. Gao, T. Kwa, Z. Matharu, and A. Revzin, "Micropatterned surfaces functionalized with electroactive peptides for detecting protease release from cells," *Anal. Chem.*, vol. 85, no. 1, pp. 220–227, 2012.

[229] J. Adjémian, A. Anne, G. Cauet, and C. Demaille, "Cleavage-sensing redox peptide monolayers for the rapid measurement of the proteolytic activity of trypsin and α-thrombin enzymes," *Langmuir*, vol. 26, no. 12, pp. 10347–10356, 2010.

[230] Y. Zheng and Z. Ma, "Dual-reaction triggered sensitivity amplification for ultrasensitive peptide-cleavage based electrochemical detection of matrix metalloproteinase-7," *Biosens. Bioelectron.*, vol. 108, pp. 46–52, 2018.

[231] A. Kirchhain *et al.*, "Biosensors for measuring matrix metalloproteinases: An emerging research field," *TrAC - Trends in Analytical Chemistry*, vol. 110. Elsevier B.V., pp. 35–50, 01-Jan-2019.

[232] F. Qu, M. Yang, and A. Rasooly, "Dual signal amplification electrochemical biosensor for monitoring the activity and inhibition of the Alzheimer's related protease β-secretase," *Anal. Chem.*, vol. 88, no. 21, pp. 10559–10565, 2016.

[233] S. Park, Y. M. Shin, J.-J. Song, and H. Yang, "Facile electrochemical detection of botulinum neurotoxin type E using a two-step proteolytic cleavage," *Biosens. Bioelectron.*, vol. 72, pp. 211–217, 2015.

[234] D. Deng *et al.*, "A signal-on electrochemical biosensor for evaluation of caspase-3 activity and cell apoptosis by the generation of molecular electrocatalysts on graphene electrode surface for water oxidation," *Sensors Actuators B Chem.*, vol. 286, pp. 415–420, 2019.

[235] L. Z. Swisher *et al.*, "Quantitative electrochemical detection of cathepsin B activity in

breast cancer cell lysates using carbon nanofiber nanoelectrode arrays toward identification of cancer formation," *Nanomedicine Nanotechnology, Biol. Med.*, vol. 11, no. 7, pp. 1695–1704, 2015.

[236] D. Wang, Y. Zheng, Y. Chai, Y. Yuan, and R. Yuan, "Target protein induced cleavage of a specific peptide for prostate-specific antigen detection with positively charged gold nanoparticles as signal enhancer," *Chem. Commun.*, vol. 51, no. 52, pp. 10521–10523, 2015.

[237] R. J. Forster, "Microelectrodes: new dimensions in electrochemistry," *Chem. Soc. Rev.*, vol. 23, no. 4, pp. 289–297, 1994.

[238] T. M. Antalis, T. Shea-Donohue, S. N. Vogel, C. Sears, and A. Fasano, "Mechanisms of disease: protease functions in intestinal mucosal pathobiology," *Nat. Rev. Gastroenterol. Hepatol.*, vol. 4, no. 7, p. 393, 2007.

[239] K. Soreide, E. A. Janssen, H. Körner, and J. P. A. Baak, "Trypsin in colorectal cancer: molecular biological mechanisms of proliferation, invasion, and metastasis," *J. Pathol. A J. Pathol. Soc. Gt. Britain Irel.*, vol. 209, no. 2, pp. 147–156, 2006.

[240] P. Charles, V. Stubbs, C. Soto, B. Martin, B. White, and C. Taitt, "Reduction of non-specific protein adsorption using poly (ethylene) glycol (PEG) modified polyacrylate hydrogels in immunoassays for staphylococcal enterotoxin B detection," *Sensors*, vol. 9, no. 1, pp. 645–655, 2009.

[241] S. Lowe, N. M. O'Brien-Simpson, and L. A. Connal, "Antibiofouling polymer interfaces: poly (ethylene glycol) and other promising candidates," *Polym. Chem.*, vol. 6, no. 2, pp. 198–212, 2015.

[242] S. Campuzano, F. Kuralay, and J. Wang, "Ternary monolayer interfaces for ultrasensitive and direct bioelectronic detection of nucleic acids in complex matrices," *Electroanalysis*, vol. 24, no. 3, pp. 483–493, 2012.

[243] A. Miodek, E. Regan, N. Bhalla, N. Hopkins, S. Goodchild, and P. Estrela, "Optimisation and characterisation of anti-fouling ternary SAM layers for impedance-based aptasensors," *Sensors*, vol. 15, no. 10, pp. 25015–25032, 2015.

[244] C. T. Buscher, D. McBranch, and D. Li, "Understanding the relationship between surface coverage and molecular orientation in polar self-assembled monolayers," *J. Am. Chem. Soc.*, vol. 118, no. 12, pp. 2950–2953, 1996.

[245] Y. Xue, X. Li, H. Li, and W. Zhang, "Quantifying thiol–gold interactions towards the efficient strength control," *Nat. Commun.*, vol. 5, p. 4348, 2014.

[246] D. Kang, X. Zuo, R. Yang, F. Xia, K. W. Plaxco, and R. J. White, "Comparing the properties of electrochemical-based DNA sensors employing different redox tags," *Anal. Chem.*, vol. 81, no. 21, pp. 9109–9113, 2009.

[247] Y. Long, E. Abu-Irhayem, and H. Kraatz, "Peptide electron transfer: more questions than answers," *Chem. Eur. J.*, vol. 11, no. 18, pp. 5186–5194, 2005.

[248] S. Sek, A. Sepiol, A. Tolak, A. Misicka, and R. Bilewicz, "Distance dependence of the electron transfer rate through oligoglycine spacers introduced into self-assembled

monolayers," *J. Phys. Chem. B*, vol. 108, no. 24, pp. 8102–8105, 2004.

[249] M. Gilbert Gatty, A. Kahnt, L. J. Esdaile, M. Hutin, H. L. Anderson, and B. Albinsson, "Hopping versus tunneling mechanism for long-range electron transfer in porphyrin oligomer bridged donor–acceptor systems," *J. Phys. Chem. B*, vol. 119, no. 24, pp. 7598–7611, 2015.

[250] E. Ostuni, R. G. Chapman, R. E. Holmlin, S. Takayama, and G. M. Whitesides, "A survey of structure− property relationships of surfaces that resist the adsorption of protein," *Langmuir*, vol. 17, no. 18, pp. 5605–5620, 2001.

[251] J. Wu *et al.*, "Binding characteristics between polyethylene glycol (PEG) and proteins in aqueous solution," *J. Mater. Chem. B*, vol. 2, no. 20, pp. 2983–2992, 2014.

[252] J.-S. Lee, A. K. R. Lytton-Jean, S. J. Hurst, and C. A. Mirkin, "Silver nanoparticle−oligonucleotide conjugates based on DNA with triple cyclic disulfide moieties," *Nano Lett.*, vol. 7, no. 7, pp. 2112–2115, 2007.

[253] T. Sakata, S. Maruyama, A. Ueda, H. Otsuka, and Y. Miyahara, "Stable immobilization of an oligonucleotide probe on a gold substrate using tripodal thiol derivatives," *Langmuir*, vol. 23, no. 5, pp. 2269–2272, 2007.

[254] N. Phares, R. J. White, and K. W. Plaxco, "Improving the stability and sensing of electrochemical biosensors by employing trithiol-anchoring groups in a six-carbon self-assembled monolayer," *Anal. Chem.*, vol. 81, no. 3, pp. 1095–1100, 2009.

[255] M. Dong, H. Qi, S. Ding, and M. Li, "Electrochemical determination of trypsin using a heptapeptide substrate self-assembled on a gold electrode," *Microchim. Acta*, vol. 182, no. 1–2, pp. 43–49, 2015.

[256] J. M. Artigas, M. E. Garcia, M. R. Faure, and A. M. Gimeno, "Serum trypsin levels in acute pancreatic and non-pancreatic abdominal conditions.," *Postgrad. Med. J.*, vol. 57, no. 666, pp. 219–222, 1981.

[257] W. S. Ruddell, C. J. Mitchell, I. Hamilton, J. P. Leek, and J. Kelleher, "Clinical value of serum immunoreactive trypsin concentration.," *Br Med J (Clin Res Ed)*, vol. 283, no. 6304, pp. 1429–1432, 1981.

[258] H. S. Mandal and H.-B. Kraatz, "Electron transfer across α-helical peptides: Potential influence of molecular dynamics," *Chem. Phys.*, vol. 326, no. 1, pp. 246–251, 2006.

[259] A. J. Wain, H. N. L. Do, H. S. Mandal, H.-B. Kraatz, and F. Zhou, "Influence of molecular dipole moment on the redox-induced reorganization of α-helical peptide self-assembled monolayers: an electrochemical SPR investigation," *J. Phys. Chem. C*, vol. 112, no. 37, pp. 14513–14519, 2008.

[260] I. Rubinstein, *Electroanalytical Chemistry: A Series Of Advances*, vol. 21. CRC Press, 1999.

[261] P. Diao, M. Guo, and R. Tong, "Characterization of defects in the formation process of self-assembled thiol monolayers by electrochemical impedance spectroscopy," *J. Electroanal. Chem.*, vol. 495, no. 2, pp. 98–105, 2001.

[262] S. D. Keighley, P. Li, P. Estrela, and P. Migliorato, “Optimization of DNA immobilization on gold electrodes for label-free detection by electrochemical impedance spectroscopy,” *Biosens. Bioelectron.*, vol. 23, no. 8, pp. 1291–1297, 2008.

[263] O. Y. F. Henry, J. G. Perez, J. L. A. Sanchez, and C. K. O’Sullivan, “Electrochemcial characterisation and hybridisation efficiency of co-assembled monolayers of PEGylated ssDNA and mercaptohexanol on planar gold electrodes,” *Biosens. Bioelectron.*, vol. 25, no. 5, pp. 978–983, 2010.

[264] Y. Wang, J. Feng, Z. Tan, and H. Wang, “Electrochemical impedance spectroscopy aptasensor for ultrasensitive detection of adenosine with dual backfillers,” *Biosens. Bioelectron.*, vol. 60, pp. 218–223, 2014.

[265] L. A. Adamczyk, “Understanding the Structure and Properties of Self-Assembled Monolayers for Interfacial Patterning.” Virginia Tech, 2009.

[266] K. Stulík, C. Amatore, K. Holub, V. Marecek, and W. Kutner, “Microelectrodes. Definitions, characterization, and applications (Technical report),” *Pure Appl. Chem.*, vol. 72, no. 8, pp. 1483–1492, 2000.

[267] M. Sheffer, V. Vivier, and D. Mandler, “Self-assembled monolayers on Au microelectrodes,” *Electrochem. commun.*, vol. 9, no. 12, pp. 2827–2832, 2007.

[268] K. Xu, F. Liu, J. Ma, and B. Tang, “A new specific fullerene-based fluorescent probe for trypsin,” *Analyst*, vol. 136, no. 6, pp. 1199–1203, 2011.

[269] M. Stoytcheva, R. Zlatev, S. Cosnier, M. Arredondo, and B. Valdez, “High sensitive trypsin activity evaluation applying a nanostructured QCM-sensor,” *Biosens. Bioelectron.*, vol. 41, pp. 862–866, 2013.

[270] G. Chen *et al.*, “A general colorimetric method for detecting protease activity based on peptide-induced gold nanoparticle aggregation,” *RSC Adv.*, vol. 4, no. 13, pp. 6560–6563, 2014.

[271] O. A. Gutierrez, M. Chavez, and E. Lissi, “A theoretical approach to some analytical properties of heterogeneous enzymatic assays,” *Anal. Chem.*, vol. 76, no. 9, pp. 2664–2668, 2004.

[272] J. G. Kenna, G. N. Major, and R. S. Williams, “Methods for reducing non-specific antibody binding in enzyme-linked immunosorbent assays,” *J. Immunol. Methods*, vol. 85, no. 2, pp. 409–419, 1985.

[273] E. H. Reimerdes and H. Klostermeyer, “[3] Determination of proteolytic activities on casein substrates,” in *Methods in enzymology*, vol. 45, Elsevier, 1976, pp. 26–28.

[274] M. A. M. Peters *et al.*, “Serotonin and dopamine receptor expression in solid tumours including rare cancers,” *Pathol. Oncol. Res.*, pp. 1–9, 2019.

[275] A. H. L. Bong and G. R. Monteith, “Calcium signaling and the therapeutic targeting of cancer cells,” *Biochim. Biophys. Acta (BBA)-Molecular Cell Res.*, vol. 1865, no. 11, pp. 1786–1794, 2018.

[276] M. J. J. M. Zvelebil and J. M. Thornton, “Peptide–protein interactions: an overview,”

Q. Rev. Biophys., vol. 26, no. 3, pp. 333–363, 1993.

[277] G. N. Somero, "Temperature adaptation of enzymes: biological optimization through structure-function compromises," *Annu. Rev. Ecol. Syst.*, vol. 9, no. 1, pp. 1–29, 1978.

[278] W. Qi and Z. He, "Enzymatic hydrolysis of protein: mechanism and kinetic model," *Front. Chem. China*, vol. 1, no. 3, pp. 308–314, 2006.

[279] E. D. Stevens and J. M. McLeese, "Why bluefin tuna have warm tummies: temperature effect on trypsin and chymotrypsin," *Am. J. Physiol. Integr. Comp. Physiol.*, vol. 246, no. 12, pp. 487–494, 1984.

[280] P. Kissinger and W. R. Heineman, *Laboratory Techniques in Electroanalytical Chemistry, revised and expanded*. CRC press, 1996.

[281] F.-M. Matysik, "Miniaturization of electroanalytical systems," *Anal. Bioanal. Chem.*, vol. 375, no. 1, pp. 33–35, 2003.

[282] P. Q. Li, A. Piper, I. Schmueser, A. R. Mount, and D. K. Corrigan, "Impedimetric measurement of DNA–DNA hybridisation using microelectrodes with different radii for detection of methicillin resistant Staphylococcus aureus (MRSA)," *Analyst*, vol. 142, no. 11, pp. 1946–1952, 2017.

[283] N. J. Ronkainen, "Micro-and Nanoelectrodes in Protein-Based Electrochemical Biosensors for Nanomedicine and Other Applications," *Adv. Bioelectron. Mater.*, p. 1, 2015.

[284] I. Palchetti, S. Laschi, and M. Mascini, "Miniaturised stripping-based carbon modified sensor for in field analysis of heavy metals," *Anal. Chim. Acta*, vol. 530, no. 1, pp. 61–67, 2005.

[285] K. Wassum, V. Tolosa, J. Wang, E. Walker, H. Monbouquette, and N. Maidment, "Silicon wafer-based platinum microelectrode array biosensor for near real-time measurement of glutamate in vivo," *Sensors*, vol. 8, no. 8, pp. 5023–5036, 2008.

[286] R. M. Wightman, "Probing cellular chemistry in biological systems with microelectrodes," *Science (80-.).*, vol. 311, no. 5767, pp. 1570–1574, 2006.

[287] A. A. Werdich *et al.*, "A microfluidic device to confine a single cardiac myocyte in a sub-nanoliter volume on planar microelectrodes for extracellular potential recordings," *Lab Chip*, vol. 4, no. 4, pp. 357–362, 2004.

[288] O. Niwa, H. Tabei, B. P. Solomon, F. Xie, and P. T. Kissinger, "Improved detection limit for catecholamines using liquid chromatography-electrochemistry with a carbon interdigitated array microelectrode," *J. Chromatogr. B Biomed. Sci. Appl.*, vol. 670, no. 1, pp. 21–28, 1995.

[289] D. W. M. Arrigan, "Nanoelectrodes, nanoelectrode arrays and their applications," *Analyst*, vol. 129, no. 12, pp. 1157–1165, 2004.

[290] R. B. Morris, D. J. Franta, and H. S. White, "Electrochemistry at platinum bane electrodes of width approaching molecular dimensions: breakdown of transport equations at very small electrodes," *J. Phys. Chem.*, vol. 91, no. 13, pp. 3559–3564,

1987.

[291] Y.-L. Ying, Z. Ding, D. Zhan, and Y.-T. Long, “Advanced electroanalytical chemistry at nanoelectrodes,” *Chem. Sci.*, vol. 8, no. 5, pp. 3338–3348, 2017.

[292] V. P. Menon and C. R. Martin, “Fabrication and evaluation of nanoelectrode ensembles,” *Anal. Chem.*, vol. 67, no. 13, pp. 1920–1928, 1995.

[293] J. C. Hulteen, V. P. Menon, and C. R. Martin, “Template preparation of nanoelectrode ensembles. Achieving the ‘pure-radial’electrochemical-response limiting case,” *J. Chem. Soc. Faraday Trans.*, vol. 92, no. 20, pp. 4029–4032, 1996.

[294] F. Grote, R.-S. Kühnel, A. Balducci, and Y. Lei, “Template assisted fabrication of free-standing MnO2 nanotube and nanowire arrays and their application in supercapacitors,” *Appl. Phys. Lett.*, vol. 104, no. 5, p. 53904, 2014.

[295] M.-S. Wu and K.-C. Huang, “Fabrication of nickel hydroxide electrodes with open-ended hexagonal nanotube arrays for high capacitance supercapacitors,” *Chem. Commun.*, vol. 47, no. 44, pp. 12122–12124, 2011.

[296] B. M. Quinn and S. G. Lemay, “Single-walled carbon nanotubes as templates and interconnects for nanoelectrodes,” *Adv. Mater.*, vol. 18, no. 7, pp. 855–859, 2006.

[297] Y. Xian, F. Liu, L. Feng, F. Wu, L. Wang, and L. Jin, “Nanoelectrode ensembles based on conductive polyaniline/poly (acrylic acid) using porous sol–gel films as template,” *Electrochem. commun.*, vol. 9, no. 4, pp. 773–780, 2007.

[298] W.-Z. Wu *et al.*, “Monitoring dopamine release from single living vesicles with nanoelectrodes,” *J. Am. Chem. Soc.*, vol. 127, no. 25, pp. 8914–8915, 2005.

[299] S. Madhurantakam, K. J. Babu, J. B. B. Rayappan, and U. M. Krishnan, “Nanotechnology-based electrochemical detection strategies for hypertension markers,” *Biosens. Bioelectron.*, vol. 116, pp. 67–80, 2018.

[300] J. Li *et al.*, “Carbon nanotube nanoelectrode array for ultrasensitive DNA detection,” *Nano Lett.*, vol. 3, no. 5, pp. 597–602, 2003.

[301] Y. Lin, F. Lu, Y. Tu, and Z. Ren, “Glucose biosensors based on carbon nanotube nanoelectrode ensembles,” *Nano Lett.*, vol. 4, no. 2, pp. 191–195, 2004.

[302] Y. Wang *et al.*, “Nanoelectrodes for determination of reactive oxygen and nitrogen species inside murine macrophages,” *Proc. Natl. Acad. Sci.*, vol. 109, no. 29, pp. 11534–11539, 2012.

[303] I. Schmueser, A. J. Walton, J. G. Terry, H. L. Woodvine, N. J. Freeman, and A. R. Mount, “A systematic study of the influence of nanoelectrode dimensions on electrode performance and the implications for electroanalysis and sensing,” *Faraday Discuss.*, vol. 164, p. 295, 2013.

[304] N. J. Freeman *et al.*, “Comparison of the performance of an array of nanoband electrodes with a macro electrode with similar overall area,” *Phys. Chem. Chem. Phys.*, vol. 15, no. 21, p. 8112, 2013.

[305] R. Sultana *et al.*, “Practical Implications of using Nanoelectrodes for Bioanalytical Measurements,” *Electrochim. Acta*, vol. 126, pp. 98–103, 2014.

[306] A. Piper, B. M. Alston, D. J. Adams, and A. R. Mount, “Functionalised microscale nanoband edge electrode (MNEE) arrays: the systematic quantitative study of hydrogels grown on nanoelectrode biosensor arrays for enhanced sensing in biological media,” *Faraday Discuss.*, vol. 210, pp. 201–217, 2018.

[307] Y. Song *et al.*, “Electrochemical Activity Assay for Protease Analysis Using Carbon Nanofiber Nanoelectrode Arrays,” *Anal. Chem.*, vol. 91, no. 6, pp. 3971–3979, 2019.

[308] A. Butterworth, E. Blues, P. Williamson, M. Cardona, L. Gray, and D. K. Corrigan, “SAM composition and electrode roughness affect performance of a DNA biosensor for antibiotic resistance,” *Biosensors*, vol. 9, no. 1, p. 22, 2019.

[309] R. F. Carvalhal, R. Sanches Freire, and L. T. Kubota, “Polycrystalline Gold Electrodes: A Comparative Study of Pretreatment Procedures Used for Cleaning and Thiol Self-Assembly Monolayer Formation,” *Electroanal. An Int. J. Devoted to Fundam. Pract. Asp. Electroanal.*, vol. 17, no. 14, pp. 1251–1259, 2005.

[310] C. G. Zoski, “Ultramicroelectrodes: design, fabrication, and characterization,” *Electroanal. An Int. J. Devoted to Fundam. Pract. Asp. Electroanal.*, vol. 14, no. 15-16, pp. 1041–1051, 2002.

[311] Y. SAITO, “A theoretical study on the diffusion current at the stationary electrodes of circular and narrow band types,” *Rev. Polarogr.*, vol. 15, no. 6, pp. 177–187, 1968.

[312] O. Köster, W. Schuhmann, H. Vogt, and W. Mokwa, “Quality control of ultra-microelectrode arrays using cyclic voltammetry, electrochemical impedance spectroscopy and scanning electrochemical microscopy,” *Sensors Actuators B Chem.*, vol. 76, no. 1–3, pp. 573–581, 2001.

[313] P. Chinwangso, A. C. Jamison, and T. R. Lee, “Multidentate adsorbates for self-assembled monolayer films,” *Acc. Chem. Res.*, vol. 44, no. 7, pp. 511–519, 2011.

[314] S. D. Cramer, *Electrodeposition of Thick Coatings of Platinum and Palladium on Refractory Metals from Aqueous Electrolytes*, vol. 7016. US Department of the Interior, Bureau of Mines, 1967.

[315] V. Branger, V. Pelosin, K. F. Badawi, and P. Goudeau, “Study of the mechanical and microstructural state of platinum thin films,” *Thin Solid Films*, vol. 275, no. 1–2, pp. 22–24, 1996.

[316] B. C. Prorok and H. D. Espinosa, “Effects of nanometer-thick passivation layers on the mechanical response of thin gold films,” *J. Nanosci. Nanotechnol.*, vol. 2, no. 3–4, pp. 427–433, 2002.

[317] S. Franssila, *Introduction to microfabrication*. John Wiley & Sons, 2010.

[318] G. M. Alonzo-Medina, A. González-González, J. L. Sacedón, and A. I. Oliva, “Understanding the thermal annealing process on metallic thin films,” in *IOP Conference Series: Materials Science and Engineering*, 2013, vol. 45, no. 1, p. 12013.

[319] A. Gencoglu and A. Minerick, “Chemical and morphological changes on platinum microelectrode surfaces in AC and DC fields with biological buffer solutions,” *Lab Chip*, vol. 9, no. 13, pp. 1866–1873, 2009.

[320] K. Wissel *et al.*, “Platinum corrosion products from electrode contacts of human cochlear implants induce cell death in cell culture models,” *PLoS One*, vol. 13, no. 5, p. e0196649, 2018.

[321] S. Dasari and P. B. Tchounwou, “Cisplatin in cancer therapy: molecular mechanisms of action,” *Eur. J. Pharmacol.*, vol. 740, pp. 364–378, 2014.

[322] C. De Haro, R. Mas, G. Abadal, J. Munoz, F. Perez-Murano, and C. Domínguez, “Electrochemical platinum coatings for improving performance of implantable microelectrode arrays,” *Biomaterials*, vol. 23, no. 23, pp. 4515–4521, 2002.

[323] H. Park, S. Zhang, A. Steinman, Z. Chen, and H. Lee, “Graphene prevents neurostimulation-induced platinum dissolution in fractal microelectrodes,” *2D Mater.*, vol. 6, no. 3, p. 35037, 2019.

[324] L. S. Robblee, J. McHardy, J. M. Marston, and S. B. Brummer, “Electrical stimulation with Pt electrodes. V. The effect of protein on Pt dissolution,” *Biomaterials*, vol. 1, no. 3, pp. 135–139, 1980.

[325] M. M. Walczak, D. D. Popenoe, R. S. Deinhammer, B. D. Lamp, C. Chung, and M. D. Porter, “Reductive desorption of alkanethiolate monolayers at gold: a measure of surface coverage,” *Langmuir*, vol. 7, no. 11, pp. 2687–2693, 1991.

[326] D.-F. Yang, C. P. Wilde, and M. Morin, “Studies of the electrochemical removal and efficient re-formation of a monolayer of hexadecanethiol self-assembled at an Au (111) single crystal in aqueous solutions,” *Langmuir*, vol. 13, no. 2, pp. 243–249, 1997.

[327] N. Kemnade, Y. Chen, M. I. Muglali, and A. Erbe, “Electrochemical reductive desorption of alkyl self-assembled monolayers studied in situ by spectroscopic ellipsometry: evidence for formation of a low refractive index region after desorption,” *Phys. Chem. Chem. Phys.*, vol. 16, no. 32, pp. 17081–17090, 2014.

[328] J. A. Williams and C. B. Gorman, “Alkanethiol reductive desorption from self-assembled monolayers on gold, platinum, and palladium substrates,” *J. Phys. Chem. C*, vol. 111, no. 34, pp. 12804–12810, 2007.

[329] A.-L. Haag, V. Toader, R. B. Lennox, and P. Grutter, “Selective in situ potential-assisted SAM formation on multi electrode arrays,” *Nanotechnology*, vol. 27, no. 45, p. 455501, 2016.

[330] L. Z. Swisher *et al.*, “Electrochemical protease biosensor based on enhanced AC voltammetry using carbon nanofiber nanoelectrode arrays,” *J. Phys. Chem. C*, vol. 117, no. 8, pp. 4268–4277, 2013.

[331] C. Cannes, F. Kanoufi, and A. J. Bard, “Cyclic voltammetry and scanning electrochemical microscopy of ferrocenemethanol at monolayer and bilayer-modified gold electrodes,” *J. Electroanal. Chem.*, vol. 547, no. 1, pp. 83–91, 2003.

[332] F. Schreiber, “Structure and growth of self-assembling monolayers,” *Prog. Surf. Sci.*,

vol. 65, no. 5–8, pp. 151–257, 2000.

[333] O. Dannenberger, M. Buck, and M. Grunze, "Self-assembly of n-alkanethiols: A kinetic study by second harmonic generation," *J. Phys. Chem. B*, vol. 103, no. 12, pp. 2202–2213, 1999.

[334] R. H. Terrill, T. A. Tanzer, and P. W. Bohn, "Structural evolution of hexadecanethiol monolayers on gold during assembly: Substrate and concentration dependence of monolayer structure and crystallinity," *Langmuir*, vol. 14, no. 4, pp. 845–854, 1998.

[335] D. Capitao, R. Sahli, N. Raouafi, B. Limoges, C. Fave, and B. Schöllhorn, "Electro-assisted Deposition of Binary Self-Assembled 1, 2-Dithiolane Monolayers on Gold with Predictable Composition," *ChemElectroChem*, vol. 3, no. 9, pp. 1422–1428, 2016.

[336] M. Riepl, V. M. Mirsky, and O. S. Wolfbeis, "Electrical control of alkanethiols self-assembly on a gold surface as an approach for preparation of microelectrode arrays," *Microchim. Acta*, vol. 131, no. 1–2, pp. 29–34, 1999.

[337] P. Diao, Q. Hou, M. Guo, M. Xiang, and Q. Zhang, "Effect of substrate potentials on the structural disorders of alkanethiol monolayers prepared by electrochemically directed assembly," *J. Electroanal. Chem.*, vol. 597, no. 2, pp. 103–110, 2006.

[338] F. Ma and R. B. Lennox, "Potential-assisted deposition of alkanethiols on Au: controlled preparation of single-and mixed-component SAMs," *Langmuir*, vol. 16, no. 15, pp. 6188–6190, 2000.

[339] D. Capitao, B. Limoges, C. Fave, and B. Schöllhorn, "On the decisive role of the sulfur-based anchoring group in the electro-assisted formation of self-assembled monolayers on gold," *Electrochim. Acta*, vol. 257, pp. 165–171, 2017.

[340] D. Jambrec, M. Gebala, F. La Mantia, and W. Schuhmann, "Potential-Assisted DNA immobilization as a prerequisite for fast and controlled formation of DNA monolayers," *Angew. Chemie Int. Ed.*, vol. 54, no. 50, pp. 15064–15068, 2015.

[341] I. Ciani *et al.*, "Development of immunosensors for direct detection of three wound infection biomarkers at point of care using electrochemical impedance spectroscopy," *Biosens. Bioelectron.*, vol. 31, no. 1, pp. 413–418, 2012.

[342] J. R. Windmiller and J. Wang, "Wearable electrochemical sensors and biosensors: a review," *Electroanalysis*, vol. 25, no. 1, pp. 29–46, 2013.

[343] J. Kim, A. S. Campbell, and J. Wang, "Wearable non-invasive epidermal glucose sensors: A review," *Talanta*, vol. 177, pp. 163–170, 2018.

[344] A. Heller, "Implanted electrochemical glucose sensors for the management of diabetes," *Annu. Rev. Biomed. Eng.*, vol. 1, no. 1, pp. 153–175, 1999.

[345] C. Ming Li, H. Dong, X. Cao, T. Luong, H. John, and X. Zhang, "Implantable electrochemical sensors for biomedical and clinical applications: progress, problems, and future possibilities.," *Curr. Med. Chem.*, vol. 14, no. 8, pp. 937–951, 2007.

[346] A. Barfidokht and J. J. Gooding, "Approaches toward allowing electroanalytical devices to be used in biological fluids," *Electroanalysis*, vol. 26, no. 6, pp. 1182–1196,

2014.

[347] A. J. T. Teo, A. Mishra, I. Park, Y.-J. Kim, W.-T. Park, and Y.-J. Yoon, "Polymeric biomaterials for medical implants and devices," *ACS Biomater. Sci. Eng.*, vol. 2, no. 4, pp. 454–472, 2016.

[348] I. M. Ward and J. Sweeney, *Mechanical properties of solid polymers*. John Wiley & Sons, 2012.

[349] I. Francolini, C. Vuotto, A. Piozzi, and G. Donelli, "Antifouling and antimicrobial biomaterials: an overview," *Apmis*, vol. 125, no. 4, pp. 392–417, 2017.

[350] J. A. Walker *et al.*, "Antibody-binding, antifouling surface coatings based on recombinant expression of zwitterionic EK peptides," *Langmuir*, vol. 35, no. 5, pp. 1266–1272, 2018.

[351] J.-G. Wu, J.-H. Chen, K.-T. Liu, and S.-C. Luo, "Engineering Antifouling Conducting Polymers for Modern Biomedical Applications," *ACS Appl. Mater. Interfaces*, vol. 11, no. 24, pp. 21294–21307, 2019.

[352] B. Zhang, A. R. Nagle, G. G. Wallace, T. W. Hanks, and P. J. Molino, "Functionalised inherently conducting polymers as low biofouling materials," *Biofouling*, vol. 31, no. 6, pp. 493–502, 2015.

[353] Z. Song *et al.*, "Low fouling electrochemical sensing in complex biological media by using the ionic liquid-doped conducting polymer PEDOT: application to voltammetric determination of dopamine," *Microchim. Acta*, vol. 186, no. 4, p. 220, 2019.

[354] C.-H. Xue, X.-J. Guo, J.-Z. Ma, and S.-T. Jia, "Fabrication of robust and antifouling superhydrophobic surfaces via surface-initiated atom transfer radical polymerization," *ACS Appl. Mater. Interfaces*, vol. 7, no. 15, pp. 8251–8259, 2015.

[355] J.-W. Lee *et al.*, "Fouling-tolerant nanofibrous polymer membranes for water treatment," *ACS Appl. Mater. Interfaces*, vol. 6, no. 16, pp. 14600–14607, 2014.

[356] M. Kyröläinen, H. Håkanson, B. Mattiasson, and P. Vadgama, "Minimal-Fouling enzyme electrode for continuous flow measurement of whole blood lactate," *Biosens. Bioelectron.*, vol. 12, no. 11, pp. 1073–1081, 1997.

[357] M.-Q. Du *et al.*, "Selective Carbon Dioxide Capture in Antifouling Indole-based Microporous Organic Polymers," *Chinese J. Polym. Sci.*, vol. 38, no. 2, pp. 187–194, 2020.

[358] A. Akthakul, R. F. Salinaro, and A. M. Mayes, "Antifouling polymer membranes with subnanometer size selectivity," *Macromolecules*, vol. 37, no. 20, pp. 7663–7668, 2004.

[359] V. Ruiz-Valdepeñas Montiel *et al.*, "Delayed sensor activation based on transient coatings: Biofouling protection in complex biofluids," *J. Am. Chem. Soc.*, vol. 140, no. 43, pp. 14050–14053, 2018.

[360] V. R.-V. Montiel, J. R. Sempionatto, S. Campuzano, J. M. Pingarrón, B. E. F. de Ávila, and J. Wang, "Direct electrochemical biosensing in gastrointestinal fluids," *Anal. Bioanal. Chem.*, vol. 411, no. 19, pp. 4597–4604, 2019.

[361] E. González-Fernández *et al.*, "In vivo application of an implantable tri-anchored methylene blue-based electrochemical pH sensor," *Manuscript_in_preparation.*

[362] Evonik Industries, "EUDRAGIT® functional polymers for oral solid dosage forms." [Online]. Available: https://healthcare.evonik.com/product/health-care/en/products/pharmaceutical-excipients/EUDRAGIT/. [Accessed: 23-Jan-2020].

[363] H. Duan *et al.*, "Mucoadhesive microparticulates based on polysaccharide for target dual drug delivery of 5-aminosalicylic acid and curcumin to inflamed colon," *Colloids Surfaces B Biointerfaces*, vol. 145, pp. 510–519, 2016.

[364] Evonik Industries, "Technical Information of Eudragit® L100 and Eudragit® S100." [Online]. Available: www.pharosproject.net/uploads/files/cml/1389279051.pdf. [Accessed: 23-Jan-2019].

[365] D. A. Nguyen and H. S. Fogler, "Facilitated diffusion in the dissolution of carboxylic polymers," *AIChE J.*, vol. 51, no. 2, pp. 415–425, 2005.

[366] G. K. Vinner, G. T. Vladisavljević, M. R. J. Clokie, and D. J. Malik, "Microencapsulation of Clostridium difficile specific bacteriophages using microfluidic glass capillary devices for colon delivery using pH triggered release," *PLoS One*, vol. 12, no. 10, 2017.

[367] M. Z. I. Khan, H. P. Štedul, and N. Kurjaković, "A pH-dependent colon-targeted oral drug delivery system using methacrylic acid copolymers. II. Manipulation of drug release using Eudragit® L100 and Eudragit S100 combinations," *Drug Dev. Ind. Pharm.*, vol. 26, no. 5, pp. 549–554, 2000.

[368] V. K. Nikam *et al.*, "Eudragit a versatile polymer: a review," *Pharmacologyonline*, vol. 1, pp. 152–164, 2011.

[369] C. Blaszykowski, S. Sheikh, and M. Thompson, "Surface chemistry to minimize fouling from blood-based fluids," *Chem. Soc. Rev.*, vol. 41, no. 17, pp. 5599–5612, 2012.

[370] E. Koutsoumpeli, J. Murray, D. Langford, R. S. Bon, and S. Johnson, "Probing molecular interactions with methylene blue derivatized self-assembled monolayers," *Sens. bio-sensing Res.*, vol. 6, pp. 1–6, 2015.

Appendix-1: Fabrication run sheet for TT and STT microelectrodes

Step	Description	Equipment	Recipe/Instructions
1	**Insulate wafer – SiO_2**		
1.1	Thermal oxidation (1000 nm SiO_2)	Furnace	WETOX14, 2.20 mins
1.2	Measure layer thickness	Nanospec	Oxide on silicon program
2	**Deposit metal – Ti and Pt**		
2.1	Deposit titanium	ANS E-Beam Evaporation	10 nm
2.2	Deposit platinum	ANS E-Beam Evaporation	50 nm
2.3	Inspect	Microscope	
2.4	Inspect	Nanospec	Measure reflectance
2.5	Inspect	Dektak	Measure step height
2.6	Inspect	4-point probe	Measure sheet resistance
3	**Photolithography – pattern metal**		
3.1	IPA clean	Solvent wet deck	IPA, DIW, N2 dry
3.2	Bake	Hot plate	90 °C, 1 min
3.3	Box Prime Wafers	Wet Bench, HMDS box	10mins, HMDS Primer
3.4	Spin on Photoresist	Spin coater	SPR 220 – 3/ 500 rpm, 5 s then 2500 rpm, 60 s
3.5	Bake photoresist	Hot plate	110 °C, 90 s
3.6	Clean mask	Solvent wet deck	Acetone clean
3.7	Inspect mask	Microscope	
3.8	Expose wafer	Karl Suss mask aligner	Low vac contact, 12 s
3.9	Develop	Solvent wet deck	MF26A developer, 1-1.5 min
3.10	Rinse & Dry	DI gun, N_2 gun	
3.11	Inspect	Microscope	
4	**Etch metal**		
4.1	Etch Pt/Ti	JLS RIE 80	Prog 8 (Ar mill), 9 mins
4.2	Measure SiO_2 conductivity	Multimeter	
4.3	Inspect	Microscope	
4.4	Inspect	Nanospec	
5	**Resist strip**		
5.1	ACT Rinse	Ultrasonic bath	15 mins, 50 °C
5.2	IPA Rinse	IPA	5 min
5.3	Rinse & Dry	DI gun, N_2 gun	
5.4	Inspect	Microscope	
6	**Coat passivation**		
6.1	500nm LPCVD SIRN	Furnace	SIRNFLAT, 5 hours
6.2	Inspect	Microscope	
6.3	Inspect	Nanospec	Measure thickness
7	**Photolithography – electrode and contact**		
7.1	IPA clean	Solvent wet deck	IPA, DIW, N_2 dry
7.2	Bake	Hot plate	90 °C, 1 min
7.3	Box Prime Wafers	Wet Bench, HMDS box	10mins, HMDS Primer
7.4	Spin on Photoresist	Spin coater	SPR 220 – 3/ 500 rpm, 5 s then 2500 rpm, 60 s

7.5	Bake photoresist	Hot plate	110 °C, 90 s
7.6	Clean mask	Solvent wet deck	Acetone clean
7.7	Inspect mask	Microscope	
7.8	Expose wafer	Karl Suss mask aligner	Low vac contact, 12 s
7.9	Develop	Solvent wet deck	MF26A developer, 1-1.5min
7.10	Rinse & Dry	DI gun, N_2 gun	
7.11	Inspect	Microscope	
8	**Etch electrode and contact**		
8.1	Etch SiN	JLS RIE 80	Prog 25, 75W, CF4 - 60/AR-4, ~25 mins
8.2	Inspect	Microscope	
8.3	Inspect	Nanospec	
9	**Resist strip**		
9.1	ACT Rinse	Ultrasonic bath	15 mins, 50 °C
9.2	IPA Rinse	IPA	5 min
9.3	Rinse & Dry	DI gun, N_2 gun	
9.4	Inspect	Microscope	
10	**Dicing**		
10.1	Photoresist coat	Solvent wet deck	Spray on resist
10.2	Bake photoresist	Hotplate	115 °C, 60 s
10.3	Frame	Extension	Frame up wafers for saw
10.4	Dicing	Disco saw	
11	**Resist strip after dicing**		
11.1	ACT Rinse	Solvent wet deck	20 s
11.2	IPA Rinse	Solvent wet deck	10 s
11.3	DI Water Rinse & N_2 Dry	Solvent wet deck	10 s
11.4	Inspect	Microscope	

Appendix-2: Fabrication run sheet for MEA and MNEE devices

Step	Description	Equipment	Recipe/Instructions
1	**Insulate wafer – SiO_2**		
1.1	Thermal oxidation (1000 nm SiO_2)	Furnace	WETOX10, 2.30 mins
1.2	Measure layer thickness	Nanospec	Oxide on silicon program
2	**Deposit metal – Ti and Pt**		
2.1	Deposit titanium	ANS E-Beam Evaporation	30 nm
2.2	Deposit platinum	ANS E-Beam Evaporation	100 nm
2.3	Inspect	Microscope	
2.4	Inspect	Nanospec	Measure reflectance
2.5	Inspect	Dektak	Measure step height
2.6	Inspect	4-point probe	Measure sheet resistance
3	**Photolithography – pattern metal**		
3.1	Barrel ash	Barrel asher	1h
3.2	Box Prime Wafers	Wet Bench, HMDS box	10mins, HMDS Primer
3.3	Spin on Photoresist	Spin coater	SPR 350 / 500 rpm, 5 s then 1800 rpm, 60 s
3.4	Bake photoresist	Hot plate	90 °C, 60 s
3.5	Expose wafer	Karl Suss mask aligner	Prox spacer, 7 s
3.6	Develop	Solvent wet deck	MF26A developer, 1 min
3.7	Rinse & Dry	DI gun, N_2 gun	
3.8	Inspect	Microscope	
4	**Etch metal**		
4.1	Etch Pt/Ti	JLS RIE 80	Prog 8 (Ar mill), 10 mins
4.2	Measure SiO_2 conductivity	Multimeter	
4.3	Inspect	Microscope	
4.4	Inspect	Nanospec	
5	**Resist strip**		
5.1	ACT Rinse	Ultrasonic bath	30 mins, 50 °C
5.2	IPA Rinse	IPA	15 min
5.3	Rinse & Dry	DI gun, N_2 gun	
5.4	Inspect	Microscope	
6	**Coat passivation**		
6.1	300 nm PECVD SiN	Furnace	
6.2	Inspect	Microscope	
6.3	Inspect	Nanospec	Measure thickness
7	**Photolithography – electrode and contact**		
7.1	Barrel ash	Barrel asher	1h
7.2	Box Prime Wafers	Wet Bench, HMDS box	10mins, HMDS Primer
7.3	Spin on Photoresist	Spin coater	SPR 220 – 3/ 500 rpm, 5 s then 1800 rpm, 60 s
7.4	Bake photoresist	Hot plate	110 °C, 90 s
7.5	Expose wafer	Karl Suss mask aligner	Low vac contact, 18 s
7.6	Develop	Solvent wet deck	MF26A developer, 1 min
7.7	Rinse & Dry	DI gun, N_2 gun	
7.8	Inspect	Microscope	

8	**Etch electrode and contact**		
8.1	Etch SiN	JLS RIE 80	Prog 25, 75W, CF4 - 60/AR-4, 13 mins
8.2	Inspect	Microscope	
8.3	Inspect	Nanospec	
9	**Resist strip**		
9.1	ACT Rinse	Ultrasonic bath	30 mins, 50 °C
9.2	IPA Rinse	IPA	15 min
9.3	Rinse & Dry	DI gun, N_2 gun	
9.4	Inspect	Microscope	
10	**Photolithography – cavities**		
10.1	Barrel ash	Barrel asher	1h
10.2	Box Prime Wafers	Wet Bench, HMDS box	10mins, HMDS Primer
10.3	Spin on Photoresist	Spin coater	SPR 220 – 3/ 500 rpm, 5 s then 2500 rpm, 60 s
10.4	Bake photoresist	Hot plate	110 °C, 90 s
10.5	Expose wafer	Karl Suss mask aligner	Low vac contact, 18 s
10.6	Develop	Solvent wet deck	MF26A developer, 1 min
10.7	Cover bond pads	Paintbrush	SPR 350
10.8	Bake photoresist	Hot plate	90 °C, 60 s
10.9	Inspect	Microscope	
11	**Etch cavities**		
11.1	Etch Pt	JLS RIE 80	Prog 8 (Ar mill), 200W, 9 mins
11.2	Inspect	Microscope	
11.3	Inspect	Nanospec	
12	**Resist strip**		
12.1	ACT Rinse	Ultrasonic bath	30 mins, 50 °C
12.2	IPA Rinse	IPA	15 min
12.3	Rinse & Dry	DI gun, N_2 gun	
12.4	Inspect	Microscope	
13	**Dicing**		
13.1	Photoresist coat	Solvent wet deck	Spray on resist
13.2	Bake photoresist	Hotplate	115 °C, 60 s
13.3	Frame	Extension	Frame up wafers for saw
13.4	Dicing	Disco saw	
14	**Resist strip after dicing**		
14.1	ACT Rinse	Solvent wet deck	20 s
14.2	IPA Rinse	Solvent wet deck	10 s
14.3	DI Water Rinse & N_2 Dry	Solvent wet deck	10 s
14.4	Inspect	Microscope	

Array Type	Number of Cavities	MEA Area (10^{-8} m^2)	MNEE Area (10^{-8} m^2)
10µm-1D	62500	491	9.82
10µm-2D	27889	220	4.38
10µm-3D	15625	123	2.45
10µm-4D	10000	79	1.57
20µm-1D	15625	491	4.91
20µm-2D	6889	216	2.16
20µm-3D	3969	125	1.25
20µm-4D	2500	79	0.79
30µm-1D	6889	487	3.25
30µm-2D	3136	123	1.48
30µm-3D	1764	69	0.83
30µm-4D	1165	46	0.55

Appendix-3: MATLAB code used for peak height calculations

```
clear all;close all;clc
% read data
data = xlsread('C:\Users\s1576099\Desktop\filename.csv');
% Consider only current data (2nd column in the data)
currentData = data(:,2:4:size(data,2));

%% Plot all measurement data
figure;
for t=1:size(currentData,2)
   plot(currentData(:,t));
   hold on;
end

%% Enter starting point
startingPoint = input('Enter the peak starting point \n');
finishingPoint = input('Enter the peak finishing point \n');
%% Determine peak height
% Initialize peakHeight
peakHeight = zeros(size(currentData,2),1);
% Find peak point and the height of the peak points
for k=1:size(currentData,2)
   % Draw a line between the starting and end point of the data graph
   y1 = currentData(startingPoint,k);
   y2 = currentData(finishingPoint,k);
   % Calculate slope
   m = (y2-y1)/((finishingPoint-startingPoint)+1);
   % Obtain the line
   lineY = y1+m.*(1:(finishingPoint-startingPoint));
   plot(startingPoint:finishingPoint-1,lineY,'--');
   % Find the maximum value and its location
   [val,loc] = max(currentData(startingPoint:finishingPoint,k));
   % Find the value of the location on the line (-1 is used due to
   % considering the starting point as 2 instead of 1)
   lineValue = y1+m*(loc-1);
   plot(startingPoint+loc-1,lineValue,' ok');
   % Calculate the height of the peak
   peakHeight(k,1) = abs(val-lineValue);
   % Clear temporary data
   clear lineValue val loc lineY m y1 y2
end
figure;
plot(peakHeight);
ylim([min(peakHeight),max(peakHeight)]);
```

Appendix-4: SWV data used to prepare respective figures

i) Figure 4-18

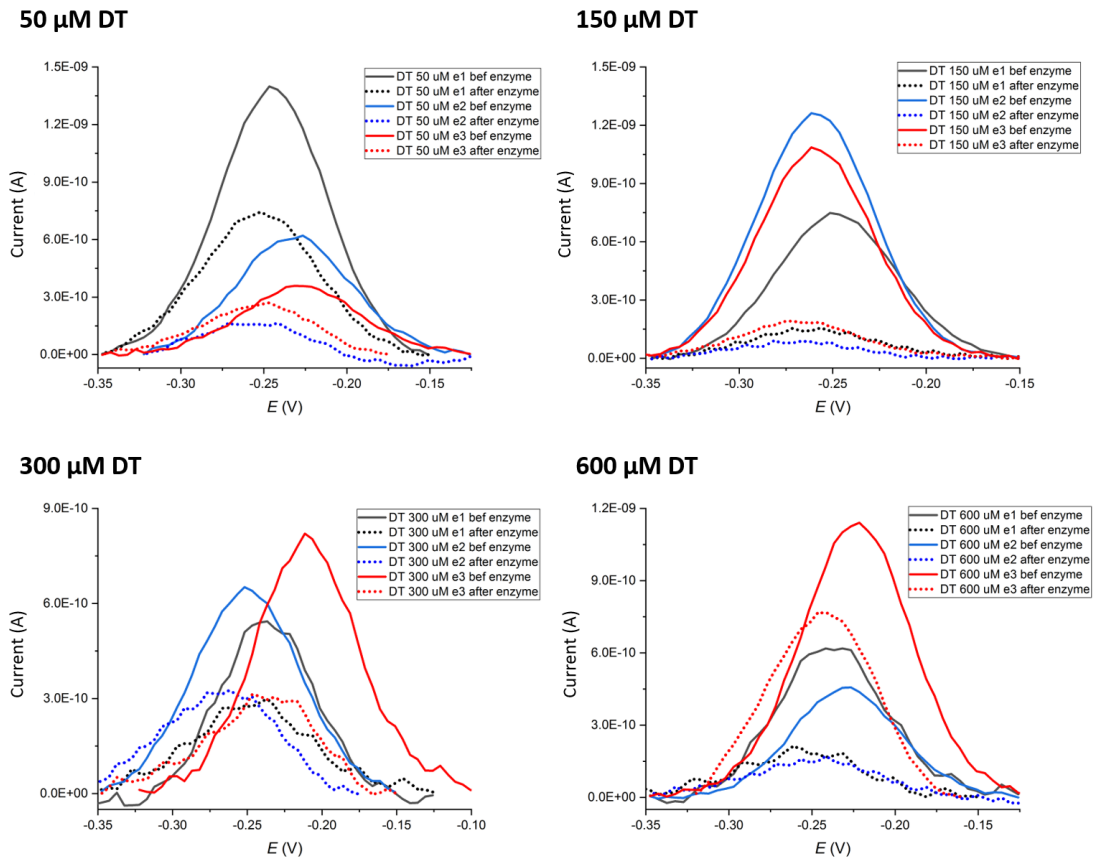

ii) Figure 5-5

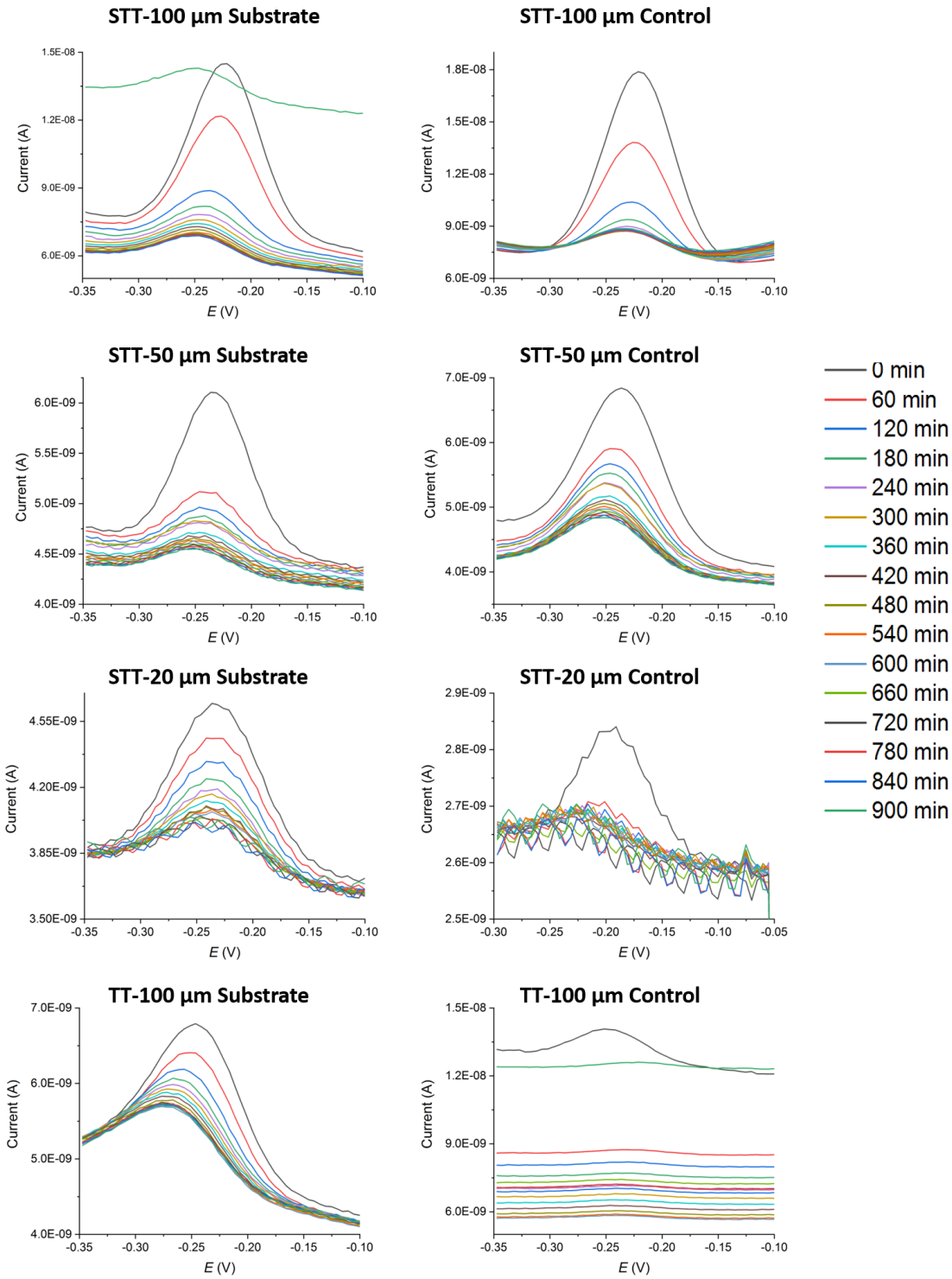
STT-100 µm Substrate
STT-100 µm Control
STT-50 µm Substrate
STT-50 µm Control
STT-20 µm Substrate
STT-20 µm Control
TT-100 µm Substrate
TT-100 µm Control
Current (A)
E (V)
0 min
60 min
120 min
180 min
240 min
300 min
360 min
420 min
480 min
540 min
600 min
660 min
720 min
780 min
840 min
900 min

iii) Figure 5-6

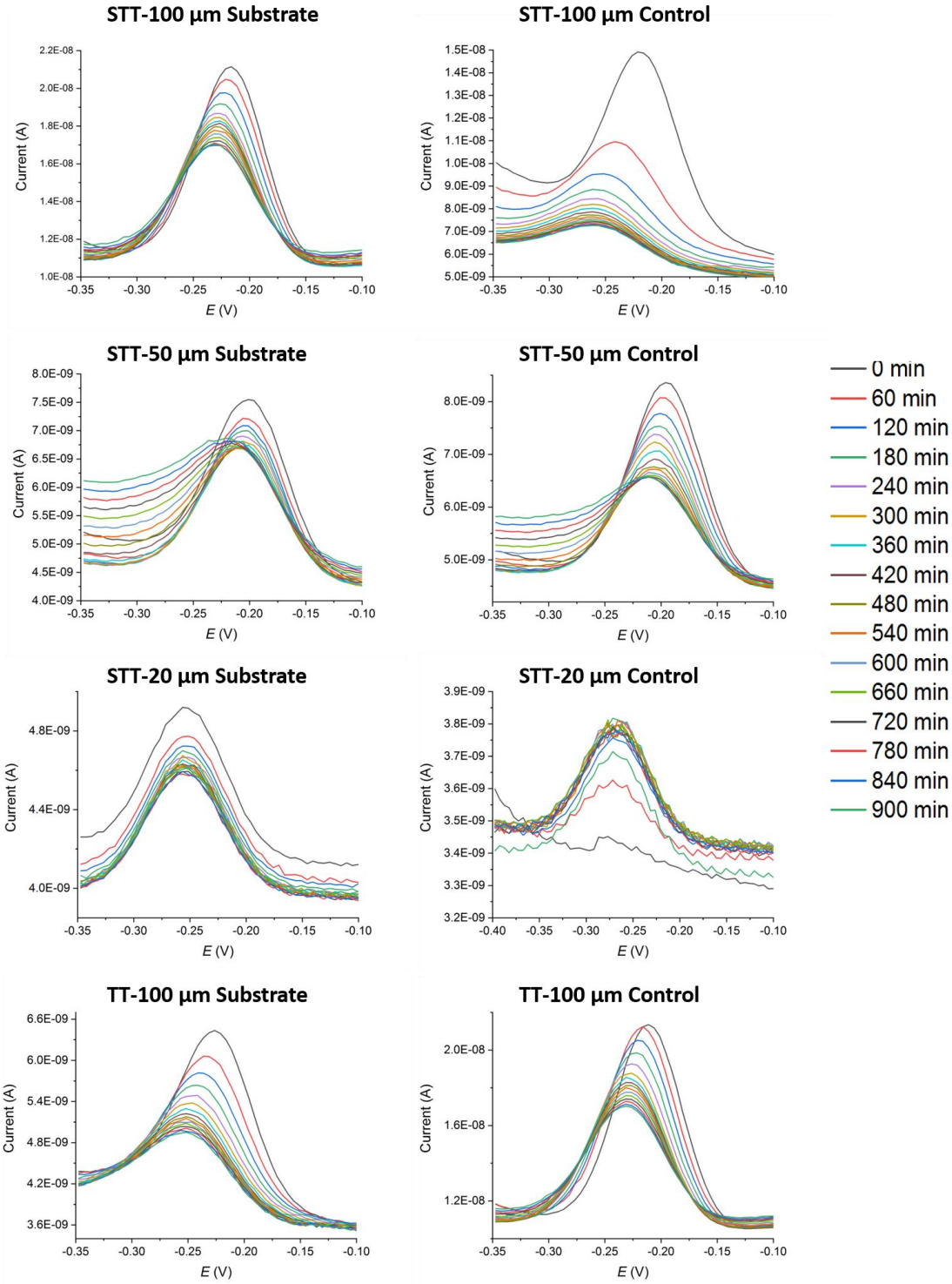

Analyst

ROYAL SOCIETY OF CHEMISTRY

PAPER

View Article Online
View Journal | View Issue

Cite this: *Analyst*, 2020, **145**, 975

Miniaturisation of a peptide-based electrochemical protease activity sensor using platinum microelectrodes

Ahmet Ucar, [a] Eva González-Fernández, [b] Matteo Staderini,[b] Nicolaos Avlonitis,[b] Alan F. Murray,[a] Mark Bradley *[b] and Andrew R. Mount *[b]

Proteases are ideal target biomarkers as they have been implicated in many disease states, including steps associated with cancer progression. Electrochemical peptide-based biosensors have attracted much interest in recent years. However, the significantly large size of the electrodes typically used in most of these platforms has led to performance limitations. These could be addressed by the enhancements offered by microelectrodes, such as rapid response times, improved mass transport, higher signal-to-noise and sensitivity, as well as more localised and less invasive measurements. We present the production and characterisation of a miniaturised electrochemical biosensor for the detection of trypsin, based on 25 μm diameter Pt microelectrodes (rather than the ubiquitous Au electrodes), benchmarked by establishing the equivalent Pt macroelectrode response in terms of quantitative response to the protease, the kinetics of cleavage and the effects of non-specific protein binding and temperature. Interestingly, although there was little difference between Au and Pt macroelectrode response, significant differences were observed between the responses of the Pt macroelectrode and microelectrode systems indicative of increased reproducibility in the microelectrode SAM structure and sensor performance between the electrodes, increased storage stability and a decrease in the cleavage rate at functionalised microelectrodes, which is mitigated by measurement at normal body temperature. Together, these results demonstrate the robustness and sensitivity of the miniaturised sensing platform and its ability to operate within the clinically-relevant concentration ranges of proteases in normal and disease states. These are critical features for its translation into implantable devices.

Received 18th November 2019,
Accepted 3rd December 2019

DOI: 10.1039/c9an02321f

rsc.li/analyst

Introduction

Proteolytic enzymes such as proteases and their dysregulation are widely recognised for playing significant roles in many disease states.[1] As such, they are attracting widespread attention as key biomarkers of disorders including cardiovascular diseases, HIV, Alzheimer's disease, thrombosis, diabetes and cancer.[2–9] Therefore, the development of both sensitive and selective assays and sensors that monitor protease activity has generated considerable interest. According to Ong *et al.*, these can be classified into two main groups: homogeneous assays (that include those based on colorimetry, mass spectrometry and fluorescence resonance energy transfer) and heterogeneous systems (that include electrochemical assays, surface-enhanced Raman scattering and surface plasmon resonance).[2]

In heterogeneous systems, the probe is typically immobilised on a solid surface (which often provides ready interrogation, signal generation and a detection interface) with the target analyte present in the neighbouring aqueous medium, whereas in homogeneous systems, both probe and analyte are present in the aqueous medium, which can present contamination and detection challenges. The principle of detection for both systems is largely based on protease recognition and catalytic cleavage of a specific peptide sequence attached to a reporter *e.g.* a fluorophore, quantum dot or redox tag. The reporter exerts analyte detection through the generation of an output signal following cleavage by the target protease.[10–13]

Amongst the various methods used for protease sensing, there has been considerable growth in the popularity of electrochemical peptide-based biosensors, particularly those where the peptide-sequence with an attached redox tag is immobilised onto an electrode surface. These sensors offer high sensitivity, rapid response times, ready applicability to computer control and multiplexing, the use of cheap instrumentation, and ease of miniaturisation for point-of-care (PoC) applications.[14] Such electrochemical peptide-based biosensors

[a]*School of Engineering, Institute for Bioengineering, The University of Edinburgh, The King's Buildings, Mayfield Road, Edinburgh EH9 3JL, UK*
[b]*EaStCHEM, School of Chemistry, University of Edinburgh, Joseph Black Building, West Mains Road, Edinburgh, EH9 3FJ, UK. E-mail: a.mount@ed.ac.uk, mark.bradley@ed.ac.uk; Tel: +44 (0)131-650-4747*

typically use a specific substrate peptide as the selective recognition moiety and the protease as the analyte. There is extensive literature reported on protease detection using this approach.[13–22] For example, Liu *et al.* described a method that allowed detection of matrix metalloproteinases (MMPs), whose proteolytic activities have close association with cancer progression, at very low concentrations (with a limit of detection of 3.4 pM).[15] An alternative approach was developed by Lee *et al.* who reported on the reference electrode-free sensing of MMP-9 using the self-gating effect on a concentric electrode system which consisted of an island and enclosing electrode.[22]

We have previously proposed, produced, characterised and optimised a macroelectrode-based sensor system for the detection of protease activity using a self-assembled monolayer (SAM) on an electrode surface, which was successfully translated to the detection of other proteases such as human neutrophil elastase, allowing clinically relevant measurements of its activity in human blood.[20,23] However, the electrodes used in most of these systems are still macroscopic which leads to limitations with respect to sensor performance as well as their applicability to implantation. Smaller, less invasive footprint, microelectrodes offer potential advantages over macroelectrodes that include more rapid diffusion (which can lead to shorter and more controlled response times through enhanced and more reproducible mass transport) and higher signal-to-noise which leads to higher sensitivity; together this makes using microelectrodes an attractive route for electrochemical biosensors.[24,25] In addition, miniaturised technologies offer advantages for biosensor design such as integrated high fidelity manufacturing with lower manufacturing costs per sensor, the ability to work with small quantities of materials and samples and ease of multiplexed measurement options.[26,27] Despite these strong drivers for the development of miniaturised SAM-based electrochemical systems for biosensors for the detection of proteases, although some examples of *in vitro* and/or *in vivo* microelectrode use in biosensing are found in the literature,[28–31] there has been little focus on the comparison of macro- and microelectrodes, especially those that are SAM-based.

The purpose of this study was to investigate the miniaturisation of our sensing platform onto novel Pt-based microelectrodes as a step towards their development and application as implantable sensors. Microelectrode sensors were produced, the resulting properties were optimised and finally evaluated in terms of sensor performance, including determining the kinetics and thermodynamics of enzyme–substrate cleavage and the effects of non-specific protein binding. This performance was compared to the analogous Au and (for the first time) equivalent Pt-based macroelectrode systems.

Experimental

Instrumentation

All electrochemical measurements were carried out using a conventional three-electrode electrochemical cell which was driven by a computer-controlled AutoLab PGstat-30 potentiostat by running the NOVA 1.11 software (Metrohm Autolab B. V., The Netherlands). An in-house built platinum-coated silicon dioxide chip was used as an auxiliary electrode, with 2 mm and 25 μm diameter platinum disc electrodes (IJ Cambria, UK) used as working electrodes for the macro- and microelectrode measurements, respectively. All the working electrode potentials, E, were applied with respect to (and are reported relative to) a Ag|AgCl|KCl (3 M) reference electrode (Bioanalytical Systems, Inc., USA). A Lauda Eco Silver thermostatic bath (VWR International Ltd, UK) with an external pumping system and a water-jacketed glass cell was used to control the temperature of all the experiments conducted at 25 °C or 37 °C.

Reagents and materials

Trypsin (MW 23.4 kDa), bovine serum albumin (BSA), casein, ethanol, 6-mercaptohexanol (MCH), 2,2′-(ethylenedioxy) diethanethiol (DT) and 10× PBS were purchased from Sigma Aldrich (UK) and used as received. All reagents were of analytical grade and all solutions were prepared using protease-free deionised water.

Synthetic methods

Two methylene blue-labelled peptides were synthesised in-house following the synthetic experimental procedures described previously.[20,21] Briefly, the redox labelled peptides (probe substrate and the control) (MB-Phe–Arg–Arg-PEG-6–Cys) were synthesised using Fmoc solid-phase chemistry on a polystyrene resin with a Rink-amide linker. First, cysteine was coupled to the resin, followed by a polyethylene glycol unit containing 6 ethylene glycol units (PEG-6) as a spacer, then a cleavable short peptide sequence (specific to trypsin) (Phe–Arg–Arg (FRR)) and finally the methylene blue redox label (MB). Finally, the probe was cleaved from the resin with a TFA cleavage mixture and purified by RP-HPLC.

Cleaning, pre-treatment and preparation of electrodes

Platinum working electrodes were first immersed in concentrated H_2SO_4 (95%) for 10 min to remove any organic residue on the surface and then successively polished to a progressively finer surface finish using a polishing cloth and a sequence of aqueous slurries containing first 1, then 0.3 and finally 0.05 μm alumina particles (Buehler, Germany). After that, each electrode was subjected to an electrochemical cleaning step by carrying out cyclic voltammetry (CV), performing cycles of E between −0.3 and +1.6 V in 0.1 M H_2SO_4 at a potential scan rate of 100 mV s^{-1} until the characteristic voltammogram of clean platinum was obtained.[32] Extending the established macroelectrode protocol,[20] the surface substrate monolayer was then formed as a mixed SAM (labelled peptide, DT and MCH) on this platinum electrode surface by immersing the electrode overnight at 4 °C in a 40 μM solution of the methylene blue-labelled peptide (either the substrate containing cleavable L-amino acids or the control containing uncleavable D-amino acids) and freshly prepared DT (600 μM for macro-

electrodes, 150 μM for microelectrodes) in ethanol. After washing with ethanol, the resulting SAM-modified electrode was immersed in 1 mM MCH in ethanol (1 h for the macroelectrodes and 10 min for the microelectrodes). It should be noted that these reductions in concentration and/or time in the optimised SAM microelectrode deposition protocol are consistent with the expected enhancement in sensitivity and mass transport kinetics of reactions at microelectrodes. Finally, washing was carried out, firstly with ethanol and then with phosphate-buffered saline (PBS) and the modified electrodes were stored in PBS at 4 °C until use.

Electrochemical sensor measurements

The SAM-modified working electrodes were immersed in 1× PBS (which has an optimum pH of 7.4 for trypsin activity) and subjected to electrochemical measurements using square wave voltammetry (SWV, applying E at a frequency of 60 Hz, with an amplitude of 25 mV and a step potential of 5 mV) until a stable background signal was obtained. After the addition of the target enzyme (trypsin), or the proteins, casein and BSA for characterisation of non-specific binding, the SWV signal was continuously monitored with time. Following the established analysis method for Au macroelectrodes,[20,21] this resulting signal is expressed as the percentage relative change in the SWV peak current with respect to the initial peak current (henceforth called the % signal change).

Results and discussion

Successful SAM modification of both macroelectrode and microelectrode surfaces was first demonstrated by recording cyclic voltammograms (CVs) in ferri/ferrocyanide ($[Fe(CN)_6]^{3-}$/$[Fe(CN)_6]^{4-}$), 1× PBS solution (Fig. 1). Notwithstanding the expected difference of peaks (macroelectrodes) and waves (microelectrodes) in the resulting clean electrode redox responses arising from linear and hemispherical diffusional control, respectively, the CVs recorded before and after the overnight incubation of the electrodes with the probe solution show the expected significant inhibition of the redox reaction of the external redox agent characteristic of blocking SAM layers.

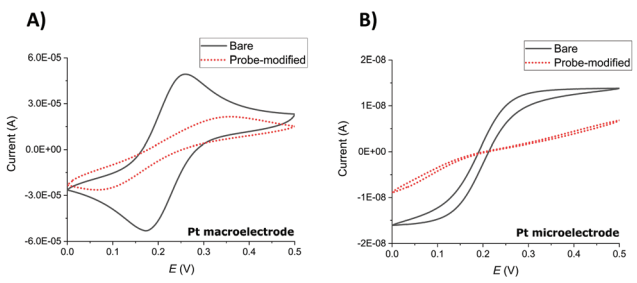

Fig. 1 CVs of (A) a Pt macroelectrode and (B) a Pt microelectrode recorded before (black) and after (red) SAM probe immobilisation in 5 mM potassium ferri/ferrocyanide in 1× PBS. CVs were recorded between potentials of 0 and 0.5 V at a scan rate of 100 mV s^{-1}.

SWV redox peak MB currents of 3.1 ± 1.0 μA (macroelectrodes) and 1.3 ± 0.4 nA (microelectrodes) were obtained in 1× PBS solution ($n \geq 9$ functionalised electrodes). This is consistent with the ratio of macroelectrode to microelectrode area of 6400 and demonstrates that these SWV parameters, previously established and optimised for Au macroelectrodes,[20,23] again provided a clear MB peak and a stable and low background signal required for both Pt macroelectrode and microelectrode SAM analysis in this study.

The electrochemical detection principle is based on the specific proteolytic cleavage of the redox-tagged peptide probes anchored onto the platinum electrode surface by the target protease, trypsin, which should lead to the release of the soluble redox-tagged peptide fragment and a corresponding decrease in the redox peak as measured by the square wave voltammetry (SWV) technique (Fig. 2A). Based on previous macroelectrode optimisation work,[20,21] the sensing layer consisted of a mixed SAM; the probe with the target peptide was tagged with MB and attached to a thiol-terminated PEG-6 spacer, backfilling MCH to minimise pinholes in the SAM layer and co-adsorbent PEG-based DT molecules to support the orientation, specificity and accessibility of the probe on the electrode surface. Two different MB-labelled peptides were used, the L-amino acid sequence for a trypsin-cleavable substrate or the D-amino acid sequence analogue as a trypsin-uncleavable control. The general sequence structure is depicted in Fig. 2B.

Analytical performance comparison of the macro- and microelectrodes as an electrochemical platform for trypsin analysis

In order to compare the analytical characteristics offered by the macro and micro platinum electrodes in protease sensing,

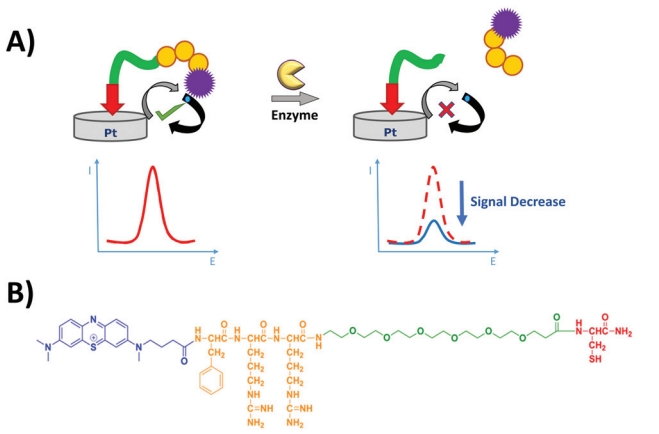

Fig. 2 (A) Principle of detection of the peptide-based electrochemical platform. The protease (trypsin) catalyses the cleavage of the immobilised redox-labelled peptide releasing the redox-containing fragment into solution and leading to a decrease of the electrochemical signal which is measured by SWV. (B) Chemical structure of the probe, containing methylene blue (blue) as the redox tag, phenylalanine–arginine–arginine (orange) as the peptide and PEG-6 (green) as the spacer and cysteine (red) as the anchor.

both macro- and microelectrode surfaces were modified with the mixed SAM as described previously. They were then immersed in buffer solutions containing varying concentrations of trypsin (1–100 nM) and the electrochemical signal was interrogated by SWV with time. The addition of trypsin caused the expected decrease in signal for the macroelectrode (Fig. 3A), with the initial rate of % signal change observed to be proportional to the trypsin concentration (Fig. 3B). Given that this system has been shown to follow Langmuir kinetics,[20] this is to be expected at these relatively low concentrations of trypsin compared to the Michaelis constant, where the proportion of surface covered by the trypsin–protein complex is expected to be low and proportional to the concentration of trypsin and the resulting rate of proteolytic cleavage is determined by this. As predicted by the method developed in previous work,[23] the natural logarithm of $A(t)$, the percentage of signal left to change at time t, calculated as $A(t)$ = [((% signal change at t) − (% signal change as $t \rightarrow \infty$))/((% signal change at t = 0) − (% signal change as $t \rightarrow \infty$ and for the highest trypsin concentration, as [E] → ∞))] × 100%, is proportional to the trypsin concentration, [E] (Fig. 3B inset), which confirms that the response is first order with respect to [E].

An equivalent proteolytic trypsin cleavage behaviour was also recorded when using microelectrodes (Fig. 4A and B and inset), also indicating a first order cleavage process, but it is interesting that the corresponding cleavage rates were significantly slower at the same trypsin concentration when using microelectrodes compared to macroelectrodes.

Microelectrodes have been reported many times to show enhanced diffusional kinetics due to hemispherical diffusion compared to the linear diffusion observed for macroelectrodes.[33] Therefore, it is clear from these observed cleavage rates that this difference in the rate of proteolytic cleavage is not as a result of the rate of trypsin diffusion. Given that the rate must therefore be determined by surface reactions, it is likely that this difference results from the macro- and microelectrode surfaces having a different SAM structure and/or probe or target surface disposition. It was previously noted that macro- and microelectrodes might differ from each other regarding the deposition and disposition of SAMs on their surfaces, which could affect the resulting properties such as electron transfer.[34] Although the trypsin cleavage reaction is not under diffusional control, such distinctions could arise from the differences in diffusional rates during SAM film formation and/or the differences in the uniformity of diffusion to macro and microelectrode surfaces when under diffusional control. A difference in the observed initial SWV peak potentials for macro and microelectrodes of around 70 mV supports a dissimilarity in the average redox environment and overall film structure. It is interesting that higher error bars were obtained for the data sets recorded for the macroelectrodes compared to the microelectrodes, reflected by the errors in the linear fit data (Fig. 3 and 4 insets). This suggests a more reproducible microelectrode film structure and resulting cleavage rate.

Using the observed and expected linear dependency of $\ln A(t)$ to concentration (Fig. 3 and 4 insets), the limit of detection (LOD) for [E] was estimated for each electrode type to be equivalent at 2.5 nM for the macroelectrode and 2.9 nM for the microelectrode with a linear dependency for sensing up to 25 nM. The calculated linear response range and LOD successfully completely cover the clinically relevant range for trypsin levels in, for example, normal patients (11 ± 4 nM), and partially cover that for chronic renal failure (47 ± 25 nM) and chronic pancreatitis conditions (60 ± 27 nM).[35,36]

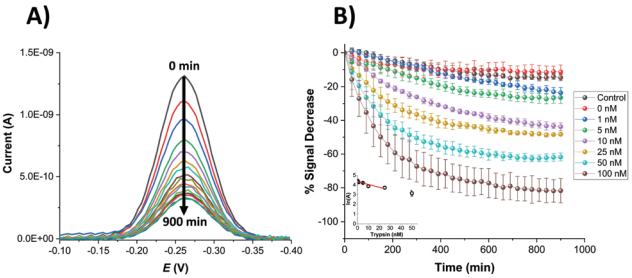

Fig. 4 (A) Typical background-subtracted SWV curves recorded for a SAM-functionalised microelectrode and 100 nM trypsin at different incubation times between 0 and 900 min (with intervals of 60 min) in 1× PBS. (B) Plot of % signal decrease *vs.* time for SAM-functionalised microelectrodes immersed in varying trypsin concentrations in 1× PBS (0, 1, 5, 10, 25, 50, 100 nM for the probe substrate and 100 nM for the negative control probe, containing D-amino acids). All data represent the average (and standard deviations) from (typically) 3 functionalised electrodes. Inset: Natural logarithm of A(%), after 900 min, plotted against the concentration of trypsin. The straight line corresponds to the best linear regression fit ($\ln A$ = −0.030 [trypsin/nM] + 4.354; r^2 = 0.84). The point of [trypsin] = 50 nM was not included again in the fit due to having large replicate errors compared to the other concentrations.

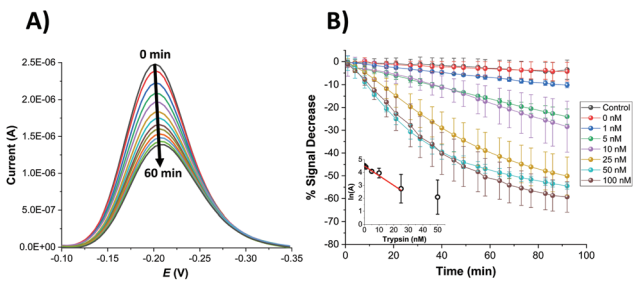

Fig. 3 (A) Typical background-subtracted SWV curves for a SAM-functionalised probe substrate macroelectrode recorded for 100 nM trypsin at different incubation times between 0 and 60 min (with intervals of 5 min) in 1× PBS. (B) Plot of % signal decrease *vs.* time for SAM-functionalised probe macroelectrodes immersed in varying trypsin concentrations in PBS (0, 1, 5, 10, 25, 50, 100 nM for the substrate probe and 100 nM for the negative control probe, containing D-amino acids). All data represent the average (and standard deviations) from (typically) 3 functionalised electrodes. Inset: Natural logarithm of the adjusted signal, A(%), after 92 min, plotted against the concentration of trypsin. The straight line corresponds to the best linear regression fit ($\ln A$ = −0.075 [trypsin]/nM + 4.498; r^2 = 0.96). The point of [trypsin] = 50 nM was not included in the fit due to having large replicate errors compared to the other concentrations.

Kinetic analysis of proteolytic cleavage

Although single time point analysis and linear calibration is a simple method, this does not apply across the entire clinically relevant range for all conditions and time-dependent analysis of multiple data points is likely to be more robust and sensitive. When combined with Michaelis–Menten kinetic analysis, which models the non-linearity of trypsin binding and the resulting response with [E], analysis should be possible over a wider range of trypsin concentration. The measured % signal changes for varying trypsin concentrations were therefore analysed as a function of time using the previously established Michaelis–Menten kinetic model.[20] According to this model, the % signal change, A, is expressed as a variation in the fraction ($\theta(t) = 1 - A(t)$) of the cleavable peptide which has been cleaved at any time, t. Data for each trypsin concentration are then fitted to the equation:

$$\theta = 1 - e^{-k_{\text{eff}}t} \quad (1)$$

Although good fits were obtained to this equation for the Pt macroelectrode system, consistent with our previous observations on gold macroelectrodes, this was not the case for the Pt microelectrode system. Inspection of Fig. 4 indicates that this is likely due to an increase in the fraction of the cleavable probe with increasing [E], as shown by the increasing maximum % signal change as $t \rightarrow \infty$. All data were therefore fitted to eqn (2), which includes the additional concentration-dependent variable, a, which is the fraction of the cleavable peptide that can be cleaved at each trypsin concentration, [E], (with $a \rightarrow 1$ and eqn (2) $\rightarrow$ eqn (1) as [E] $\rightarrow \infty$ and at all [E] for macroelectrodes):

$$\theta = a[1 - e^{-k_{\text{eff}}t}] \quad (2)$$

This simple equation was shown to fit well to all data and generally enabled the extraction of both a and k_{eff} (effective rate constant) values for each trypsin concentration (both Fig. 5, for which $a = 1$ and eqn (2) collapses to eqn (1), and Fig. 6). The only exception was for the lowest [E] in Fig. 6, where over this measurement time range the product $k_{\text{eff}}t$ was sufficiently small for eqn (2) to become effectively linear and only a combined constant ak_{eff} could be determined.

For the estimation of k_{cat} (enzyme turn-over number) and K_{M} (Michaelis–Menten binding constant) values, these extracted k_{eff} values were plotted as a function of trypsin concentration (Fig. 5B and 6B) and fitted to the Michaelis–Menten enzyme cleavage model using the equation:

$$k_{\text{eff}} = k_{\text{cat}}/(1 + K_{\text{M}}/[\text{E}]) \quad (3)$$

This non-linear fitting enabled us to estimate the values of k_{cat} and K_{M} as 0.035 min^{-1} and 19 ± 3 nM for macroelectrodes and, 0.0075 min^{-1} and 15 ± 3 nM for microelectrodes, respectively.

These calculated K_{M} values are comparable to each other and also to previously reported values by Anne *et al.* (~17 nM) and also to our previous work on gold macroelectrodes (28 ± 3 nM).[13,20] These comparable K_{M} values suggest that there is little difference between the thermodynamics of the trypsin binding to the probe substrate to form the enzyme–substrate complex in all cases. However, the markedly lower k_{cat} value indicates that it is the significantly lower kinetics of the reaction of this enzyme–substrate complex on the SAM-functionalised microelectrodes which gives rise to the markedly lower cleavage rates. This indicates that the catalytic efficiency ($k_{\text{cat}}/K_{\text{M}}$) of the enzyme is lower for this surface, and that although absolute and relative enzyme–substrate association and dissociation rates appear similar (which given the size and multiple interactions of the enzyme with the surface is likely to be reflective of more general enzyme-SAM surface association and dissociation) the trypsin–substrate complex cleavage rates are different (which are likely to reflect variations in probe accessibility). Therefore, the rationale for slower proteolytic cleavage observed is lower probe accessibility to the enzyme active site on the SAM microelectrode surface, which would result in lower probe reactivity. It is possible that this (and the fact that

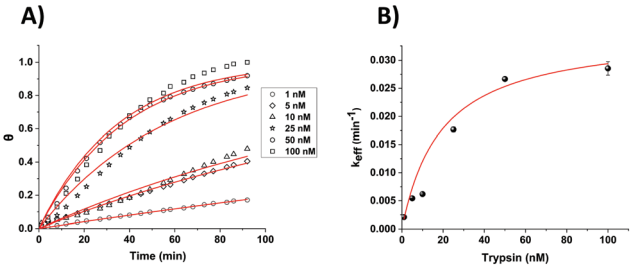

Fig. 5 (A) Calculated fractional cleavage, θ, *vs.* time plots for data for macroelectrode cleavage data from Fig. 3. The data points (from bottom to top) correspond to immersion in varying trypsin concentrations in 1× PBS (namely 1, 5, 10, 25, 50 and 100 nM), whilst each line shows the best fit to eqn (1). (B) Effective rate constant, k_{eff}, as a function of the bulk trypsin solution concentration. Data represented by dots correspond to the experimental data obtained from the fits to the data in (a) and the solid red line shows the fitting processed according to eqn (3).

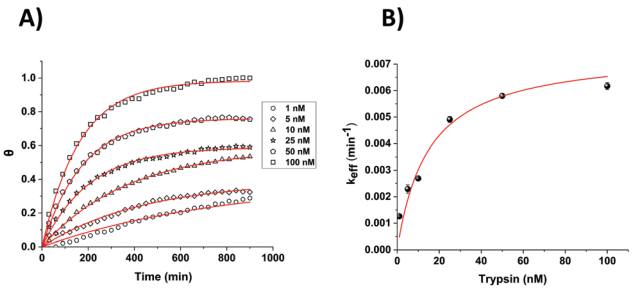

Fig. 6 (A) Calculated fractional cleavage, θ, *vs.* time plots for data for microelectrode cleavage data from Fig. 4. The data points (from bottom to top) correspond to immersion in varying trypsin concentrations in 1× PBS (namely 1, 5, 10, 25, 50 and 100 nM), whilst each line shows the best fit to eqn (2) from which values of a = 0.39, 0.39, 0.58, 0.59, 0.76 and 0.98 respectively have been obtained. (B) Effective rate constant, k_{eff}, as a function of the bulk trypsin solution concentration. Data represented by dots correspond to the experimental data obtained from the fits to the data in (a) and the solid red line shows the best iterative fit to eqn (3).

$a < 1$ in eqn (2) for microelectrodes) is due to the relative inaccessibility of the enhanced proportion of the probe nearer to the electrode edge, due to the dramatic increase in the amount and importance of edge per unit area on decreasing from the macro to the microelectrode dimension. This is in addition to the uncleavable subset of the immobilised peptides at all [E] for both electrode types, previously attributed to electrode roughness and probe orientation variation as the sources of local site inaccessibility.[21,23]

It is clear that this analysis method has now extended the trypsin measurement range to 100 nM, covering the clinically relevant range even for chronic pancreatitis conditions (60 ± 27 nM).

Characterisation of selectivity for the microelectrodes

In order to assess the selectivity of the miniaturised trypsin sensor, the modified microelectrodes were exposed to solutions containing BSA and casein, as models for evaluating the potential for interference in real-world samples arising from non-specific binding of proteins. Fig. 7 shows the % signal decrease of both the substrate (orange) and the control (cyan) SAM structures upon the addition either of the non-specific proteins or the target enzyme trypsin. Although there was a significant amount of signal decrease recorded for both casein and BSA at these very long measurement times, no statistically significant difference between the substrate and control probe responses was observed, which confirms that the signal decrease in both cases was due to non-specific binding occurring presumably due to the consequent reduction in probe flexibility that hinders the redox tag–electrode interaction and therefore, the redox activity. This is in contrast to the maximum signal decrease of ~80% recorded for substrate-modified surfaces upon the addition of trypsin, which was markedly and statistically different to the relatively small response of the control-modified probe surface. This clear difference highlights that the proposed microelectrode-based sensing system is highly selective towards trypsin, and that a combination of substrate and control measurement offers potential for direct measurements in real-world samples containing proteins.

Effect of temperature on microelectrode-based proteolytic cleavage

It is known that temperature has an important role in the functional activity characteristics of most enzymes.[37] Therefore, the kinetics of proteolytic trypsin cleavage was determined on the microelectrode-based sensor not only at room temperature (25 °C) but also at the clinically relevant normal body temperature (37 °C). Fig. 8A shows the comparative signal decrease recorded for both control- and substrate-modified microelectrodes at these temperatures with time. For both temperature cases, it is clearly seen that the signal decrease for the trypsin-cleavable substrate-modified electrodes is higher than the control-modified electrodes, which again demonstrates the trypsin selectivity of the sensor. A higher rate of signal decrease (~30% after 200 min) was observed for the control-modified surfaces at 37 °C, compared to that (~10% after 200 min) recorded at 25 °C, which is indicative of an enhanced detachment and loss of the probe from the surface at these elevated temperatures. The fact that this is an additional and parallel process also present in the substrate-modified surfaces which, like trypsin cleavage, results in probe signal loss is shown by subtracting the time dependent control-modified electrode response from that of the substrate-modified electrode. This was then converted to fractional cleavage, θ and $A(t)$ following the same process as detailed before, but in this case this was normalised to the signal for these data as $t \rightarrow \infty$ at this value of [E] (Fig. 8B). This shows the expected characteristic change in signal with time due only to probe loss arising from trypsin cleavage, as shown by the good fit to eqn (2) (which is equivalent to eqn (1), as this normalisation by definition fixes a as 1 in eqn (2)) (Fig. 8B). This fit gives k_{eff} = 0.082 ± 0.004 min^{-1} at 37 °C, which is around four-times larger than the 0.021 ± 0.002 min^{-1} obtained at 25 °C. This enhancement in kinetics is consistent with the previously reported work,[38]

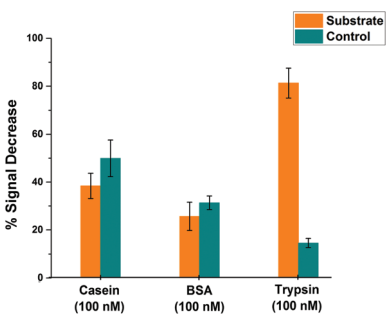

Fig. 7 Comparative % signal decrease recorded for SAM-functionalised microelectrodes after 900 minutes upon the addition of 100 nM trypsin or non-specific binding proteins; casein and BSA for both substrate- (orange) and control-modified (cyan) sensing layers. Average data and error bars are typically from 3 individual SAM sensing layers.

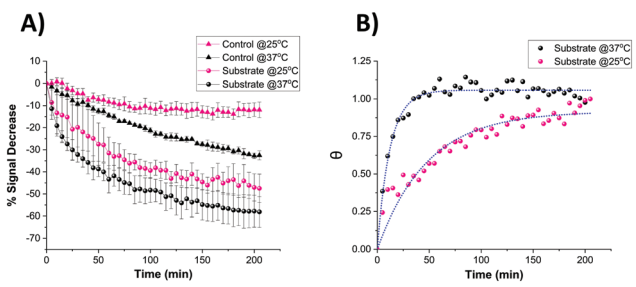

Fig. 8 (A) Comparative signal decrease *vs.* time curves recorded for the miniaturised sensor upon the addition of 100 nM trypsin in 1× PBS at 25 °C (pink) and 37 °C (black) for both control- (triangle) and substrate-modified (circle) microelectrodes. (B) Calculated fractional cleavage, θ, *vs.* time plots for control-subtracted substrate data from (A). The data points correspond to temperatures of 25 °C (pink) and 37 °C (black) whilst the green dotted lines show the best iterative fits to eqn (1) with k_{eff} = 0.021 ± 0.002 min^{-1} and 0.082 ± 0.004 min^{-1} respectively.

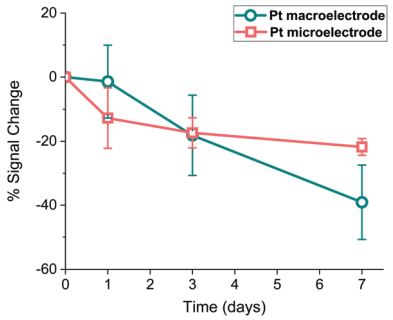

Fig. 9 Percentage signal change recorded for probe-modified Pt macroelectrodes (circles, cyan) and microelectrodes (squares, pink) when stored in 1× PBS at 4 °C for 7 days. Mean signal losses and associated errors recorded after 7 days are 2.14 ± 1.72 μA (macroelectrodes) and 0.24 ± 0.06 nA (microelectrodes).

which suggests an activation energy of around 90 kJ mol^{-1} and indicates the potential for markedly faster trypsin measurement *in vivo* on implanted microelectrodes. It is also worth noting that the undesirable need for control data subtraction arising from the significant parallel probe loss at normal body temperature could be addressed by use of a stronger tri-branched thiol anchor as previously demonstrated on a similarly functionalised electrode surface.[39]

Characterisation of sensor storage stability

It is widely accepted that the storage stability is quite significant for SAM-based biosensors and much effort is being devoted in the literature to enhancing this storage lifetime.[40] Therefore, Pt macro- and microelectrodes were modified with the probe as detailed above and their storage stability at 4 °C was investigated by monitoring their SWV signal over one week period. Fig. 9 shows that the macroelectrodes showed a higher rate of decrease in signal (~40%) than the microelectrodes (~20%) over this period. This amount of decrease observed in the Pt macroelectrodes was also consistent with the previous work,[39] where the storage stability of Au macroelectrodes was assessed for 30 days, confirming that Au or Pt macroelectrode surfaces do not differ significantly in this respect. Additionally, there is some evidence that the drop in the signal on microelectrodes occurs within one day, with little evidence of a statistically significant decrease after this. Again, there is also more variation between individual electrodes in the macroelectrode set, compared to the microelectrode set. This supports the suggestion that more reproducible as well as durable SAM probes are formed on these miniaturised electrodes.

Conclusions

This paper presents results which demonstrate the successful development of a peptide-based electrochemical microelectrode biosensor system for protease detection. Using a previously developed detection mechanism based on the signal change due to the proteolytic cleavage by trypsin of a SAM-immobilised peptide sequence resulting in the loss of the redox tag, the performance of this miniaturised electrode in terms of trypsin detection was assessed and compared to the results of previously reported (gold) and new (platinum) macroelectrodes. These comparisons demonstrated the feasibility of using microelectrodes, with comparable analytical performance being observed in terms of target binding and specificity, and with enhanced reproducibility of the response between electrodes, which we attribute to the enhanced reproducibility of SAM film formation and the resulting structure. We have also shown insensitivity to the non-specific adsorption of proteins through comparison of the responses of control and substrate systems, showing its potential for measurement in natural biological media. This system was also shown to give a quantitative response across a measured concentration range which encompassed the clinically relevant concentration range for trypsin detection for normal and diseased states, and fits well to a Michaelis–Menten surface cleavage model, which enabled the estimation of k_{cat} and K_M values and the ready extraction of trypsin concentration from measured signals. Some interesting differences were also observed between the microelectrode and macroelectrode systems, attributed to the differences in the SAM film structure. First the reproducibility of response was enhanced on microelectrodes, indicating less variability in SAM formation and structure. It is to be recognised that analysis of additional microelectrode data collected across this concentration range should further increase the accuracy of modelling and concentration determination. Secondly the overall cleavage rate was seen to be markedly slower at room temperature on microelectrodes, as a result of a slower trypsin-substrate cleavage rate. Although this was significantly increased at normal body temperature, reducing required measurement times, future work will focus on minimising response times and translating these findings to electrode-on-silicon chip technologies.

Conflicts of interest

There are no conflicts to declare.

Acknowledgements

This work was supported by funding from the UK Engineering and Physical Sciences Research Council (EPSRC), through the Implantable Microsystems for Personalised Anti-Cancer Therapy (IMPACT) programme grant (EP/K034510/1). AU acknowledges the doctoral scholarship from the Republic of Turkey, Ministry of National Education through the YLSY programme.

Data used within this publication can be accessed at: https://doi.org/10.7488/ds/2720.

Notes and references

1 H. Neurath and K. A. Walsh, *Proc. Natl. Acad. Sci. U. S. A.*, 1976, **73**, 3825–3832.

2 I. L. H. Ong and K.-L. Yang, *Analyst*, 2017, **142**, 1867–1881.
3 R. D. A. Wilkinson, R. Williams, C. J. Scott and R. E. Burden, *Biol. Chem.*, 2015, **396**, 867–882.
4 Y. Hua and S. Nair, *Biochim. Biophys. Acta, Mol. Basis Dis.*, 2015, **1852**, 195–208.
5 J. Yuan and B. A. Yankner, *Nature*, 2000, **407**, 802–809.
6 H. Haim, I. Salas and J. Sodroski, *J. Virol.*, 2013, **87**, 1884–1889.
7 A. Doucet and C. M. Overall, *Mol. Aspects Med.*, 2009, **29**, 339–358.
8 S. H. Havale and M. Pal, *Bioorg. Med. Chem.*, 2009, **17**, 1783–1802.
9 J. E. Koblinski, M. Ahram and B. F. Sloane, *Clin. Chim. Acta*, 2000, **291**, 113–135.
10 E. Pazos, O. Vázquez, J. L. Mascareñas and M. E. Vázquez, *Chem. Soc. Rev.*, 2009, **38**, 3348.
11 T. Zeng, T. Zhang, W. Wei, Z. Li, D. Wu, L. Wang, J. Guo, X. He and N. Ma, *ACS Appl. Mater. Interfaces*, 2015, **7**, 11849–11856.
12 S. B. Lowe, J. A. G. Dick, B. E. Cohen and M. M. Stevens, *ACS Nano*, 2012, **6**, 851–857.
13 A. Anne, A. Chovin and C. Demaille, *Langmuir*, 2012, **28**, 8804–8813.
14 M. Puiu and C. Bala, *Bioelectrochemistry*, 2018, **120**, 66–75.
15 G. Liu, J. Wang, D. S. Wunschel and Y. Lin, *J. Am. Chem. Soc.*, 2006, **128**, 12382–12383.
16 H. Xiao, L. Liu, F. Meng, J. Huang and G. Li, *Anal. Chem.*, 2008, **80**, 5272–5275.
17 J. Adjémian, A. Anne, G. Cauet and C. Demaille, *Langmuir*, 2010, **26**, 10347–10356.
18 N. Zhao, Y. He, X. Mao, Y. Sun, X. Zhang, C. Z. Li, Y. Lin and G. Liu, *Electrochem. Commun.*, 2010, **12**, 471–474.
19 D.-S. Shin, Y. Liu, Y. Gao, T. Kwa, Z. Matharu and A. Revzin, *Anal. Chem.*, 2012, **85**, 220–227.
20 E. González-Fernández, N. Avlonitis, A. F. Murray, A. R. Mount and M. Bradley, *Biosens. Bioelectron.*, 2016, **84**, 82–88.
21 E. González-Fernández, M. Staderini, N. Avlonitis, A. F. Murray, A. R. Mount and M. Bradley, *Sens. Actuators, B*, 2018, **255**, 3040–3046.
22 J. W. Lee, J. Y. Yun, W. C. Lee, S. Choi, J. H. Lim, H. Jeong, D. S. Shin and Y. J. Park, *Sens. Actuators, B*, 2017, **240**, 735–741.
23 E. González-Fernández, M. Staderini, A. Yussof, E. Scholefield, A. F. Murray, A. R. Mount and M. Bradley, *Biosens. Bioelectron.*, 2018, **119**, 209–214.
24 J. Heinze, *Angew. Chem., Int. Ed. Engl.*, 1993, **32**, 1268–1288.
25 R. J. Forster, *Chem. Soc. Rev.*, 1994, **23**, 289–297.
26 B. Derkus, *Biosens. Bioelectron.*, 2016, **79**, 901–913.
27 L. Soleymani and F. Li, *ACS Sens.*, 2017, **2**, 458–467.
28 E. Llaudet, S. Hatz, M. Droniou and N. Dale, *Anal. Chem.*, 2005, **77**, 3267–3273.
29 K. Wassum, V. Tolosa, J. Wang, E. Walker, H. Monbouquette and N. Maidment, *Sensors*, 2008, **8**, 5023–5036.
30 R. E. Ionescu, C. Fillit, N. Jaffrezic-Renault and S. Cosnier, *Biosens. Bioelectron.*, 2008, **24**, 489–492.
31 L. Shi, X. Rong, Y. Wang, S. Ding and W. Tang, *Biosens. Bioelectron.*, 2018, **102**, 41–48.
32 L. Jacobse, S. J. Raaijman and M. T. M. Koper, *Phys. Chem. Chem. Phys.*, 2016, **18**, 28451–28457.
33 K. Stulík, C. Amatore, K. Holub, V. Marecek and W. Kutner, *Pure Appl. Chem.*, 2000, **72**, 1483–1492.
34 M. Sheffer, V. Vivier and D. Mandler, *Electrochem. Commun.*, 2007, **9**, 2827–2832.
35 J. M. Artigas, M. E. Garcia, M. R. Faure and A. M. Gimeno, *Postgrad. Med. J.*, 1981, **57**, 219–222.
36 W. S. Ruddell, C. J. Mitchell, I. Hamilton, J. P. Leek and J. Kelleher, *Br. Med. J.*, 1981, **283**, 1429–1432.
37 G. N. Somero, *Annu. Rev. Ecol. Syst.*, 1978, **9**, 1–29.
38 E. D. Stevens and J. M. McLeese, *Am. J. Physiol.: Regul., Integr. Comp. Physiol.*, 1984, **246**, 487–494.
39 M. Staderini, E. González-Fernández, A. F. Murray, A. R. Mount and M. Bradley, *Sens. Actuators, B*, 2018, **274**, 662–667.
40 F. Kuralay, S. Campuzano and J. Wang, *Talanta*, 2012, **99**, 155–160.